UNIVERSITY OF SOUTHAMPTON

FACULTY OF ENGINEERING AND THE ENVIRONMENT

Institute of Sound and Vibration Research

Propagation In Waveguides With Slowly Changing Variability

by

Adriano Todorovic Fabro

Thesis for the degree of Doctor of Philosophy

February, 2014

UNIVERSITY OF SOUTHAMPTON

ABSTRACT

FACULTY OF ENGINEERING AND THE ENVIRONMENT

INSTITUTE OF SOUND AND VIBRATION RESEARCH

Thesis for the degree of Doctor of Philosophy

PROPAGATION IN WAVEGUIDES WITH SLOWLY CHANGING VARIABILITY

by Adriano Todorovic Fabro

This thesis investigates structural wave propagation in waveguides with randomly varying material and geometrical properties along the axis of propagation, specifically when the properties vary slowly enough such that there is no or negligible backscattering due to any changes in the propagation medium. This variability plays a significant role in the so called mid-frequency region, but wave-based methods are typically only applicable to homogeneous and uniform waveguides.

An analytical tool, the WKB (after Wentzel, Kramers and Brillouin) approximation, is used in order to find a suitable generalisation of the wave solutions for finite waveguides undergoing longitudinal and flexural motion. An alternative wave formulation approximation with piecewise constant properties is derived so that the internal reflections are taken into account, requiring a discretisation of the waveguide. In addition, a Finite Element approximation using an enriched hierarchical basis or Hierarchical Finite Element (HFE) is created, where the variability in the properties of the waveguide is included within the element formulation, thus not requiring a mesh discretisation as opposed to a standard FE solution.

A Fourier like series, the Karhunen-Loeve expansion, is used to represent homogeneous and spatially correlated randomness and statistics of the natural frequencies and forced response are derived.

Experimental validation is carried out, using firstly a cantilever beam with small masses attached along its length according to a given random field. In the second experiment, an ensemble of glass-fibre reinforced free-free beams, whose variability is characterised by light transmissibility images, is measured.

It has been found that the correlation length of the random fields or the scale of the spatial fluctuation is shown to play an important role in the dynamic response statistics. Moreover, the proposed formulations show good agreement with the standard approaches but at a fraction of the computational cost, providing a good framework for uncertainty quantification.

Contents

List of tables

List of figures

DECLARATION OF AUTHORSHIP

I, Adriano Todorovic Fabro

declare that the thesis entitled

Propagation on Waveguides with Slowly Changing Variability

and the work presented in the thesis are both my own, and have been generated by me as the result of my own original research. I confirm that:

- this work was done wholly or mainly while in candidature for a research degree at this University;
- where any part of this thesis has previously been submitted for a degree or any other qualification at this University or any other institution, this has been clearly stated;
- where I have consulted the published work of others, this is always clearly attributed;
- where I have quoted from the work of others, the source is always given. With the exception of such quotations, this thesis is entirely my own work;
- I have acknowledged all main sources of help;
- where the thesis is based on work done by myself jointly with others, I have made clear exactly what was done by others and what I have contributed myself;
- parts of this work have been published as:
    - A.T. Fabro, N.S. Ferguson and B. R. Mace, *Wavenumber and natural frequency statistics of waveguides with spatially correlated material variability from finite element analysis*, ICSV2011, Rio de Janeiro, 2011;
    - A. T. Fabro, N. S. Ferguson, J. M. Gan, B. R. Mace, S. Bickerton, M. Battley, *Vibration response statistics of fibre composite panels from optical translucence*, DYNACOMP2012, Arcachon, France, 2012;

- A.T. Fabro, N.S. Ferguson and B. R. Mace, *Natural Frequency Statistics of Waveguides with Slowly Changing Spatially Correlated Material Variability*, ISMA2012, Leuven, Belgium, 2012.

Siged: ……..

Date:…….

Acknowledgements

I would like to thank Doctor Neil Ferguson and Professor Brian Mace for their invaluable guidance and supervision in this work, as well as for their support, friendship and patience.

I also appreciate the helpful comments given by Doctor Maryam Tehrani and Professor Barry Gibbs for their much helpful comments and suggestions on the work. I also appreciate the helpful interaction with all those at ISVR that I had the opportunity to discuss with about this work.

I also would like to thank the friends and colleagues from ISVR for the invaluable moments of happiness and laughs.

I would to acknowledge the financial support given by the EU FP7 ITN Marie Curie grant and the Brazilian National Research Council (CNPq) scholarship, which allowed me to pursue this research.

And also, I would like to thank my wife Daniela, for her kind hearted love, support, help and understanding.

Abbreviations

FE	Finite Element
HFE	Hierarchical Finite Element
WKB	Wentzel, Kramers and Brillouin
KL	Karhunen-Loeve
MC	Monte Carlo
PDF	Probability Density Function
COV	Coefficient of Variation
LDV	Laser Doppler Vibrometer
CSM	Chopped Strand Mat
STD	Standard Deviation
DSLR	Digital Single Lens Reflex
EB	Euler-Bernoulli
WFE	Wave and Finite Element

Symbols

$\mathbf{a}, \mathbf{b}, \mathbf{q}$	Wave amplitude vectors
b	Correlation length
f	Probability density function
i	Imaginary number
k	Wavenumber
A	Cross section area
D	Local plate bending stiffness
E	Young's modulus of elasticity
$\mathbf{G}$	Scattering Matrix
H	Gaussian zero mean random field
I_{yy}	Area moment of inertia
$\mathbf{M}$	Mass matrix
$\mathbf{K}$	Stiffness matrix
$\mathbf{N}$	Shape functions matrix
N_{KL}	Number of terms in the KL expansion

Greek symbols

γ	Amplitude change of a travelling wave
δ	Attenuation constant in the plate strip
ε	Phase Change in the plate strip
θ	Phase change of a travelling wave
λ	Eigenvalue
ρ	Mass density
σ	Dispersion coefficient
ν	Poisson ratio
ξ	Gaussian zero-mean and standard unit random variable
ω	Angular frequency
$\mathbf{\Gamma}$	Boundary reflection matrix
$\mathbf{\Lambda}$	Propagation Matrix

Superscripts

$+$	Positive going waves
-	Negative going waves
T	Transpose of a vector or matrix

Subscripts

0	Nominal homogeneous property
e	Element matrix
m	m^{th} wave mode
ij	The i^{th} row and j^{th} column element of the corresponding matrix

Other symbols

$\langle\cdot\rangle$	Average

1. Introduction

1.1 Introduction

Manufacturing processes often result in variability of properties compared to the nominal designed product. As the requirements for optimum design increase and include a broader frequency range, it is important to improve the prediction capability. Element based techniques, like the Finite Element (FE) method [1, 2], are the main prediction tool for structural dynamics in industrial applications. However, the higher the frequency range under analysis using FE, the finer the mesh requirement, with increased computational cost. The pollution effect, i.e. when the accuracy of the FE solution degenerates as the wavenumber increases [3], must also be taken into account, further increasing the computation cost. In addition, even small variability starts to play an important role such that the deterministic FE approach by itself is no longer able to predict the structure's behaviour. It is then necessary to add some level of random description and therefore increasing even more the computational cost.

A typical industrial problem is represented, in Figure 1.1, by a simplified car model, modelled using FE, where one is interested in calculating the mechanical energy in different parts of the assembly, identified by the areas A1 to A12. The force excitation is applied within the frequency range from 0 to 300 Hz. It is randomly distributed over the firewall panel (A7), which is an important noise transmission path between the engine and the passenger cavity. It is also considered that the firewall panel has a known spatial distribution for the variability of the Young's modulus, given by the manufacturing processes, that can change for assembled car. Three typical samples of this spatial distribution are given in Figure 1.2.

If the effects of the material variability on the dynamic response of all of the possible cars produced are evaluated, the typical 95% percentile of frequency response of the mechanical energy in one the panels is given by Figure 1.3. This result is calculated by running the FE analysis typically hundreds or even thousands of times, each time using different samples with the same statistical features of the material distribution of the firewall panel. Depending on the size of the FE model, this kind of procedure, also known as Monte Carlo sampling [4], can be computationally too costly, or even prohibitive.

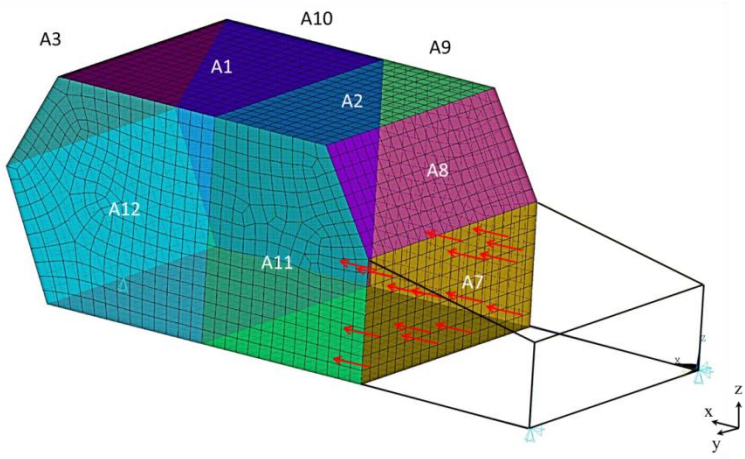

Figure 1.1. Simplified car model FE mesh for the panels and identifications of the components analyzed. Red arrows indicate the excitation points and the blue triangles the constrained nodes

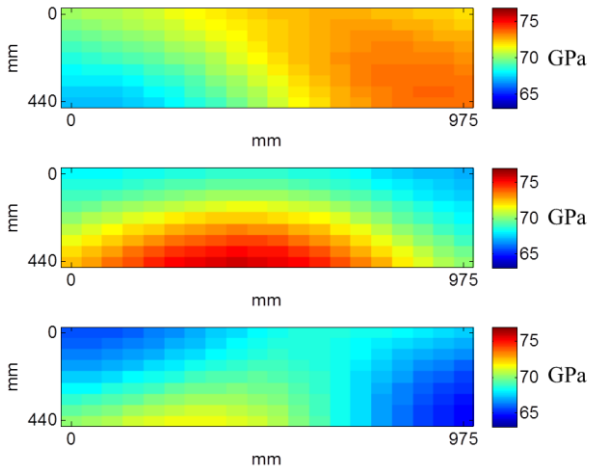

Figure 1.2. Three typical samples of the Young's modulus spatial distribution in the firewall plate (A7) with the same statistical features.

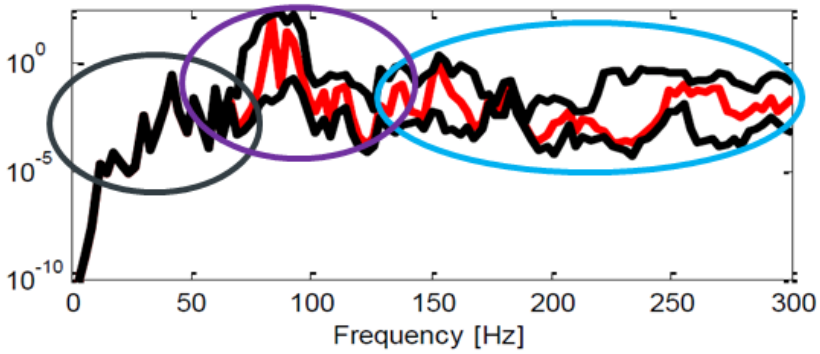

Figure 1.3. 95% percentile of the potential energy in the windshield and three distinct frequency bands highlighted: low frequency (black), mid frequency (magenta) and high frequency (cyan).

However, a closer inspection of the results in Figure 1.3 shows three distinguishable frequency bands [5, 6]. One first band is given by the low-frequency range, with low modal density and low sensitivity to the given variability. In this region, purely deterministic models and a FE-like approach are mainly applicable, with no need of a Monte Carlo-like sampling procedure. The second region is given by the high frequency range, with high modal density and highly sensitive to the given variability. In this region, energy-like methods (for instance, Statistical Energy Analysis – SEA [7]) are well suited and have been successfully applied. In between these two regions there is the mid-frequency range, where individual modal behaviour is still distinguishable and affected by variability. It is too high in frequency to be efficiently treated using FE methods, but not high enough for energy-based methods to be applicable.

Wave-based methods are one of the tools that have been studied in order to attempt to bridge this gap in the prediction capabilities, by increasing computational efficiency, and therefore extending the applicability of the deterministic models to higher frequencies.

Examples of such approaches include the Wave Based Method (WBM) [6, 8, 9], based on the indirect Trefftz approach, spectral element methods [10, 11], that uses analytical solutions of waveguides to assemble dynamic stiffness matrices for waveguides, the Semi Analytical FE method [12], that uses a FE formulation for the cross section of waveguides and assumes a wave like solution on the travelling wave directions, and the Wave Finite Element (WFE) method [13-15], that applies the theory of periodic structures for homogeneous waveguides using a FE model of the cross section. Most recently, a numerical approach, using the WFE method, has been proposed by Ichchou [16] to include spatially homogeneous variability in waveguides by using a first order perturbation [17, 18]. However, most of the wave base methods assume that waveguide properties are homogeneous in the direction of the travelling wave [19-21], limiting the application of such approaches A generalized approach for one-dimension waveguides in terms of propagation, reflection and transmission can be found in [22].

1.1.1 Spatially correlated random variability

Structural uncertainty modelling often involves modelling of the spatial random variability. It becomes even more relevant, when dealing with, for instance, composite materials [23-26]. One of the available tools to model spatially correlated variability is

the random field theory [27-30]. They are multidimensional random processes and can be used to model spatially distributed variability using a probability measure, and ideally their representation should succeed in capturing the essential features of a complex random phenomenon in terms of a minimum number of physically meaningful and experimentally accessible parameters[27].

A random field $H(x,p)$ can be defined as a collection of random variables indexed by a continuous parameter $x \in D$, where D describes the system geometry [31]. In other words, for a given position x_0, $H(x_0,p)$ is a random variable, and for a given outcome p, $H(x,p)$ is a realization of the field. The mathematical expectation is usually denoted by $\langle\cdot\rangle$, such that the mean value and the variance of a random variable $X(p)$ are defined as

$$\mu_X = \langle X(p)\rangle = \int_{-\infty}^{\infty} x f_X(x)dx, \tag{1.1}$$

and

$$\sigma_X^2 = \int_{-\infty}^{\infty} (x-\mu_X)^2 f_X(x)dx. \tag{1.2}$$

Moreover, its n^{th} statistical moment is defined as

$$\langle X(p)^n\rangle = \int_{-\infty}^{\infty} x^n f_X(x)dx. \tag{1.3}$$

A random field $H(x,p)$ is said to of second order if completely defined by its mean value μ_H and auto covariance function, or autocorrelation for zero-mean process, defined as

$$C(x_1,x_2) = \langle [H(x_1,p)-\mu_H][H(x_2,p)-\mu_H]\rangle. \tag{1.4}$$

The correlation length is a characteristic parameter of this function and gives the spatial variability of the random field. The larger the correlation length the smoother is the spatial variability, as it is show for a one dimensional case in Figure 1.4. It is also said to be homogeneous if its autocorrelation function depends only on the difference between two positions, i.e. $C(x_1,x_2) = C(x_1-x_2)$. The random field is specifically Gaussian if at any given position x_0, $H(x_0,p)$ is a Gaussian random variable. Figure 1.5 shows different realizations of a zero-mean homogeneous Gaussian random field with the same statistical features, i.e., the same correlation function and correlation length.

Figure 1.4. General effect of the correlation length on the spatial distribution of the random field.

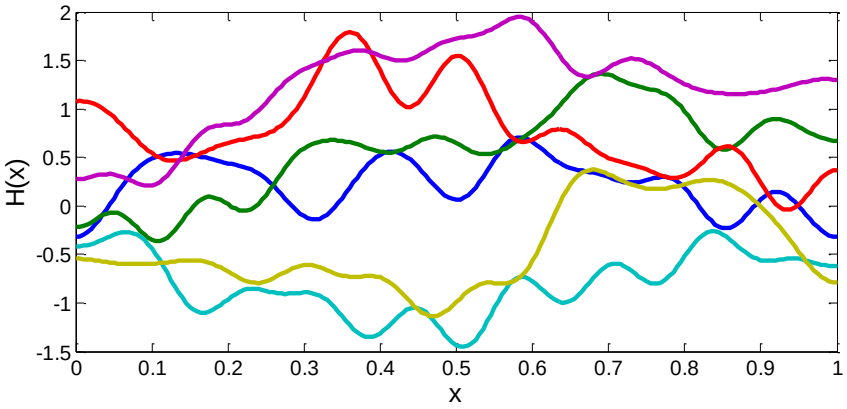

Figure 1.5. Samples of a zero-mean homogeneous Gaussian random field with the same statistical features, i.e., the same correlation function and correlation length.

A solution of the physical problem might require the variability to be incorporated within a spatial discretisation of the physical domain [32]. A number of discretisation methods are available, among them being the midpoint method. This was first introduced by Der Kiureguian [33] and is used in this study. It consists in approximating the random field in a spatial domain, previously discretised by a given mesh, by using a constant, but random, value within each element, or group of elements. This value is given by a sample of the random field specified at the geometrical centre of the element. This approach is very appealing, because it does not require any modifications of the FE code making it suitable to be used with commercial FE in a framework of Monte Carlo sampling.

In addition, a Karhunen-Loeve (KL) expansion [28], a Fourier-like series, provides characterisation of the random field in terms of deterministic eigenfunctions weighted by uncorrelated random variables. For some families of correlation functions and specific geometries, there exist analytical expressions for the KL expansion, but, in general, a numerical approach has to be used [34].

The KL expansion allows significant reduction in the number of random variables required for a random field simulation, since the number of KL modes N_{kl} are usually much smaller the number of elements in the mesh. Moreover the expansion is optimal in a mean square sense [28].

1.1.2 Non-uniform waveguides

Although homogeneous waveguides have been extensively studied, analytical solutions for the waveguides are only possible for very particular cases, and have received much attention for acoustic horns, ducts, rods and beams - e.g. [35-39] - particularly when the variation is small compared to the wavelength. Langley [40] has shown, using a perturbation approach, that the amplitude of a wave travelling along a non-homogeneous one dimensional waveguide changes and then the power flow is conserved. Also addressed was the issue of wave reflection at a cut off section. Lee et al. [41] has shown that the velocity of energy propagation is different from the group velocity for a class of deterministic non-homogeneity in one-dimensional waveguides, such that no wave conversion occurs. Moreover, Scott [42] has also considered the statistics of the wave intensity and phase for a class of one dimensional random waveguides, in specific cases, also considering negligible scattering. Randomness in waveguides has also been considered in the context of SEA. Manohar and Keane [43] have derived expressions for the PDF of the natural frequencies and mode shapes of a class of stochastic rods, given a Gaussian random field, and also the flow of energy between coupled stochastic rods [44].

1.1.3 The WKB approximation

The classical WKB approximation, a method for finding suitable modifications of plane-wave solutions for propagation in slowly varying media [45] when compared to the wavelength, named after Wentzel, Kramers and Brillouin, was initially developed for solving the Schrödinger equation in quantum mechanics. It is also called the semi-classical method [46] or the geometrical optics approximation [45, 47, 48]. The formulation assumes that the waveguide properties vary slowly enough such that there is none or negligible reflections due to local changes, even if the net change is large. The method has been applied in many fields of engineering, including ocean acoustics

[49], acoustics [50-54], structural dynamics [45, 46, 55-57] and also for cochlear models [58, 59].

The application of the WKB, or eikonal approximation, is relatively simple, although it can rapidly become arduous for more complicated structures, and has the advantage of preserving the interpretation of travelling waves. This allows the use of the same systematic approach used for homogenous waveguides, as developed by Mace et al. [22, 60, 61].

Bretherton [62] has extended the approximation for general linear systems, and shown that the variations in the amplitude of the waves along rays are governed by conservation of an adiabatic invariant. The method consists of writing the solution in terms of an asymptotic expansion in powers of a small parameter, using the local wavenumber and wave amplitude, and then matching the asymptotic expansion to a certain order, usually the first order. Pierce [45] has derived WKB solutions for Euler-Bernoulli and Timoshenko beams as well as for thin plates by using a conservation of energy approach, with less mathematic formalism, but which is more physically comprehensive.

However, the WKB approximation breaks down when the travelling wave reaches a local cut-off, or cut on, section. This transition, also known as turning points, leads to an internal reflection, breaking down its main assumption, requiring a different approximation for certain frequency bands (e.g. [47]). This approximation can be done in terms uniformly valid solutions, i.e. solutions also valid for the frequency band away from the cut on frequency, and have been derived using a slight modification on the WKB method for different applications, for instance [50, 53, 63]

1.1.4 Hierarchical Finite Element Method

Another approach that can be used together with a random field formulation, in order to reduce computation cost, is the hierarchical finite element (HFE) formulation [1], also known as p-element formulation. It can also be considered as a special case of the Rayleigh-Ritz method, with a different choice of admissible functions, improving versatility and convergence rate [64]. As opposed to the FE approach, where mesh refinement is required for solutions at high frequencies and conversely smaller wavelengths, the HFE formulation keeps the mesh size fixed and increases the degree of the approximating functions used in the element formulation.

Although, it does not offer the wave interpretation of the wave-based methods, it can be applied to more general cases, like beam [65], shafts [66], plates and cylinders, with different composite laminates or stiffened structures [64, 67, 68]. It consists in enriching the displacement field by a series of polynomial of increasing order, without changing the number of nodes of the element. Different hierarchical shape functions can be used, including of trigonometric functions [69], but usually are applied the Rodrigues's form of the Legendre polynomial [68].

Compared to the standard h-version FE, the hierarchical FE produces smaller mass and stiffness matrices and tends to be computationally more efficient. These are key factors not only when considering the solution in higher frequencies but also in the calculation of response statistics using a sampling method like Monte Carlo sampling.

1.2 Outline of the thesis

The research aims to investigate the propagation phenomenon in waveguides with spatially correlated variability of its geometrical and/or material properties and the influence of this randomness on the wave propagation. The investigation is focused on the Mid-Frequency gap that concerns the region between low-frequency deterministic methods, such as Finite Element (FE) Analysis (numerical method) and high-frequency methods, e.g. energy methods like Statistical Energy Analysis.

In Chapter 1 an introduction is given and relevant literature is reviewed. The thesis is outlined and contributions of this thesis are then briefly described.

In Chapter 2 a one dimensional waveguide undergoing longitudinal vibration is modelled using the WKB approximation for the wave propagation. A formulation for the wavenumber is given considering slowly varying properties, i.e. the material and geometrical changes along the waveguide are such that there is no backscattering from a propagating wave. It is assumed that when propagating over a finite distance, the total phase change of a wave is given by the integral of the spatially distributed wavenumber. This is used to find an analytical expression for the natural frequencies and input mobility of a finite length thin rod. In addition, a formulation, considering piecewise constant properties along the waveguide propagation axis, is presented together with expressions for the natural frequencies and input mobility. This formulation, unlike the previous one, takes internal reflections into account, and is used for comparison with the previous results. For comparison, a FE approximation using an enriched hierarchical

basis or Hierarchical Finite Element (HFE) is also presented, where the variability in the properties of the waveguide is included in the element formulation. A FE model of the waveguide, with the element properties assumed piecewise constant, is also assembled and included for comparison. A single sample of a random field, for cases with different spatial properties, is used to carry out the numerical analysis, so that all the formulations are purely deterministic.

In Chapter 3 a one dimensional waveguide undergoing flexural vibration is modelled using an analytical formulation for wave propagation and a formulation for the wavenumber is given also considering slowly varying properties. Both propagating and evanescent waves are considered. Analytical expressions for the natural frequencies of a finite length beam are given, dependent on the evaluation of transcendental equations. Expressions for the input mobility are also presented, expressed using the evaluation of the integral of the spatially distributed wavenumber. The piecewise constant formulation and the HFE approach are also extended for the flexural case. A FE model of the waveguide, with the element properties assumed piecewise constant, is also assembled for comparison, and using a large number of elements for accurate bandwidth prediction.

In Chapter 4 a plate strip with simply supported edges undergoing flexural vibration is modelled using the same approach, considering slowly varying properties. This assumption is used in order to find an analytical expression for the natural frequencies, phase change, attenuation and input mobility of a finite rectangular thin plate in bending. The HFE approach is also extended for this case and a FE model, with the element properties assumed piecewise constant, is assembled for comparison. This problems differs from the previous in that the structure is now two-dimension in terms of waves.

In Chapter 5 the spatially varying material properties are considered to be random fields and they are included in the proposed formulations. It means that both the natural frequency and the input mobility, for each frequency, are themselves random variables. Analytical expressions given by the Karhunen-Loeve expansion and a first order approximation are used to derive closed form solutions for the probability density function of the natural frequencies. It is also shown that even when only numerical solutions for the Karhunen-Loeve expansion are available, the proposed approach is well suited for numerically evaluating the expressions for the phase change, in the input mobility, and the integral in the denominator, for the natural frequencies. In this way, it

provides an adequate framework for Monte Carlo simulation using a fraction of the time consumed by the FE analysis of the number of Monte Carlo samples.

In Chapter 6 experimental validations are carried out using two different sets of experiments. The first consists of measuring the natural frequencies of a cantilever beam with added masses along its length. The masses are added according to different correlation lengths in order to approximate a continuous random field with spatially varying density. Results are compared with the presented theory. The second consists of characterising the variability of the natural frequency and mobility in beams made of glass-fibre composite material. The spatial changes of the Young's modulus are first characterised from optical measurements, using a DSLR camera, and then a Gaussian random field model is given, based on the identified correlation length. Results are compared with those predicted by the presented theory.

In Chapter 7 a summary of the work is discussed together with the final conclusions. Moreover, further steps for the research are suggested.

1.3 Contributions of the thesis

The thesis investigated the propagation in waveguides with spatially correlated variability on the direction of the travelling wave and the influence of this randomness on the structural dynamics, within the framework of mid-frequency methods. The original contributions of this thesis are as follows:

- The WKB approximation is presented in terms of propagation matrices, producing a systematic formulation of the free-wave propagation and forced response problem for one-dimensional waveguides, in the same manner as used for homogeneous waveguides.

- Input mobility expressions for a finite length rod, beam and plate strip are derived using the WKB approximation.

- The KL expansion is used to include random spatially correlated variability into the WKB approximation. The correlation length of the random field is used to apply the slowly varying condition required for the WKB assumptions.

- The PDF of the natural frequency of finite length rods, beams and plate strip with spatially correlated material random variability are derived using a first order approximation.

- A piecewise constant wave approach is proposed, in terms of propagating and scattering matrices. The formulation, unlike the WKB approach, takes internal reflections into account, and it is used to calculate the forced response. Also, an approximation is proposed for calculating the natural frequencies, neglecting the internal reflections.

- A novel approach including the KL expansion for the variability in the HFE formulation for rods, beam and thin plate element is proposed and used to calculate the free vibration and forced response. It avoids the element integration procedure that can be computationally costly, for each MC sample, and it is particularly efficient for highly correlated random fields, because it needs fewer terms in the expansion.

- An experimental approach is proposed to assess the influence of material spatial correlation on the statistics of the natural frequency. Masses are attached to a cantilever beam in order to fit continuous mass density random field distributions. Issues regarding this discretisation are discussed, and the results are used to validate the formulations proposed in this thesis.

- A random field model is proposed for the spatial material variability estimated from an experimental setup using light transmissibility measurements of a fibre reinforced panel. This model is used to predict the response statistics of beams made of the composite material, and experimental validation is carried out using mobility measurements from an ensemble of beams.

2. Longitudinal waves in one-dimensional waveguides

2.1 Introduction

In this chapter the key assumption on the propagating wave is made that there is negligible or no backscattering from a longitudinal wave in a one dimensional waveguide with slowly changing material variability, using the WKB approximation. The method is also used as an analytical tool to find asymptotically approximate expressions. The main idea is that it is possible to find suitable generalisation of the wave solutions [45], considering slowly varying properties, in terms of an expression for the wavenumber for a system with distributed properties. All of the results are considered and presented in terms of variability in the Young's modulus, although they can also be extended for varying material density, cross-sectional area, etc., or varying characteristic impedance in general. This is then used to find analytical expressions for the natural frequencies and input mobility of a finite length thin rod, using the same wave formulation for homogeneous waveguides, developed by Mace at al. [22, 60, 61, 70, 71].

In addition, a wave formulation considering piecewise constant properties along the waveguide propagation axis [40] is presented, together with corresponding expressions for the natural frequencies and input mobility. This formulation, unlike the previous one, takes internal reflections into account, and is used for comparison with the WKB results.

Finally, two Finite Element approximations are also proposed. One using an enriched hierarchical basis, or Hierarchical Finite Element (HFE) [1, 2], is presented, where the variability in the properties of the waveguide is included in the element formulation. The other, widely used in the literature, assumes that the element properties are piecewise constant. A single sample of a random field is used to carry out the numerical analysis, as all of the formulations, Figure 2.1, are purely deterministic.

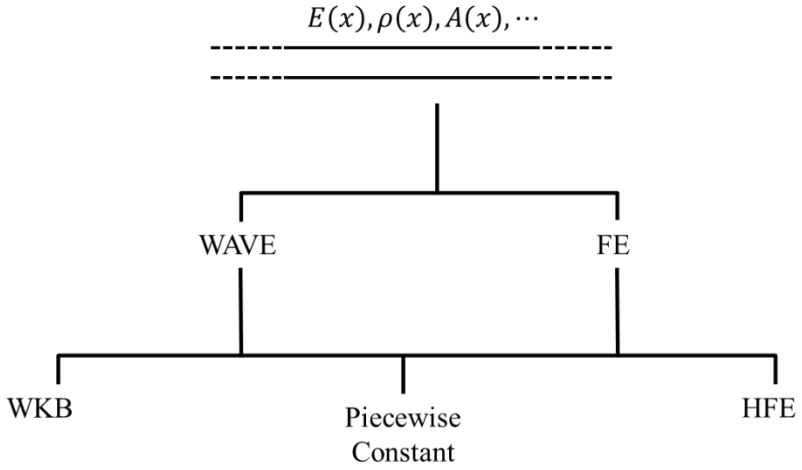

Figure 2.1. Relation between the approaches used to model waveguides with spatially varying properties.

2.2 Waves in a finite length rod with slowly changing material variability

Spatial variability can be represented as perturbation over a certain mean, or nominal, value. It is usually represented in the design variables that for longitudinal vibration of rods can be the mass density, cross-sectional area or Young's modulus. For the sake of simplicity, in this chapter only the Young's modulus of elasticity is considered spatially varying, although the other quantities can also be taken into account following the same rationale, according to a description

$$E(x) = E_0[1 + \sigma H(x)], \tag{2.1}$$

where E_0 is the nominal value for the Young's modulus, $H(x)$ a zero-mean spatially varying term either assumed or estimated from measurements, representing the variation along the waveguide within $0 < x < L$, where L is its length, and σ is a dispersion term, quantifying the influence of $H(x)$ in the mean nominal value E_0.

The term $H(x)$ can be obtained by experimental identification of the material properties or by an assumed model assumption. The model follows an analytical derivation using the Karhunen-Loeve expansion

$$H(x,p) = \sum_{j=1}^{N_{kl}} \left[\alpha_j \xi_{1j}(p) \sin\left[w_{1j}\left(x - \frac{L}{2}\right)\right] + \beta_j \xi_{2j}(p) \cos\left[w_{2j}\left(x - \frac{L}{2}\right)\right]\right], \tag{2.2}$$

where p is the index for each random realization of the field and N_{kl} is the number of terms actually retained in the expansion, which must be sufficient to achieve

convergence [34]. The assumptions needed to obtain this analytical expression, in terms of the random field theory, are explained in Chapter 5. In this chapter, the results will be derived for a single realization of the Young's modulus, i.e. $E(x,p) = E(x)$, then p is going to be omitted to make it clear that the variability is purely deterministic.

2.2.1 WKB approximation for longitudinal waves in rods

Consider a rod undergoing longitudinal vibration, with slowly changing Young's modulus along its length, such that a propagating wave has negligible reflections due to the local impedance change. Given the governing equation

$$\frac{\partial^2 u(x,t)}{\partial t^2} = c_L^2(x)\frac{\partial^2 u(x,t)}{\partial x^2} \tag{2.3}$$

where $c_L(x) = \sqrt{E(x)/\rho}$ is the local phase velocity at position x, and $u(x,t)$ the axial displacement.

Assuming a time harmonic solution, $u(x,t) = U(x)\, e^{i\omega t}$, it is possible to define a local wavenumber $k_L(x) = \omega/c_L(x)$, by analogy to the homogeneous case, leading to

$$\frac{\partial^2 U(x)}{\partial x^2} = -k_L^2(x)U(x). \tag{2.4}$$

The WKB method consists in looking for generalized approximate wave solutions, when the properties vary slowly, even though the net change over a large distance may be considerable [45]. Thus, the *eikonal* function $S(x) = \ln \widetilde{U}(x) + i\theta(x)$ [48, 72] is introduced, in order to find wave solutions of the kind

$$U(x) = e^{S(x)} = \widetilde{U}(x)e^{\pm i\theta(x)}. \tag{2.5}$$

Back substituting it into Eq. (2.4), and neglecting the higher order terms it is possible to find two solutions of the kind:

$$U(x) = C_1 e^{-i\int_{x_0}^{x} k_L(x)dx - \frac{1}{2}\ln k_L(x)} + C_2 e^{i\int_{x_0}^{x} k_L(x)dx - \frac{1}{2}\ln k_L(x)}, \tag{2.6}$$

where C_1 and C_2 are arbitrary constants and the two terms correspond to positive going and negative going travelling waves. Note that the term in the exponential $\theta(x) = \int_{x_0}^{x} k_L(x)dx$ corresponds to a phase change of a propagating wave along the waveguide and the term $\widetilde{U}(x) = C_{1,2}k_L(x)^{-\frac{1}{2}}$ corresponds to an amplitude change and x_0 is arbitrary point in the waveguide. In a homogenous rod, only the phase would be changed in a propagating wave, but local changes in the impedance also lead to an amplitude change.

Then, the phase and amplitude change of the positive and negative wave travelling through a distance L, Figure 2.2, from $x = 0$ to $x = L$, is given by

$$b^+ = \sqrt{\frac{k_L(0)}{k_L(L)}} e^{-i\int_0^L k_L(x)dx} a^+, \tag{2.7}$$

$$b^- = \sqrt{\frac{k_L(0)}{k_L(L)}} e^{i\int_0^L k_L(x)dx} a^-, \tag{2.8}$$

where $k_L(0)$ and $k_L(L)$ are the wavenumber $k_L(x) = \sqrt{\rho/E(x)}\omega$ evaluated at $x = 0$ and $x = L$, respectively.

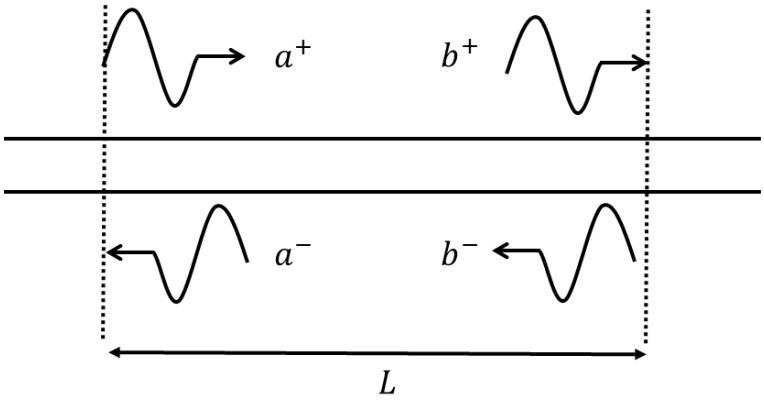

Figure 2.2. Positive going and negative going waves travelling distance L along a rod.

It also can be shown [49] that the WKB approximation, i.e. the variation on the wavenumber is small compared to the wavelength, holds if

$$\frac{1}{k_L(x)}\left|\frac{d}{dx}\ln k_L(x)\right| \ll 1. \tag{2.9}$$

If only the Young's modulus variability is considered, then this is equivalent to

$$\frac{1}{2\sqrt{\rho}\omega E(x)^2}\frac{dE(x)}{dx} \ll 1. \tag{2.10}$$

2.2.2 Free wave propagation

Considering a finite waveguide with length L, undergoing a free longitudinal wave propagation, Figure 2.3, then the positive going and the negative going wave amplitudes on the left hand boundary, a^+ and a^-, and on the right hand boundary, b^+ and b^-, can be related by $\mathbf{b} = \mathbf{\Lambda a}$, where

$$\mathbf{\Lambda} = \begin{bmatrix} e^{-i\theta_T+\gamma_T} & 0 \\ 0 & e^{i\theta_T+\gamma_T} \end{bmatrix}, \tag{2.11}$$

is a propagation matrix, obtained from Eq. (2.7)-(2.8), $i = \sqrt{-1}$. The wave amplitudes are given by the vectors

$$\mathbf{a} = \begin{Bmatrix} a^+ \\ a^- \end{Bmatrix}, \mathbf{b} = \begin{Bmatrix} b^+ \\ b^- \end{Bmatrix}. \tag{2.12}$$

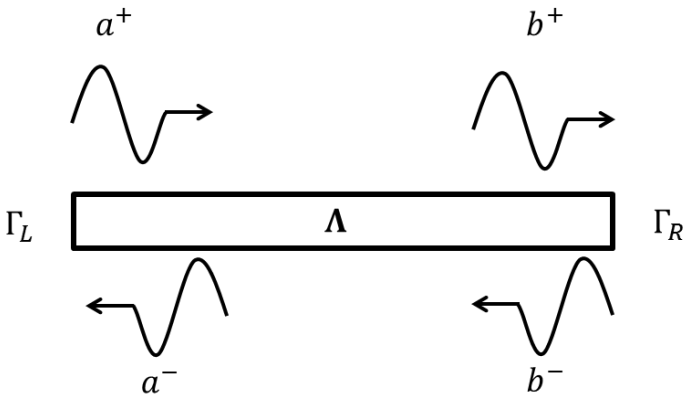

Figure 2.3. Finite waveguide undergoing free wave propagation, with slowly varying material properties, considering no internal reflections.

The total phase θ_T and amplitude change γ_T for a wave propagating from one boundary to the other can be given by

$$\theta_T = \int_0^L k_L(x)dx. \tag{2.13}$$

and

$$\gamma_T = \frac{1}{2}\ln\left[\frac{k_L(0)}{k_L(L)}\right]. \tag{2.14}$$

For a homogeneous waveguide, then $k_L(x) = k_L = constant$ and the total phase change reduces to $\theta_T = kL$, as well as no change in amplitude, i.e. $\gamma = 0$.

The reflected waves from energy conserving boundaries at the left and the right hand ends are given by the respective reflection coefficients as $a^+ = \Gamma_L a^-$ and $b^- = \Gamma_R b^+$. They can also be defined in terms of phase changes ϕ_L and ϕ_R, i.e., $\Gamma_L = e^{-i\phi_L}$ and $\Gamma_R = e^{-i\phi_R}$.

The waveguide natural frequencies can be determined by applying the phase-closure principle, tracing the round-trip propagating wave [19]. Thus, from Eq. (2.11)

$$b^+ = \Lambda_{11}a^+ + \Lambda_{12}a^-, \tag{2.15}$$

$$b^- = \Lambda_{21} a^+ + \Lambda_{22} a^-, \tag{2.16}$$

where $(\cdot)_{ij}$ is the i^{th} row and j^{th} column element of the corresponding matrix, applying the reflections at the boundaries and noting that $\Lambda_{12} = \Lambda_{21} = 0$, then

$$b^+ = \Lambda_{11} \Gamma_L a^-, \tag{2.17}$$

$$\Gamma_R b^+ = \Lambda_{22} a^-. \tag{2.18}$$

Rearranging and substituting, the natural frequencies correspond to the zeros of the characteristic equation [19, 61]

$$\Lambda_{22}^{-1} \Gamma_R \Lambda_{11} \Gamma_L - 1 = 0. \tag{2.19}$$

Back substituting the terms of the reflection and propagation matrices in this equation leads to

$$e^{-i2\theta_T - i\phi_R - i\phi_L} - 1 = 0, \tag{2.20}$$

from which an expression for n^{th} natural frequency ω_n of the inhomogeneous rod can be written in terms of an integral of an expression involving $H(x)$ as

$$\omega_n = \sqrt{\frac{E_0}{\rho}} \frac{2n\pi - \phi_R - \phi_L}{2 \int_0^L \sqrt{\frac{1}{1 + \sigma H(x)}} dx}, \tag{2.21}$$

if only the varying Young's modulus, Eq. (2.1), is considered. The integral in the denominator of Eq. (2.21) might have an explicit solution only for a limited number of families of the functions used for $H(x)$. Otherwise, it can either be evaluated numerically, or some sort of approximation sought. For the cases where the Young's modulus is not only slowly varying, but also presents small dispersion around the nominal value, i.e. $|\sigma H(x)| \ll 1$, a first order approximation can be used such that $\sqrt{1/[1 + \sigma H(x)]} \approx 1 - \sigma/2\, H(x)$, then

$$\omega_n \approx \sqrt{\frac{E_0}{\rho}} \frac{2n\pi - \phi_R - \phi_L}{2L - \sigma \int_0^L H(x) dx}. \tag{2.22}$$

Moreover, if $H(x)$ is expressed by Eq. (2.2), then its integral has a closed form and the first order approximation for the natural frequency is given by

$$\omega_n \approx \sqrt{\frac{E_0}{\rho}} \frac{2n\pi - \phi_R - \phi_L}{2L - 2\sigma \sum_{j=1}^{N_{kl}} \xi_{2j}(p) \frac{\beta_j}{w_{2j}} \sin\left(\frac{w_{2j} L}{2}\right)}. \tag{2.23}$$

These expressions show that the natural frequencies are affected by the contributions of the terms in the KL expansion. If there is no variation and $\sigma = 0$, the expression reduces

to the homogenous case. This expression will be used in Chapter 5 in order to find analytical expressions for the PDF of the natural frequency.

2.2.3 Point excitation

An expression for the input mobility due to a point excitation, Figure 2.4, can be derived following the above analysis. The point harmonic excitation force F, applied at $x = L_1$, creates a positive going q^+ and a negative going q^- propagating wave, so that the waves at this point are given by the sum of these directly excited q^+ and q^- and the incident ones b_1^+ and a_2^- such that

$$a_2^+ = b_1^+ + q^+, \tag{2.24}$$

and

$$b_1^- = a_2^- + q^-. \tag{2.25}$$

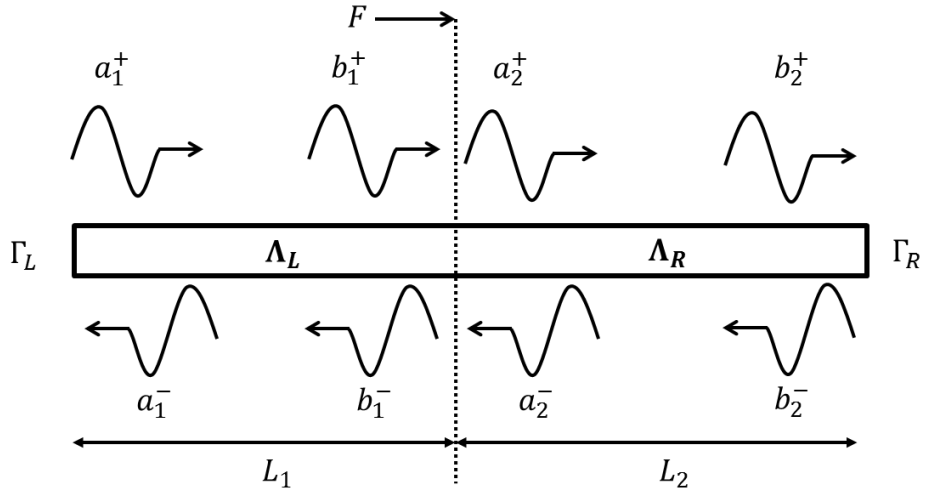

Figure 2.4. Point excitation on finite length rod, with slowly varying material properties, considering no internal reflections.

Propagation from the boundaries to the excitation point is given $\mathbf{b_1} = \mathbf{\Lambda_L a_1}$ and $\mathbf{b_2} = \mathbf{\Lambda_R a_2}$, where

$$\mathbf{\Lambda_L} = \begin{bmatrix} e^{-i\theta_L+\gamma_L} & 0 \\ 0 & e^{i\theta_L+\gamma_L} \end{bmatrix}, \mathbf{\Lambda_R} = \begin{bmatrix} e^{-i\theta_R+\gamma_R} & 0 \\ 0 & e^{i\theta_R+\gamma_R} \end{bmatrix}, \tag{2.26}$$

and

$$\mathbf{a_1} = \begin{Bmatrix} a_1^+ \\ a_1^- \end{Bmatrix}, \mathbf{a_2} = \begin{Bmatrix} a_2^+ \\ a_2^- \end{Bmatrix}, \mathbf{b_1} = \begin{Bmatrix} b_1^+ \\ b_1^- \end{Bmatrix}, \mathbf{b_2} = \begin{Bmatrix} b_2^+ \\ b_2^- \end{Bmatrix}. \tag{2.27}$$

Moreover, θ_L and γ_L gives total phase and amplitude change of the propagating wave to the left side of the point excitation on the waveguide and θ_R and γ_R the total phase and amplitude change on its right side, where

$$\theta_L = \int_0^{L_1} k_L(x)dx \text{ and } \gamma_L = \frac{1}{2}\ln\left[\frac{k_L(0)}{k_L(L_1)}\right], \tag{2.28}$$

$$\theta_R = \int_{L_1}^{L} k_L(x)dx \text{ and } \gamma_R = \frac{1}{2}\ln\left[\frac{k_L(L_1)}{k_L(L)}\right], \tag{2.29}$$

Note that the total phase and amplitude change θ_T and γ_T are given by the summation of the left θ_L and right θ_R phase changes, i.e., $\theta_T = \theta_L + \theta_R$ and $\gamma_T = \gamma_L + \gamma_R$. In the same way, if the waveguide is homogeneous, then $k_L(x) = k_L$ and the total phase changes reduce to $\theta_L = k_L L_1$. $\theta_R = k_L L_2$, where $L_2 = L - L_1$, and $\gamma_L = \gamma_R = 0$. The reflected waves from energy conserving boundaries at the left and the right hand ends are given by the respective reflection coefficients as $a_1^+ = \Gamma_L a_1^-$ and $b_2^- = \Gamma_R b_2^+$.

Using the force-deformation relationship for a rod under harmonic excitation, it is possible to find the internal forces related to the positive going q^+ and negative going q^- travelling wave when the rod is excited by a harmonic force F:

$$P^+ = E(L_1)A\frac{\partial U^+(x)}{\partial x}, \tag{2.30}$$

and

$$P^- = E(L_1)A\frac{\partial U^-(x)}{\partial x}, \tag{2.31}$$

where A is the cross-section area and, from Eq. (2.6), $U^+(x) = C_1 e^{-i\int_{x_0}^{x} k_L(x)dx - \frac{1}{2}\ln k(x)}$ is the positive going wave and $U^-(x) = C_1 e^{i\int_{x_0}^{x} k_L(x)dx - \frac{1}{2}\ln k(x)}$ is the negative going one. Introducing a factor λ to explicitly split the two terms in the asymptotic approximation, such that $U(x) = Cexp\left(\pm i\int_{x_0}^{x} k_L(x)dx - \frac{\lambda}{2}\ln k_L(x)\right)$, its derivatives can be found as

$$\frac{\partial U^+(x)}{\partial x} = \left[-k_L(x)\left(i + \frac{\lambda}{2}\frac{1}{k_L^2(x)}\frac{\partial k_L(x)}{\partial x}\right)\right] U^+(x), \tag{2.32}$$

$$\frac{\partial U^-(x)}{\partial x} = \left[k_L(x)\left(i + \frac{\lambda}{2}\frac{1}{k_L^2(x)}\frac{\partial k_L(x)}{\partial x}\right)\right] U^-(x). \tag{2.33}$$

Then, because the WKB assumptions require that $k_L(x) \gg 1$ and $\partial k_L(x)/\partial x$ to be small [49, 73], the second term of the expression can be neglected. This leads to expressions for the internal forces as

$$P^+ = -ik_L(x)E(x)AU(x)^+ , \tag{2.34}$$

and

$$P^- = ik_L(x)E(x)AU(x)^- . \tag{2.35}$$

Note that they are analogous to the homogeneous case. Equilibrium and continuity of displacement gives the amplitudes of the positive going q^+ and negative going q^- travelling waves induced by an external point harmonic force F applied at $x = L_1$ as

$$q = q^+ = q^- = -\frac{i}{2k_L(L_1)E(L_1)A}F, \tag{2.36}$$

where $E(L_1)$ is the Young's modulus evaluated at $x = L_1$.

This is applied in Eq. (2.24) and Eq. (2.25), together with the propagation and reflection properties, and noting that, ${\Lambda_L^{-1}}_{11} = 1/\Lambda_{L_{11}}$, ${\Lambda_R^{-1}}_{11} = 1/\Lambda_{R_{11}}$ – then the positive going wave a_2^+ is given by

$$a_2^+ = \Lambda_{L_{11}}\Gamma_L{\Lambda_L^{-1}}_{22}\left({\Lambda_R^{-1}}_{22}\,\Gamma_R\Lambda_{R_{11}}a_2^+ + q^-\right) + q^+, \tag{2.37}$$

and it is related to the negative going a_2^- by

$$a_2^- = {\Lambda_R^{-1}}_{22}\,\Gamma_R\Lambda_{R_{11}}a_2^+. \tag{2.38}$$

The input mobility $Y(\omega) = i\omega(a_2^+ + a_2^-)/F$, which can be calculated by using the superposition principle of a positive going a_2^+ and a negative going a_2^- propagating wave at the point of excitation,

$$a_2^+ + a_2^- = \frac{\left(1 + {\Lambda_R^{-1}}_{22}\,\Gamma_R\Lambda_{R_{11}}\right)\left(1 + \Lambda_{L_{11}}\Gamma_L{\Lambda_L^{-1}}_{22}\right)}{1 - \Lambda_{L_{11}}\Gamma_L{\Lambda_L^{-1}}_{22}\,{\Lambda_R^{-1}}_{22}\,\Gamma_R\Lambda_{R_{11}}}q, \tag{2.39}$$

such that

$$Y(\omega) = \frac{\omega}{2k(L_1)E(L_1)A}\frac{1 + \Gamma_L e^{-i\theta_L} + \Gamma_R e^{-i\theta_R} + \Gamma_L\Gamma_R e^{-i\theta_T}}{1 - \Gamma_L\Gamma_R e^{-i\theta_T}}. \tag{2.40}$$

These relations can be used to find the wave amplitudes at any point of the rod. Expressions for θ_T, θ_L and θ_R are given analytically by using Eq. (2.2), and whose integrals can be solved numerically, assuming a Karhunen-Loeve expansion:

$$\theta_L = \sqrt{\frac{\rho}{E_0}}\omega\int_0^{L_1}\sqrt{\frac{1}{1 + \sigma\sum_{j=1}^{N_{kl}}\alpha_j\xi_{1j}(p)\sin(w_{1i}x) + \beta_j\xi_{2j}(p)\cos(w_{2j}x)}}\,dx. \tag{2.41}$$

$$\theta_R = \sqrt{\frac{\rho}{E_0}}\omega \int_{L_1}^{L} \sqrt{\frac{1}{1+\sigma\sum_{j=1}^{N_{kl}} \alpha_j \xi_{1j}(p)\sin(w_{1i}x)+\beta_j \xi_{2j}(p)\cos(w_{2j}x)}}\,dx, \quad (2.42)$$

$$\theta_T = \sqrt{\frac{\rho}{E_0}}\omega \int_{0}^{L} \sqrt{\frac{1}{1+\sigma\sum_{j=1}^{N_{kl}} \alpha_j \xi_{1j}(p)\sin(w_{1i}x)+\beta_j \xi_{2j}(p)\cos(w_{2j}x)}}\,dx. \quad (2.43)$$

2.3 Waves in finite length rod with piecewise constant material variability

The key assumption made in the previous section was that there is negligible backscattering of the propagating wave due to local properties changes. A more general approximation can be achieved if one considers a rod with piecewise constant material variability, separated into a finite number of discrete sections and undergoing longitudinal vibration. This can be an approximate representation for the more general spatial varying system. The wavenumber for the j^{th} element is

$$k_{L_j} = \sqrt{\frac{\rho}{E_j}}\omega. \quad (2.44)$$

In this way, internal reflections due to the local changes in the impedance inside the rod can be taken into account. A more general analysis of this kind of system can be found in [74, 75].

Equation (2.2) is evaluated at the geometrical centre of the elements and is used to estimate the values used in the piecewise constant description, by simply sampling the random field at the centroid of each element x_{cj}, such that

$$E_j(p) = E(x_{cj}, p). \quad (2.45)$$

2.3.1 Free wave propagation

For a finite waveguide with length L, undergoing free wave propagation, Figure 2.5, with piecewise constant properties, divided into N elements, such that for the j$^{\text{th}}$ element the positive going and the negative going waves on the left $\mathbf{a_j}$ and on the right side $\mathbf{b}_j$, are related by $\mathbf{b_j} = \mathbf{\Lambda_j a_j}$, where

$$\mathbf{\Lambda}_{\mathrm{j}} = \begin{bmatrix} e^{-i\theta_j} & 0 \\ 0 & e^{i\theta_j} \end{bmatrix}, \quad (2.46)$$

$$\mathbf{a}_{\mathrm{j}} = \begin{Bmatrix} a_j^+ \\ a_j^- \end{Bmatrix}, \mathbf{b}_j = \begin{Bmatrix} b_j^+ \\ b_j^- \end{Bmatrix}, \tag{2.47}$$

and $\theta_j = k_{Lj} l$ is the phase change within the j^{th} element. For the sake of simplicity, all the elements are assumed to be the same length $l = L/N$.

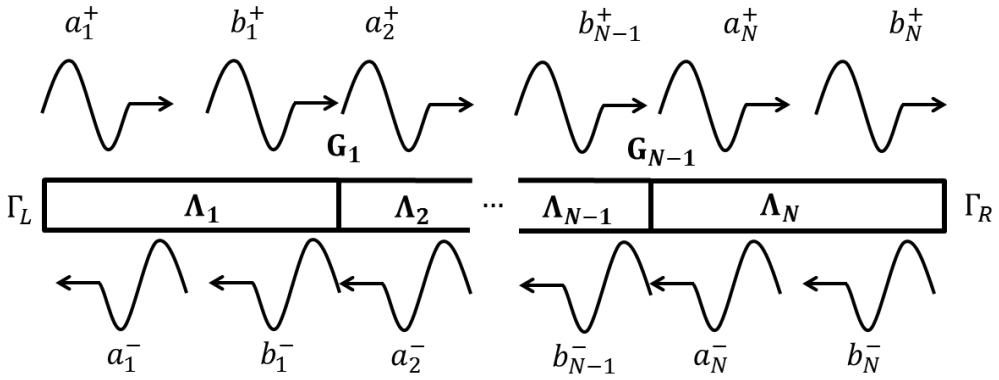

Figure 2.5. Free wave propagation in piecewise constant waveguide considering internal reflections.

When a wave reaches the junction between the element j and $(j+1)$, the transmission and reflection can be taken into account as $a_{j+1}^+ = t_j^+ b_j^+ + r_j^+ a_{j+1}^-$ and $b_j^- = t_j^- a_{j+1}^- + r_j^- b_j^+$ [60] where t_j^+ is the transmission coefficient from the j^{th} junction from the left to the right, t_j^- is the transmission coefficient from the right to the left, r_j^+ is the reflection coefficient of the propagating wave reflecting at the junction j from the left to the right and r_j^- is the reflection coefficient for a propagating wave reflecting at the same junction but from the right to the left. These equations can be rewritten in terms of a scattering matrix such that $\mathbf{a}_{j+1} = \mathbf{G}_j \mathbf{b}_j$, where

$$\mathbf{G}_j = \frac{1}{t_j^+} \begin{bmatrix} t_j^+ t_j^- - r_j^+ r_j^- & r_j^+ \\ -r_j^- & 1 \end{bmatrix}. \tag{2.48}$$

It follows that the wave amplitudes on the left of the waveguide $\mathbf{a}_1$ and the ones at the right hand boundary $\mathbf{b}_N$, considering N elements and, consequently, at the $(N-1)^{th}$ junction is given by $\mathbf{b}_N = \widetilde{\mathbf{\Lambda}} \mathbf{a}_1$, where [74]

$$\widetilde{\mathbf{\Lambda}} = \mathbf{\Lambda}_{\mathrm{N}} \prod_{j=1}^{N-1} \mathbf{G}_{\mathrm{N-j}} \mathbf{\Lambda}_{\mathrm{N-j}} \,. \tag{2.49}$$

Once more, the natural frequencies can be sought by applying the phase-closure principle, tracing the round-trip propagating wave, and, differently from the previous case, considering the internal reflections, using Eq. (2.46) to Eq. (2.49) together with the

reflections at the boundaries, so that they correspond to the zeroes of the characteristic equation

$$\Gamma_R \widetilde{\mathbf{\Lambda}}_{11} \Gamma_L + \Gamma_R \widetilde{\mathbf{\Lambda}}_{12} - \widetilde{\mathbf{\Lambda}}_{21} \Gamma_L - \widetilde{\mathbf{\Lambda}}_{22} = 0, \tag{2.50}$$

where $(\cdot)_{ij}$ is the i^{th} row and j^{th} column element of the corresponding matrix.

For slowly varying properties, it is possible to approximate the scattering matrix by an identity matrix $\mathbf{G}_{\text{j}} \approx \mathbf{I}$, meaning the wave is fully transmitted, i.e. $t_j^+ = t_j^- = 1$, with negligible reflections, i.e. $r_j^+ = r_j^- = 0$. This simplifies $\widetilde{\mathbf{\Lambda}}$, Eq. (2.49), to a block diagonal matrix, i.e. $\widetilde{\mathbf{\Lambda}}_{12} = \widetilde{\mathbf{\Lambda}}_{21} = \mathbf{0}$, where $\mathbf{0}$ is a null matrix, which, in turn would lead Eq. (2.50) to a much simpler form

$$\mathbf{\Gamma}_R \widetilde{\mathbf{\Lambda}}_{11} \mathbf{\Gamma}_L - \widetilde{\mathbf{\Lambda}}_{22} \approx 0, \tag{2.51}$$

whose solution is given by

$$\omega_n = \frac{2n\pi - (\phi_R + \phi_L)}{2L \sum_{j=1}^{N} \sqrt{\rho / E_j}}. \tag{2.52}$$

This is analogous to Eq. (2.21), but changing the integral term by a summation over the properties of each element.

2.3.2 Point excitation

By analogy to the previous case, an expression for the input mobility due to a point excitation can be obtained by using the wave relations, Figure 2.6. The excitation is given by a harmonic force F applied at the M^{th} junction, at L_1 from the left boundary, so that it creates a positive going q^+ and a negative going q^- propagating wave. The waves at this point are given by the sum of these directly excited waves plus the transmitted and reflected ones such that

$$a_{\text{M}+1}^+ = t_{\text{M}}^+ b_{\text{M}}^+ + r_{\text{M}}^+ a_{\text{M}+1}^- + q^+, \tag{2.53}$$

and

$$b_{\text{M}}^- = t_{\text{M}}^- a_{\text{M}+1}^- + r_{\text{M}}^- b_{\text{M}}^+ + q^-. \tag{2.54}$$

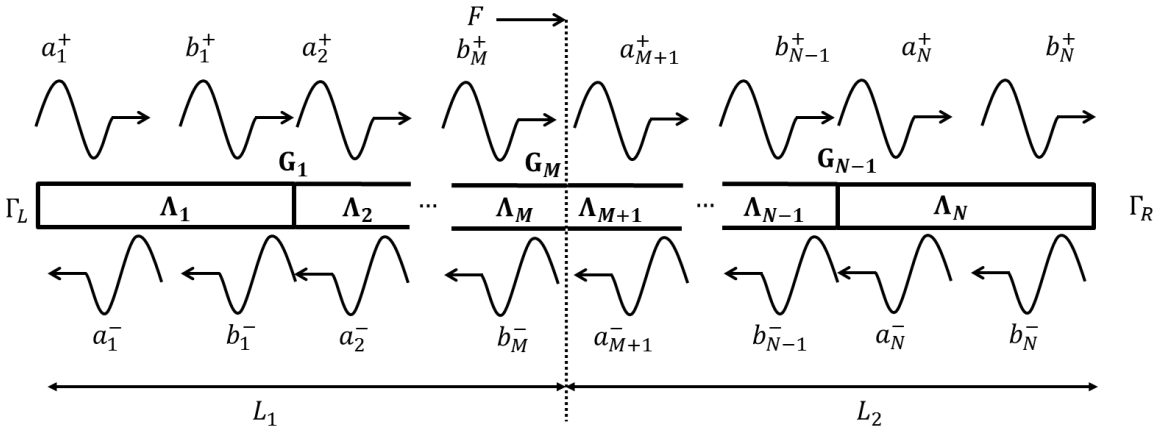

Figure 2.6. Point excitation of a finite length rod with piecewise constant properties and non-dissipative junctions, taking into account internal reflections.

The wave amplitudes on the left of the waveguide $\mathbf{a}_1$ and the ones on the right of the M^{th} element $\mathbf{b}_M$, are related by $\mathbf{b}_\mathrm{M} = \widetilde{\mathbf{\Lambda}}_\mathrm{L}\mathbf{a}_1$; also the wave amplitudes on the right of the waveguide $\mathbf{b}_N$ and the ones on the left of the $(\mathrm{M}+1)^{th}$ element $\mathbf{a}_{M+1}$, are related by $\mathbf{b}_\mathrm{N} = \widetilde{\mathbf{\Lambda}}_\mathrm{R}\mathbf{a}_{M+1}$, where

$$\widetilde{\mathbf{\Lambda}}_\mathrm{L} = \mathbf{\Lambda}_\mathrm{M} \prod_{j=1}^{M-1} \mathbf{G}_{\mathrm{M-j}}\mathbf{\Lambda}_{\mathrm{M-j}}\,, \tag{2.55}$$

$$\widetilde{\mathbf{\Lambda}}_\mathrm{R} = \mathbf{\Lambda}_\mathrm{N} \prod_{j=1}^{\mathrm{N-M-1}} \mathbf{G}_{\mathrm{N-j}}\mathbf{\Lambda}_{\mathrm{N-j}}\,. \tag{2.56}$$

Moreover, assuming continuity of the displacement leads to $q = q^+ = q^-$; and equilibrium of the forces at the excitation, as shown in Figure 2.7, i.e. $F + P^+ - P^- = 0$, where $P^+ = -ik_{L_{M+1}}E_{M+1}Aq^+$ and $P^- = ik_{L_M}E_MAq^-$, leads to the directly excited waves amplitudes as

$$q = -\frac{i}{(k_{L_M}E_M + k_{L_{M+1}}E_{M+1})A}F. \tag{2.57}$$

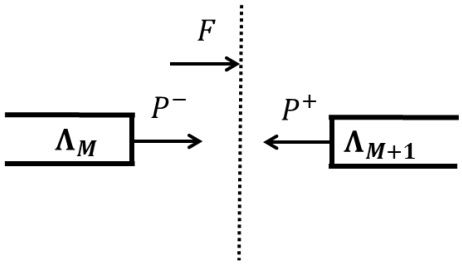

Figure 2.7. Equilibrium at the excitation point.

Following the same rationale as in the previous case, the input mobility can be calculated by solving these equations and for the wave amplitudes. Using Eq. (2.53) and Eq. (2.54) and defining $T_R = \frac{\widetilde{\Lambda}_{R21} - \widetilde{\Lambda}_{R11}\Gamma_R}{\widetilde{\Lambda}_{R12} - \widetilde{\Lambda}_{R22}\Gamma_R}, T_L = \frac{\widetilde{\Lambda}_{L11}\Gamma_L + \widetilde{\Lambda}_{L12}}{\Gamma_L\widetilde{\Lambda}_{L21} + \widetilde{\Lambda}_{L22}}$. where $a_{M+1}^- = T_R a_{M+1}^+$, $b_M^+ = T_L b_M^-$, leads to

$$a_{M+1}^+ = \left(\frac{t_M^- T_L}{1 - r_M^- T_L}\right)(t_M^+ T_R a_{M+1}^+ + q^-) + r_M^+ T_R a_{M+1}^+ + q^+. \tag{2.58}$$

After some algebra, and using $q = q^+ = q^-$,

$$a_{M+1}^+ = \frac{(1 + t_M^- T_L - r_M^- T_L)}{(1 - r_M^+ T_R)(1 - r_M^- T_L) - t_M^+ t_M^- T_L T_R} q. \tag{2.59}$$

The input mobility $Y_{CTE}(\omega) = i\omega(a_{M+1}^+ + a_{M+1}^-)/F$ can be calculated by using the superposition principle of a positive going a_{M+1}^+ and a negative going a_{M+1}^- propagating wave at the point of excitation,

$$a_{M+1}^+ + a_{M+1}^- = \frac{(1 + t_M^- T_L - r_M^- T_L)\,(1 + T_R)}{(1 - r_M^+ T_R)(1 - r_M^- T_L) - t_M^+ t_M^- T_L T_R} q. \tag{2.60}$$

such that

$$Y_{CTE}(\omega) = \frac{\omega}{(k_M E_M + k_{M+1} E_{M+1})A} \frac{(1 + t_M^- T_L - r_M^- T_L)(1 + T_R)}{(1 - r_M^+ T_R)(1 - r_M^- T_L) - t_M^+ t_M^- T_L T_R}. \tag{2.61}$$

2.4 Finite element approximation using a hierarchical basis (HFE)

A formulation of the hierarchical finite element formulation, also known as p-element formulation [1], is presented in this section including the spatial variability as presented in Eq. (2.1). This formulation not only improves the computational cost by decreasing the number of elements necessary to accurately represent a higher frequency band, but also takes advantage of the formulation of Eq. (2.2) to be explored within a MC framework, as is going to be shown later in Chapter 5.

The axial displacement along the element can be described in terms of p assumed functions [1]

$$u = \sum_{r=1}^{p} g_r(\xi) q_r = \mathbf{N}(\xi)\mathbf{q} \tag{2.62}$$

where $-1 \leq \xi \leq 1$, is local element coordinate, and $\lfloor \mathbf{N}(\xi) \rfloor$ is a row-matrix containing the functions $g_r(\xi)$ and $\mathbf{q}$ is a column matrix containing the degrees of freedom q_r. The

first two are the usual finite element shape functions $g_1(\xi) = \frac{1}{2}(1-\xi)$, $g_2 = \frac{1}{2}(1-\xi)$. The most commonly used hierarchical functions $g_r(\xi)$, are derived from the Legendre polynomial. For the rod element they are given by

$$g_r(\xi) = \sum_{n=0}^{(r-1)/2} \frac{(-1)^n}{2^n n!} \frac{(2r-2n-5)!!}{(r-2n-1)!} \xi^{r-2n-1}, \tag{2.63}$$

for $r > 2$, where $m!! = m(m-2)\ldots(2 \text{ or } 1)$, $0!! = 1$, $(-1)!! = 1$ and $(r-1)/2$ stands for its integer part. This ensures that their contribution at the nodes $\xi = \pm 1$ is zero, therefore there is no increase in the number of nodes.

Assuming spatial variability in the material and geometrical properties, i.e. $EA = EA(x)$ and $\rho A = \rho A(x)$, the element matrices can be written as

$$\mathbf{K}_e = \frac{1}{a}\int_{-1}^{1} EA(x)\lfloor \mathbf{N}(\xi)' \rfloor^T \lfloor \mathbf{N}(\xi)' \rfloor d\xi, \tag{2.64}$$

$$\mathbf{M}_e = a\int_{-1}^{1} \rho A(x)\lfloor \mathbf{N}(\xi) \rfloor^T \lfloor \mathbf{N}(\xi) \rfloor d\xi, \tag{2.65}$$

where $a = L/2$, being L the element size, and $'$ stands for the first derivative. Moreover, the force vector for element can be calculated as $\mathbf{f_e} = a\int_{-1}^{1} p_x \lfloor \mathbf{N}(\xi) \rfloor d\xi$. For point excitation $p_x = f_x \delta(x - x_e)$ at x_e, where $\delta(x)$ is the Dirac delta function, then

$$\mathbf{f_e} = a f_x \lfloor \mathbf{N}(x_e) \rfloor. \tag{2.66}$$

If the spatially varying properties are described in the same manner as given in Eq. (2.2), with a change of variable such that $-L/2 < x < L/2$, i.e.

$$EA(x) = EA_0\left[1 + \sigma_{EA}\sum_{j=1}^{N_{KL}}\left(\alpha_j \sin(w_{1j}x) + \beta_j \cos(w_{2j}x)\right)\right] \tag{2.67}$$

$$\rho A(x) = \rho A_0\left[1 + \sigma_{\rho A}\sum_{j=1}^{N_{KL}}\left(\gamma_j \sin(w_{3j}x) + \delta_j \cos(w_{4j}x)\right)\right] \tag{2.68}$$

then the element matrices can be rewritten as $\mathbf{K}_e = \mathbf{K}_{e0} + \mathbf{\Delta K}_e$ and $\mathbf{M}_e = \mathbf{M}_{e0} + \mathbf{\Delta M}_e$, where

$$\mathbf{\Delta K}_e = \frac{\sigma}{a}\sum_{j=1}^{N_{KL}}\int_{-1}^{1}\left(\alpha_j \sin\left(\frac{2w_1}{L}\xi\right) + \beta_j \cos\left(\frac{2w_2}{L}\xi\right)\right)\lfloor \mathbf{N}(\xi)' \rfloor^T \lfloor \mathbf{N}(\xi)' \rfloor d\xi \tag{2.69}$$

$$\mathbf{\Delta M}_e = a\sigma \sum_{j=1}^{N_{KL}} \int_{-1}^{1} \left(\gamma_j \sin\left(\frac{2w_3}{L}\xi\right) + \delta_j \cos\left(\frac{2w_4}{L}\xi\right) \right) \lfloor \mathbf{N}(\xi) \rfloor^T \lfloor \mathbf{N}(\xi) \rfloor d\xi \qquad (2.70)$$

and $\mathbf{K}_{e0}$ and $\mathbf{M}_{e0}$ are the usual stiffness and mass matrices found with homogeneous properties. These integrals can be numerically evaluated by using, for instance, a quadrature rule. However, this approach does not ensure the so called k-orthogonality [1] for the matrix $\mathbf{\Delta K}_e$. This property ensures that the inclusion of more hierarchical functions, for higher order approximations, which does not affect the elements of the matrices that were already calculated, therefore increasing the overall numerical efficiency of the method. Nevertheless, the spatially varying properties, Eq. (2.67) and Eq. (2.68), can also be described using a set of polynomial basis orthogonal to the hierarchical functions, as suggested in [28], thus, also ensuring the k-orthogonality for the matrix $\mathbf{\Delta K}_e$.

2.5 Numerical results and discussion

Numerical analysis was carried out aiming to compare the results obtained with WKB for longitudinal waves in a rod with other methodologies, i.e. the piecewise constant wave approach, HFE and FE. The rod properties were assumed to be a Young's modulus with mean value $E_0 = 70$ GPa, cross-sectional area $A = 0.1 \times 5$ cm^2, total length $L = 4$ m, and density $\rho = 2700$ kg/m^3, with free-free boundary conditions, i.e. $\Gamma_L = \Gamma_R = 1$ and $\phi_L = \phi_R = 0$, for all the cases. The frequency band under analysis was chosen from 1 Hz to 6 kHz, discretised by 1Hz, such that at least the first nine axial modes could be observed in the forced response. Moreover, the excitation point was at $x = L_1 = 0.35L$. Structural damping was included by making the Young's modulus of elasticity a complex number $E_0 = E_0(1 + i\eta)$, with $\eta = 10^{-3}$. This change does not affect the analytical results for forced vibration as long as η is constant over the waveguide. Figure 2.8 presents the wavenumber over the given frequency band of this rod, but with homogeneous Young's modulus and Table 2.1 presents its first ten non-zero natural frequencies, calculated using the analytical expression of an homogeneous rod , i.e. $\omega_{n0} = \frac{n\pi}{L}\sqrt{\frac{E_0}{\rho_0}}$.

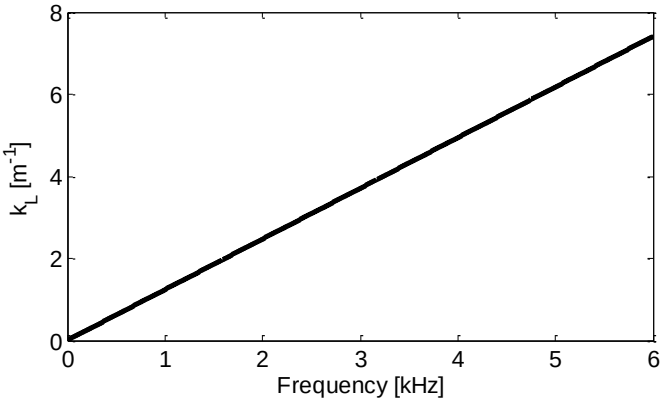

Figure 2.8. Wavenumber of the nominal rod within 1Hz to 6kHz.

Table 2.1. Lowest ten longitudinal natural frequencies [Hz] of the rod with homogeneous properties (excluding rigid body modes).

Mode #	Natural Frequency [Hz]	Mode #	Natural Frequency [Hz]
1	636.5	6	3818.8
2	1272.9	7	4455.3
3	1909.4	8	5091.8
4	2545.9	9	5728.2
5	3182.3	10	6364.7

The only spatially varying property is the Young's modulus and it is described analytically according to Eq. (2.1) and Eq. (2.2). Although this is a truncated Karhunen-Loeve expansion of a Gaussian random field with exponentially decaying correlation function, it is used here as a deterministic expression, i.e., given a correlation length, one sample of the random field is generated and then, the same sample is used for all the methods in order to compare the results. They were all generated using $N_{kl} = 40$ terms in the KL expansion, whose convergence is further discussed in Chapter 5.

Moreover, the FE model was assembled with 100 elements such that each element has a constant value of a Young's modulus given by Eq. (2.1), evaluated at the centre of the element, likewise the piecewise constant approach, Eq. (2.45).

The integrals of the phase changes θ_L, θ_R and θ_T, Eq. (2.41) to Eq. (2.43) were numerically evaluated, using a Gauss-Legendre quadrature rule. The input mobility using the WKB method was evaluated using Eq. (2.40) and the input mobility of the piecewise constant waveguide approach was evaluated using Eq. (2.61). For the FE and HFE, direct inversion of the dynamic matrix was used. Natural frequencies for the wave piecewise constant approach was calculated by using the approximation in Eq. (2.52).

For the WKB method the natural frequencies were calculated using Eq. (2.21), being that the integral was numerically calculated by a Gauss-Legendre quadrature, and also by its first order approximation, as given in Eq. (2.23).

Five different cases of spatial distribution of the Young's modulus were constructed in order to check the performance of the assumptions made so far; they were made by changing the dispersion parameter σ, i.e. how likely the values are to deviate from the mean value, and the correlation length b, i.e. the rate of fluctuation of the spatial distribution: $\sigma = 0.1$, $b = 2L$; $\sigma = 0.2$, $b = 2L$; $\sigma = 0.1$, $b = 0.8L$; $\sigma = 0.1$, $b = 0.1L$; and $\sigma = 0.2$, $b = 0.05L$. Figure 2.9 shows generated values of the Young's modulus spatial distribution normalized by the nominal values E_0. It is possible to note that for the higher correlation lengths, the spatial distribution has very distinguishable component of a long wavelength with some small variations from the underlying longer wavelength. It is because, from Eq. (2.2), the sine and cosine terms with larger wavelengths have relatively more importance in the series summation than the shorter ones. That relative importance decreases for smaller correlation lengths.

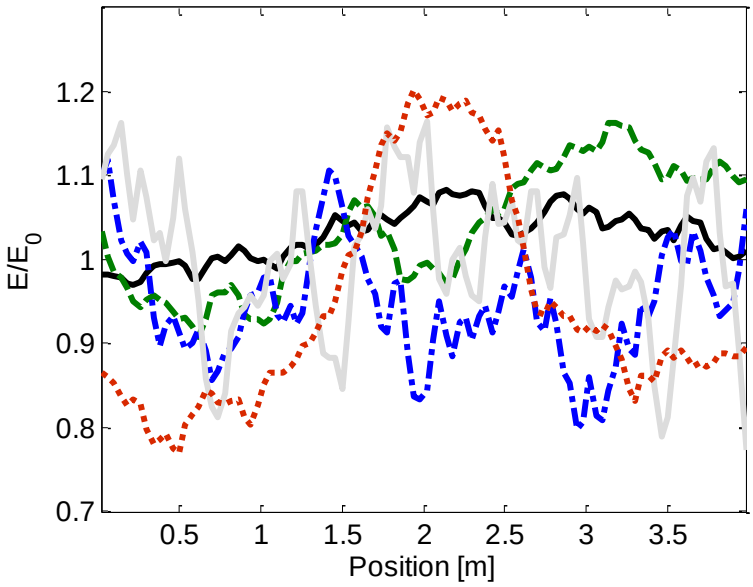

Figure 2.9. Normalized Young's value along the rod axis generated for all the cases: $\sigma = 0.1$, $b = 2L$ (black solid); $\sigma = 0.2$, $b = 2L$ (red dotted); $\sigma = 0.1$, $b = 0.8L$ (green dashed); $\sigma = 0.1$, $b = 0.1L$ (blue dash-dotted); and $\sigma = 0.2$, $b = 0.05L$ (grey solid).

For the dispersion parameter set to $\sigma = 0.1$ and correlation length $b = 2L$, Figure 2.10 shows the amplitude and phase of the input mobility obtained using the WKB approach, the piecewise constant formulation, HFE and the FE method along with the input mobility for the homogeneous equivalent rod, obtained using an

analytical expression available. Table 2.2 gives the lowest ten natural frequencies obtained using the FE, excluding the rigid body mode, as well as the percentage variation from FE of the results obtained using HFE, the WKB approach with numerical integration and with the first order approximation as well as using the wave piecewise constant approach. In this case, the Young's modulus varies slowly along the waveguide, so the WKB and FE methods agree very well, as expected, although the WKB method only required a fraction of the computational cost.

For the case when $\sigma = 0.2$ and $b = 2L$, the spatial distribution is generated expected to have the same effect on the results, but the bigger dispersion is expected to affect the first order approximations. From Figure 2.11, it is possible to note that the input mobility obtained using the WKB, HFE and FE methods are in very good agreement for all of the frequency range. Table 2.3 shows that the natural frequencies also produce very good agreement with the FE and HFE solutions from the third mode onwards, with less than one percent difference. For the two first modes, the difference is bigger, but not larger than 3.5%. This expected because the WKB approach is a high frequency approximation [73].

When $\sigma = 0.1$ and $b = 0.8L$, the generated spatial distribution is expected to have a less smooth spatial distribution, but still smooth enough so that there is good agreement between the input mobility using the WKB approach and the other solutions, Figure 2.12, as well as the natural frequencies as shown in Table 2.4.

Very good agreement is also found for the case when $\sigma = 0.1$ and $b = 0.1L$, for the input mobilities, Figure 2.13, and natural frequencies, Table 2.5, closer to the FE and HFE solution for the higher order modes.

For the cases when $\sigma = 0.2$ and $b = 0.05L$, Figure 2.14 shows the input mobility obtained using all of the above methods. Note that none of the methods produces the same agreement as found previously, although they are all follow the same trend of the shifts in frequencies. The good agreement between HFE and FE shows that random field discretisation is well represented in the FE model.

Generally, the higher the frequency the more sensitive is the dynamic response to variabilities in the waveguide properties. Nevertheless, the higher the frequency the better the WKB approximation becomes. In general, all of the methods used to represent variability along the axis of propagation very much agree for the point forced response and free vibration. Overall, for the cases with larger correlation lengths over the waveguide, i.e. greater values for b/L, the difference in the natural frequencies from the

WKB compared to the FE approximation is less than 1%, but using just a fraction of the computational cost. This can be extremely relevant when considering not only spatial variability but also randomness in the waveguide properties, in order to evaluate response statistics, typically using sampling methods. The first order approximation for the natural frequencies also gave very good results for relatively small dispersion σ values, with increasing accuracy the higher the order of the mode, even for higher σ values. Moreover, it has a simple closed form expression.

The piecewise constant wave approach also produced very good agreement with the FE approach, but not as computationally efficient as the WKB approach. It is also more prone to numerical rounding errors. The HFE method also produced, for all the cases considered, a very good agreement with the FE solution, being, however, computationally more efficient than the FE. More importantly it does not require slowly varying properties, being potentially more effective to more general cases.

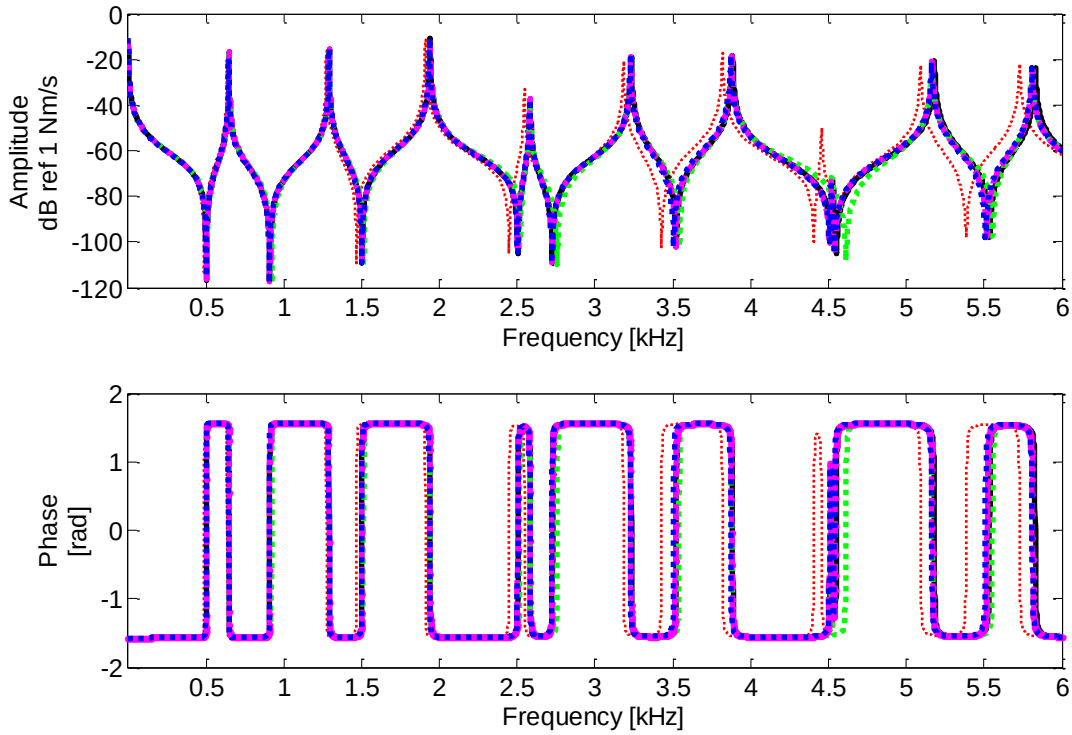

Figure 2.10. Input mobility amplitude and phase with nominal values (dotted red), WKB approximation (dotted blue), piecewise constant properties (dashed magenta) and FE approach (black) and HFE (dotted green); the dispersion parameter is set to $\sigma = 0.1$ and correlation length $b = 2L$.

Table 2.2. Percentage variation of the first ten natural frequencies [kHz] the rod with Young's modulus variability using HFE, WKB and its 1st order approximation, and piecewise constant. The dispersion parameter is set to $\sigma = 0.1$ and correlation length $b = 2L$. The piecewise constant FE is the reference case.

FE [kHz]	(HFE-FE)FE %	(WKB-FE)/FE %	(WKB 1st-FE)/FE %	(Piecewise-FE)/FE %
0.6502	-0.0255	-0.5935	-0.6415	-0.7071
1.2911	0.0078	0.1276	0.0792	0.0131
1.9410	-0.0400	-0.0972	-0.1454	-0.2113
2.5835	-0.0487	0.0768	0.0284	-0.0376
3.2332	-0.1094	-0.0418	-0.0901	-0.1560
3.8837	-0.1497	-0.1411	-0.1893	-0.2552
4.5280	-0.1728	-0.0760	-0.1243	-0.1902
5.1797	-0.2733	-0.1697	-0.2179	-0.2838
5.8290	-0.3497	-0.2010	-0.2492	-0.3151
6.4746	-0.4334	-0.1691	-0.2173	-0.2831

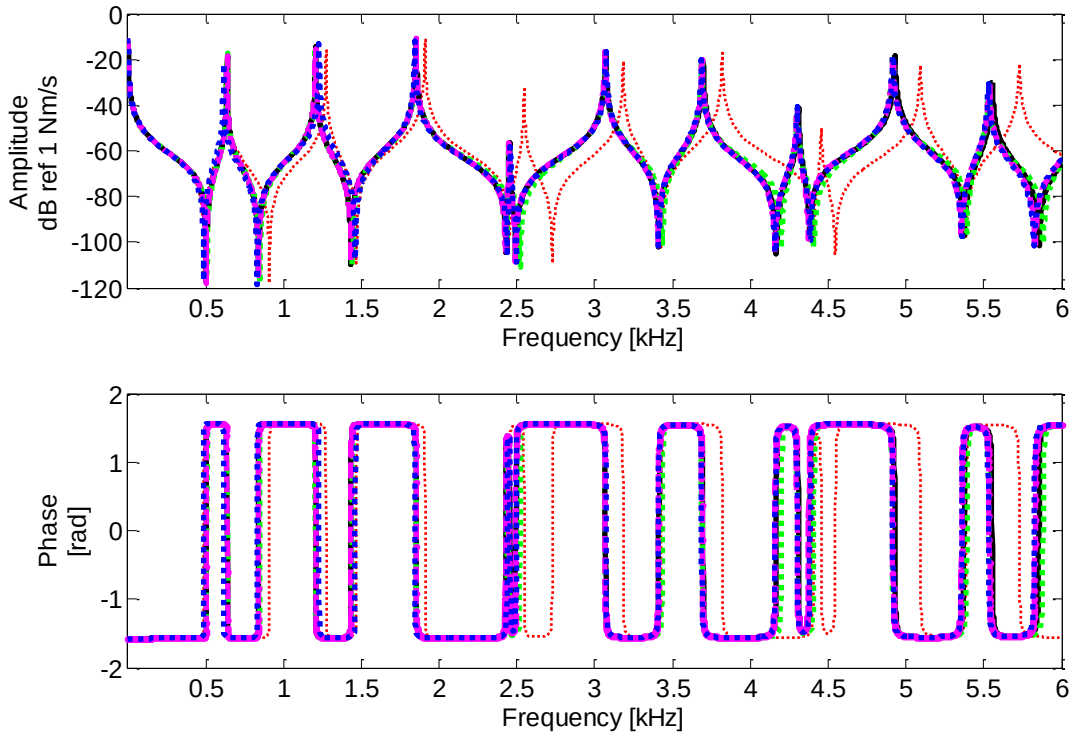

Figure 2.11. Input mobility amplitude and phase with nominal values (dotted red), WKB approximation (dotted blue), piecewise constant properties (dashed magenta) and FE approach (black) and HFE (dotted green); the dispersion parameter is set to $\sigma = 0.2$ and correlation length $b = 2L$.

Table 2.3. Percentage variation of the first ten natural frequencies [kHz] the rod with Young's modulus variability using HFE, WKB and its 1st order approximation, and piecewise constant. The dispersion parameter is set to $\sigma = 0.2$ and correlation length $b = 2L$. The piecewise constant FE is the reference case.

FE [kHz]	(HFE-FE)FE %	(WKB-FE)/FE %	(WKB 1st-FE)/FE %	(Piecewise-FE)/FE %
0.6368	0.0316	-3.4750	-2.7486	-3.4900
1.2057	-0.1000	1.9594	2.7267	1.9436
1.8525	-0.0937	-0.4549	0.2942	-0.4703
2.4517	-0.1129	0.2885	1.0433	0.2730
3.0687	-0.0407	0.1524	0.9061	0.1369
3.6953	-0.1701	-0.1946	0.5565	-0.2100
4.3084	-0.1798	-0.1315	0.6201	-0.1470
4.9283	-0.2890	-0.2209	0.5300	-0.2364
5.5533	-0.3840	-0.3817	0.3679	-0.3972
6.1673	-0.5550	-0.3317	0.4184	-0.3471

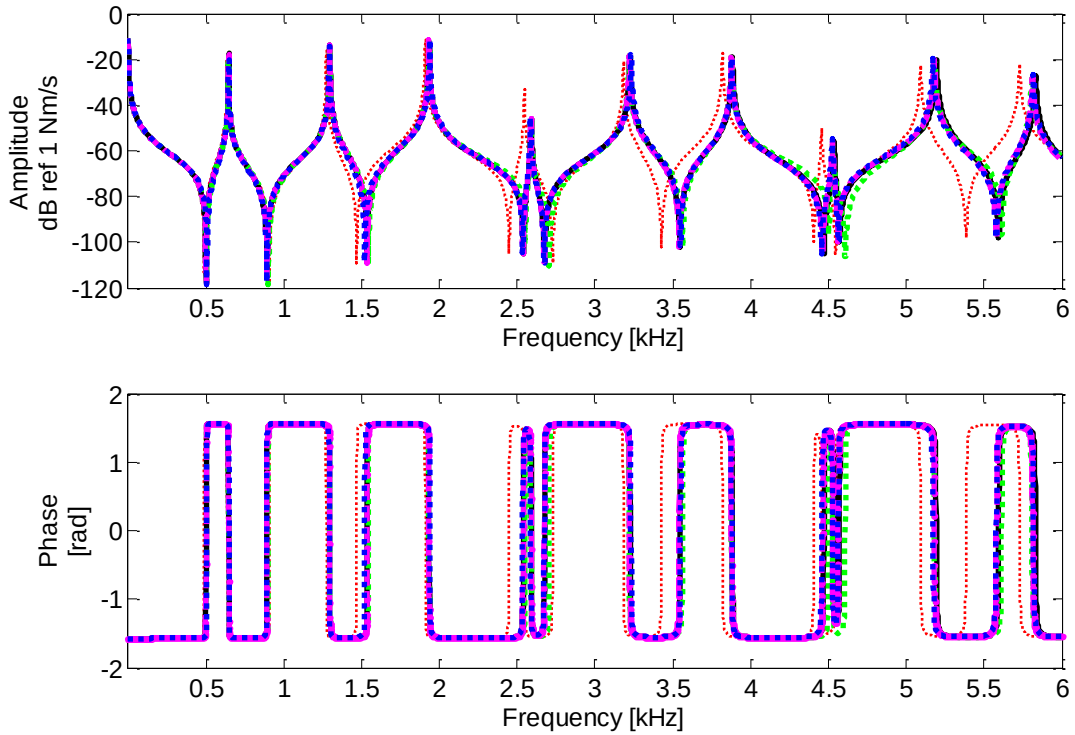

Figure 2.12. Input mobility amplitude and phase with nominal values (dotted red), WKB approximation (dotted blue), piecewise constant properties (dashed magenta) and FE approach (black) and HFE (dotted green); the dispersion parameter is set to $\sigma = 0.1$ and correlation length $b = 0.8L$.

Table 2.4. Percentage variation of the first ten natural frequencies [kHz] the rod with Young's modulus variability using HFE, WKB and its 1st order approximation, and piecewise constant. The dispersion parameter is set to $\sigma = 0.1$ and correlation length $b = 0.8L$. The piecewise constant FE is the reference case.

FE [kHz]	(HFE-FE)FE %	(WKB-FE)/FE %	(WKB 1st-FE)/FE %	(Piecewise-FE)/FE %
0.6457	-0.0122	0.0115	0.3535	0.1226
1.2961	-0.0377	-0.3445	-0.0037	-0.2338
1.9336	0.0062	0.2001	0.5427	0.3114
2.5904	-0.1112	-0.2758	0.0652	-0.1650
3.2246	-0.1380	0.1377	0.4801	0.2489
3.8827	-0.1517	-0.2020	0.1393	-0.0911
4.5354	-0.1924	-0.3259	0.0150	-0.2151
5.1934	-0.2219	-0.5178	-0.1776	-0.4072
5.8312	-0.3968	-0.3239	0.0169	-0.2131
6.4797	-0.3495	-0.3334	0.0074	-0.2226

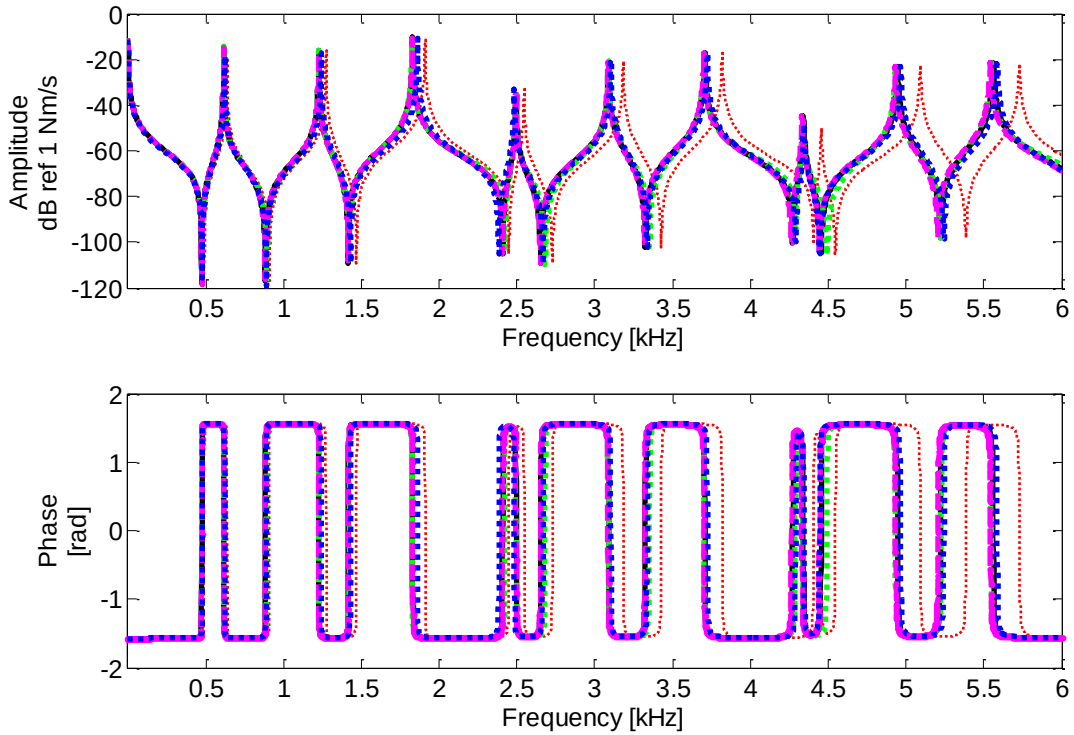

Figure 2.13. Input mobility amplitude and phase with nominal values (dotted red), WKB approximation (dotted blue), piecewise constant properties (dashed magenta) and FE approach (black) and HFE (dotted green); the dispersion parameter is set to $\sigma = 0.1$ and correlation length $b = 0.1$L.

Table 2.5. Percentage variation of the first ten natural frequencies [kHz] the rod with Young's modulus variability using HFE, WKB and its 1st order approximation, and piecewise constant. The dispersion parameter is set to $\sigma = 0.1$ and correlation length $b = 0.1L$. The piecewise constant FE is the reference case.

FE [kHz]	(HFE-FE)FE %	(WKB-FE)/FE %	(WKB 1st-FE)/FE %	(Piecewise-FE)/FE %
0.6151	0.1261	0.5643	0.8054	0.5019
1.2258	-0.0032	0.9314	1.1734	0.8687
1.8301	-0.1968	1.4093	1.6524	1.3464
2.4951	-0.0536	-0.8279	-0.5901	-0.8894
3.0887	0.0045	0.1430	0.3831	0.0808
3.7068	-0.1028	0.1333	0.3733	0.0711
4.3400	-0.1137	-0.2227	0.0165	-0.2847
4.9461	-0.2939	0.0576	0.2975	-0.0045
5.5605	-0.2719	0.1262	0.3663	0.0641
6.2194	-0.6079	-0.5346	-0.2962	-0.5964

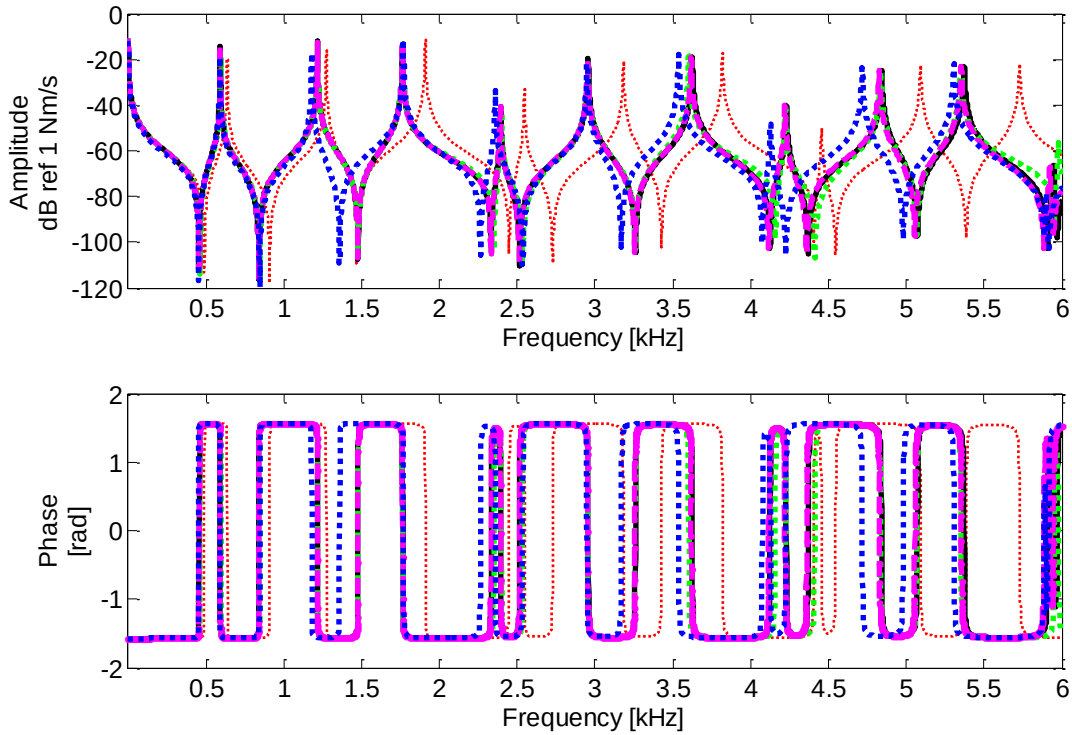

Figure 2.14. Input mobility amplitude and phase with nominal values (dotted red), WKB approximation (dotted blue), piecewise constant properties (dashed magenta) and FE approach (black) and HFE (dotted green); the dispersion parameter is set to $\sigma = 0.2$ and correlation length $b = 0.05L$.

Table 2.6. Percentage variation of the first ten natural frequencies [kHz] the rod with Young's modulus variability using HFE, WKB and its 1st order approximation, and piecewise constant. The dispersion parameter is set to $\sigma = 0.2$ and correlation length $b = 0.05L$. The piecewise constant FE is the reference case.

FE [kHz]	(HFE-FE)FE %	(WKB-FE)/FE %	(WKB 1st-FE)/FE %	(Piecewise-FE)/FE %
0.5929	0.5978	-1.5208	3.0132	0.5157
1.2159	-0.0293	-3.9617	0.4598	-1.9758
1.7633	-0.0306	-0.6601	3.9134	1.3941
2.3937	0.1712	-2.4279	2.0642	-0.4103
2.9560	-0.0613	-1.2386	3.3083	0.8036
3.6248	-0.6103	-3.3504	1.0993	-1.3518
4.2291	-0.1347	-3.3553	1.0942	-1.3568
4.8408	-0.1060	-3.5069	0.9356	-1.5115
5.3721	-0.3884	-2.1812	2.3223	-0.1584
5.9484	0.4953	-1.8424	2.6767	0.1873

2.6 Conclusions

In this chapter the WKB approximation for longitudinal waves in one-dimensional waveguides was used along with a series expansion, the KL expansion, for the spatially correlated variability in order to provide analytical expressions for the natural frequencies and point forced response. The WKB approximation assumes that the waveguide properties along the propagation axis vary slowly enough with respect to the wavelength such that the internal reflections due to local impedance changes are negligible; it also has the advantage of retaining the physical interpretation of positive going and negative going travelling waves. This formulation allows one to approach the problem using a wave formulation similarly to homogeneous waveguides and provides a framework to include random variability in terms of random fields.

The KL expansion, although usually used to generate random samples for a random field, was used here in a purely deterministic sense. A correlation function is assumed such that an analytical expression for the expansion is available, although numerical formulations would be well suited by numerically evaluating the expressions for the phase changes, in the input mobility, and the integral in the denominator, for the natural frequencies. This analytical expression is used to find a first order approximation, assuming low values of σ, for the natural frequencies, since a general closed form solution for the given integral is not readily available.

In addition, a wave formulation considering piecewise constant properties along the waveguide propagation axis is also presented. This approach, unlike the previous one, takes into account internal reflections and an expression for the input mobility was derived. The properties inside each element are constant and given in the same way as in the finite element approach. An expression for the natural frequencies was also derived, but neglecting the internal reflection by imposing reflection coefficients to be equal to zero and also transmission coefficients equal to unity. This leads to a simpler expression for natural frequencies, similar to the one obtained by WKB approximation.

A Finite Element approach using enriched basis (HFEM) was also proposed, where the variability in the properties of the waveguide is included in the element formulation. However this formulation does not ensure the so called k-orthogonality, reducing its numerical efficiency. Nevertheless, this issue could be overcome by choosing an appropriate basis function to represent the variability, but this is beyond the scope of this work. It produced very good agreement with the FE solution, in fact always closer

than the other methods. Although it does not allow closed form solutions for input mobility and natural frequencies, it is computationally more efficient than standard FE (h-version) and also does not require slowly varying properties, being potentially applicable to more general cases.

In the next chapter the formulation presented is extended to a one dimensional waveguide with slowly varying properties taking into account wavenumber dispersion and also non-propagating waves.

3. Flexural waves in one-dimensional waveguides

3.1 Introduction

In this chapter the WKB approximation [45, 49, 67, 72, 73] for flexural waves in one dimensional waveguide with slowly varying properties is applied using the same framework as for the longitudinal waves. The Euler-Bernoulli beam theory is used and, although the phase change is also given by the integral of the wavenumber over the propagation length, in this case the expressions for the amplitude change are slightly different, due to the higher order of the differential equation governing the motion. An extension of the piecewise constant approach for flexural waves is also presented and expressions for the natural frequencies and input mobility are also derived for both cases, taking into account the evanescent term from the flexural wave propagation.

A Finite Element approximation using an enriched hierarchical basis, or Hierarchical Finite Element (HFE) [1, 2], is presented for the flexural case, using a different hierarchical shape function, where the variability in the properties of the waveguide is included in the element formulation. Again, a single sample of a random field is used to carry out the numerical analysis, as all of the formulations are purely deterministic.

3.2 Waves in a finite length beam with slowly changing material variability

The description for the spatial variability in the material and geometrical properties follows the same framework as previously used for the longitudinal vibrations Eq. (2.1), i.e., as a spatial perturbation over a mean, or nominal, value. Also, for sake of simplicity, only the Young's modulus of elasticity is considered spatially varying. Moreover, the analytical solution of the KL expansion, Eq. (2.2), is also used in the analytical formulation, in the same way as in the previous chapter.

3.2.1 WKB approximation for flexural waves in beams

Considering a thin beam undergoing flexural vibration, with slowly changing Young's modulus along its length, such that a propagating wave suffer negligible reflections due to the local impedance change. It is possible to derive the governing (Euler-Bernoulli) equation [19]

$$\frac{\partial^2}{\partial x^2}\left(EI_{yy}(x)\frac{\partial^2 w(x,t)}{\partial x^2}\right)+\rho A(x)\frac{\partial^2 w(x,t)}{\partial t^2}=0, \tag{3.1}$$

where $EI_{yy}(x)$ and $\rho A(x)$ are the spatially varying flexural stiffness and mass per unit length, respectively, and $w(x,t)$ is the transverse displacement along the beam. In order to attend the assumption of Eq. (2.1), the spatial variability has to be simplified to $EI_{yy}(x)=E(x)I_{yy}$ and $\rho A(x)=\rho A$. However, the WKB derivation will follow assuming the more general case.

Assuming a time harmonic solution $w(x,t)=W(x)e^{i\omega t}$, thus, the *eikonal* $S(x)=\ln\widetilde{U}(x)+i\theta(x)$ is introduced, in order to find wave solutions of the kind

$$W(x)=e^{S(x)}=\widetilde{W}(x)e^{\pm i\theta(x)}. \tag{3.2}$$

Back substituting it into Eq.(3.1), and neglecting the higher order terms it is possible to find solutions of the kind [45]:

$$\begin{aligned}W(x)=\left(\rho A(x)\right)^{-\frac{3}{8}}\left(EI_{yy}(x)\right)^{-\frac{1}{8}}\Big[&C_1e^{-i\int_{x_0}^{x}k_B(x)dx}+C_2e^{-\int_{x_0}^{x}k_B(x)dx}\\&+C_3e^{i\int_{x_0}^{x}k_B(x)dx}+C_4e^{\int_{x_0}^{x}k_B(x)dx}\Big],\end{aligned} \tag{3.3}$$

where C_1, C_2, C_3 and C_4 are arbitrary constants and the four terms correspond to positive going and negative going propagating and evanescent waves. Moreover, the exponential terms $\theta(x)=\pm i\int_{x_0}^{x}k_B(x)dx$ and $\theta(x)=\pm\int_{x_0}^{x}k_B(x)dx$ correspond to a phase change of the respective waves and the term $\widetilde{W}(x)=\left(\rho A(x)\right)^{-\frac{3}{8}}\left(EI_{yy}(x)\right)^{-\frac{1}{8}}$ corresponds to an amplitude change because of the changes of the beams properties, and $k_B(x)=\left(\frac{\rho A(x)}{EI_{yy}(x)}\right)^{1/4}\sqrt{\omega}$ is the local free wavenumber for bending waves.

Then, the phase and amplitude change of the positive going and negative going propagating and evanescent waves travelling through a distance L, from $x=0$ to $x=L$, are given by

$$b^{+}=\frac{\widetilde{W}(L)}{\widetilde{W}(0)}e^{-i\int_0^L k_B(x)dx}a^{+}, \tag{3.4}$$

$$b^{-}=\frac{\widetilde{W}(L)}{\widetilde{W}(0)}e^{i\int_0^L k_B(x)dx}a^{-}, \tag{3.5}$$

$$b_N^+ = \frac{\widetilde{W}(L)}{\widetilde{W}(0)} e^{-\int_0^L k_B(x)dx} a_N^+, \tag{3.6}$$

$$b_N^- = \frac{\widetilde{W}(L)}{\widetilde{W}(0)} e^{\int_0^L k_B(x)dx} a_N^-, \tag{3.7}$$

Where $\widetilde{W}(0)$ and $\widetilde{W}(L)$ are the amplitude given by $\widetilde{W}(x) = \left(\rho A(x)\right)^{-\frac{3}{8}} \left(EI_{yy}(x)\right)^{-\frac{1}{8}}$ evaluated at the points $x = 0$ and $x = L$, respectively.

3.2.2 Free wave propagation

Considering a finite waveguide with length L, undergoing free flexural wave behaviour, Figure 3.1, then the positive going and the negative going wave amplitudes on the left hand boundary, $\mathbf{a}^+$ and $\mathbf{a}^-$, and on the right hand boundary, $\mathbf{b}^+$ and $\mathbf{b}^-$, can be related by $\mathbf{b} = \mathbf{\Lambda a}$ from Eq. (3.4)-(3.7), where

$$\mathbf{\Lambda} = \begin{bmatrix} \mathbf{\Lambda}_{11} & \mathbf{0} \\ \mathbf{0} & \mathbf{\Lambda}_{22} \end{bmatrix} \tag{3.8}$$

is a propagation matrix and

$$\mathbf{\Lambda}_{11} = \begin{bmatrix} e^{-i\theta_T + \gamma_T} & 0 \\ 0 & e^{-\theta_T + \gamma_T} \end{bmatrix}, \tag{3.9}$$

$$\mathbf{\Lambda}_{22} = \begin{bmatrix} e^{i\theta_T + \gamma_T} & 0 \\ 0 & e^{\theta_T + \gamma_T} \end{bmatrix}, \tag{3.10}$$

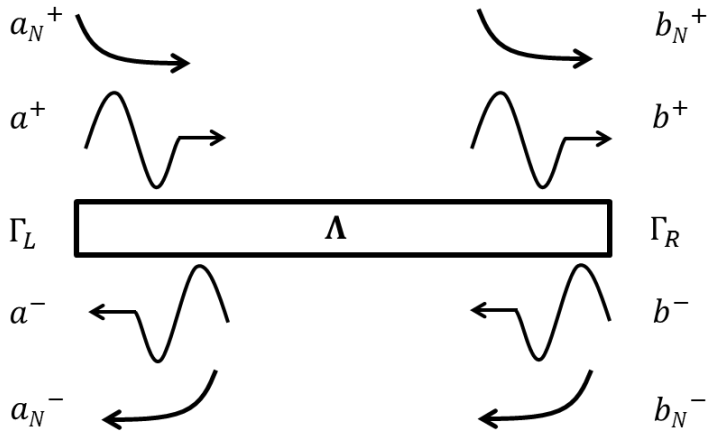

Figure 3.1. Finite waveguide undergoing free flexural wave behaviour, with slowly varying material properties and considering no internal reflections.

The wave amplitudes are given by the vectors

$$\mathbf{a} = \begin{Bmatrix} \mathbf{a}^+ \\ \mathbf{a}^- \end{Bmatrix}, \mathbf{b} = \begin{Bmatrix} \mathbf{b}^+ \\ \mathbf{b}^- \end{Bmatrix}. \tag{3.11}$$

where the propagating and evanescent waves are, respectively, given as $\mathbf{a}^+ = [a^+ \quad a_N^+]^T$, $\mathbf{a}^- = [a^- \quad a_N^-]^T$, $\mathbf{b}^+ = [b^+ \quad b_N^+]^T$ and $\mathbf{b}^- = [b^- \quad b_N^-]^T$. The total phase and amplitude change for a travelling wave propagating from one boundary to the other θ_T can be given by

$$\theta_T = \int_0^L k_B(x)dx. \tag{3.12}$$

and

$$\gamma_T = \ln\left[\frac{\widetilde{W}(L)}{\widetilde{W}(0)}\right]. \tag{3.13}$$

The waveguide natural frequencies can be determined by applying the wave train closure principle, tracing the round-trip propagating wave, as described in Chapter 2, and finding the zeros of the characteristic equation [19, 61]

$$\det(\mathbf{\Lambda}_{22}^{-1}\mathbf{\Gamma}_R\mathbf{\Lambda}_{11}\mathbf{\Gamma}_L - \mathbf{I}) = 0. \tag{3.14}$$

where $\mathbf{I}$ is a 2×2 identity matrix and the reflection matrices follow from the relations between the waves in the boundaries $\mathbf{a}^+ = \mathbf{\Gamma}_L\mathbf{a}^-$ and $\mathbf{b}^- = \mathbf{\Gamma}_R\mathbf{b}^+$. They can be found by writing the equation for equilibrium and continuity in a systematic framework [22, 70, 71]. Solving Equation (3.14) will usually lead to the problem of finding the n^{th} root of a transcendental equation θ_{Tn}, such that the n^{th} natural frequency ω_n is given by θ_{Tn}

$$\omega_n = \frac{\theta_{Tn}^2}{\left(\int_0^L \sqrt[4]{\frac{\rho A(x)}{EI_{yy}(x)}}\, dx\right)^2}. \tag{3.15}$$

This transcendental equations depends only on the boundary condition, or the matrices $\mathbf{\Gamma}_L$ and $\mathbf{\Gamma}_R$, and they are analogous to the homogenous case. Their roots for typical boundary conditions can be found on tables (for instance, in [20]) where the results can be directly applied in Equation (3.15). This is shown for a particular boundary condition by Pierce [45].

If only the Young's modulus is considered to be varying, Eq. (2.1), while the other properties are constant, a first order approximation can be used for the cases where one

assumes small dispersion around the nominal value, i.e. $|\sigma H(x)| \ll 1$, such that $[1+\sigma H(x)]^{-1/4} \approx 1 - \sigma/4\, H(x)$, then

$$\widetilde{\omega}_n \approx \sqrt[4]{\frac{E_0 I_{yy}}{\rho A}} \left(\frac{\theta_{Tn}}{L - \frac{\sigma}{4}\int_0^L H(x)dx} \right)^2 . \tag{3.16}$$

This expression shows that the natural frequencies are affected by the contributions of the terms in the KL expansion. If there is no variation and $\sigma = 0$, the expression reduces to the homogenous case. Moreover, if $H(x)$, is expressed by Eq. (2.2), then its integral has a closed form and the first order approximation for the natural frequency is given by

$$\widetilde{\omega}_n \approx \sqrt[4]{\frac{E_0 I_{yy}}{\rho A}} \left(\frac{\theta_{Tn}}{L - \frac{\sigma}{2}\sum_{j=1}^{N_{kl}} \xi_{2j}(p) \frac{\beta_j}{w_{2j}} \sin(w_{2j}x)} \right)^2 . \tag{3.17}$$

3.2.3 Point excitation

The expression for the input mobility due to a point excitation, Figure 3.2, can be derived following the above analysis. The point harmonic excitation force F, applied at L_1, creates a positive going $\mathbf{q}^+ = [q^+ \quad q_N^+]^T$ and a negative going $\mathbf{q}^- = [q^- \quad q_N^-]^T$ propagating and evanescent wave, so that the waves at this point are given by the sum of these directly excited and the incident ones such that

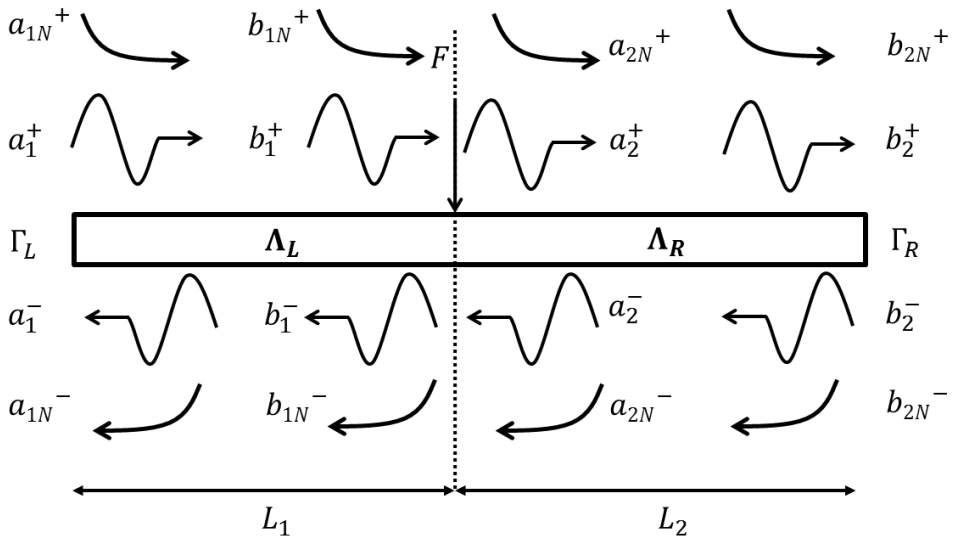

Figure 3.2. Point excitation on finite length beam, with slowly varying material properties, considering no internal reflections.

$$\mathbf{a}_2^+ = \mathbf{b}_1^+ + \mathbf{q}^+, \tag{3.18}$$

and

$$\mathbf{b}_1^- = \mathbf{a}_2^- + \mathbf{q}^-. \tag{3.19}$$

Propagation from the boundaries to the excitation point is given by $\mathbf{b_1} = \mathbf{\Lambda_L a_1}$ and $\mathbf{b_2} = \mathbf{\Lambda_R a_2}$, where

$$\mathbf{\Lambda_L} = \begin{bmatrix} \mathbf{\Lambda_{L_{11}}} & \mathbf{0} \\ \mathbf{0} & \mathbf{\Lambda_{L_{22}}} \end{bmatrix}, \qquad \mathbf{\Lambda_R} = \begin{bmatrix} \mathbf{\Lambda_{R_{11}}} & \mathbf{0} \\ \mathbf{0} & \mathbf{\Lambda_{R_{22}}} \end{bmatrix} \tag{3.20}$$

and

$$\mathbf{\Lambda_{L_{11}}} = \begin{bmatrix} e^{-i\theta_L+\gamma_L} & 0 \\ 0 & e^{-\theta_L+\gamma} \end{bmatrix}, \tag{3.21}$$

$$\mathbf{\Lambda_{L_{22}}} = \begin{bmatrix} e^{i\theta_L+\gamma_L} & 0 \\ 0 & e^{\theta_L+\gamma} \end{bmatrix}, \tag{3.22}$$

$$\mathbf{\Lambda_{R_{11}}} = \begin{bmatrix} e^{-i\theta_R+\gamma_R} & 0 \\ 0 & e^{-\theta_R+\gamma_R} \end{bmatrix}, \tag{3.23}$$

$$\mathbf{\Lambda_{R_{22}}} = \begin{bmatrix} e^{i\theta_R+\gamma_R} & 0 \\ 0 & e^{\theta_R+\gamma_R} \end{bmatrix}. \tag{3.24}$$

Moreover, θ_L and γ_L gives the total phase and amplitude change of the propagating wave to the left side of the point excitation on the waveguide and θ_R and γ_R the total phase and amplitude change on its right side, where

$$\theta_L = \int_0^{L_1} k_B(x)dx \text{ and } \gamma_L = \ln\left[\frac{\widetilde{W}(L_1)}{\widetilde{W}(0)}\right], \tag{3.25}$$

$$\theta_R = \int_{L_1}^{L} k_B(x)dx \text{ and } \gamma_R = \ln\left[\frac{\widetilde{W}(L)}{\widetilde{W}(L_1)}\right], \tag{3.26}$$

and

$$\mathbf{a}_1 = \begin{Bmatrix} \mathbf{a}_1^+ \\ \mathbf{a}_1^- \end{Bmatrix}, \mathbf{a}_2 = \begin{Bmatrix} \mathbf{a}_2^+ \\ \mathbf{a}_2^- \end{Bmatrix} \mathbf{b}_1 = \begin{Bmatrix} \mathbf{b}_1^+ \\ \mathbf{b}_1^- \end{Bmatrix}, \mathbf{b}_2 = \begin{Bmatrix} \mathbf{b}_2^+ \\ \mathbf{b}_2^- \end{Bmatrix}, \tag{3.27}$$

includes propagating and evanescent waves. The reflected waves from the energy conserving boundaries at the left and the right hand ends are given by the respective reflection matrices as $\mathbf{a}_1^+ = \mathbf{\Gamma}_L \mathbf{a}_1^-$ and $\mathbf{b}_2^- = \mathbf{\Gamma}_R \mathbf{b}_2^+$.

Under the assumptions of the WKB approximations, the n^{th} derivative with respect to x of the positive and negative going propagating waves $\partial^n W^+(x)/\partial x = \left(-ik_B(x)\right)^n W^+(x)$, $\partial^n W^-(x)/\partial x = \left(ik_B(x)\right)^n W^-(x)$, and the evanescent waves $\partial W_N^+(x)/\partial x = \left(-k_B(x)\right)^n W_N^+(x)$, $\partial W_N^-(x)/\partial x = k_B^n(x) W_N^-(x)$. Equilibrium and continuity of displacement gives the amplitudes of the waves produced by an external point harmonic force F as

$$\mathbf{q} = \mathbf{q}^+ = \mathbf{q}^- = \frac{i}{4iEI_{yy}(L_1)k_B^3(L_1)} \begin{bmatrix} 1 \\ -i \end{bmatrix} F. \tag{3.28}$$

where $E(L_1)$ and $k_B(L_1)$ is the Young's modulus and local wavenumber, both evaluated at $x = L_1$.

Solving these equations is straightforward and gives expressions for the wave amplitudes. Using Eqs. (3.18) and (3.19) together with the propagation and reflection properties, and noting that the inverse of the matrices $\mathbf{\Lambda}_{L_{11}}$ and $\mathbf{\Lambda}_{R_{11}}$ are simply the inverse of each of its diagonal elements, then the positive going wave $\mathbf{a}_2^+$ is given by

$$\mathbf{a}_2^+ = \mathbf{\Lambda}_{\mathrm{L}_{11}} \mathbf{\Gamma}_{\mathrm{L}} \mathbf{\Lambda}_{\mathrm{L}}^{-1}{}_{22} \left(\mathbf{\Lambda}_{\mathrm{R}}^{-1}{}_{22} \mathbf{\Gamma}_{\mathrm{R}} \mathbf{\Lambda}_{\mathrm{R}_{11}} \mathbf{a}_2^+ + \mathbf{q}^- \right) + \mathbf{q}^+, \tag{3.29}$$

and it is related to the negative going $\mathbf{a}_2^-$ by

$$\mathbf{a}_2^- = \mathbf{\Lambda}_{\mathrm{R}}^{-1}{}_{22} \mathbf{\Gamma}_{\mathrm{R}} \mathbf{\Lambda}_{R_{11}} \mathbf{a}_2^+. \tag{3.30}$$

The input mobility $\mathbf{Y}(\omega) = i\omega(\mathbf{a}_2^+ + \mathbf{a}_2^-)/F$ can be calculated by using the superposition principle of a positive going $\mathbf{a}_2^+$ and a negative going $\mathbf{a}_2^-$ wave at the point of excitation,

$$\mathbf{w} = \mathbf{a}_2^+ + \mathbf{a}_2^- = \frac{\left(\mathbf{I} + \mathbf{\Lambda}_{\mathrm{R}}^{-1}{}_{22} \mathbf{\Gamma}_{\mathrm{R}} \mathbf{\Lambda}_{R_{11}}\right)\left(\mathbf{I} + \mathbf{\Lambda}_{\mathrm{L}_{11}} \mathbf{\Gamma}_{\mathrm{L}} \mathbf{\Lambda}_{\mathrm{L}}^{-1}{}_{22}\right)}{\mathbf{I} - \mathbf{\Lambda}_{\mathrm{L}_{11}} \mathbf{\Gamma}_{\mathrm{L}} \mathbf{\Lambda}_{\mathrm{L}}^{-1}{}_{22} \mathbf{\Lambda}_{\mathrm{R}}^{-1}{}_{22} \mathbf{\Gamma}_{\mathrm{R}} \mathbf{\Lambda}_{R_{22}}} \mathbf{q}, \tag{3.31}$$

These relationships can be used to find the wave amplitudes at any point of the waveguide. The input mobility due to a point force is given by the contributions of the propagating and evanescent components of the response $\mathbf{w} = [w \quad w_N]^T$:

$$\mathrm{Y}(\omega) = \frac{i\omega(w + w_N)}{F}. \tag{3.32}$$

3.3 Waves in finite length beams with piecewise constant material variability

Consider a beam with piecewise constant material variability, separated into a finite number of discrete sections and undergoing flexural vibration. This can be an approximation representation for the more general spatial varying system. The wavenumber for the j^{th} element is

$$k_{B_j} = \sqrt[4]{\frac{\rho A_j}{E I_{yy_j}}}\sqrt{\omega}. \tag{3.33}$$

In this way, internal reflections due to the local changes in the impedance inside the rod can be taken into account, analogous to the case for longitudinal waves, presented previously.

Equation (2.1) is evaluated at the geometrical centre of the elements and is used to estimate the values used in the piecewise constant description, by simply sampling the random field at the centroid of each element x_{cj}, such that

$$E_j(p) = E\left(x_{cj}, p\right). \tag{3.34}$$

3.3.1 Free wave propagation

For a finite waveguide with length L, undergoing free wave propagation, with piecewise constant properties, divided into N elements, such that for the j^{th} element the positive going and the negative going waves on the left $\mathbf{a_j}$ and on the right side $\mathbf{b}_j$, are related by $\mathbf{b}_j = \mathbf{\Lambda}_j \mathbf{a}_j$, where

$$\mathbf{\Lambda}_j = \begin{bmatrix} \mathbf{\Lambda}_{j_{11}} & \mathbf{0} \\ \mathbf{0} & \mathbf{\Lambda}_{j_{22}} \end{bmatrix} \tag{3.35}$$

is a propagation matrix and $\mathbf{\Lambda}_{j11} = diag\left(e^{-i\theta_j}, e^{-\theta_j}\right)$, $\mathbf{\Lambda}_{j22} = diag\left(e^{i\theta_j}, e^{\theta_j}\right)$

$$\mathbf{a}_j = \begin{Bmatrix} \mathbf{a}_j^+ \\ \mathbf{a}_j^- \end{Bmatrix}, \mathbf{b}_j = \begin{Bmatrix} \mathbf{b}_j^+ \\ \mathbf{b}_j^- \end{Bmatrix}, \tag{3.36}$$

where the propagating and evanescent waves are, respectively, given as $\mathbf{a}_j^+ = \begin{bmatrix} a_j^+ & a_{Nj}^+ \end{bmatrix}^T$, $\mathbf{a}_j^- = [a_j^- \quad a_{Nj}^-]^T$, $\mathbf{b}_j^+ = \begin{bmatrix} b_j^+ & b_{Nj}^+ \end{bmatrix}^T$ and $\mathbf{b}_j^- = [b_j^- \quad b_{Nj}^-]^T$.

Assuming that there are no energy losses from a wave transmitted from one element to another, two consecutives elements are connected by a scattering matrix $\mathbf{a}_{j+1} = \mathbf{G}_j \mathbf{b}_j$, which can be partitioned as

$$\begin{Bmatrix} \mathbf{a}_{j+1}^{+} \\ \mathbf{a}_{j+1}^{-} \end{Bmatrix} = \begin{bmatrix} \mathbf{G}_{j11} & \mathbf{G}_{j12} \\ \mathbf{G}_{j21} & \mathbf{G}_{j22} \end{bmatrix} \begin{Bmatrix} \mathbf{b}_{j}^{+} \\ \mathbf{b}_{j}^{-} \end{Bmatrix}, \tag{3.37}$$

where

$$\mathbf{G}_{j11} = \frac{1}{4Z_{j+1}k_{Bj+1}} \begin{bmatrix} \left(k_{Bj} + k_{Bj+1}\right)\left(Z_j + Z_{j+1}\right) & i\left(k_{Bj} + ik_{Bj+1}\right)\left(Z_j - Z_{j+1}\right) \\ -i\left(k_{Bj} - ik_{Bj+1}\right)\left(Z_j - Z_{j+1}\right) & \left(k_{Bj} + k_{Bj+1}\right)\left(Z_j + Z_{j+1}\right) \end{bmatrix}, \tag{3.38}$$

$$\mathbf{G}_{j12} = \frac{1}{4Z_{j+1}k_{Bj+1}} \begin{bmatrix} -\left(k_{Bj} - k_{Bj+1}\right)\left(Z_j + Z_{j+1}\right) & -i\left(k_{Bj} - ik_{Bj+1}\right)\left(Z_j - Z_{j+1}\right) \\ i\left(k_{Bj} + ik_{Bj+1}\right)\left(Z_j - Z_{j+1}\right) & -\left(k_{Bj} - k_{Bj+1}\right)\left(Z_j + Z_{j+1}\right) \end{bmatrix}, \tag{3.39}$$

$$\mathbf{G}_{j21} = \mathbf{G}_{j12}, \tag{3.40}$$

$$\mathbf{G}_{j22} = \mathbf{G}_{j11}, \tag{3.41}$$

and $Z_j = EI_j k_{Bj}^2$. It follows that the wave amplitudes on the left of the waveguide $\mathbf{a}_1$ and the ones at the right hand boundary $\mathbf{b}_N$, considering N elements and, consequently, at the $(N-1)^{th}$ junction is given by $\mathbf{b}_N = \widetilde{\mathbf{\Lambda}}\mathbf{a}_1$, where [74]

$$\widetilde{\mathbf{\Lambda}} = \mathbf{\Lambda}_N \prod_{j=1}^{N-1} \mathbf{G}_{N-j} \mathbf{\Lambda}_{N-j} \,. \tag{3.42}$$

Natural frequencies can be sought by applying the wave-train closure principle, tracing the round-trip propagating wave, and, differently from the previous case, considering the internal reflections, using the partitioned matrix

$$\begin{Bmatrix} \mathbf{b}_N^{+} \\ \mathbf{b}_N^{-} \end{Bmatrix} = \begin{bmatrix} \widetilde{\mathbf{\Lambda}}_{11} & \widetilde{\mathbf{\Lambda}}_{12} \\ \widetilde{\mathbf{\Lambda}}_{21} & \widetilde{\mathbf{\Lambda}}_{22} \end{bmatrix} \begin{Bmatrix} \mathbf{a}_1^{+} \\ \mathbf{a}_1^{-} \end{Bmatrix}, \tag{3.43}$$

together with the reflections matrices at the boundaries $\mathbf{\Gamma}_R$ and $\mathbf{\Gamma}_L$, so that they correspond to the zeros of the characteristic equation

$$\det\left(\mathbf{\Gamma}_R \widetilde{\mathbf{\Lambda}}_{11} \mathbf{\Gamma}_L + \mathbf{\Gamma}_R \widetilde{\mathbf{\Lambda}}_{12} - \widetilde{\mathbf{\Lambda}}_{21} \mathbf{\Gamma}_L - \widetilde{\mathbf{\Lambda}}_{22}\right) = 0, \tag{3.44}$$

where $(\cdot)_{ij}$ is the i^{th} row and j^{th} column element of the partitioned matrix.

For slowly varying properties, it is possible to approximate the scattering matrix to an identity matrix $\mathbf{G}_j \approx \mathbf{I}$, meaning that the wave is fully transmitted, with negligible reflections. This simplifies $\widetilde{\mathbf{\Lambda}}$, Eq. (2.49), such that it becomes a block diagonal matrix,

i.e. $\widetilde{\mathbf{\Lambda}}_{12} = \widetilde{\mathbf{\Lambda}}_{21} = \mathbf{0}$, where $\mathbf{0}$ is a null matrix, which, in turn leads to Eq. (3.43) in a much simpler form

$$\det\left(\mathbf{\Gamma}_R \widetilde{\mathbf{\Lambda}}_{11} \mathbf{\Gamma}_L - \widetilde{\mathbf{\Lambda}}_{22}\right) \approx 0, \tag{3.45}$$

whose solution is analogous to Eq. (3.15), but changing the integral term by a summation over the properties of each element

$$\omega_n = \frac{\theta_{Tn}^2}{\left(\sum_{j=1}^{N} \sqrt[4]{\frac{\rho A_j}{E I_{yy_j}}} L\right)^2}, \tag{3.46}$$

and θ_{Tn} is the n^{th} root of the same transcendental equation depending on the boundary conditions.

3.3.2 Point excitation

The excitation is given by a harmonic force F applied at the M^{th} junction, at L_1 from the left boundary, so that it creates a positive going $\mathbf{q}^+$ and a negative going $\mathbf{q}^-$ propagating wave. The waves at this point are given by the sum of these directly excited waves plus the transmitted and reflected ones such that

$$\begin{Bmatrix} \mathbf{a}_{M+1}^+ \\ \mathbf{b}_M^- \end{Bmatrix} = \begin{bmatrix} \mathbf{r}_M^+ & \mathbf{t}_M^+ \\ \mathbf{t}_M^- & \mathbf{r}_M^- \end{bmatrix} \begin{Bmatrix} \mathbf{a}_{M+1}^- \\ \mathbf{b}_M^+ \end{Bmatrix} + \begin{Bmatrix} \mathbf{q}^+ \\ \mathbf{q}^- \end{Bmatrix}, \tag{3.47}$$

where the reflection and transmission matrices $\mathbf{r}_M^+$, $\mathbf{t}_M^+$, $\mathbf{t}_M^-$ and $\mathbf{r}_M^-$ are related to the scattering matrix $\mathbf{G}_M$ at the excitation point by

$$\mathbf{r}_M^+ = \mathbf{G}_{M12} \mathbf{G}_{M22}^{-1} \tag{3.48}$$

$$\mathbf{t}_M^+ = \mathbf{G}_{M11} - \mathbf{G}_{M12} \mathbf{G}_{M22}^{-1} \mathbf{G}_{M21} \tag{3.49}$$

$$\mathbf{t}_M^- = \mathbf{G}_{M22}^{-1} \tag{3.50}$$

$$\mathbf{r}_M^- = -\mathbf{G}_{M22}^{-1} \mathbf{G}_{M21} \tag{3.51}$$

and $\mathbf{G}_{Mij}$ stands for the i^{th} row and j^{th} column element of the partitioned scattering matrix at the M^{th} junction and $\mathbf{G}_{Mij}^{-1}$ stands for its inverse.

Moreover, assuming continuity of the displacement leads to $\mathbf{q} = \mathbf{q}^+ = \mathbf{q}^-$; and equilibrium of the shear forces with the externally applied force, and bending momentum at the excitation, then the directly excited waves amplitudes due to a point force are given as

$$\mathbf{q} = \frac{-iF}{2I_{yy}(E_M k_M^3 + E_{M+1} k_{M+1}^3)} \begin{bmatrix} 1 \\ -1i \end{bmatrix}. \tag{3.52}$$

The wave amplitudes on the left end of the waveguide $\mathbf{a}_1$ and the ones on the right end of the M^{th} element $\mathbf{b}_M$, are related by $\mathbf{b}_\mathrm{M} = \widetilde{\mathbf{\Lambda}}_\mathrm{L}\mathbf{a}_1$; also the wave amplitudes on the right end of the waveguide $\mathbf{b}_N$ and the ones on the left end of the $(\mathrm{M}+1)^{th}$ element $\mathbf{a}_{M+1}$, are related by $\mathbf{b}_\mathrm{N} = \widetilde{\mathbf{\Lambda}}_\mathrm{R}\mathbf{a}_{M+1}$, where

$$\widetilde{\mathbf{\Lambda}}_\mathrm{L} = \mathbf{\Lambda}_\mathrm{M} \prod_{j=1}^{\mathrm{M}-1} \mathbf{G}_{\mathrm{M}-\mathrm{j}}\mathbf{\Lambda}_{\mathrm{M}-\mathrm{j}}\,, \tag{3.53}$$

$$\widetilde{\mathbf{\Lambda}}_\mathrm{R} = \mathbf{\Lambda}_\mathrm{N} \prod_{j=1}^{\mathrm{N}-\mathrm{M}-1} \mathbf{G}_{\mathrm{N}-\mathrm{j}}\mathbf{\Lambda}_{\mathrm{N}-\mathrm{j}}\,. \tag{3.54}$$

Also, these matrices are related to the free wave propagation matrix by $\widetilde{\mathbf{\Lambda}} = \widetilde{\mathbf{\Lambda}}_L\mathbf{G}_M\widetilde{\mathbf{\Lambda}}_R$. Applying the boundary conditions, i.e. $\mathbf{a}_1^+ = \mathbf{\Gamma}_L\mathbf{a}_1^-$ and $\mathbf{b}_N^- = \mathbf{\Gamma}_R\mathbf{b}_N^+$, to these expressions leads to

$$\begin{Bmatrix} \mathbf{b}_N^+ \\ \mathbf{\Gamma}_R\mathbf{b}_N^+ \end{Bmatrix} = \begin{bmatrix} \widetilde{\mathbf{\Lambda}}_{R11} & \widetilde{\mathbf{\Lambda}}_{R12} \\ \widetilde{\mathbf{\Lambda}}_{R21} & \widetilde{\mathbf{\Lambda}}_{R22} \end{bmatrix} \begin{Bmatrix} \mathbf{a}_{M+1}^+ \\ \mathbf{a}_{M+1}^- \end{Bmatrix}, \tag{3.55}$$

$$\begin{Bmatrix} \mathbf{b}_M^+ \\ \mathbf{b}_M^- \end{Bmatrix} = \begin{bmatrix} \widetilde{\mathbf{\Lambda}}_{L11} & \widetilde{\mathbf{\Lambda}}_{L12} \\ \widetilde{\mathbf{\Lambda}}_{L21} & \widetilde{\mathbf{\Lambda}}_{L22} \end{bmatrix} \begin{Bmatrix} \mathbf{\Gamma}_L\mathbf{a}_1^- \\ \mathbf{a}_1^- \end{Bmatrix}, \tag{3.56}$$

from which it is possible to find that $\mathbf{a}_{M+1}^- = \mathbf{T}_R\mathbf{a}_{M+1}^+$ and $\mathbf{b}_M^+ = \mathbf{T}_L\mathbf{b}_M^-$, where

$$\mathbf{T}_R = \left(\mathbf{\Gamma}_R\widetilde{\mathbf{\Lambda}}_{R12} - \widetilde{\mathbf{\Lambda}}_{R22}\right)^{-1}\left(\widetilde{\mathbf{\Lambda}}_{R21} - \mathbf{\Gamma}_R\widetilde{\mathbf{\Lambda}}_{R11}\right), \tag{3.57}$$

$$\mathbf{T}_L = \left(\widetilde{\mathbf{\Lambda}}_{L11}\mathbf{\Gamma}_L + \widetilde{\mathbf{\Lambda}}_{L12}\right)\left(\widetilde{\mathbf{\Lambda}}_{L21}\mathbf{\Gamma}_L + \widetilde{\mathbf{\Lambda}}_{L22}\right)^{-1}. \tag{3.58}$$

This, in turn, can be applied to Eq. (3.47) such that

$$\mathbf{a}_{M+1}^+ = [\mathbf{I} - \mathbf{r}_M^+\mathbf{T}_R - \mathbf{t}_M^+\mathbf{T}_L(\mathbf{I} - \mathbf{r}_M^-\mathbf{T}_L)^{-1}\mathbf{t}_M^-\mathbf{T}_R]^{-1}[\mathbf{t}_M^+\mathbf{T}_L(\mathbf{I} - \mathbf{r}_M^-\mathbf{T}_L)^{-1}\mathbf{q}^- + \mathbf{q}^+] \tag{3.59}$$

The total response at the point of excitation $\mathbf{w}$ can be calculated by using the superposition principle of a positive going $\mathbf{a}_{M+1}^+$ and a negative going $\mathbf{a}_{M+1}^-$ propagating wave at the point of excitation, such that

$$\mathbf{w} = (\mathbf{I} + \mathbf{T}_R)\mathbf{a}_{M+1}^+. \tag{3.60}$$

The input mobility due to a point force is given by the contributions of the propagating and evanescent components of the response $\mathbf{w} = [w \quad w_N]^T$ as before, i.e.

$$\boldsymbol{Y}_{\mathrm{CTE}}(\omega) = \frac{i\omega(w + w_N)}{F}. \tag{3.61}$$

3.4 Finite element approximation using a hierarchical basis (HFE)

The hierarchical finite element including material variability in the element formulation is extended for flexural beams, using Euler-Bernoulli elements. The formulation follows the same procedure than for the rod element, but using a different set of hierarchical functions. It also produces smaller matrices than the usual FE approach would, with no increase in the number of the degrees of freedom, only enriching the internal displacement field. The flexural displacement along the element can be described in terms of p assumed functions, as shown in Eq. (2.62).

The first four shape functions are the usual finite element shape functions $g_1(\xi) = \frac{1}{4}(2 - 3\xi + \xi^2)$, $g_2 = \frac{1}{4}(1 - \xi - \xi^2 + x^3)$, $g_3 = \frac{1}{4}(2 + 3\xi - x^3)$, $g_4 = \frac{1}{4}(-1 - \xi + \xi^2 + x^3)$, and the hierarchical functions $g_r(\xi)$, for $r > 4$ are also derived from the Legendre polynomial, but with a slight modification

$$g_r(\xi) = \sum_{n=0}^{(r-1)/2} \frac{(-1)^n}{2^n n!} \frac{(2r - 2n - 7)!!}{(r - 2n - 1)!} \xi^{r-2n-1}. \tag{3.62}$$

where $m!! = m(m-2)\ldots(2 \text{ or } 1)$, $0!! = 1$, $(-1)!! = 1$ and $(r-1)/2$ stands for its integer part. This ensures that their contribution at the nodes $\xi = \pm 1$ is zero, therefore there is no increase in the number of nodes.

Assuming spatial variability in the material and geometrical properties as $EI_{yy} = EI_{yy}(x)$ and $\rho A = \rho A(x)$, the element matrices can be written as

$$\mathbf{K}_e = \frac{1}{a^3} \int_{-1}^{1} EI_{yy}(x) \lfloor \mathbf{N}(\xi)'' \rfloor^T \lfloor \mathbf{N}(\xi)'' \rfloor d\xi, \tag{3.63}$$

$$\mathbf{M}_e = a \int_{-1}^{1} \rho A(x) \lfloor \mathbf{N}(\xi) \rfloor^T \lfloor \mathbf{N}(\xi) \rfloor d\xi, \tag{3.64}$$

where $a = L/2$, being L the element size, and $''$ stands for the second derivative. Moreover, the force vector can be calculated as $\mathbf{f_e} = a \int_{-1}^{1} p_x \lfloor \mathbf{N}(\xi) \rfloor d\xi$. For point excitation $p_x = f_x \delta(x - x_e)$, where $\delta(x)$ is the Dirac delta function, then

$$\mathbf{f_e} = a f_x \lfloor \mathbf{N}(x_e) \rfloor. \tag{3.65}$$

If the spatially varying properties are described in the same manner as Eq. (2.2), with a change of variable such that $-L/2 < x < L/2$, i.e.

$$EI_{yy}(x) = EI_{yy_0}\left[1 + \sigma_{EI}\sum_{j=1}^{N_{KL}}\left(\alpha_j \sin(w_{1j}x) + \beta_j \cos(w_{2j}x)\right)\right] \tag{3.66}$$

$$\rho A(x) = \rho A_0\left[1 + \sigma_{\rho A}\sum_{j=1}^{N_{KL}}\left(\gamma_j \sin(w_{3j}x) + \delta_j \cos(w_{4j}x)\right)\right] \tag{3.67}$$

then the element matrices can be rewritten as $\mathbf{K}_e = \mathbf{K}_{e0} + \mathbf{\Delta K}_e$ and $\mathbf{M}_e = \mathbf{M}_{e0} + \mathbf{\Delta M}_e$, where

$$\mathbf{\Delta K}_e = \frac{\sigma}{a^3}\sum_{j=1}^{N_{KL}}\int_{-1}^{1}\left(\alpha_j \sin\left(\frac{2w_1}{L}\xi\right) + \beta_j \cos\left(\frac{2w_2}{L}\xi\right)\right)\lfloor \mathbf{N}(\xi)'' \rfloor^T \lfloor \mathbf{N}(\xi)'' \rfloor d\xi \tag{3.68}$$

$$\mathbf{\Delta M}_e = 2a\sigma\sum_{j=1}^{N_{KL}}\int_{-1}^{1}\left(\gamma_j \sin\left(\frac{2w_3}{L}\xi\right) + \delta_j \cos\left(\frac{2w_4}{L}\xi\right)\right)\lfloor \mathbf{N}(\xi) \rfloor^T \lfloor \mathbf{N}(\xi) \rfloor d\xi \tag{3.69}$$

and $\mathbf{K}_{e0}$ and $\mathbf{M}_{e0}$ are the usual stiffness and mass matrices found with homogeneous properties. These integrals can be numerically evaluated by using, for instance, a quadrature rule. Analogously to the rod elements, this approach does not ensure the so called k-orthogonality [1] for the matrix $\mathbf{\Delta K}_e$.

3.5 Numerical results and discussion

Numerical analysis was carried out aiming to compare the results obtained with WKB for flexural waves in a beam with the other methodologies, i.e. the piecewise constant wave approach, HFE and FE. The beam properties were assumed to possess a mean value for the Young's modulus $E_0 = 70$ GPa, with rectangular cross-section and thickness 1 mm and width 30 mm, i.e. A $=$ 30 mm^2, total length $L =$ 0.5 m, and density $\rho =$ 2700 kg/m^3, with free-free boundary conditions, i.e. reflection matrices at left and right $\mathbf{\Gamma}_L = \mathbf{\Gamma}_R = \begin{bmatrix} -i & 1+i \\ 1-i & i \end{bmatrix}$. Structural damping was included by making the Young's modulus a complex number $E_0 = E_0(1 + i\eta)$, with $\eta = 10^{-3}$. This change would not affect the theoretical results as long as η is constant over the waveguide. The frequency band under analysis was chosen from 1 Hz to 1.2 kHz, discretised by 1Hz,

such that at least the first ten modes could be seen. Moreover, the excitation point was at $x = L_1 = 0.35L$.

Figure 3.3 gives the nominal wavenumber for the beam with nominal properties over the given frequency band. Table 3.7 presents the first ten non-zero natural frequencies of this homogeneous beam using an analytical expression.

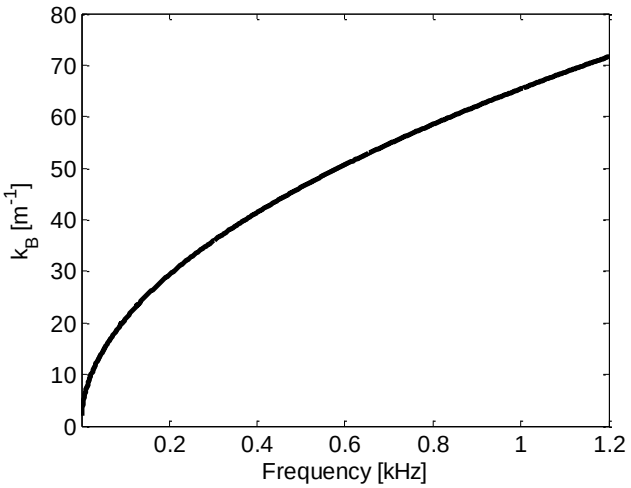

Figure 3.3. Wavenumber of the nominal beam within 1Hz to 1.2 kHz.

Table 3.7. First ten flexural natural frequencies [Hz] for a beam with homogeneous properties.

Mode #	Natural Frequency [Hz]	Mode #	Natural Frequency [Hz]
1	20.9	6	390.2
2	57.7	7	519.5
3	113.1	8	667.3
4	187.0	9	833.5
5	279.4	10	1018.2

Similarly to the case in the longitudinal waves, the only spatially varying property is the Young's modulus and it is described analytically according to Eq. (2.2), also using $N_{kl} = 40$. Moreover, a FE model was built with $N = 100$ elements, and the random field was simulated by using the analytical solution available for the Karhunen-Loeve expansion, evaluated at the centre of each element, likewise the piecewise constant approach. The integrals for the phase changes θ_L, θ_R and θ_T, Eq. (3.12), Eq. (3.25) and Eq. (3.26) were evaluated numerically, using a Gauss-Legendre quadrature rule. The input mobility using the WKB method was evaluated using Eq. (3.32) and the input mobilities of the piecewise constant waveguide approach was evaluated using Eq. (3.61). For the FE and HFE, direct inversion of the dynamic matrix was used. Natural

frequencies for the wave piecewise constant approach was calculated by using the approximation in Eq. (3.46). For the WKB method, natural frequencies were calculated using Eq. (3.15), where the integral was numerically calculated by a Gauss-Legendre quadrature, and also by its first order approximation, as given in Eq. (3.17).

Five different cases of spatial distribution of the Young's modulus were implemented in order to check the performance of the assumptions made so far; they were made by changing the dispersion parameter σ, i.e. how likely the values are to deviate from the mean value, and the correlation length b, i.e. the rate of fluctuation of the spatial distribution: $\sigma = 0.1$, $b = 2L$; $\sigma = 0.2$, $b = 2L$; $\sigma = 0.1$, $b = 0.8L$; $\sigma = 0.1$, $b = 0.1L$; and $\sigma = 0.2$, $b = 0.05L$. Figure 3.4 gives the generated values of the Young's modulus with the spatial distribution normalized by the nominal value for E_0. They are different from the ones used in the previous chapter, Figure 2.9, but they present the same spatial behaviour, i.e. for the longer correlation lengths, the spatial distribution has a very distinguishable component possessing a long wavelength in addtion to small oscillations, and for the shorter correlation length the oscillations have a much shorter wavelength.

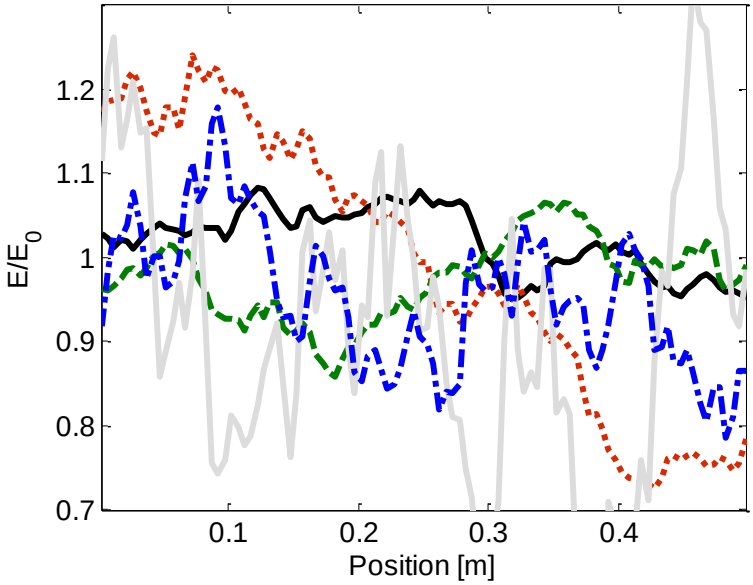

Figure 3.4. Normalized Young's value along the beam axis generated for all the cases: $\sigma = 0.1$, $b = 2L$ (black solid); $\sigma = 0.2$, $b = 2L$ (red dotted); $\sigma = 0.1$, $b = 0.8L$ (green dashed); $\sigma = 0.1$, $b = 0.1L$ (blue dash-dotted); and $\sigma = 0.2$, $b = 0.05L$ (grey solid).

The amplitude and phase of the input mobility along with natural frequencies using these cases and simulated by the methods presented in this chapter are shown along with the input mobility of the same beam but with homogeneous properties.

For the dispersion parameter set to $\sigma = 0.1$ and correlation length $b = 2L$, Figure 3.5 shows the amplitude and phase of the input mobility and Table 3.8 provides the first ten natural frequencies obtained using FE as well as the percentage variation from FE of the ones obtained by using HFE, the WKB approach with numerical integration and with the first order approximation as well as by using the wave piecewise constant approach. In this case, Young's modulus varies slowly along the waveguide, so the WKB and FE methods agree very well, as expected.

Figure 3.6 shows the amplitude and phase of the input mobility for the case when $\sigma = 0.2$ and $b = 2L$ and Table 3.9 shows that the natural frequencies obtained. The generated spatial distribution is expected to have the same effect on the results, but the bigger dispersion is expected to affect the first order approximations. The methods also display very good agreement with the FE and HFE solutions. Figure 3.7 presents the input mobility when $\sigma = 0.1$ and $b = 0.8L$ and Table 3.10 the natural frequencies obtained. For this case, the generated spatial distribution varies slowly enough so that there is good agreement between the input mobility using the WKB approach and the other methods. Very good agreement is also found for the input mobilities, Figure 3.8, and natural frequencies, Table 3.11, for the case when $\sigma = 0.1$ and $b = 0.1L$.

Figure 3.9 shows the input mobilities and Table 3.12 presents the natural frequencies obtained using all the methods for the cases when $\sigma = 0.2$ and $b = 0.05L$. It is possible to note that none of the methods exhibit the same agreement as found previously, although they are all follow the same trend in terms of the shifts in the natural frequencies. The good agreement between HFE and FE natural frequencies shows that random field discretisation is well represented in the FE model. However, the assumption of negligible internal reflections starts to fail in representing the first few modes, shown by the bigger differences of the natural frequencies with respect to the piecewise constant FE results, which are taken as the reference case.

For all the cases in general, the piecewise constant wave approach also produced very good agreement with the FE approach, but it not as computationally efficient as the WKB approach. The HFE method also produced a very good agreement with the FE solution, being, however, computationally more efficient than the FE. More importantly it does not require slowly varying properties, being potentially more effective to more general cases.

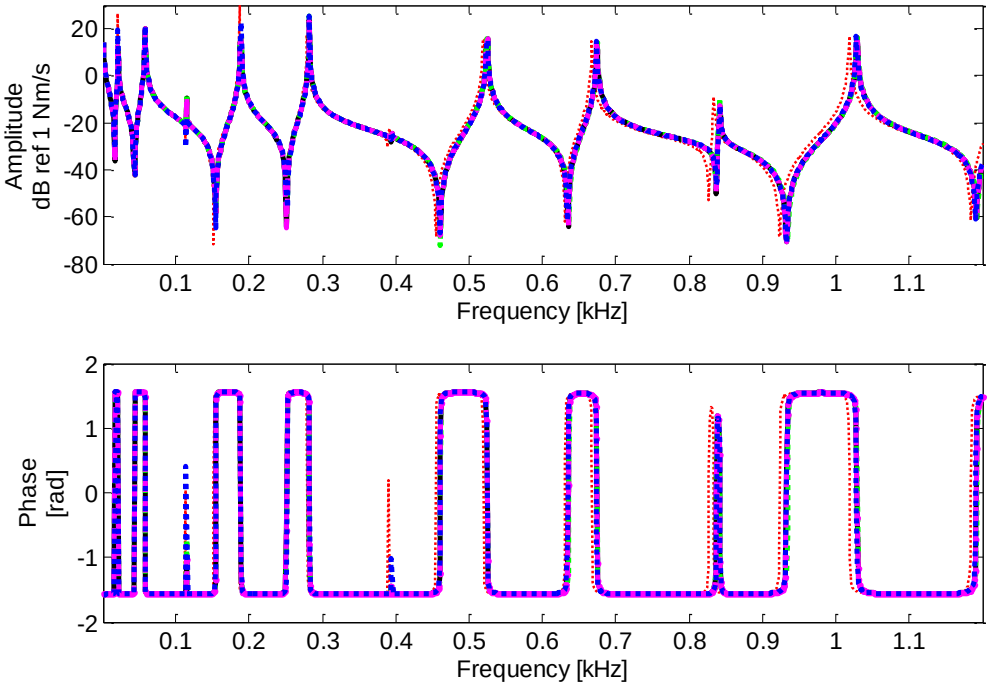

Figure 3.5. (a) Input mobility amplitude and phase with nominal values (dotted red), WKB approximation (dotted blue), piecewise constant properties (dashed magenta) and FE approach (black) and HFE (dotted green); the dispersion parameter is set to $\sigma = 0.1$ and correlation length $b = 2L$.

Table 3.8. Percentage variation of the ten first natural frequencies [Hz] the beam with Young's modulus variability using HFE, WKB and its 1st order approximation, and piecewise constant. The dispersion parameter is set to $\sigma = 0.1$ and correlation length $b = 2L$.

FE [Hz]	**(HFE-FE)/FE %**	**(WKB-FE)/FE %**	**(WKB 1st-FE)/FE %**	**(Piecewise-FE)/FE %**
21.3	-0.0341	-0.7849	-0.6933	-0.7511
58.3	0.0141	-0.0945	-0.0022	-0.0604
114.9	0.0285	-0.6484	-0.5566	-0.6145
188.5	0.0260	0.1170	0.2094	0.1511
281.9	0.0259	0.0406	0.1330	0.0746
394.5	-0.0064	-0.1567	-0.0645	-0.1227
524.5	-0.0157	-0.0400	0.0523	-0.0059
674.4	0.0409	-0.1337	-0.0415	-0.0997
841.3	-0.0364	-0.0099	0.0825	0.0242
1028.8	0.0372	-0.1076	-0.0153	-0.0735

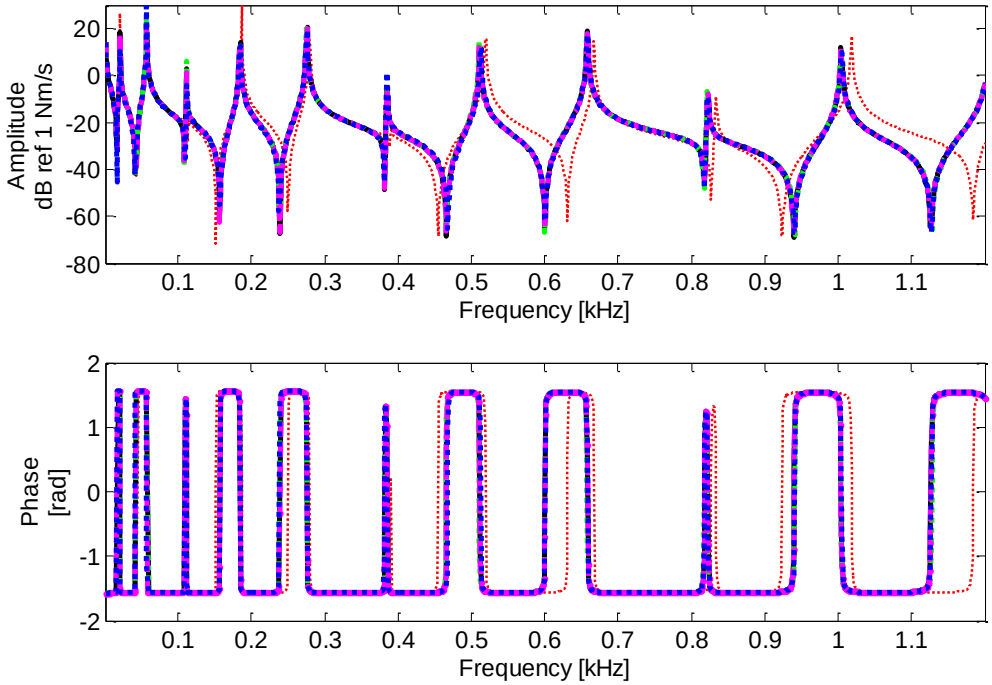

Figure 3.6. (a) Input mobility amplitude and phase with nominal values (dotted red), WKB approximation (dotted blue), piecewise constant properties (dashed magenta) and FE approach (black) and HFE (dotted green); the dispersion parameter is set to $\sigma = 0.2$ and correlation length $b = 2L$.

Table 3.9. Percentage variation of the ten first natural frequencies [Hz] the beam with Young's modulus variability using HFE, WKB and its 1st order approximation, and piecewise constant. The dispersion parameter is set to $\sigma = 0.2$ and correlation length $b = 2L$.

FE [Hz]	**(HFE-FE)/FE %**	**(WKB-FE)/FE %**	**(WKB 1st-FE)/FE %**	**(Piecewise-FE)/FE %**
20.9	-0.1810	-1.0404	-0.0496	-0.9586
57.2	-0.1019	-0.6048	0.3903	-0.5227
111.1	-0.0404	0.3676	1.3725	0.4506
184.6	-0.0466	-0.1369	0.8630	-0.0543
275.7	-0.1388	-0.1043	0.8958	-0.0217
385.3	-0.0003	-0.1665	0.8330	-0.0839
511.6	-0.1612	0.1135	1.1159	0.1963
658.2	-0.0959	-0.0626	0.9379	0.0200
822.5	-0.0935	-0.1047	0.8955	-0.0221
1004.1	-0.0385	-0.0275	0.9734	0.0551

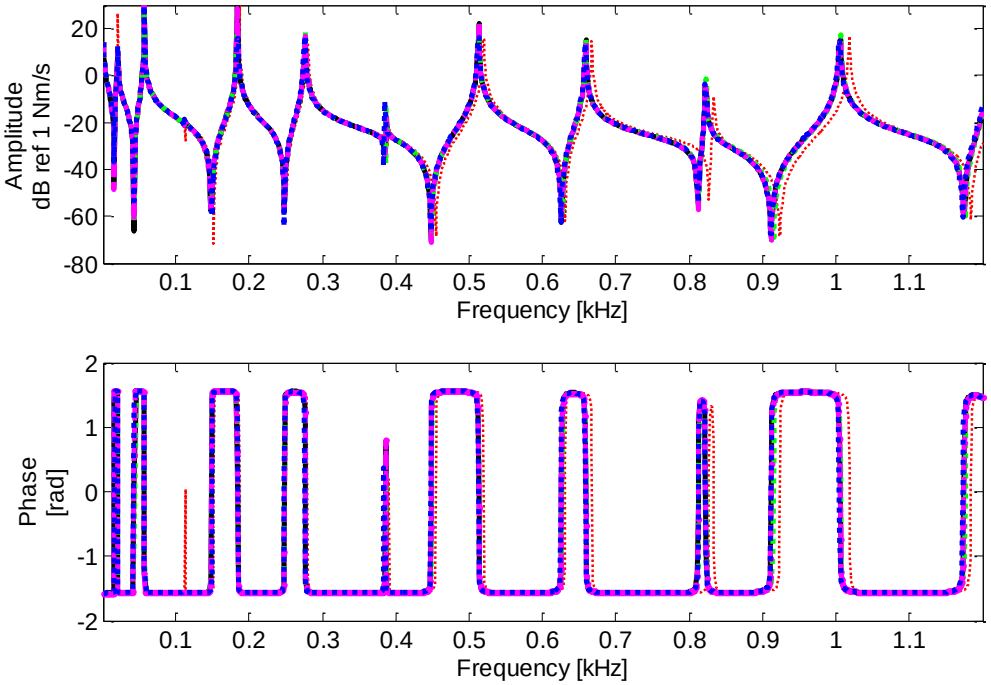

Figure 3.7. (a) Input mobility amplitude and phase with nominal values (dotted red), WKB approximation (dotted blue), piecewise constant properties (dashed magenta) and FE approach (black) and HFE (dotted green); the dispersion parameter is set to $\sigma = 0.1$ and correlation length $b = 0.8L$.

Table 3.10. Percentage variation of the ten first natural frequencies [Hz] the beam with Young's modulus variability using HFE, WKB and its 1st order approximation, and piecewise constant. The dispersion parameter is set to $\sigma = 0.1$ and correlation length $b = 0.8L$.

FE [Hz]	**(HFE-FE)/FE %**	**(WKB-FE)/FE %**	**(WKB 1st-FE)/FE %**	**(Piecewise-FE)/FE %**
20.5	0.0448	0.5782	0.7426	0.6447
56.9	0.0685	-0.0301	0.1333	0.0360
111.6	0.0874	-0.0222	0.1412	0.0439
184.0	0.0789	0.1880	0.3518	0.2543
276.4	-0.0452	-0.3526	-0.1897	-0.2867
386.5	0.0832	-0.4585	-0.2958	-0.3926
512.9	0.0383	-0.1385	0.0247	-0.0725
658.9	0.0202	-0.1470	0.0162	-0.0810
822.4	0.0735	-0.0771	0.0862	-0.0110
1005.5	0.0593	-0.1616	0.0016	-0.0956

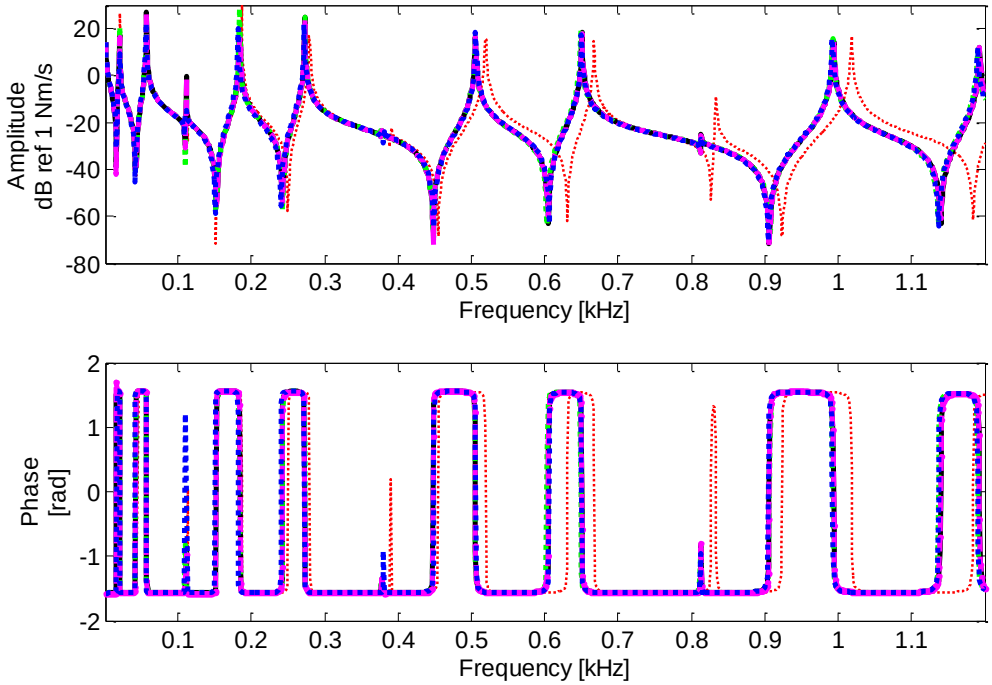

Figure 3.8. (a) Input mobility amplitude and phase with nominal values (dotted red), WKB approximation (dotted blue), piecewise constant properties (dashed magenta) and FE approach (black) and HFE (dotted green); the dispersion parameter is set to $\sigma = 0.1$ and correlation length $b = 0.1L$.

Table 3.11. Percentage variation of the ten first natural frequencies [Hz] the beam with Young's modulus variability using HFE, WKB and its 1st order approximation, and piecewise constant. The dispersion parameter is set to $\sigma = 0.1$ and correlation length $b = 0.1L$.

FE [Hz]	**(HFE-FE)/FE %**	**(WKB-FE)/FE %**	**(WKB 1st-FE)/FE %**	**(Piecewise-FE)/FE %**
20.2	-0.2887	0.9346	1.4114	1.1055
56.9	-0.1634	-1.2742	-0.8079	-1.1070
110.9	-0.1995	-0.7985	-0.3299	-0.6305
184.4	-0.1989	-1.3133	-0.8471	-1.1462
272.9	0.0791	-0.4107	0.0597	-0.2421
377.9	-0.3116	0.4546	0.9291	0.6247
505.7	-0.0406	-0.0572	0.4149	0.1121
650.9	-0.2831	-0.2685	0.2026	-0.0996
812.9	-0.1244	-0.2594	0.2118	-0.0904
993.6	-0.0762	-0.3129	0.1580	-0.1441

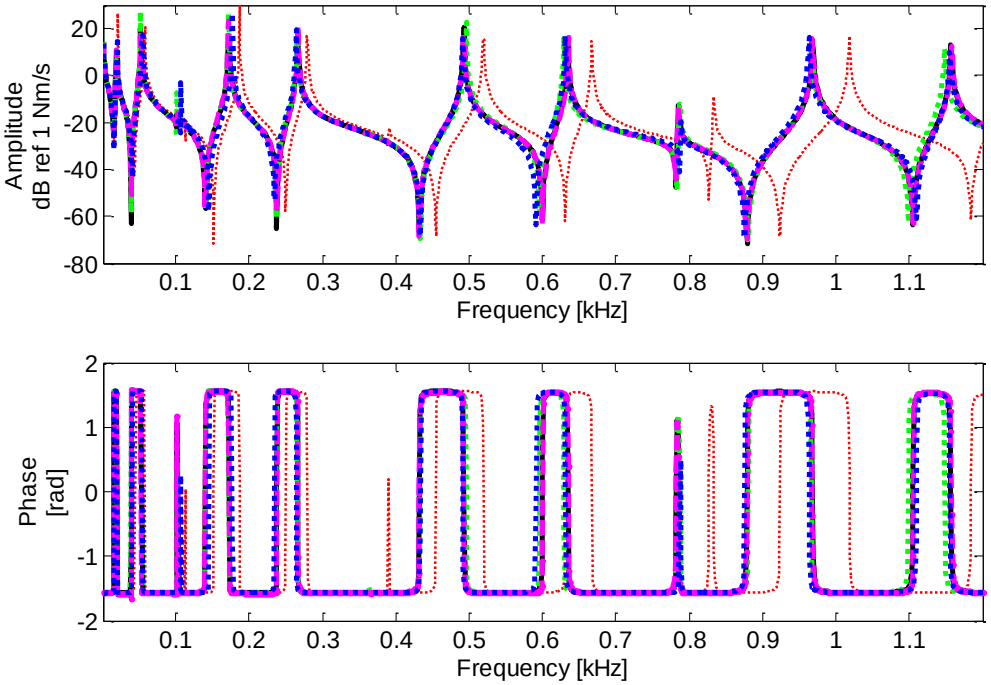

Figure 3.9. (a) Input mobility amplitude and phase with nominal values (dotted red), WKB approximation (dotted blue), piecewise constant properties (dashed magenta) and FE approach (black) and HFE (dotted green); the dispersion parameter is set to $\sigma = 0.2$ and correlation length $b = 0.05L$.

Table 3.12. Percentage variation of the ten first natural frequencies [Hz] the beam with Young's modulus variability using HFE, WKB and its 1st order approximation, and piecewise constant. The dispersion parameter is set to $\sigma = 0.2$ and correlation length $b = 0.05L$.

FE [Hz]	**(HFE-FE)FE %**	**(WKB-FE)/FE %**	**(WKB 1st-FE)/FE %**	**(Piecewise-FE)/FE %**
19.4	-0.1500	1.5034	3.3783	1.9548
52.3	-0.3311	3.8651	5.7837	4.3270
102.2	-0.3211	4.2384	6.1639	4.7020
172.5	-0.2339	2.0593	3.9445	2.5132
266.5	-0.3078	-1.3026	0.5205	-0.8637
366.1	-0.7117	0.3455	2.1991	0.7918
492.8	0.6375	-0.7706	1.0623	-0.3293
634.6	-0.9049	-1.0139	0.8146	-0.5737
785.6	0.2318	-0.1190	1.7260	0.3252
968.3	-0.1558	-1.0073	0.8213	-0.5670

3.6 Conclusions

In this chapter the WKB approximation has been used together with the KL expansion, which was extended for flexural waves in a thin straight beam, with slowly varying properties along the axis of propagation. The approximation also retains the physical interpretation of positive going and negative going propagating and evanescent waves. The formulation allows one to approach the problem using a wave formulation in a similar manner to homogeneous waveguides and provides a framework to include random variability in terms of random fields.

The KL expansion was also used here in a purely deterministic sense, assuming the same correlation function such that the same analytical expression is used to generate the spatial variability. This analytical expression is used to find a first order approximation for the natural frequencies of a finite beam, since a general closed form solution for the given integral is not readily available.

In addition, the wave formulation considering piecewise constant properties along the waveguide propagation axis was also extended for the flexural waves case. This approach, unlike the previous one, takes into account internal reflections and an expression for the input mobility was derived. The properties inside each element are constant and given in the same way as in the FE approach. An expression for the natural frequencies was also derived, but neglecting the internal reflection by imposing the scattering matrix to be equal to the identity matrix. This leads to a simpler expression for the natural frequencies, similar to the one obtained by the WKB approximation.

The FE approach using an enriched basis (HFE) was applied to beam elements, including the variability in the properties of the waveguide in the element formulation. In the same manner as for the rod element, this formulation does not ensure the so called k-orthogonality, impoverishing its numerical efficiency. It gave a very good agreement with the FE solution, in fact always closer than the other methods considered. Although it does not allow closed form solutions for the input mobility and natural frequencies, it is computationally more efficient than standard FE (h-version) and it does not require slowly varying properties, being potentially applicable in more general cases.

So far, only one-dimensional waveguides with and without dispersion and propagating and non-propagating waves were considered. In the next chapter, the presented formulation is extended for a simple two-dimensional system.

4. Flexural waves in a plate strip with simply supported edges

4.1 Introduction

In this chapter the WKB approximation is applied for flexural waves in a plate strip with simply supported edges and slowly varying properties using the framework developed so far. The change in properties is given only in the direction of propagation, while the properties across the plate strip are homogeneous.

The problem is treated using the same wave framework as used for the one-dimensional beam and rod. The main difference is the presence of cut on frequencies for different wave modes. Their occurrence, however, breaks down the WKB approximation at certain frequency bands, in the same way that the presence of the turning points at the Schrodinger's equation [47, 50]. Moreover, a closed form expression for the natural frequencies is derived for the case of simply supported boundary conditions on the parallel edges of the plate strip using a first order approximation.

A Finite Element approximation using enriched hierarchical basis, or Hierarchical Finite Element (HFE) [1, 2], is also presented for thin rectangular flexural plate elements, where the variability in the properties of the waveguide is included in the element formulation. A Finite Element model of the waveguide is assembled for comparison and numerical validation.

Unlike the previous chapters, no piecewise constant formulation is presented for the two-dimensional case, although the formulation procedure could be likewise followed. A single sample of a random field is used to carry out the numerical analysis, as all of the formulations are purely deterministic.

4.2 Waves in a finite length plate with slowly changing material variability

In this section, the WKB approximation for a plate strip will be carried out considering the spatially varying plate bending stiffness and mass per unit length, only in the direction of the travelling wave. After that, further analysis will be performed by

considering only the Young's modulus to be spatially varying, according to Eq. (2.1) and also using the analytical expression of the KL expansion, as expressed in Eq. (2.2).

4.2.1 WKB approximation

Considering a thin plate undergoing out-of-plane flexural vibration with varying material properties and assuming harmonic motion, it is possible to derive the governing equation [20]

$$\begin{aligned}\frac{\partial^2}{\partial x^2}\left[D(x,y)\left(\frac{\partial^2}{\partial x^2}w(x,y)+\nu\frac{\partial^2}{\partial y^2}w(x,y)\right)\right]\\ +\frac{2\partial^2}{\partial x\partial y}\left[D(x,y)(1-\nu)\frac{\partial^2}{\partial x\partial y}w(x,y)\right]\\ +\frac{\partial^2}{\partial y^2}\left[D(x,y)\left(\frac{\partial^2}{\partial y^2}w(x,y)+\nu\frac{\partial^2}{\partial x^2}w(x,y)\right)\right]\\ =\rho h(x,y)\omega^2 w(x,y),\end{aligned} \tag{4.1}$$

where $w(x,y)$ is the out-of-plane harmonic displacement, $\rho h(x,y)$ is the product of the mass density and thickness, and $D(x,y)$ is the plate bending stiffness. Setting a small parameter ϵ such that $\epsilon^{-4}=\omega^2$ and assuming solutions of the kind

$$w(x,y)=A(x,y)e^{-i\frac{\phi(x,y)}{\epsilon}} \tag{4.2}$$

where the amplitude is expanded in terms of the parameter ϵ as

$$A(x,y)=A_0(x,y)+A_1(x,y)\epsilon \tag{4.3}$$

it is possible to match the terms with equal power of ϵ on both left hand side and right hand side of Eq. (4.1). In most engineering applications, the natural frequencies are greater than unity, and therefore ϵ has a small value [46]. This procedure will lead to a number of differential equations to solve for each term on the expansion. From the ϵ^0 order, one can find the eikonal equation for the phase change as

$$\left[\left(\frac{\partial}{\partial x}\phi(x,y)\right)^2+\left(\frac{\partial}{\partial y}\phi(x,y)\right)^2\right]^2=\frac{\rho h(x,y)}{D(x,y)}, \tag{4.4}$$

and the higher orders terms of ϵ give expressions for the amplitude terms. This equation cannot be solved by a simple integration in the same manner as in the case for the one-dimensional structures, but one can solve it in a parametric form using, for instance,

Cauchy's methods of characteristics for the general case [45, 48]. However, if a plate strip with simply supported boundary conditions at $y = 0$ and $y = L_y$ is considered, also assuming the material variability only in the direction of propagation, i.e. the x axis, $D(x, y) = D(x)$, and $\rho h(x, y) = \rho h(x)$, then it is possible to assume the phase change, from Eq. (4.2), of the form

$$\phi(x, y)/\epsilon = \phi_{xm}(x) + k_{ym} y \tag{4.5}$$

where $k_{ym} = m\pi/L_y$ is the m^{th} wave mode in the y direction and $\phi_{xm}(x)$ is the phase change in the x direction. Using this expression and direct integration of Eq. (4.4) gives

$$\phi_{xm}(x) = \pm \int_{x_0}^{x} k_{xm}(\xi)\, d\xi, \tag{4.6}$$

with four solutions for the phase change in the x direction, where $k_{xm}(x) = \sqrt{\pm k_p^2(x) - k_{ym}^2}$, $k_p(x) = \sqrt{\omega}\left(\frac{\rho h(x)}{D(x)}\right)^{1/4}$ is the local free bending wavenumber in a thin plate and x_0 is an arbitrary point in the waveguide. From this solution, one can distinguish two wave types. One wavenumber being

$$k_{x1m}(x) = \sqrt{k_p^2(x) - k_{ym}^2}, \tag{4.7}$$

which is real, and represents a propagating wave if $k_p(x)^2 > k_{ym}^2$, and it is imaginary and represent an evanescent mode if $k_p(x)^2 < k_{ym}^2$. The other one is

$$k_{x2m}(x) = \sqrt{-k_p^2(x) - k_{ym}^2}, \tag{4.8}$$

which is imaginary and thus always evanescent.

In homogenous waveguides, $k_p(x) = k_p$, there is no transition from propagating to evanescent waves, cut off, or evanescent to propagating waves, cut on, at the same frequency, i.e. given a frequency ω, Eq. (4.6) is always either real or imaginary. That is not the case when the wavenumber varies with the position, and the wave mode can cut on, or cut-off at a certain position x_e, for a given frequency, when $k_p(x_e) = k_{ym}$. This transition leads to an internal wave reflection, breaking down the WKB main assumption of negligible internal reflections and, consequently, requiring a different local approximation for these frequency bands (e.g. [47]). In addition, uniformly valid solutions, i.e. solutions also valid for a frequency band away from the cut on frequency, have been derived using a slight modification on the WKB method for different applications, for instance [50, 53, 63]. This is, however, out of the scope of this work,

and the WKB approximation is carried forward considering that it will not be valid at these particular frequencies.

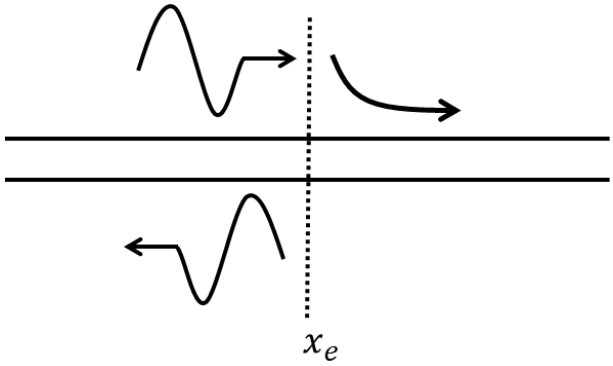

Figure 4.1. m^{th} wave mode cutting off at x_e when its wavenumber $k_{x1m}(x_e)$ changes from real to imaginary, at a particular frequency.

In that sense, for a plate strip with simply supported edges, the displacement can be written as

$$w(x,y) = \sum_{m=1}^{\infty} w_m(x)\sin(k_{my}y), \tag{4.9}$$

and therefore for the m^{th} wave mode, the amplitude change can be written using only the first order as

$$A(x,y) = [A_{x0}(x) + A_{x1}(x)\epsilon]\sin(k_{my}y). \tag{4.10}$$

The amplitude term $A_{x0}(x,y)$ is found from matching the ϵ^1 order of the expansion and using the solution for the phase term $\phi(x,y)$ and for $k_p^2(x) \gg 0$, it is possible to obtain the differential equation

$$\frac{2}{A_{x0}}\frac{\partial A_{x0}}{\partial x} + \frac{1}{\phi_{xm}(x)}\frac{\partial \phi_{xm}(x)}{\partial x} = 0, \tag{4.11}$$

whose solution gives the typical WKB wave amplitude change expression

$$A_{x0}(x) = \frac{A_{x0}(x_0)\sqrt{k_{xm}(x_0)}}{\sqrt{k_{xm}(x)}}. \tag{4.12}$$

This result can also be derived by applying the energy conservation principle together with Eq. (4.2) [45]. Moreover, the inclusion of higher order terms in Eq. (4.10) does not affect these results. This approximation is used to rewrite Eq. (4.9) using the four wave solutions as

$$w(x,y)=\sum_{m=1}^{\infty}\sin(k_{my}y)\left[\frac{C_{1m}}{\sqrt{k_{x1m}(x)}}e^{-i\int_{x_0}^{x}k_{x1m}(x)dx}\right.$$
$$+\frac{C_{2m}}{\sqrt{k_{x1m}(x)}}e^{i\int_{x_0}^{x}k_{x1m}(x)dx}+\frac{C_{3m}}{\sqrt{k_{x2m}(x)}}e^{-i\int_{x_0}^{x}k_{x2m}(x)dx} \quad (4.13)$$
$$\left.+\frac{C_{4m}}{\sqrt{k_{x2m}(x)}}e^{i\int_{x_0}^{x}k_{x2m}(x)dx}\right],$$

where C_{1m}, C_{2m}, C_{3m} and C_{4m} are arbitrary constants depending on the wave phase and amplitude at an arbitrary position x_0. Then, the phase and amplitude change of both kinds of positive and negative going waves travelling through a distance L_x, from $x=0$ to $x=L_x$, are given by

$$b_m^+=\sqrt{\frac{k_{x1m}(L_x)}{k_{x1m}(0)}}e^{-i\int_0^L k_{x1m}(x)dx}a_m^+, \quad (4.14)$$

$$b_m^-=\sqrt{\frac{k_{x1m}(L_x)}{k_{x1m}(0)}}e^{i\int_0^L k_{x1m}(x)dx}a_m^-, \quad (4.15)$$

$$b_{Nm}^+=\sqrt{\frac{k_{x2m}(L_x)}{k_{x2m}(0)}}e^{-i\int_0^L k_{x2m}(x)dx}a_{Nm}^+, \quad (4.16)$$

$$b_{Nm}^-=\sqrt{\frac{k_{x2m}(L_x)}{k_{x2m}(0)}}e^{i\int_0^L k_{x2m}(x)dx}a_{Nm}^-, \quad (4.17)$$

4.2.2 Free wave propagation

The WKB approximation for a thin plate strip can be used to derive expressions for the free wave propagation in a finite waveguide of length L_x, Figure 4.2. The positive going and the negative going wave amplitudes of the m^{th} wave mode on the left hand boundary, $\mathbf{a}_m^+$ and $\mathbf{a}_m^-$, and on the right hand boundary, $\mathbf{b}_m^+$ and $\mathbf{b}_m^-$, can be related by $\mathbf{b_m}=\mathbf{\Lambda_m a_m}$ from Eq.(4.14) to (4.17), where

$$\mathbf{\Lambda_m}=w_{ym}\begin{bmatrix}\mathbf{\Lambda_{m11}} & \mathbf{0}\\ \mathbf{0} & \mathbf{\Lambda_{m22}}\end{bmatrix} \quad (4.18)$$

is a propagation matrix and

$$\mathbf{\Lambda_{m11}} = \begin{bmatrix} e^{-i\theta_{Tm}+\gamma_{Tm}} & 0 \\ 0 & e^{-i\theta_{NTm}+\gamma_{NTm}} \end{bmatrix}, \tag{4.19}$$

$$\mathbf{\Lambda_{m22}} = \begin{bmatrix} e^{i\theta_{Tm}+\gamma_{Tm}} & 0 \\ 0 & e^{i\theta_{NTm}+\gamma_{NTm}} \end{bmatrix}, \tag{4.20}$$

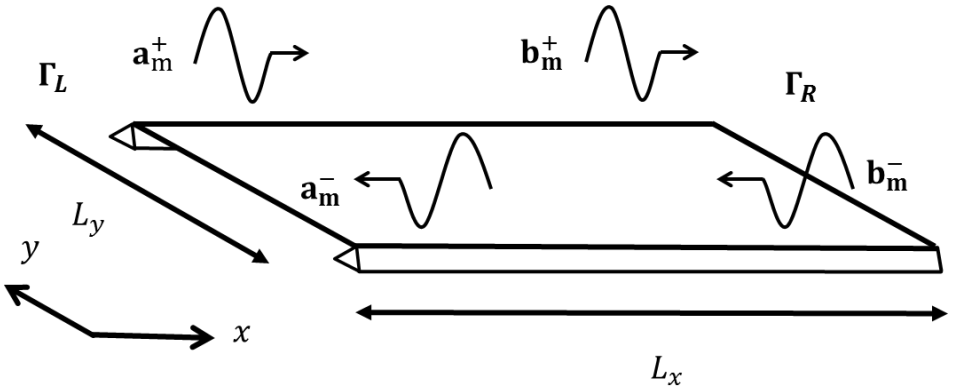

Figure 4.2. Finite plate strip undergoing flexural wave behaviour, with slowly varying material properties and considering no internal reflections.

The wave amplitudes for each wave mode are given by the vectors

$$\mathbf{a_m} = \begin{Bmatrix} \mathbf{a_m^+} \\ \mathbf{a_m^-} \end{Bmatrix}, \mathbf{b_m} = \begin{Bmatrix} \mathbf{b_m^+} \\ \mathbf{b_m^-} \end{Bmatrix}. \tag{4.21}$$

where $\mathbf{a}_m^+ = [a_m^+ \quad a_{Nm}^+]^T$, $\mathbf{a}_m^- = [a_m^- \quad a_{Nm}^-]^T$, $\mathbf{b}_m^+ = [b_m^+ \quad b_{Nm}^+]^T$ and $\mathbf{b}_m^- = [b_m^- \quad b_{Nm}^-]^T$, $w_{ym} = \sin(k_{ym}y)$ and the total phase and amplitude change for both wave kinds travelling from one boundary to the other can be given by

$$\theta_{Tm} = \int_0^{L_x} k_{x1m}(x)\mathrm{d}x, \tag{4.22}$$

$$\theta_{NTm} = \int_0^{L_x} k_{x2m}(x)\mathrm{d}x. \tag{4.23}$$

and

$$\gamma_{Tm} = \frac{1}{2}\ln\left[\frac{k_{x1m}(L_x)}{k_{x1m}(0)}\right], \tag{4.24}$$

$$\gamma_{NTm} = \frac{1}{2}\ln\left[\frac{k_{x2m}(L_x)}{k_{x2m}(0)}\right]. \tag{4.25}$$

The waveguide natural frequencies can be determined by applying the wave train closure principle, tracing the round-trip propagating wave, as described in Chapter 2 and 3, and finding the zeros of the characteristic equation [19, 61]

$$\det(\mathbf{\Lambda}_{m22}^{-1}\mathbf{\Gamma}_R\mathbf{\Lambda}_{m11}\mathbf{\Gamma}_L - \mathbf{I}) = 0. \tag{4.26}$$

where $\mathbf{I}$ is a 2×2 identity matrix and the reflection matrices follow from the relations between the waves in the boundaries $\mathbf{a}_m^+ = \mathbf{\Gamma}_L\mathbf{a}_m^-$ and $\mathbf{b}_m^- = \mathbf{\Gamma}_R\mathbf{b}_m^+$.

For the simply supported boundary conditions on the left and the right of the plate strip, i.e. $\mathbf{\Gamma}_L = \mathbf{\Gamma}_R = \begin{bmatrix} -1 & 0 \\ 0 & -1 \end{bmatrix}$, Eq. (4.26) reduces to

$$\int_0^{L_x} \sqrt{\sqrt{\frac{\rho h}{D(x)}}\omega_{mn} - k_{ym}^2}\,dx = n\pi, \tag{4.27}$$

where ω_{mn} is the natural frequency of the (m, n) simply supported rectangular plate mode.

Solving for ω_{mn} is not straightforward, but the expression inside the integral can be approximated by a first order expansion given $D(x) = D_0[1 + \sigma H(x)]$ and assuming $|\sigma H(x)| \ll 1$, as

$$\sqrt{k_{p0}^2 \frac{1}{\sqrt{1+\sigma H(x)}} - k_{ym}^2} \approx \sqrt{k_{p0}^2 - k_{ym}^2} - \frac{\sigma k_{p0}^2}{4\sqrt{k_{p0}^2 - k_{ym}^2}} H(x) \tag{4.28}$$

where $k_{p0}^2 = \sqrt{\rho h/D_0}\omega_{mn}$, leading to

$$L_x\sqrt{k_{p0}^2 - k_{ym}^2} - \frac{\sigma k_{p0}^2}{4\sqrt{k_{p0}^2 - k_{ym}^2}} \int_0^{L_x} H(x)dx = n\pi, \tag{4.29}$$

Rearranging the terms it is possible to write the expression as

$$L_x^2\left(k_{p0}^2 - k_{ym}^2\right) - \frac{L_x k_{p0}^2}{2}\sigma\int_0^{L_x} H(x)dx + \frac{k_{p0}^4}{16\left(k_{p0}^2 - k_{ym}^2\right)}\left[\sigma\int_0^{L_x} H(x)dx\right]^2 = (n\pi)^2 \tag{4.30}$$

and considering the term $\left[\sigma\int_0^{L_x} H(x)dx\right]^2$ is much smaller than the other terms in the equation, one can solve for ω_{mn} as

$$\omega_{mn} = \frac{\omega_{0mn}}{1 - \frac{\sigma}{2L_x}\int_0^{L_x} H(x)dx}. \tag{4.31}$$

Moreover, to be consistent with the assumption $|\sigma H(x)| \ll 1$, this expression can be given as

$$\omega_{mn} = \omega_{0mn}\left(1 + \frac{\sigma}{2L_x}\int_0^{L_x} H(x)dx\right), \tag{4.32}$$

where ω_{0mn} is the natural frequency for the homogeneous simply supported rectangular plate of dimensions L_x and L_y, i.e. $\omega_{0mn} = \left[\left(\frac{m\pi}{L_y}\right)^2 + \left(\frac{n\pi}{L_x}\right)^2\right]\sqrt{\frac{D_0}{\rho h}}$. Moreover, if $H(x)$, is expressed by Eq. (2.2), then its integral has a closed form and the first order approximation for the natural frequency is given by

$$\omega_{mn} = \omega_{0mn}\left(1 + \frac{\sigma}{L_x}\sum_{j=1}^{N_{kl}} \xi_{2j}(p)\frac{\beta_j}{w_{2j}}\sin(w_{2j}x)\right), \tag{4.33}$$

4.2.3 Point excitation

An expression for the input mobility due to a point excitation can be derived following the same approach as used in the previous chapters. The point harmonic excitation force F, applied at $x = L_{1x}$ and $y = L_{1y}$, Figure 4.3, creates a positive going $\mathbf{q}^+ = [q^+ \quad q_N^+]^T$ and a negative going $\mathbf{q}_m^- = [q_m^- \quad q_{Nm}^-]^T$ wave train, so that at this point they are given by the sum of these directly excited and the incident ones such that

$$\mathbf{a}_{2\mathrm{m}}^+ = \mathbf{b}_{1m}^+ + \mathbf{q}_m^+, \tag{4.34}$$

and

$$\mathbf{b}_{1m}^- = \mathbf{a}_{2m}^- + \mathbf{q}_m^-. \tag{4.35}$$

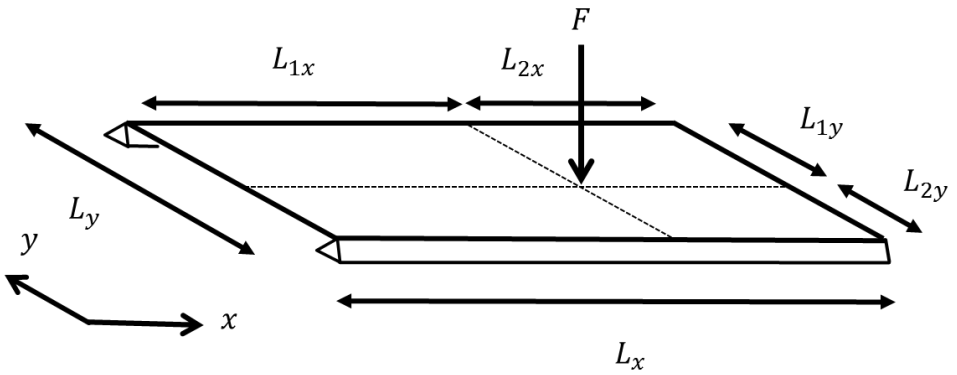

Figure 4.3. Point excitation positions on finite length plate strip, with slowly varying material properties, considering no internal reflections.

Propagation from the boundaries to the excitation point is given by $\mathbf{b_{1m}} = \mathbf{\Lambda_{Lm}} \mathbf{a_{1m}}$ and $\mathbf{b_{2m}} = \mathbf{\Lambda_{Rm}} \mathbf{a_{2m}}$, where

$$\mathbf{\Lambda_{Lm}} = w_{ym} \begin{bmatrix} \mathbf{\Lambda_{Lm_{11}}} & \mathbf{0} \\ \mathbf{0} & \mathbf{\Lambda_{Lm_{22}}} \end{bmatrix}, \qquad \mathbf{\Lambda_{Rm}} = w_{ym} \begin{bmatrix} \mathbf{\Lambda_{Rm_{11}}} & \mathbf{0} \\ \mathbf{0} & \mathbf{\Lambda_{Rm_{22}}} \end{bmatrix}, \tag{4.36}$$

end

$$\mathbf{\Lambda_{Lm_{11}}} = \begin{bmatrix} e^{-i\theta_{Lm}+\gamma_{Lm}} & 0 \\ 0 & e^{-i\theta_{NLm}+\gamma_{NLm}} \end{bmatrix}, \tag{4.37}$$

$$\mathbf{\Lambda_{Lm_{22}}} = \begin{bmatrix} e^{i\theta_{Lm}+\gamma_{Lm}} & 0 \\ 0 & e^{i\theta_{NLm}+\gamma_{NLm}} \end{bmatrix}, \tag{4.38}$$

$$\mathbf{\Lambda_{Rm_{11}}} = \begin{bmatrix} e^{-i\theta_{Rm}+\gamma_{Rm}} & 0 \\ 0 & e^{-i\theta_{NRm}+\gamma_{NRm}} \end{bmatrix}, \tag{4.39}$$

$$\mathbf{\Lambda_{Rm_{22}}} = \begin{bmatrix} e^{i\theta_{Rm}+\gamma_{Rm}} & 0 \\ 0 & e^{i\theta_{NRm}+\gamma_{NRm}} \end{bmatrix}. \tag{4.40}$$

Moreover, θ_{Lm} and γ_{Lm} gives the total phase and amplitude change of the propagating wave to the left side of the point excitation on the waveguide and θ_{Rm} and γ_{Rm} the total phase and amplitude change on its right side, for the m^{th} wave mode, where

$$\theta_{Lm} = \int_0^{L_{1x}} k_{x1m}(x)dx \text{ and } \gamma_{Lm} = \frac{1}{2}\ln\left[\frac{k_{x1m}(L_{1x})}{k_{x1m}(0)}\right], \tag{4.41}$$

$$\theta_{NLm} = \int_0^{L_{1x}} k_{x2m}(x)dx \text{ and } \gamma_{NLm} = \frac{1}{2}\ln\left[\frac{k_{x2m}(L_{1x})}{k_{x2m}(0)}\right], \tag{4.42}$$

$$\theta_{Rm} = \int_{L_{1x}}^{L_x} k_{x1m}(x)dx \text{ and } \gamma_{Rm} = \frac{1}{2}\ln\left[\frac{k_{x1m}(L)}{k_{x1m}(L_{1x})}\right], \tag{4.43}$$

$$\theta_{NRm} = \int_{L_{1x}}^{L_x} k_{x2m}(x)dx \text{ and } \gamma_{Rm} = \frac{1}{2}\ln\left[\frac{k_{x2m}(L)}{k_{x2m}(L_{1x})}\right], \tag{4.44}$$

and

$$\mathbf{a}_{1\mathrm{m}} = \begin{Bmatrix}\mathbf{a}_{1\mathrm{m}}^{+}\\ \mathbf{a}_{1\mathrm{m}}^{-}\end{Bmatrix}, \mathbf{a}_{2\mathrm{m}} = \begin{Bmatrix}\mathbf{a}_{2\mathrm{m}}^{+}\\ \mathbf{a}_{2\mathrm{m}}^{-}\end{Bmatrix}, \mathbf{b}_{1\mathrm{m}} = \begin{Bmatrix}\mathbf{b}_{1\mathrm{m}}^{+}\\ \mathbf{b}_{1\mathrm{m}}^{-}\end{Bmatrix}, \mathbf{b}_{\mathrm{m}2} = \begin{Bmatrix}\mathbf{b}_{2\mathrm{m}}^{+}\\ \mathbf{b}_{2\mathrm{m}}^{-}\end{Bmatrix}. \tag{4.45}$$

The total phase and amplitude change, Eq. (4.22)-(4.25) are given by the summation of the phase changes at the left and the right of excitation, Eq. (4.41)-(4.44). In the same way, if the waveguide is homogeneous, then $k_{x1}(x) = k_{x1}$ and $k_{x2}(x) = k_{x2}$ then total phase changes reduce to the homogeneous case, i.e. $\theta_L = k_B L_{1x}$. $\theta_R = k_B L_{2x}$, where $L_{2x} = L_x - L_{1x}$, and $\gamma_L = \gamma_R = 0$.

The reflected waves from the energy conserving boundaries at the left and the right hand ends are given by the respective reflection matrices as $\mathbf{a}_{1m}^{+} = \mathbf{\Gamma}_L \mathbf{a}_{1m}^{-}$ and $\mathbf{b}_{2m}^{-} = \mathbf{\Gamma}_R \mathbf{b}_{2m}^{+}$.

Under the assumptions of the WKB approximations, the n^{th} derivative with respect to x of the positive and negative going propagating waves

$$\frac{\partial^n w^+}{\partial x^n} = \left(-ik_{x1}(x)\right)^n w^+, \tag{4.46}$$

$$\frac{\partial^n w^+}{\partial x^n} = \left(ik_{x1}(x)\right)^n w^+, \tag{4.47}$$

$$\frac{\partial^n w_N^+}{\partial x^n} = \left(-k_{x2}(x)\right)^n w_N^+, \tag{4.48}$$

$$\frac{\partial^n w_N^-}{\partial x^n} = k_{x2}^n(x) w_N^-. \tag{4.49}$$

Equilibrium of forces and continuity of displacements give the amplitudes of the waves produced by an external point harmonic force $f(x,y) = F\delta(x - L_{1x})\delta\left(y - L_{1y}\right)$ at $\left(L_{1x}, L_{1y}\right)$, where $\delta(x)$ is the Dirac delta function, as

$$\mathbf{q_m} = \mathbf{q}_m^+ = \mathbf{q}_m^- = \frac{F_m i}{2D(L_{1x})\left(k_{x1}^2(L_{1x}) - k_{x2}^2(L_{1x})\right)} \begin{bmatrix} -\dfrac{1}{k_{x1}(L_{1x})} \\ \dfrac{1}{k_{x2}(L_{1x})} \end{bmatrix} F. \tag{4.50}$$

where $\mathrm{D}(L_{1x})$, $k_{x1}(L_{1x})$ and $k_{x2}(L_{1x})$ are the bending stiffness and local wavenumbers, both evaluated at the excitation point $x = L_{1x}$ and F_m is a Fourier coefficient given by [19]

$$F_m = \frac{2}{L_y} \int_0^{L_y} F\delta\left(y - L_{1y}\right) \sin\left(\frac{m\pi}{L_y} y\right) dy, \tag{4.51}$$

Therefore

$$F_m = \frac{2F}{L_y} \sin\left(\frac{m\pi}{L_y} L_{1y}\right). \tag{4.52}$$

and

$$F = \sum_{m=1}^{\infty} F_m \sin\left(\frac{m\pi}{L_y} L_{1y}\right). \tag{4.53}$$

This express the excitation as many plane waves added up until they converge to the point excitation. Using Eq. (2.24) and Eq. (2.25) together with the propagation and reflection properties, and noting that the inverse of the matrices $\mathbf{\Lambda}_{Lm_{11}}$ and $\mathbf{\Lambda}_{Rm_{11}}$ are simply the inverse of each of its diagonal elements, then the positive going wave $\mathbf{a}_{2m}^+$ is given by

$$\mathbf{a}_{2\mathrm{m}}^+ = \mathbf{\Lambda}_{\mathrm{Lm}_{11}} \mathbf{\Gamma}_{\mathrm{L}} \mathbf{\Lambda}_{\mathrm{Lm}_{22}}^{-1} \left(\mathbf{\Lambda}_{\mathrm{Rm}_{22}}^{-1} \mathbf{\Gamma}_{\mathrm{R}} \mathbf{\Lambda}_{\mathrm{Rm}_{11}} \mathbf{a}_{2\mathrm{m}}^+ + \mathbf{q}_m^- \right) + \mathbf{q}_m^+, \tag{4.54}$$

and it is related to the negative going $\mathbf{a}_{2m}^-$ by

$$\mathbf{a}_{2m}^- = \mathbf{\Lambda}_{\mathrm{Rm}_{22}}^{-1} \mathbf{\Gamma}_{\mathrm{R}} \mathbf{\Lambda}_{Rm_{11}} \mathbf{a}_{2\mathrm{m}}^+. \tag{4.55}$$

The wave amplitude can be calculated by using the superposition principle of a positive going $\mathbf{a}_{2m}^+$ and a negative going $\mathbf{a}_{2m}^-$ wave at the point of excitation,

$$\mathbf{w}_{\mathrm{m}} = \mathbf{a}_{2m}^+ + \mathbf{a}_{2m}^- = \frac{\left(\mathbf{I} + \mathbf{\Lambda}_{\mathrm{Rm}_{22}}^{-1} \mathbf{\Gamma}_{\mathrm{R}} \mathbf{\Lambda}_{Rm_{11}}\right)\left(\mathbf{I} + \mathbf{\Lambda}_{\mathrm{Lm}_{11}} \mathbf{\Gamma}_{\mathrm{L}} \mathbf{\Lambda}_{\mathrm{Lm}_{22}}^{-1}\right)}{\mathbf{I} - \mathbf{\Lambda}_{\mathrm{Lm}_{11}} \mathbf{\Gamma}_{\mathrm{L}} \mathbf{\Lambda}_{\mathrm{Lm}_{22}}^{-1} \mathbf{\Lambda}_{\mathrm{Rm}_{22}}^{-1} \mathbf{\Gamma}_{\mathrm{R}} \mathbf{\Lambda}_{Rm_{22}}} \mathbf{q_m}\,, \tag{4.56}$$

These relationships can be used to find the wave amplitudes at any point of the waveguide. The input mobility due to a point force is given by the contributions of each wave mode in to the response $\mathbf{w_m} = [w_m \quad w_{Nm}]^T$:

$$\mathrm{Y}(\omega) = i\omega \sum_{m=1}^{N_m} \frac{(w_m + w_{Nm})}{F_m}. \tag{4.57}$$

4.3 Finite element approximation using a hierarchical basis

Two-dimensional spatial variability can also be approached by using the HFE method, although it does not give analytical expressions it can be more convenient for more general applications, e.g. [68, 76-78]. In this section, the two-dimensional thin, rectangular and isotropic plate element is used. It has three degrees of freedom per node, and four nodes, enriched with the most commonly used trigonometric type hierarchical functions [1, 67]

$$g_r(\xi) = \frac{1}{4}(1-\xi^2)\sin\left[\frac{\pi}{2}(r-4)(1+\xi)\right] \tag{4.58}$$

for $r > 4$. It is recommended that trigonometric functions are used instead of the polynomial one for higher dynamic range. Two-dimensional elements are more sensitive to this choice due to rounding errors [1]. The first four functions are the standard shape function for the bending plate FE. The plate was modelled using a single element, and the displacement field is given by

$$\mathrm{w}(\xi,\eta) = \sum_{r=1}^{p}\sum_{s=1}^{p} g_r(\xi)g_s(\eta)W_{rs} = \mathbf{N}(\xi,\eta)\{\mathbf{q}\}, \tag{4.59}$$

where the row matrix $\mathbf{N}(\xi,\eta)$ of shape functions, $\{\mathbf{q}\}$ is the column matrix of degrees of freedom, ξ and η are internal element coordinates and p is the maximum order of the hierarchical functions. They are chosen such that the number of half waves in the highest hierarchical function must be greater than the number of half waves in the mode whose natural frequency is being calculated [67].

Assuming two-dimensional spatial variability in the material properties the element matrices are $p^2 \times p^2$ and can be written as

$$\mathbf{K}_e = \frac{abh^3}{12}\int_{-1}^{1}\int_{-1}^{1}[\mathbf{B}(\xi,\eta)]^T[\mathbf{D}(\xi,\eta)][\mathbf{B}(\xi,\eta)]d\xi\, d\eta, \tag{4.60}$$

$$\mathbf{M}_e = abh\int_{-1}^{1}\int_{-1}^{1}\rho(\xi,\eta)\mathbf{N}(\xi,\eta)^T\mathbf{N}(\xi,\eta)d\xi\, d\eta, \tag{4.61}$$

where $a = L_x/2$, $b = L_y/2$ and h is the plate thickness. From the stress-strain relations of an isotropic plate,

$$\mathbf{D}(\xi,\eta) = E(\xi,\eta)\begin{bmatrix} \frac{1}{(1-\nu^2)} & \frac{\nu}{(1-\nu^2)} & 0 \\ \frac{\nu}{(1-\nu^2)} & \frac{1}{(1-\nu^2)} & 0 \\ 0 & 0 & \frac{1}{2(1+\nu)} \end{bmatrix} \tag{4.62}$$

and

$$\mathbf{B}(\xi,\eta) = \begin{bmatrix} \frac{1}{a^2}\frac{\partial^2}{\partial\xi^2} \\ \frac{1}{b^2}\frac{\partial^2}{\partial\eta^2} \\ \frac{2}{ab}\frac{\partial^2}{\partial\xi\partial\eta} \end{bmatrix}\mathbf{N}(\xi,\eta). \tag{4.63}$$

Moreover, the force vector can be calculated as $\mathbf{f_e} = ab\int_{-1}^{1}\int_{-1}^{1} p_{xy}\lfloor\mathbf{N}(\xi,\eta)\rfloor d\xi\, d\eta$**.** For point harmonic excitation $p_{xy} = F\delta(x - L_{1x})\delta(y - L_{1y})$ at (L_{1x}, L_{1y}), where $\delta(x)$ is the Dirac delta function, then

$$\mathbf{f_e} = abF\lfloor\mathbf{N}(x_e, y_e)\rfloor. \tag{4.64}$$

The material properties can be written in terms of a KL expansion as

$$E(\xi,\eta) = E_0\left[1 + \sigma_E\sum_{j=1}^{N_{KL}}\alpha_j\,\mathrm{f}(\xi,\eta)\right], \tag{4.65}$$

$$\rho(\xi,\eta) = \rho_0\left[1 + \sigma_\rho\sum_{j=1}^{N_{KL}}\beta_j\,\mathrm{g}(\xi,\eta)\right], \tag{4.66}$$

where E_0 and ρ_0 are the mean homogeneous Young's modulus and mass density, the terms $\alpha_j\,\mathrm{f}(\xi,\eta)$ and $\beta_j\,\mathrm{g}(\xi,\eta)$ describe the spatial variability, σ_E and σ_ρ are the dispersion parameters, and N_{KL} is the number of terms need used in the expansion. The element matrices can be rewritten as a sum of the usual stiffness and mass matrices found with homogeneous properties and a term accounting for the spatially varying properties $\mathbf{K}_e = \mathbf{K}_{e0} + \mathbf{\Delta K}_e$ and $\mathbf{M}_e = \mathbf{M}_{e0} + \mathbf{\Delta M}_e$, where

$$\mathbf{\Delta K}_e = \sigma_E E_0 \frac{abh^3}{12} \sum_{j=1}^{N_{KL}} \int_{-1}^{1} \int_{-1}^{1} \alpha_j \, \mathrm{f}(\xi,\eta) \, \mathbf{B}(\xi,\eta)^T \widetilde{\mathbf{D}} \mathbf{B}(\xi,\eta) d\xi \, d\eta \tag{4.67}$$

$$\mathbf{\Delta M}_e = \sigma_\rho \rho_0 abh \sum_{j=1}^{N_{KL}} \int_{-1}^{1} \int_{-1}^{1} \beta_j \, \mathrm{g}(\xi,\eta) \, \mathbf{N}(\xi,\eta)^T \mathbf{N}(\xi,\eta) d\xi \, d\eta \tag{4.68}$$

and

$$\widetilde{\mathbf{D}} = \begin{bmatrix} \frac{1}{(1-\nu^2)} & \frac{\nu}{(1-\nu^2)} & 0 \\ \frac{\nu}{(1-\nu^2)} & \frac{1}{(1-\nu^2)} & 0 \\ 0 & 0 & \frac{1}{2(1+\nu)} \end{bmatrix}. \tag{4.69}$$

4.4 Numerical Results

Numerical simulations were carried out aiming to compare the results obtained with WKB for flexural waves in a plate strip with the HFE and FE approaches. The plate strip material properties were assumed to possess a mean Young's modulus $E_0 = 70$ GPa and density $\rho = 2700$ kg/m^3, with thickness 0.01 m, width $L_y = 0.3$ m and total length $L_x = 1$ m, with free-free boundary conditions, i.e. reflection matrices at left and right $\mathbf{\Gamma}_L = \mathbf{\Gamma}_R = \begin{bmatrix} -1 & 0 \\ 0 & -1 \end{bmatrix}$ and the excitation point at $x = L_{1x} = 0.65L_x$ and $y = L_{1y} = 0.375L_y$. Structural damping was included by making the Young's modulus a complex number $E_0 = E_0(1 + i\eta)$, with $\eta = 10^{-3}$.This change would not affect the theoretical results as long as η is constant over the waveguide.

The frequency band under analysis was chosen from 1 Hz to 1.5 kHz, discretised by 1Hz, such that at least the first ten modes of the plate could be excited. The first ten natural frequencies of the homogeneous plate from an analytical expression are shown in Table 4.1. Also, two wave modes cut on in this frequency band, at 269.3 Hz and 1075.7 Hz, as it can be seen from the dispersion curves plotted in Figure 4.4. It is expected that the WKB solution will not be accurate around the cut on frequencies due to the internal reflections caused by this cut on or cut off transition.

Table 4.1. First ten bending natural frequencies [Hz] for a plate with homogeneous properties.

Mode #	Natural Frequency [Hz]	Mode #	Natural Frequency [Hz]
1	293.1	6	1099.9
2	365.7	7	1140.2
3	486.8	8	1172.5
4	656.2	9	1293.5
5	874.0	10	1454.9

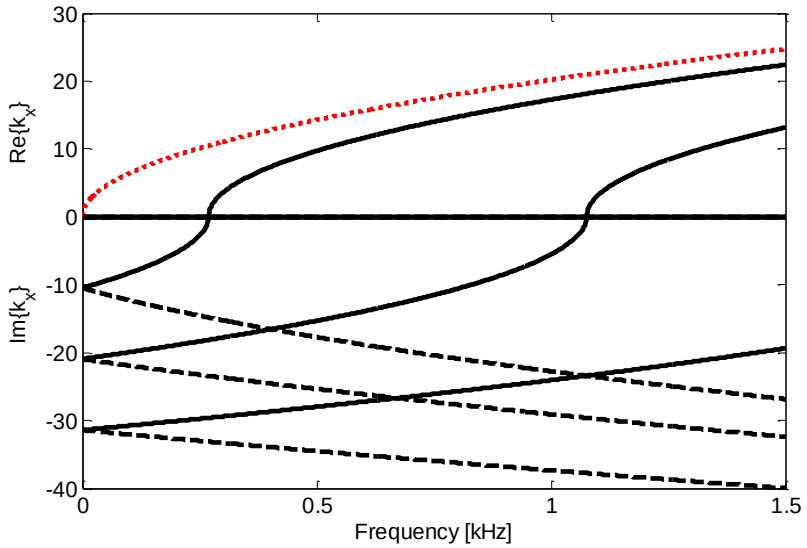

Figure 4.4. Dispersion curves of the two wavenumber types k_{x10} (full black line) and k_{x20} (dashed black line) and also the free bending wavenumber k_{p0} (dotted red line) of the plate with nominal properties within 1Hz to 1.2 kHz.

The integrals for the phase changes, Eq. (4.41)-(4.44), were evaluated numerically, using a Gauss-Legendre quadrature rule. Moreover, the input mobility using the WKB method was evaluated using Eq. (4.57) and $m = 4$ wave modes. The addition of higher order wave mode would have negligible effects on the response within the frequency band. The natural frequencies were calculated using the closed form expression Eq. (4.33), from the first order approximation. For the FE approach a modal summation was used with the first 25 modes.

The HFE input mobility was calculated using direct inversion of the dynamic matrix produced. Special care has to be taken to impose the correct boundary condition on the matrices. In addition to imposing zeros displacement at the four nodes, at the corners of the element, the internal contributions of the hierarchical shape functions that do not

have zero displacement at the edges also have to be set to zero. The element matrix was assembled using $p = 16$ shape functions, Eq. (4.59), leading to 256×256 matrices, reduced to 196×196 after imposing the boundary conditions.

Five different cases for the spatial distribution of the Young's modulus were implemented in order to check the performance of the assumptions made so far. They were made by changing the dispersion parameter σ, i.e. how likely the values are to deviate from the mean value, and the correlation length b, i.e. the rate of fluctuation of the spatial distribution: $\sigma = 0.1$, $b = 2L_x$; $\sigma = 0.2$, $b = 2L_x$; $\sigma = 0.1$, $b = 0.8L_x$; $\sigma = 0.1$, $b = 0.1L_x$; and $\sigma = 0.2$, $b = 0.05L_x$. Figure 4.5 gives the generated values of the Young's modulus with the spatial distribution normalized by the nominal value for E_0.

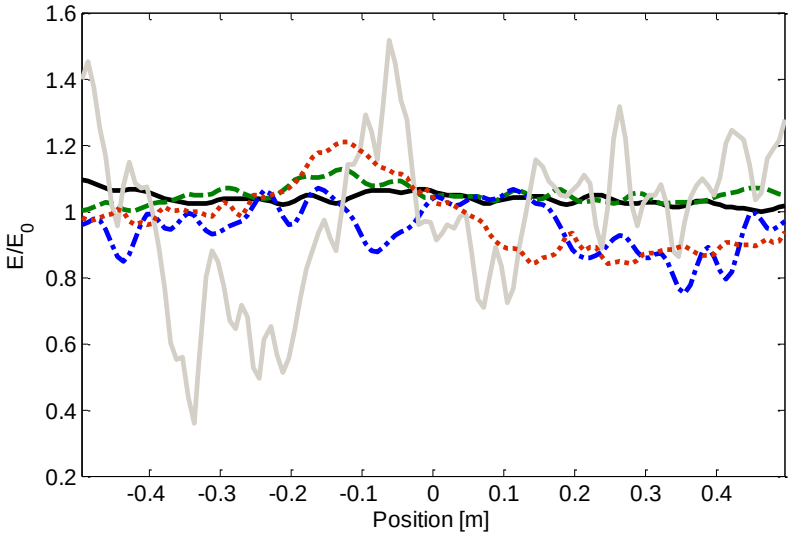

Figure 4.5. Normalized Young's value along the beam axis generated for all the cases: $\sigma = 0.1$, $b = 2L_x$ (black solid); $\sigma = 0.2$, $b = 2L_x$ (red dotted); $\sigma = 0.1$, $b = 0.8L_x$ (green dashed); $\sigma = 0.1$, $b = 0.1L_x$ (blue dash-dotted); and $\sigma = 0.2$, $b = 0.05L_x$ (grey solid).

The amplitude and phase of the input mobilities along with natural frequencies using these cases and simulated by the methods presented in this chapter are shown along with the input mobility of the same beam but with homogeneous properties.

For the dispersion parameter set to $\sigma = 0.1$ and correlation length $b = 2L_x$, Figure 4.6 shows the amplitude and phase of the input mobility. Table 4.2 provides the first ten natural frequencies obtained using FE, as well as the percentage variation from FE of the ones obtained using HFE and the WKB approach. In this case, the Young's modulus varies slowly along the waveguide, so the WKB and FE methods agree very well, as expected. The cut on cut off transition affects the input mobility from the WKB

approach in a very limited frequency band around the two wave modes cutting on. This effect is more noticeable on the phase change, that it expected to be between $-\pi/2$ and $\pi/2$ for input mobility, but lies outside this region for the WKB results at these transition frequencies.

Figure 4.7 shows the amplitude and phase of the input mobilities for the case when $\sigma = 0.2$ and $b = 2L_x$ and Table 4.3 shows that the natural frequencies obtained. The spatial distribution generated is expected to have the same effect on the results, but the larger dispersion is expected to affect the first order approximations. The WKB method also displays very good agreement with the FE and HFE solutions, apart from the frequency bands affected by the cut on cut-off transition is larger. It affects the phase change and also the amplitude of the input mobility.

Figure 4.8 presents the input mobilities when $\sigma = 0.1$ and $b = 0.8L_x$ and Table 4.4 the natural frequencies obtained. For this case, the spatial distribution generated varies slowly enough so that there is good agreement between the input mobility using the WKB approach and the other methods. Very good agreement is also found for the input mobilities apart from the cut on cut-off transition. Figure 4.9 and Table 4.5 gives the input mobilities and natural frequencies for the case when $\sigma = 0.1$ and $b = 0.1L_x$, also showing a good agreement overall.

Figure 4.10 shows the input mobilities for the case when $\sigma = 0.2$ and $b = 0.05L_x$. It is possible to note that the WKB solution follows the same trend as the FE and HFE, but it is not as good as for the previous cases. From Table 4.6, the natural frequencies for both FE and HFE are in very good agreement, but the WKB has a worse performance when compared to the other cases, particularly with Table 4.3, with an equally big dispersion parameter. The WKB cut on cut-off transition severely affects the input mobility response in the frequency around the 6^{th} to 8^{th} mode, but the natural frequencies approximation are still very accurate. The good agreement between HFE and FE natural frequencies shows that random field discretisation is well represented in the FE model.

Overall, the WKB approach presents a very good agreement for the point forced response and free vibration, apart from the cut on cut-off transition frequency bands. Analogous to the beam and rod cases, the difference in the natural frequencies between the WKB compared to the FE approximation is less than 1%, but using just a fraction of the computational cost when the correlation lengths are large over the waveguide, i.e. for larger values for $b = L$. This provides an adequate framework when considering not

only spatial variability but also randomness in the waveguide properties, in order to evaluate response statistics, typically using sampling methods.

The HFE method also produced, for all of the cases considered, a very good agreement with the FE solution. It does not require any slowly spatially varying assumption and being potentially more applicable to more general cases, and different elements.

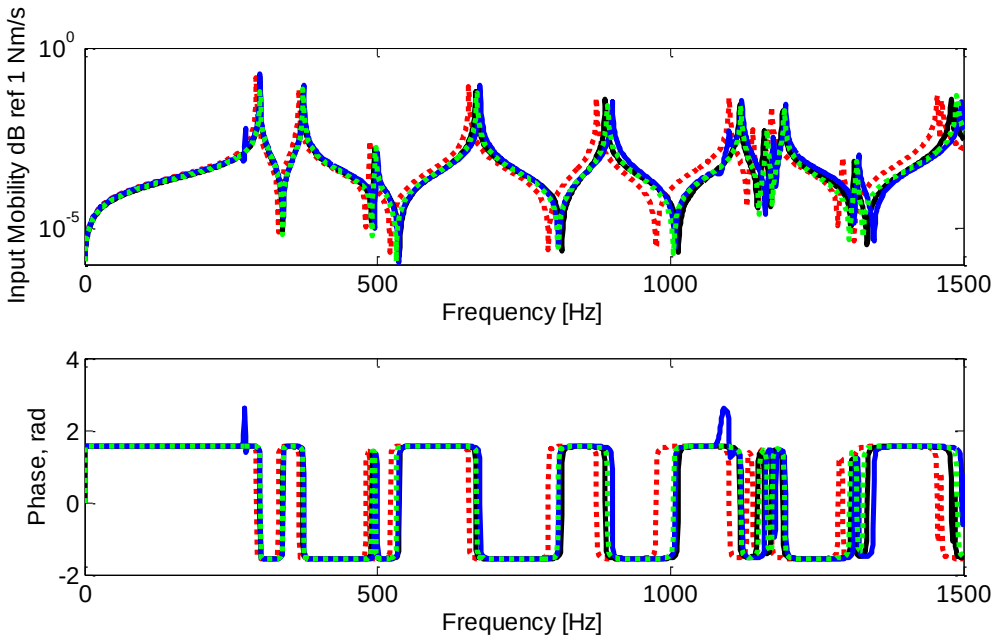

Figure 4.6. (a) Input mobility amplitude and phase with nominal values (dotted red), WKB approximation (blue), FE approach (black) and HFE (dotted green); the dispersion parameter is set to $\sigma = 0.1$ and correlation length $b = 2L$.

Table 4.2. Percentage variation in the ten first natural frequencies [Hz] of the beam with Young's modulus variability using HFE and WKB with respect to the reference FE. The dispersion parameter is set to $\sigma = 0.1$ and correlation length $b = 2L_x$.

FE [Hz]	**(HFE-FE)/FE %**	**(WKB-FE)/FE %**
298.9	0.1550	-0.0994
372.6	0.1745	0.0081
495.5	0.2194	0.0831
667.7	0.2879	0.1301
889.0	0.3909	0.1576
1117.8	0.2126	0.2457
1159.7	0.4706	0.1737
1191.7	0.2235	0.2434
1314.2	0.2716	0.2747
1479.5	0.6473	0.1831

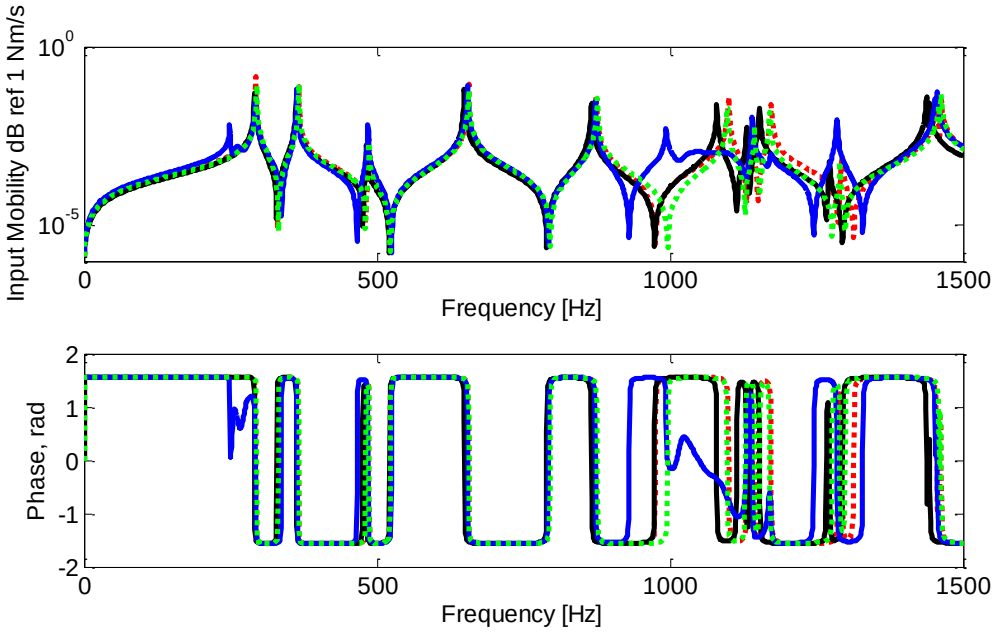

Figure 4.7. (a) Input mobility amplitude and phase with nominal values (dotted red), WKB approximation (blue), FE approach (black) and HFE (dotted green); the dispersion parameter is set to $\sigma = 0.2$ and correlation length $b = 2L_x$.

Table 4.3. Percentage variation in the ten first natural frequencies [Hz] of the beam with Young's modulus variability using HFE and WKB with respect to the reference FE. The dispersion parameter is set to $\sigma = 0.2$ and correlation length $b = 2L_x$.

FE [Hz]	**(HFE-FE)/FE %**	**(WKB-FE)/FE %**
284.4	0.5060	0.6592
355.8	0.0586	0.3904
473.7	-0.0398	0.3592
638.2	0.0441	0.4133
849.4	0.2251	0.4935
1057.5	0.1992	1.5813
1107.3	0.3933	0.5712
1131.0	-0.0007	1.2470
1250.0	-0.0229	1.0683
1411.7	0.2515	0.6524

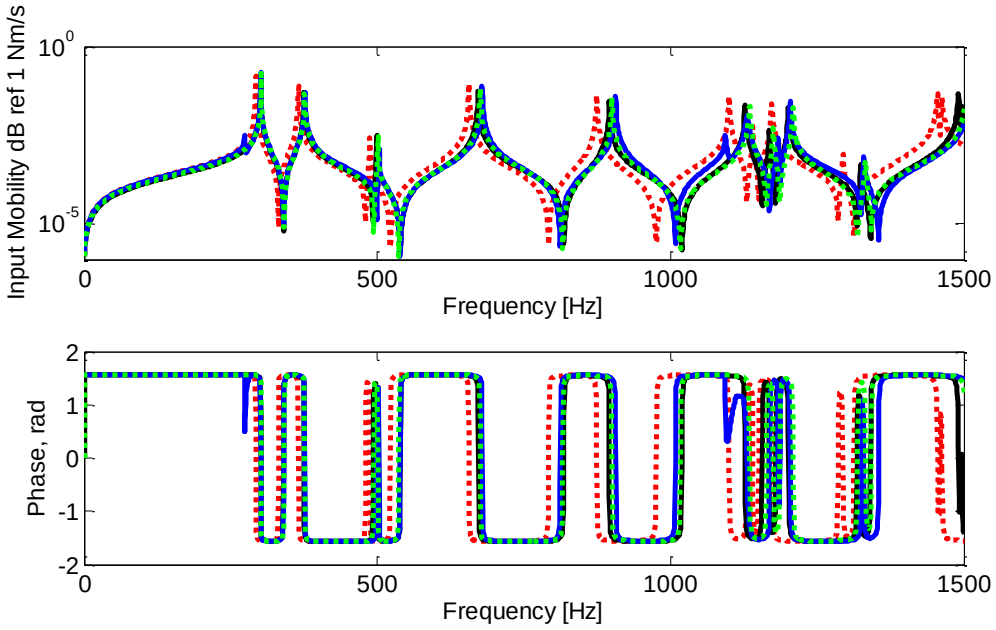

Figure 4.8. (a) Input mobility amplitude and phase with nominal values (dotted red), WKB approximation (blue), FE approach (black) and HFE (dotted green); the dispersion parameter is set to $\sigma = 0.1$ and correlation length $b = 0.8L_x$.

Table 4.4. Percentage variation in the ten first natural frequencies [Hz] of the beam with Young's modulus variability using HFE and WKB with respect to the reference FE. The dispersion parameter is set to $\sigma = 0.1$ and correlation length $b = .08L_x$.

FE [Hz]	**(HFE-FE)/FE %**	**(WKB-FE)/FE %**
301.2	0.2728	-0.2000
375.4	0.2840	-0.0944
499.0	0.3656	0.0190
672.4	0.4295	0.0595
895.6	0.5109	0.0629
1127.3	0.6396	0.0421
1168.6	0.5661	0.0527
1201.4	0.6166	0.0752
1324.3	0.6274	0.1512
1491.1	0.7254	0.0438

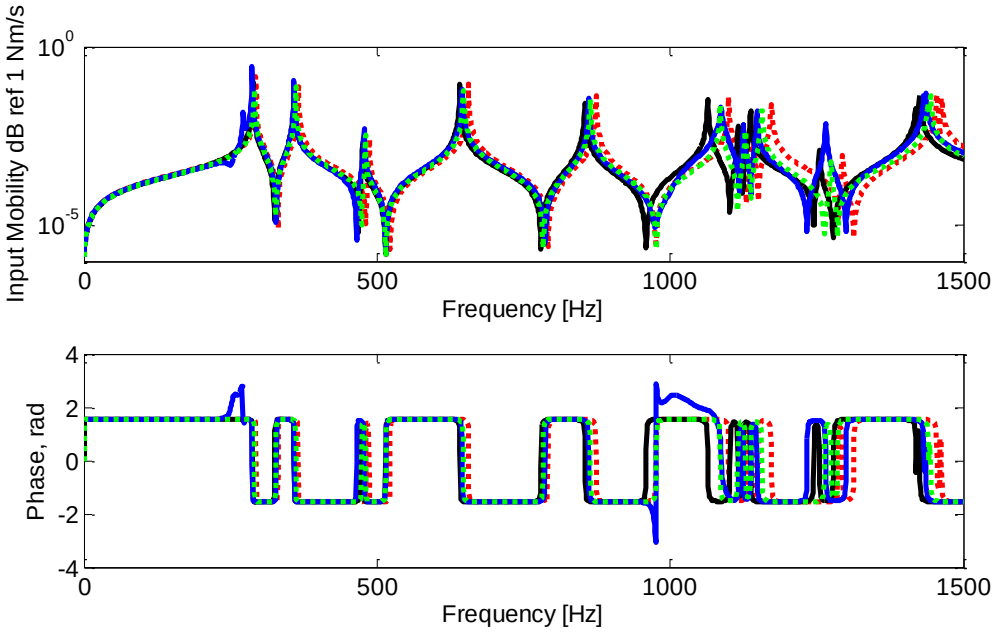

Figure 4.9. (a) Input mobility amplitude and phase with nominal values (dotted red), WKB approximation (blue), FE approach (black) and HFE (dotted green); the dispersion parameter is set to $\sigma = 0.1$ and correlation length $b = 0.1L_x$.

Table 4.5. Percentage variation in the ten first natural frequencies [Hz] of the beam with Young's modulus variability using HFE and WKB with respect to the reference FE. The dispersion parameter is set to $\sigma = 0.1$ and correlation length $b = 0.1L_x$.

FE [Hz]	**(HFE-FE)/FE %**	**(WKB-FE)/FE %**
287.8	0.9763	-0.5811
358.1	0.8740	-0.3018
475.6	0.9218	-0.1036
641.1	0.9792	-0.0970
854.6	1.0689	-0.1709
1064.2	2.0245	0.8830
1115.9	1.1383	-0.2594
1136.7	1.7427	0.6892
1254.3	1.6157	0.6617
1418.7	1.5331	0.1034

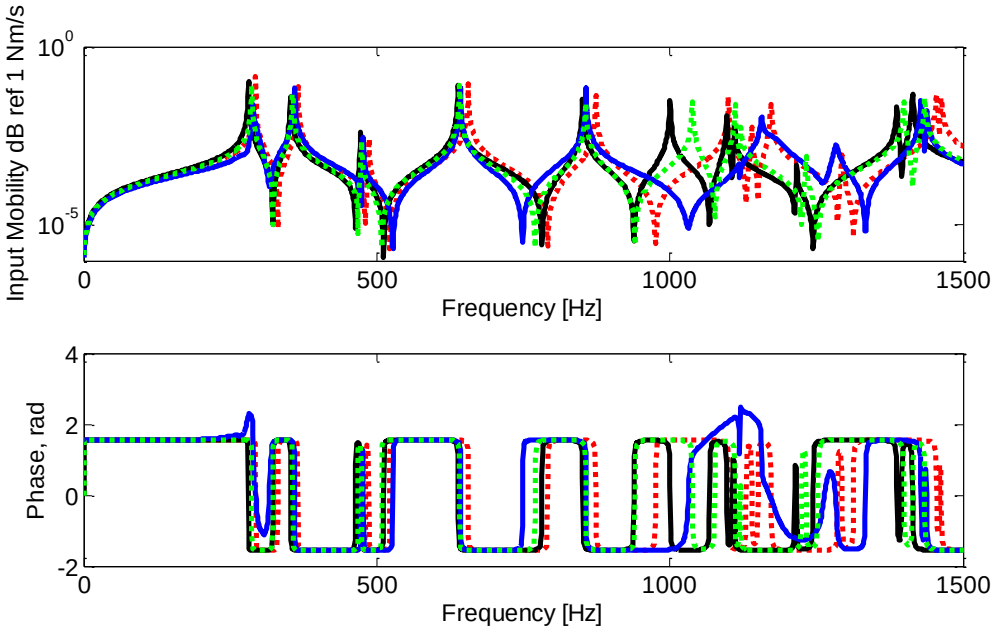

Figure 4.10. (a) Input mobility amplitude and phase with nominal values (dotted red), WKB approximation (blue), FE approach (black) and HFE (dotted green); the dispersion parameter is set to $\sigma = 0.2$ and correlation length $b = 0.05L_x$.

Table 4.6. Percentage variation in the ten first natural frequencies [Hz] of the beam with Young's modulus variability using HFE and WKB with respect to the reference FE. The dispersion parameter is set to $\sigma = 0.2$ and correlation length $b = 0.05L_x$.

FE [Hz]	**(HFE-FE)/FE %**	**(WKB-FE)/FE %**
280.7	2.1238	3.2678
353.5	0.8382	2.3439
472.8	0.3174	1.8367
638.8	0.3246	1.6050
851.2	0.6121	1.5552
1000.1	3.8118	8.7719
1096.7	1.3245	2.8339
1110.1	0.9411	4.4699
1216.0	1.3072	5.2168
1387.2	0.8700	3.7357

4.5 Conclusions

In this chapter the WKB approximation has been used together with the KL expansion for flexural waves in a plate strip with simply supported edges, with slowly varying properties along the axis of propagation. The approximation also retains the physical interpretation of positive and negative going propagating and evanescent waves, but it breaks down at the cut on cut off transition zones, caused by internal reflections due to the local change of the wavenumber.

The formulation allows one to approach the problem using a wave formulation in a similar manner to homogeneous waveguides and, analogous to the rod and beam cases shown in the previous chapters, it provides a framework to include random variability in terms of random fields, on the direction of the propagation. This is because this approach for the plate strip is effectively a one-dimensional approach, and extension to two dimensional waveguides should require further investigation.

The KL expansion was also used here in a purely deterministic sense, assuming the same correlation function such that the same analytical expression is used to generate the spatial variability. This analytical expression is used to find a first order approximation for the natural frequencies of a finite plate strip.

The FE approach using an enriched basis (HFE) was applied to thin and rectangular plate elements, with four nodes and three degrees of freedom per node, including the variability in the properties of the waveguide in the element formulation. Although it does not allow closed form solutions for the input mobilities and natural frequencies, it does not require slowly varying properties, being potentially applicable in more general cases.

So far, even though the KL expansion has been used to generate slowly varying properties, all of the formulations are purely deterministic. In the next chapter, the main expressions derived are extended to also include the ensemble variability, i.e., the statistics of the response given a set of slowly varying properties.

5. Random spatially correlated variability in waveguides

5.1 Introduction

In the previous chapters, the spatially correlated variability has been represented by using a series of trigonometric functions chosen according to a certain scale of fluctuation or correlation length. The choice of this value is made such that the slowly varying assumption for the WKB approximation is valid, i.e. a wave train suffers negligible reflection due to local changes on the waveguide properties. In that sense, longitudinal and flexural propagation in one dimensional waveguides and flexural propagation in a plate strip with simply supported edges are considered using the WKB theory to derive analytical expressions for the natural frequency and input mobility.

In this chapter, the spatially varying material properties are considered to be random fields and they are included in the proposed framework.

Therefore, the natural frequency and the phase change and input mobility, for each frequency, are themselves random variables. Analytical expressions given by the Karhunen-Loeve expansion and a first order approximation are used to derive closed form solutions for the phase change and for the probability density function of the natural frequencies.

The HFE formulation including the spatially varying properties can benefit from the KL expansion in a series of deterministic functions with random coefficients to reduce the computation time under a Monte Carlo (MC) sampling framework, particularly from strongly correlated random fields.

The response statistics are obtained and compared with the piecewise constant approximation, for the rod and the beam, and FE approaches. In both cases, the mid-point discretisation approach is used to represent the random field properties, and MC sampling is used to calculate the PDF of the natural frequencies and envelopes of the input mobilities.

5.1.1 Series representation of random fields

Amongst the methods of generating random fields [29, 30, 79], the formulation using series expansions are able to represent the field using deterministic spatial functions and

random variables. The Karhunen-Loeve expansion is a special case where these deterministic spatial functions are orthogonal and derived from the covariance function. It is especially suited for strongly correlated random field, i.e. slowly varying, because only a few terms on the series are necessary to accurately represent the field.

A Gaussian homogeneous random field $H(x,p)$ with a finite, symmetric and positive definite covariance function $C(x_1,x_2)$, defined over a geometrical domain D, has a spectral decomposition in a generalized Fourier type of series as [28]:

$$H(\boldsymbol{x},p) = H_0(\boldsymbol{x}) + \sum_{j=1}^{\infty} \sqrt{\lambda_j}\, \xi_j(p) f_j(\boldsymbol{x}), \tag{5.1}$$

where $\xi_j(p)$ are Gaussian uncorrelated random variables, λ_j and $f_j(x)$ are eigenvalues and eigenfunctions, solutions of the Fredholm integral equation of the second kind

$$\int_D C(x_1,x_2) f_j(x_1) = \lambda_j f_j(x_2) \tag{5.2}$$

The eigenvalues and eigenfunctions can be ordered in descending order of eigenvalues to truncate Eq. (5.1) to a finite number of terms N_{kl}. In general, this problem can only be solved numerically by discretizing the covariance function, using some collocation method, and finding its eigenvalues and eigenvectors [29].

However, for some families of correlation functions and specific geometries, there exist analytical solutions for this integral equation. One such case is the one dimensional exponentially decaying autocorrelation function,

$$C(x_1,x_2) = e^{-|x_1-x_2|/b}, \tag{5.3}$$

where b is the correlation length, in the interval $0 \leq x \leq L$, where L is the length of the domain. The Karhunen-Loeve expansion, for the zero-mean random field, can be written as [28]:

$$H(x,p) = \sum_{j=1}^{N_{kl}} \left[\alpha_j \xi_{1j}(p) \sin\left[w_{1j}\left(x - \frac{L}{2}\right)\right] + \beta_j \xi_{2j}(p) \cos\left[w_{2j}\left(x - \frac{L}{2}\right)\right]\right] \tag{5.4}$$

where ξ_{1j} and ξ_{2j} are Gaussian zero-mean, unity standard-deviation, independent random variables with the properties

$$\langle \xi_{1j} \rangle = \langle \xi_{1i} \rangle = 0, \langle \xi_{1i}\xi_{2j} \rangle = 0\ , \langle \xi_{1i}\xi_{1j} \rangle = \delta_{ij} \tag{5.5}$$

where $\delta_{ij} = 1$ for $i = j$ and $\delta_{ij} = 0$ for $i \neq j$, and

$$\alpha_j = \sqrt{\frac{\lambda_{1j}}{\frac{L}{2} - \frac{\sin(w_{1j}L)}{2w_{1j}}}}, \beta_j = \sqrt{\frac{\lambda_{2j}}{\frac{L}{2} + \frac{\sin(w_{2j}L)}{2w_{2j}}}}, \tag{5.6}$$

$$\lambda_{1j} = \frac{2c}{w_{1i}^2 + c^2}, \lambda_{2j} = \frac{2c}{w_{2i}^2 + c^2},$$

where $c = 1/b$ and w_{1j} and w_{2j} are the j^{th} roots of the transcendental equations $c \tan w_1 + w_1 = 0$ and $w_2 \tan w_2 - c = 0$, respectively.

This expansion is truncated to N_{kl} terms according the weight of the higher order eigenvalue in the series. Figure 5.1 shows the normalized eigenvalues obtained for different correlation lengths normalized by the total length of the domain. Note that the larger the correlation length the smaller the magnitude of the eigenvalues with respect to the first one, meaning that fewer terms are need to accurately represent the series. The first four eigenfunctions, obtained using the correlation length $b/L = 1$, are shown in Figure 5.2.

The KL expansion is then used to describe the Young's modulus as a random field, given by

$$E(x,p) = E_0[1 + \sigma H(x,p)], \tag{5.7}$$

where E_0 is the nominal value for the Young's modulus and σ is a dispersion term, quantifying the influence of $H(x)$ in the mean nominal value E_0.

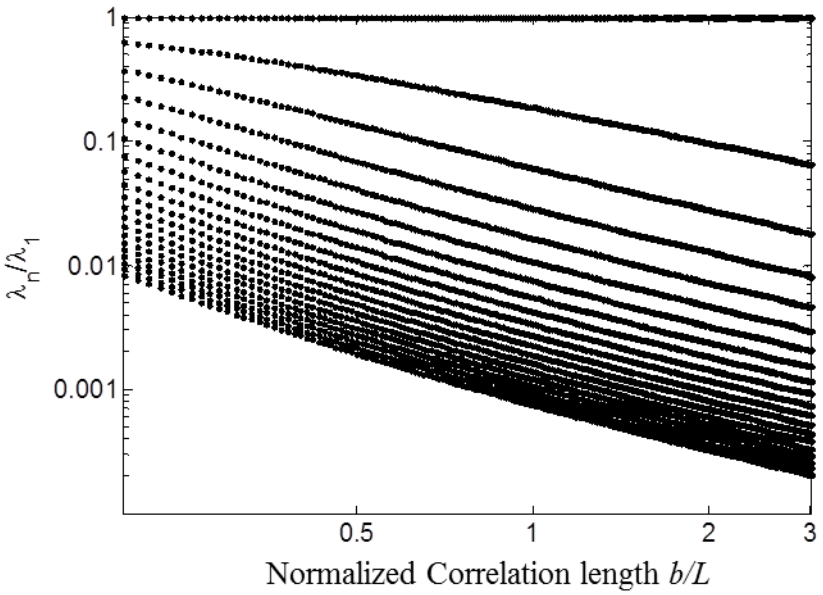

Figure 5.1. Eigenvalues with respect to the normalized correlation length of the analytical solution of the Karhunen-Loeve expansion.

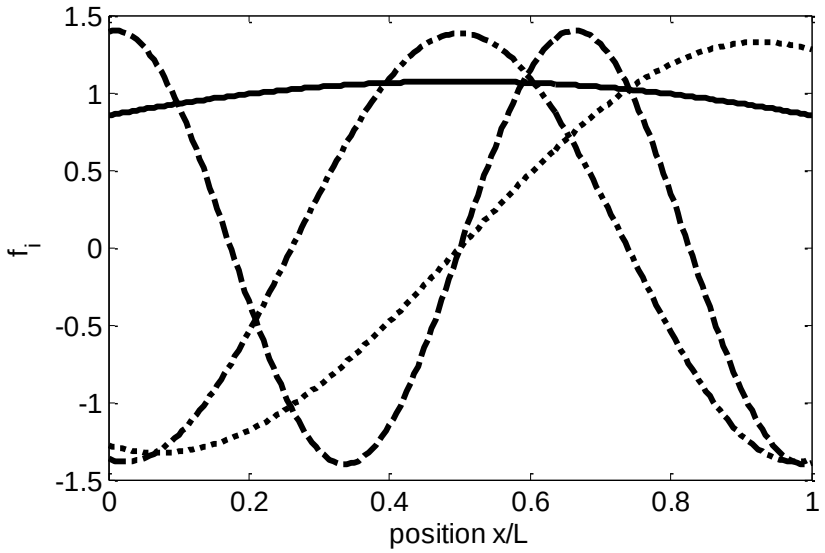

Figure 5.2. First (full line), second (dotted line), third (dashed line) and fourth (dash-dotted line) eigenfunctions of the Karhunen-Loeve expansion using the exponentially decaying correlation function and normalized correlation length $b/L = 1$.

5.1.2 Transformation of a function of random variables

The expressions for natural frequencies are given by a function of a set of random variables to a single random variable. A change of variable method can be used to find an analytical expression for the PDF of a function of random variables. Let the transformation

$$y_i = \mathrm{g_i}(\xi_1, \xi_2, \dots, \xi_N), \tag{5.8}$$

where ξ_i, for $i = 1,2,\dots,N$ and is a vector of random variables. Assuming g_i are continuous function, then it is possible to relate their joint PDFs by [27, 80]

$$f_{\mathbf{y}}(y_1, y_2, \dots, y_N) = \frac{f_{\boldsymbol{\xi}}(\xi_1, \xi_2, \dots, \xi_N)}{|\mathbf{J}|}, \tag{5.9}$$

where $|\mathbf{J}|$ is determinant of the Jacobian matrix given by

$$\mathbf{J} = \begin{bmatrix} \frac{\partial y_1}{\partial \xi_1} & \frac{\partial y_1}{\partial \xi_2} & \dots & \frac{\partial y_1}{\partial \xi_N} \\ \frac{\partial y_2}{\partial \xi_1} & \frac{\partial y_2}{\partial \xi_2} & \dots & \frac{\partial y_2}{\partial \xi_N} \\ \vdots & \vdots & \ddots & \vdots \\ \frac{\partial y_N}{\partial \xi_1} & \frac{\partial y_N}{\partial \xi_2} & \dots & \frac{\partial y_N}{\partial \xi_N} \end{bmatrix}. \tag{5.10}$$

By making a convenient choice of variables $y_1 = \omega_n$, $y_2 = \xi_N$, $y_3 = \xi_{N-1}$,…, $y_N = \xi_2$, it possible to write the Jacobian as

$$\mathbf{J} = \begin{bmatrix} \frac{\partial \omega_n}{\partial \xi_1} & \frac{\partial \omega_n}{\partial \xi_2} & \cdots & \frac{\partial \omega_n}{\partial \xi_N} \\ 0 & 0 & \cdots & 1 \\ \vdots & \vdots & \ddots & \vdots \\ 0 & 1 & \cdots & 0 \end{bmatrix}, \tag{5.11}$$

and the PDF of the natural frequency is the marginal PDF

$$f_\Omega(\omega_n) = \int \cdots \int \frac{f_{\boldsymbol{\xi}}(\xi_1, \xi_2, \ldots, \xi_N)}{|\mathbf{J}|} \prod_{i=2}^{N} d\xi_i. \tag{5.12}$$

In the case of the random variables ξ_i being independent, zero-mean unity standard gaussian variables, then the integral simplifies to

$$f_\Omega(\omega_n) = \int \cdots \int \frac{f(\xi_1) f(\xi_2) \cdots f(\xi_N)}{|\mathbf{J}|} \prod_{i=2}^{N} d\xi_i, \tag{5.13}$$

where $f(\xi_i) = \frac{1}{\sqrt{2\pi}} e^{-\xi_i^2/2}$ and the inverse function $\xi_1 = \mathrm{g}_i^{-1}(\omega_n, \xi_2, \ldots, \xi_N)$ exists.

5.2 Longitudinal waves in one-dimensional waveguides

In Chapter 2, an expression for the natural frequencies in a waveguide undergoing longitudinal vibration was found using the WKB approximation and considering a varying Young's modulus. Considering this variability as a random field, as described in Eq. (5.4), then the natural frequencies are, consequently, random variables

$$\omega_n = \sqrt{\frac{E_0}{\rho}} \frac{2n\pi - \phi_R - \phi_L}{2\int_0^L \sqrt{\frac{1}{1+\sigma H(x)}}\, dx}. \tag{5.14}$$

In addition, considering that the Young's modulus is not only slowly varying, but also presents small dispersion around the nominal value, i.e. $|\sigma H(x)| \ll 1$, a first order approximation can be used such that $\sqrt{1/[1+\sigma H(x)]} \approx 1 - \sigma/2\, H(x)$, then

$$\widetilde{\omega}_n \approx \sqrt{\frac{E_0}{\rho}} \frac{2n\pi - \phi_R - \phi_L}{2L - \sigma \int_0^L H(x) dx}. \tag{5.15}$$

Also, if $|\sigma H(x)| \ll 1$ then $|\sigma H(x)| 2L \ll 2L$ and $\int_0^L \sigma H(x) dx \ll \int_0^L max|\sigma H(x)|\, dx = max|\sigma H(x)|\, L$, so the first order approximation can be written as

$$\widetilde{\omega}_n \approx \omega_{n0} \left(1 + \frac{\sigma}{2L} \int_0^L H(x) dx \right), \tag{5.16}$$

where $\omega_{n0} = \sqrt{\frac{E_0}{\rho}}\frac{(2n\pi-\phi_R-\phi_L)}{2L}$ is the natural frequency of rod with nominal homogeneous properties. Using the KL expansion expression, from Eq. (5.4), the integral can be analytically evaluated as

$$\int_0^L H(x)dx = 2\sum_{j=1}^{N_{kl}} \xi_j(p)\frac{\beta_j}{w_{2j}}\sin\left(\frac{w_{2j}L}{2}\right), \tag{5.17}$$

and Eq. (5.16) can be rewritten in terms of a summation of Gaussian random variables as

$$\widetilde{\omega}_n(p) \approx g_L\left(\xi_1, \xi_2, \dots, \xi_{N_{kl}}, p\right) = \omega_{n0} + \sum_{j=1}^{N_{kl}} \mathrm{B}_{\mathrm{L}j}\xi_j(p), \tag{5.18}$$

where $\omega_{n0} = \sqrt{\frac{E_0}{\rho}}\frac{(2n\pi-\phi_R-\phi_L)}{2L}$ is the natural frequency for the homogeneous deterministic rod and $\mathrm{B}_{\mathrm{L}j} = \omega_{n0}\frac{\sigma}{L}\frac{\beta_j}{w_{2j}}\sin\left(\frac{w_{2j}L}{2}\right)$ are the terms included by the spatially varying Young's modulus. This expression can be applied to Eq. (5.13), to derive a closed form expression for the PDF of the natural frequencies as

$$f_{\Omega_n}(\omega_n) = \frac{1}{\sqrt{2\pi}\,\sigma_\Omega}\exp\left(-\frac{(\omega_n-\omega_{n0})^2}{2\sigma_\Omega^2}\right), \tag{5.19}$$

where $\sigma_\Omega = \sqrt{\sum_{j=1}^{N_{KL}} \mathrm{B}_{Lj}^2}$. Note that this is a Gaussian PDF with mean value ω_{n0} and standard deviation σ_Ω. It is expected that a first order approximation of Eq. (2.21), that is a function of a Gaussian random field into a random variable, would lead to a Gaussian random variable with the mean equals its nominal value. This approximation shows clearly that the statistics of the n^{th} natural frequency depends on the spatial variability, given by the coefficients B_{Lj}.

In addition, another expression for the natural frequencies using the piecewise constant approach was derived by assuming negligible reflection

$$\omega_n(p) = \frac{2n\pi + (\phi_R + \phi_L)}{2L\sum_{j=1}^{N}\sqrt{\rho/E_j(p)}}. \tag{5.20}$$

where E_j is evaluated by sampling the random field at the centroid of each element. This expression was obtained approximating the scattering matrix to the identity matrix and it is very similar to the one obtained by using the WKB approach.

Moreover, an expression for the phase change $\theta(x_0, x, p)$ for a wave travelling from and arbitrary point x_0 until x, also using the WKB approximation, was given by

$$\theta(\omega, \mathrm{x_0}, \mathrm{x}, \mathrm{p}) = \sqrt{\frac{\rho}{\mathrm{E_0}}}\omega \int_{\mathrm{x_0}}^{\mathrm{x}} \sqrt{\frac{1}{1+\sigma \mathrm{H(x,p)}}}\,\mathrm{dx}, \tag{5.21}$$

whose first order approximation is given by

$$\theta(\omega, x_0, x, p) = \sqrt{\frac{\rho}{\mathrm{E_0}}}\omega \left[1 - \frac{\sigma}{2}\int_{\mathrm{x_0}}^{x} \mathrm{H}(x,p)\mathrm{dx}\right]. \tag{5.22}$$

And expression for the input mobility, using the WKB approach, for a force applied at $x = L_1$ is given as

$$\mathrm{Y}(\omega, p) = \frac{\omega}{2\mathrm{k(L_1)E(L_1)A}} \frac{1 + \Gamma_\mathrm{L} \mathrm{e}^{-\mathrm{i}\theta_\mathrm{L}(\mathrm{p})} + \Gamma_\mathrm{R} \mathrm{e}^{-\mathrm{i}\theta_\mathrm{R}(\mathrm{p})} + \Gamma_\mathrm{L}\Gamma_\mathrm{R} \mathrm{e}^{-\mathrm{i}\theta_\mathrm{T}(\mathrm{p})}}{1 - \Gamma_\mathrm{L}\Gamma_\mathrm{R} \mathrm{e}^{-\mathrm{i}\theta_\mathrm{T}(\mathrm{p})}}. \tag{5.23}$$

where the phase changes from the left boundary to the excitation point $\theta_\mathrm{L}(\mathrm{p}) = \theta(0, \mathrm{L_1}, \mathrm{p})$, from the excitation point to the right boundary $\theta_\mathrm{R}(\mathrm{p}) = \theta(\mathrm{L_1}, \mathrm{L}, \mathrm{p})$ and the total phase change from the left boundary to the right boundary $\theta_\mathrm{T}(\mathrm{p}) = \theta_\mathrm{L}(\mathrm{p}) + \theta_\mathrm{R}(\mathrm{p}) = \theta(0, \mathrm{L}, \mathrm{p})$, are given by

$$\theta_\mathrm{L}(\omega, p) = \sqrt{\frac{\rho}{\mathrm{E_0}}}\omega \int_{0}^{\mathrm{L_1}} \sqrt{\frac{1}{1+\sigma \mathrm{H}(x,p)}}\,\mathrm{dx}. \tag{5.24}$$

$$\theta_\mathrm{R}(\omega, p) = \sqrt{\frac{\rho}{\mathrm{E_0}}}\omega \int_{\mathrm{L_1}}^{\mathrm{L}} \sqrt{\frac{1}{1+\sigma \mathrm{H}(x,p)}}\,\mathrm{dx}, \tag{5.25}$$

$$\theta_\mathrm{T}(\omega, p) = \sqrt{\frac{\rho}{\mathrm{E_0}}}\omega \int_{0}^{\mathrm{L}} \sqrt{\frac{1}{1+\sigma \mathrm{H}(x,p)}}\,\mathrm{dx}. \tag{5.26}$$

Using a first order approximation and the KL expansion from Eq. (5.4), the integrals can be analytically evaluated, and then the phase changes are approximated by

$$\theta_L(\omega, p) \approx \sqrt{\frac{\rho}{E_0}}\omega[L_1 - \sigma \Delta\theta_L(p)]. \tag{5.27}$$

$$\theta_R(\omega, p) \approx \sqrt{\frac{\rho}{E_0}}\omega\left[L - L_1 - \frac{\sigma}{2}\Delta\theta_R(p)\right]. \tag{5.28}$$

$$\theta_T(\omega,p) \approx \sqrt{\frac{\rho}{E_0}}\omega\left[L-\frac{\sigma}{2}\Delta\theta_T(p)\right]. \tag{5.29}$$

where

$$\begin{aligned}\Delta\theta_L(p) = \sum_{j=1}^{N_{kl}}\Bigg[&\xi_{1j}(p)\frac{\alpha_j}{w_{1j}}\left[\cos\left(\frac{w_{1j}L}{2}\right)-\cos\left(\frac{w_{1j}}{2}(L-2L_1)\right)\right]\\ &+\xi_{2j}(p)\frac{\beta_j}{w_{2j}}\left[\sin\left(\frac{w_{2j}L}{2}\right)-\sin\left(\frac{w_{2j}}{2}(L-2L_1)\right)\right]\Bigg].\end{aligned} \tag{5.30}$$

$$\begin{aligned}\Delta\theta_R(p) = \sum_{j=1}^{N_{kl}}\Bigg[&\xi_{1j}(p)\frac{\alpha_j}{w_{1j}}\left[\cos\left(\frac{w_{1j}}{2}(L-2L_1)\right)-\cos\left(\frac{w_{1j}L}{2}\right)\right]\\ &+\xi_{2j}(p)\frac{\beta_j}{w_{2j}}\left[\sin\left(\frac{w_{2j}L}{2}\right)+\sin\left(\frac{w_{2j}}{2}(L-2L_1)\right)\right]\Bigg].\end{aligned} \tag{5.31}$$

$$\Delta\theta_T(p) = 2\sum_{j=1}^{N_{kl}}\xi_{2j}(p)\frac{\beta_j}{w_{2j}}\sin\left(\frac{w_{2j}L}{2}\right). \tag{5.32}$$

These expressions for the phase changes are single random variables, for each frequency ω. Mean value and standard deviation can be calculated by using the properties of the independent and identically distributed random as

$$\langle\theta_L(\omega)\rangle = \sqrt{\frac{\rho}{E_0}}\omega L_1. \tag{5.33}$$

$$\langle\theta_R(\omega)\rangle = \sqrt{\frac{\rho}{E_0}}\omega(L-L_1). \tag{5.34}$$

$$\langle\theta_T(\omega)\rangle = \sqrt{\frac{\rho}{E_0}}\omega L. \tag{5.35}$$

and

$$\begin{aligned}\sigma_{\theta_L}(\omega) = \frac{\sigma}{2}\omega\sqrt{\frac{\rho}{E_0}}\Bigg(\sum_{j=1}^{N_{kl}}\Bigg[&\left[\frac{\alpha_j}{w_{1j}}\left(\cos\left(\frac{w_{1j}L}{2}\right)-\cos\left(\frac{w_{1j}}{2}(L-2L_1)\right)\right)\right]^2\\ &+\left[\frac{\beta_j}{w_{2j}}\left[\sin\left(\frac{w_{2j}L}{2}\right)-\sin\left(\frac{w_{2j}}{2}(L-2L_1)\right)\right]\right]^2\Bigg]\Bigg)^{\frac{1}{2}},\end{aligned} \tag{5.36}$$

$$\sigma_{\theta_R}(\omega) = \frac{\sigma}{2}\omega\sqrt{\frac{\rho}{E_0}}\left(\sum_{j=1}^{N_{kl}}\left[\left[\frac{\alpha_j}{w_{1j}}\left[\cos\left(\frac{w_{1j}}{2}(L-2L_1)\right)-\cos\left(\frac{w_{1j}L}{2}\right)\right]\right]^2 + \left[\frac{\beta_j}{w_{2j}}\left[\sin\left(\frac{w_{2j}L}{2}\right)+\sin\left(\frac{w_{2j}}{2}(L-2L_1)\right)\right]\right]^2\right]\right)^{\frac{1}{2}}, \tag{5.37}$$

$$\sigma_{\theta_T}(\omega) = 2\sigma\omega\sqrt{\frac{\rho}{E_0}}\left[\sum_{j=1}^{N_{kl}}\left[\frac{\beta_j}{w_{2j}}\sin\left(\frac{w_{2j}L}{2}\right)\right]^2\right]^{\frac{1}{2}} \tag{5.38}$$

The piecewise constant formulation was also used to derived and expression for the input mobility for the finite rod, as shown in chapter 2, taking into account the internal reflection caused by the changes of properties, unlike the WKB approach, where the properties of the random field are evaluated by sampling it at the centroid of each element.

5.3 Flexural waves in one-dimensional waveguides

An expression for the natural frequency of a beam with random Young's modulus was found in Chapter 3. Likewise as for the longitudinal case, it is also considered from here on as random variable

$$\omega_n(p) = \frac{\theta_{Tn}^2}{\left(\int_0^L \sqrt[4]{\frac{\rho A}{E(x,p)I_{yy}}}\,dx\right)^2}. \tag{5.39}$$

In addition, considering that the Young's modulus is not only slowly varying, but also presents small dispersion around the nominal value, i.e. $|\sigma H(x)| \ll 1$, a first order approximation can be used such that $\sqrt[4]{1/[1+\sigma H(x)]} \approx 1 - \sigma/4\, H(x)$, then the same procedure for longitudinal waves can be applied, using the KL expansion, leading to

$$\widetilde{\omega}_n(p). \approx \mathrm{g_B}\left(\xi_1, \xi_2, \ldots, \xi_{N_{kl}}, p\right) = \omega_{n0} + \sum_{j=1}^{N_{kl}} \mathrm{B_{B}}_j \xi_j(p), \tag{5.40}$$

where $\omega_{n0} = \frac{\theta_{Tn}^2}{L^2}\sqrt{\frac{E_0 I_{yy}}{\rho A}}$ is the natural frequency for the homogeneous deterministic beam and $\mathrm{B_{B}}_j = \omega_{n0}\frac{\sigma}{L}\frac{\beta_j}{w_{2j}}\sin\left(\frac{w_{2j}L}{2}\right)$ are the terms included by the spatially varying

Young's modulus. An analytical expression for the PDF of the natural frequencies is also derived applying the transformation method from Eq. (5.13) as

$$f_{\Omega_n}(\omega_n) = \frac{1}{\sqrt{2\pi}\,\sigma_\Omega}\exp\left(-\frac{(\omega_n-\omega_{n0})^2}{2\sigma_\Omega^2}\right), \tag{5.41}$$

where $\sigma_\Omega = \sqrt{\sum_{\mathrm{j=1}}^{\mathrm{N_{KL}}} \mathrm{B}_{\mathrm{B}j}^2}$. It is also a Gaussian PDF with mean value ω_{n0} and standard deviation σ_Ω. This approximation clearly shows that the statistics of the n^{th} natural frequency depends on the spatial variability, given by the coefficients $\mathrm{B}_{\mathrm{B}j}$.

In addition, another expression for the natural frequencies was derived by assuming negligible reflection on the piecewise constant approach

$$\omega_n(p) = \frac{\theta_{Tn}^2}{\left(\sum_{j=1}^{N}\sqrt[4]{\frac{\rho A_j}{E_j(p)I_{yy}}}\,L\right)^2}, \tag{5.42}$$

where E_j is evaluated by sampling the random field at the centroid of each element. Also, the expression for the phase change $\theta(x_0,x,p)$ for a wave travelling from and arbitrary point x_0 until x, also using the WKB approximation, given by

$$\theta(\omega,x_0,x,p) = \sqrt{\omega}\int_{x_0}^{x}\sqrt[4]{\frac{\rho A}{EI_{yy}(x,p)}}\,dx. \tag{5.43}$$

and also the amplitude change

$$\gamma(x_0,x,p) = \ln\left[\frac{\widetilde{W}(x,p)}{\widetilde{W}(x_0,p)}\right]. \tag{5.44}$$

where $\widetilde{W}(x,p) = \left(\rho A(x,p)\right)^{-\frac{3}{8}}\left(EI_{yy}(x,p)\right)^{-\frac{1}{8}}$.

An expression for the input mobility, for a force applied at $x = L_1$ was given as

$$\mathrm{Y}(\omega,p) = \frac{\mathrm{i}\omega(w+w_{\mathrm{N}})}{F}, \tag{5.45}$$

from which

$$\mathbf{w} = \frac{\left(\mathbf{I}+\mathbf{\Lambda}_{\mathrm{R}}^{-1}{}_{22}\mathbf{\Gamma}_{\mathrm{R}}\mathbf{\Lambda}_{R_{11}}\right)\left(\mathbf{I}+\mathbf{\Lambda}_{\mathrm{L}_{11}}\mathbf{\Gamma}_{\mathrm{L}}\mathbf{\Lambda}_{\mathrm{L}}^{-1}{}_{22}\right)}{\mathbf{I}-\mathbf{\Lambda}_{\mathrm{L}_{11}}\mathbf{\Gamma}_{\mathrm{L}}\mathbf{\Lambda}_{\mathrm{L}}^{-1}{}_{22}\,\mathbf{\Lambda}_{\mathrm{R}}^{-1}{}_{22}\mathbf{\Gamma}_{\mathrm{R}}\mathbf{\Lambda}_{R_{22}}}\mathbf{q}, \tag{5.46}$$

$\mathbf{w} = [w \quad w_N]^T$, and $\mathbf{\Lambda_{L_{11}}}$, $\mathbf{\Lambda_{L_{22}}}$, $\mathbf{\Lambda_{R_{11}}}$ and $\mathbf{\Lambda_{R_{22}}}$ are the transmission matrices from chapter 3, depending on the phase changes from the left boundary to the excitation point

$\theta_L(p) = \theta(0, L_1, p)$, the phase change from the excitation point to the right boundary $\theta_R(p) = \theta(L_1, L, p)$ and the total phase change from the left boundary to the right boundary $\theta_T(p) = \theta_L(p) + \theta_R(p) = \theta(0, L, p)$, given as

$$\theta_L(\omega, p) = \sqrt{\omega} \int_0^{L_1} \sqrt[4]{\frac{\rho A}{E I_{yy}(x,p)}}\, dx, \tag{5.47}$$

$$\theta_R(\omega, p) = \sqrt{\omega} \int_{L_1}^{L} \sqrt[4]{\frac{\rho A}{E I_{yy}(x,p)}}\, dx, \tag{5.48}$$

$$\theta_T(\omega, p) = \sqrt{\omega} \int_0^{L} \sqrt[4]{\frac{\rho A}{E I_{yy}(x,p)}}\, dx. \tag{5.49}$$

Using a first order approximation and the KL expansion from Eq. (5.4), the integrals can be analytically evaluated, and then the phase changes are approximated by

$$\theta_L(\omega, p) \approx \sqrt{\omega} \sqrt[4]{\frac{\rho A}{E_0 I_{yy}}} \left[L_1 - \frac{\sigma}{4} \Delta\theta_L(p)\right]. \tag{5.50}$$

$$\theta_R(\omega, p) \approx \sqrt{\omega} \sqrt[4]{\frac{\rho A}{E_0 I_{yy}}} \left[L - L_1 - \frac{\sigma}{4} \Delta\theta_R(p)\right]. \tag{5.51}$$

$$\theta_T(\omega, p) \approx \sqrt{\omega} \sqrt[4]{\frac{\rho A}{E_0 I_{yy}}} \left[L - \frac{\sigma}{4} \Delta\theta_T(p)\right]. \tag{5.52}$$

where $\Delta\theta_L(p)$, $\Delta\theta_R(p)$ and $\Delta\theta_T(p)$ are given by Eq. (5.30), Eq. (5.31) and Eq. (5.32), respectively. These expressions for the phase changes are single random variables, for each frequency ω. The mean value and standard deviation can be calculated as

$$\langle \theta_L(\omega) \rangle = \sqrt{\omega} \sqrt[4]{\frac{\rho A}{E_0 I_{yy}}} L_1. \tag{5.53}$$

$$\langle \theta_R(\omega) \rangle = \sqrt{\omega} \sqrt[4]{\frac{\rho A}{E_0 I_{yy}}} (L - L_1). \tag{5.54}$$

$$\langle \theta_T(\omega) \rangle = \sqrt{\omega} \sqrt[4]{\frac{\rho A}{E_0 I_{yy}}} L. \tag{5.55}$$

and

$$\sigma_{\theta_L}(\omega) = \frac{\sigma}{4}\sqrt{\omega}^4\sqrt{\frac{\rho A}{E_0 I_{yy}}}\left(\sum_{j=1}^{N_{kl}}\left[\left[\frac{\alpha_j}{w_{1j}}\left(\cos\left(\frac{w_{1j}L}{2}\right)-\cos\left(\frac{w_{1j}}{2}(L-2L_1)\right)\right)\right]^2 + \left[\frac{\beta_j}{w_{2j}}\left[\sin\left(\frac{w_{2j}L}{2}\right)-\sin\left(\frac{w_{2j}}{2}(L-2L_1)\right)\right]\right]^2\right]\right)^{\frac{1}{2}}, \tag{5.56}$$

$$\sigma_{\theta_R}(\omega) = \frac{\sigma}{4}\sqrt{\omega}^4\sqrt{\frac{\rho A}{E_0 I_{yy}}}\left(\sum_{j=1}^{N_{kl}}\left[\left[\frac{\alpha_j}{w_{1j}}\left[\cos\left(\frac{w_{1j}}{2}(L-2L_1)\right)-\cos\left(\frac{w_{1j}L}{2}\right)\right]\right]^2 + \left[\frac{\beta_j}{w_{2j}}\left[\sin\left(\frac{w_{2j}L}{2}\right)+\sin\left(\frac{w_{2j}}{2}(L-2L_1)\right)\right]\right]^2\right]\right)^{\frac{1}{2}}, \tag{5.57}$$

$$\sigma_{\theta_T}(\omega) = \sigma\sqrt{\omega}^4\sqrt{\frac{\rho A}{E_0 I_{yy}}}\left[\sum_{j=1}^{N_{kl}}\left[\frac{\beta_j}{w_{2j}}\sin\left(\frac{w_{2j}L}{2}\right)\right]^2\right]^{\frac{1}{2}} \tag{5.58}$$

The piecewise constant formulation was also used to derived and expression for the input mobility for the finite beam, as shown in chapter 3, taking into account the internal refection caused by the changes of properties, unlike the WKB approach, where the properties of the random field are evaluated by sampling it at the centroid of each element.

5.4 Flexural waves in a plate strip with simply supported edges

From Chapter 4, the natural frequency of a plate strip with simply supported edges and random Young's modulus, using the WKB approximation, is given by

$$\omega_{mn}(p) = \omega_{0mn}\left(1+\frac{\sigma}{2L_x}\int_0^{L_x}H(x,p)dx\right), \tag{5.59}$$

where ω_{0mn} is the natural frequency for the homogeneous simply supported rectangular plate of dimensions L_x and L_y, i.e. $\omega_{0mn} = \left[\left(\frac{m\pi}{L_y}\right)^2+\left(\frac{n\pi}{L_x}\right)^2\right]\sqrt{\frac{D_0}{\rho h}}$. Moreover, if $H(x,p)$, is expressed by Eq.(5.4), then its integral has a closed form and the first order approximation for the natural frequency is given by

$$\omega_{mn}(p). \approx \mathrm{g_P}\left(\xi_1, \xi_2, \ldots, \xi_{N_{kl}}, p\right) = \omega_{0mn} + \sum_{j=1}^{N_{kl}} \mathrm{B_P}_j \xi_j(p), \tag{5.60}$$

where $\mathrm{B_P}_j = \omega_{0mn} \frac{\sigma}{L_x} \frac{\beta_j}{w_{2j}} \sin\left(\frac{w_{2j} L}{2}\right)$ are the terms included by the spatially varying Young's modulus.

This expression can also be used to derive an analytical expression for the PDF of the natural frequencies, applying the transformation method from Eq. (5.13) as

$$f_{\Omega_{mn}}(\omega_{mn}) = \frac{1}{\sqrt{2\pi}\,\sigma_\Omega} \exp\left(-\frac{(\omega_{mn} - \omega_{mn0})^2}{2\sigma_\Omega^2}\right), \tag{5.61}$$

where $\sigma_\Omega = \sqrt{\sum_{j=1}^{N_{KL}} \mathrm{B}_{\mathrm{P}j}^2}$. Note that this is a Gaussian PDF with mean value ω_{n0} and standard deviation σ_Ω.

Two distinct wave types are present in the plate strip, for each standing wave mode m across the plate strip width, each one with an expression for the phase and amplitude change for a wave travelling down the plate strip from and arbitrary point $\mathrm{x_0}$ until x

$$\theta_m(\omega, x_0, x, p) = \int_{x_0}^{x} \sqrt{\omega \sqrt{\frac{\rho h}{D(x)}} - k_{ym}^2}\,\mathrm{d}x, \tag{5.62}$$

$$\theta_{Nm}(\omega, x_0, x, p) = \int_{x_0}^{x} \sqrt{-\omega \sqrt{\frac{\rho h}{D(x)}} - k_{ym}^2}\,\mathrm{d}x, \tag{5.63}$$

and also the amplitude change

$$\gamma_m = \frac{1}{2} \ln\left[\frac{k_{x1m}(x,p)}{k_{x1m}(x_0,p)}\right], \tag{5.64}$$

$$\gamma_{Nm} = \frac{1}{2} \ln\left[\frac{k_{x2m}(x,p)}{k_{x2m}(x_0,p)}\right]. \tag{5.65}$$

where

$$k_{x1m}(x,p) = \sqrt{k_p^2(x,p) - k_{ym}^2}, \tag{5.66}$$

$$k_{x2m}(x,p) = \sqrt{-k_p^2(x,p) - k_{ym}^2}, \tag{5.67}$$

are the local wavenumber for the two wave kinds, $k_p(x) = \sqrt{\omega}\left(\frac{\rho h(x)}{D(x)}\right)^{1/4}$ is the free plate wavenumber, $k_{ym} = \frac{m\pi}{L_y}$ is the wavenumber in the *y* direction, due to the simply supported edges, and $D(x,p) = \frac{E(x,p)h^3}{12(1-\nu^2)}$ is the flexural stiffness of the plate. Note that θ_m can be either imaginary, in which case represents a propagating wave, with phase change ε, or real, in which case a non-propagating wave with attenuation constant, δ, causing an amplitude change $e^{-\delta}$. The other wave kind is always non-propagating, therefore always with amplitude change, or attenuation constant δ.

And expression for the input mobility, for a force applied at $x = L_{1x}$ and $y = L_{1y}$ was given as

$$\mathrm{Y}(\omega,p) = i\omega \sum_{m=1}^{N_m} \frac{(w_m + w_{Nm})}{F_m}. \tag{5.68}$$

from which

$$\mathbf{w}_\mathrm{m} = \frac{\left(\mathbf{I} + \mathbf{\Lambda}_{\mathrm{Rm}_{22}}^{-1}\mathbf{\Gamma}_\mathrm{R}\mathbf{\Lambda}_{Rm_{11}}\right)\left(\mathbf{I} + \mathbf{\Lambda}_{\mathrm{Lm}_{11}}\mathbf{\Gamma}_\mathrm{L}\mathbf{\Lambda}_{\mathrm{Lm}_{22}}^{-1}\right)}{\mathbf{I} - \mathbf{\Lambda}_{\mathrm{Lm}_{11}}\mathbf{\Gamma}_\mathrm{L}\mathbf{\Lambda}_{\mathrm{Lm}_{22}}^{-1}\,\mathbf{\Lambda}_{\mathrm{Rm}_{22}}^{-1}\mathbf{\Gamma}_\mathrm{R}\mathbf{\Lambda}_{Rm_{22}}}\mathbf{q}_\mathbf{m}\,, \tag{5.69}$$

$\mathbf{w}_\mathrm{m} = [w_m \quad w_{Nm}]^T$, and $\mathbf{\Lambda}_{\mathrm{Lm}_{11}}$, $\mathbf{\Lambda}_{\mathrm{Lm}_{22}}$, $\mathbf{\Lambda}_{\mathbf{Rm}_{11}}$ and $\mathbf{\Lambda}_{\mathbf{Rm}_{22}}$ are the transmission matrices from chapter 3, depending on the phase changes from the left boundary to the excitation point $\theta_{\mathrm{Lm}}(p) = \theta_\mathrm{m}(0, L_{1x}, p)$, the phase change from the excitation point to the right boundary $\theta_{\mathrm{Rm}}(p) = \theta_\mathrm{m}(L_{1x}, L_x, p)$ and the total phase change from the left boundary to the right boundary $\theta_{\mathrm{Tm}}(p) = \theta_{\mathrm{Lm}}(p) + \theta_{\mathrm{Rm}}(p) = \theta_\mathrm{m}(0, L_x, p)$, given as

$$\theta_{Lm}(\omega,p) = \int_0^{L_{1x}} \sqrt{\omega\sqrt{\frac{\rho h}{D(x,p)}} - k_{ym}^2}\,\mathrm{d}x, \tag{5.70}$$

$$\theta_{LNm}(\omega,p) = \int_0^{L_{1x}} \sqrt{-\omega\sqrt{\frac{\rho h}{D(x,p)}} - k_{ym}^2}\,\mathrm{d}x, \tag{5.71}$$

$$\theta_{\mathrm{Rm}}(\omega,p) = \int_{L_1}^{L_x} \sqrt{\omega\sqrt{\frac{\rho h}{D(x,p)}} - k_{ym}^2}\,\mathrm{d}x. \tag{5.72}$$

$$\theta_{RNm}(\omega,p)=\int_{L_{1x}}^{L_x}\sqrt{-\omega\sqrt{\frac{\rho h}{D(x,p)}}-k_{ym}^2}\,\mathrm{d}x, \tag{5.73}$$

$$\theta_{Tm}(\omega,p)=\int_{0}^{L_x}\sqrt{\omega\sqrt{\frac{\rho h}{D(x,p)}}-k_{ym}^2}\,\mathrm{d}x, \tag{5.74}$$

$$\theta_{\mathrm{TNm}}(\omega,p)=\int_{0}^{L_x}\sqrt{-\omega\sqrt{\frac{\rho h}{D(x,p)}}-k_{ym}^2}\,\mathrm{d}x. \tag{5.75}$$

Using a first order approximation and the KL expansion from Eq (5.4), the integrals can be analytically evaluated, and then the phase changes are approximated by

$$\theta_{Lm}(\omega,p)\approx k_{1x0}\left[L_{1x}-\sigma\left(\frac{k_{p0}}{2k_{1x0}}\right)^2\Delta\theta_L(p)\right], \tag{5.76}$$

$$\theta_{LNm}(\omega,p)\approx\ k_{2x0}\left[L_{1x}+\sigma\left(\frac{k_{p0}}{2k_{2x0}}\right)^2\Delta\theta_L(p)\right], \tag{5.77}$$

$$\theta_{Rm}(\omega,p)\approx k_{1x0}\left[L_x-L_{1x}-\sigma\left(\frac{k_{p0}}{2k_{1x0}}\right)^2\Delta\theta_R(p)\right]. \tag{5.78}$$

$$\theta_{RNm}(\omega,p)\approx k_{2x0}\left[L_x-L_{1x}+\sigma\left(\frac{k_{p0}}{2k_{2x0}}\right)^2\Delta\theta_R(p)\right], \tag{5.79}$$

$$\theta_{Tm}(\omega,p)\approx k_{1x0}\left[L_x-\sigma\left(\frac{k_{p0}}{2k_{1x0}}\right)^2\Delta\theta_T(p)\right], \tag{5.80}$$

$$\theta_{TNm}(\omega,p)\approx k_{2x0}\left[L_x+\sigma\left(\frac{k_{p0}}{2k_{2x0}}\right)^2\Delta\theta_T(p)\right]. \tag{5.81}$$

where $\Delta\theta_L(p)$, $\Delta\theta_R(p)$ and $\Delta\theta_T(p)$ are given by Eq. (5.30), Eq. (5.31) and Eq. (5.32), respectively. These expressions are only valid when $k_{1x0}\neq 0$ or $k_{2x0}\neq 0$, which is due to the breaking down of the WKB assumption at the cut on frequencies.

The mean value and standard deviation can be calculated by using the properties of the random variable $\langle\xi_{1j}\rangle=\langle\xi_{1j}\rangle=0$, $\langle\xi_{1i}\xi_{1j}\rangle=\delta_{ij}$ and $\langle\xi_{1i}\xi_{2j}\rangle=0$ as

$$\langle \theta_{Lm}(\omega) \rangle = k_{1x0} L_{1x}, \tag{5.82}$$

$$\langle \theta_{LNm}(\omega) \rangle = k_{2x0} L_{1x}, \tag{5.83}$$

$$\langle \theta_{\mathrm{Rm}}(\omega) \rangle = k_{1x0}(L_x - L_1). \tag{5.84}$$

$$\langle \theta_{RNm}(\omega) \rangle = k_{2x0}(L_x - L_1), \tag{5.85}$$

$$\langle \theta_{Tm}(\omega) \rangle = k_{1x0} L_x, \tag{5.86}$$

$$\langle \theta_{\mathrm{TNm}}(\omega) \rangle = k_{2x0} L_x. \tag{5.87}$$

and

$$\sigma_{\theta_{Lm}}(\omega) = \frac{\sigma}{4}\frac{k_{p0}^2}{k_{1x0}}\left(\sum_{j=1}^{N_{kl}}\left[\left[\frac{\alpha_j}{w_{1j}}\left(\cos\left(\frac{w_{1j}L_x}{2}\right) - \cos\left(\frac{w_{1j}}{2}(L_x - 2L_{1x})\right)\right)\right]^2 + \left[\frac{\beta_j}{w_{2j}}\left[\sin\left(\frac{w_{2j}L_x}{2}\right) - \sin\left(\frac{w_{2j}}{2}(L_x - 2L_{1x})\right)\right]\right]^2\right]\right)^{\frac{1}{2}}, \tag{5.88}$$

$$\sigma_{\theta_{LNm}}(\omega) = \frac{\sigma}{4}\frac{k_{p0}^2}{k_{2x0}}\left(\sum_{j=1}^{N_{kl}}\left[\left[\frac{\alpha_j}{w_{1j}}\left(\cos\left(\frac{w_{1j}L_x}{2}\right) - \cos\left(\frac{w_{1j}}{2}(L_x - 2L_{1x})\right)\right)\right]^2 + \left[\frac{\beta_j}{w_{2j}}\left[\sin\left(\frac{w_{2j}L_x}{2}\right) - \sin\left(\frac{w_{2j}}{2}(L_x - 2L_{1x})\right)\right]\right]^2\right]\right)^{\frac{1}{2}}, \tag{5.89}$$

$$\sigma_{\theta_{Rm}}(\omega) = \frac{\sigma}{4}\frac{k_{p0}^2}{k_{1x0}}\left(\sum_{j=1}^{N_{kl}}\left[\left[\frac{\alpha_j}{w_{1j}}\left[\cos\left(\frac{w_{1j}}{2}(L_X - 2L_{1x})\right) - \cos\left(\frac{w_{1j}L_x}{2}\right)\right]\right]^2 + \left[\frac{\beta_j}{w_{2j}}\left[\sin\left(\frac{w_{2j}L_x}{2}\right) + \sin\left(\frac{w_{2j}}{2}(L_x - 2L_{1x})\right)\right]\right]^2\right]\right)^{\frac{1}{2}}, \tag{5.90}$$

$$\sigma_{\theta_{RNm}}(\omega) = \frac{\sigma}{4}\frac{k_{p0}^2}{k_{2x0}}\left(\sum_{j=1}^{N_{kl}}\left[\left[\frac{\alpha_j}{w_{1j}}\left[\cos\left(\frac{w_{1j}}{2}(L_x - 2L_{1x})\right) - \cos\left(\frac{w_{1j}L_x}{2}\right)\right]\right]^2 + \left[\frac{\beta_j}{w_{2j}}\left[\sin\left(\frac{w_{2j}L_X}{2}\right) + \sin\left(\frac{w_{2j}}{2}(L_x - 2L_{1x})\right)\right]\right]^2\right]\right)^{\frac{1}{2}}, \tag{5.91}$$

$$\sigma_{\theta_{Tm}}(\omega) = \frac{\sigma k_{p0}^2}{k_{1x0}}\left[\sum_{j=1}^{N_{kl}}\left[\frac{\beta_j}{w_{2j}}\sin\left(\frac{w_{2j}L_X}{2}\right)\right]^2\right]^{\frac{1}{2}}, \tag{5.92}$$

$$\sigma_{\theta_{TNm}}(\omega) = \frac{\sigma k_{p0}^2}{k_{2x0}}\left[\sum_{j=1}^{N_{kl}}\left[\frac{\beta_j}{w_{2j}}\sin\left(\frac{w_{2j}L_X}{2}\right)\right]^2\right]^{\frac{1}{2}}. \tag{5.93}$$

5.5 HFE sampling procedure

The formulation of the element matrices using the KL expansion, as presented in the previous chapters for the rod, beam and thin plate element, allows it to be rewritten as a sum of the nominal stiffness and mass matrices, calculated with the homogeneous properties, and a term accounting for the spatially varying properties

$$\mathrm{K_e} = \mathrm{K_{e0}} + \Delta\mathrm{K_e}, \tag{5.94}$$

$$\mathrm{M_e} = \mathrm{M_{e0}} + \Delta\mathrm{M_e}, \tag{5.95}$$

using the spatial functions of the KL expansion Eq. (5.4) in order to represent the random field. Thus, the element integration can be performed for each one of the terms individually

$$\Delta\mathrm{K_e} = \sum_{\mathrm{j}=1}^{\mathrm{N_{KL}}} \xi_{\mathrm{j}}\Delta\mathrm{K_{je}}, \tag{5.96}$$

$$\Delta\mathrm{M_e} = \sum_{\mathrm{j}=1}^{\mathrm{N_{KL}}} \xi_{\mathrm{j}}\Delta\mathrm{M_{je}}. \tag{5.97}$$

In this way, the element assembly process is performed only once and the random terms $\Delta\mathrm{K_e}$ and $\Delta\mathrm{M_e}$ can be sampled in a Monte Carlo scheme with no need to repeat the process. This approach particularly benefits from strongly correlated random field since

they need fewer terms in the KL expansion, and it is used in this chapter to calculate the statistics of the natural frequencies and input mobility. Other sampling approaches, like line-sampling [23, 81] can take advantage from this formulation and reduce the number of samples needed to accurately calculate the response statistics.

5.6 Numerical results

Numerical analysis was carried out aiming to compare the results obtained with WKB and the other methodologies, for the three types of waveguides derived in the previous chapters. Their properties and the cases compared are the same, but only the statistics of the response are of interest, i.e., the PDF of the natural frequencies as well as envelopes for the phase changes and input mobility in the frequency band. Monte Carlo simulations were performed using is $N_s = 5{,}000$ samples.

Five different cases of the Young's modulus random field were constructed, for all of the waveguide types, by changing the dispersion parameter σ, i.e. how likely the values are to deviate from the mean value, and the correlation length b, i.e. the rate of fluctuation of the spatial distribution: $\sigma = 0.1$, $b = 2L$; $\sigma = 0.2$, $b = 2L$; $\sigma = 0.1$, $b = 0.8L$; $\sigma = 0.1$, $b = 0.1L$; and $\sigma = 0.2$, $b = 0.05L$.

Moreover, the FE formulation, for the rod, beam and plate elements, used the mid-point discretisation the Young's modulus random field and MC sampling to calculate the PDF of the natural frequencies and envelopes of the input mobilities.

The rod, beam and plate strip properties were assumed to be a Young's modulus with mean value $E_0 = 70$ GPa and density $\rho = 2700$ kg/m^3, but with different geometries. Structural damping was included by making the Young's modulus a complex number $E_0 = E_0(1 + i\eta)$, with $\eta = 10^{-3}$. Those are the same baseline values used in the previous chapters. For the rod, the cross-sectional area A $= 0.1 \times 5$ cm^2, total length $L = 4$ m, with free-free boundary conditions, i.e. $\Gamma_L = \Gamma_R = 1$ and $\phi_L = \phi_R = 0$, for all the cases. The frequency band under analysis was chosen from 1 Hz to 6 kHz, discretised by 1Hz, such that at least the first nine axial modes could be observed in the forced response. Moreover, the excitation point was at $x = L_1 = 0.35L$. For the beam properties, the rectangular cross-section, with thickness 1 mm and width 3 mm, i.e. A $= 30$ mm^2, total length $L = 0.5$ m, , with free-free boundary conditions, i.e. reflection matrices at left and right $\mathbf{\Gamma_L} = \mathbf{\Gamma_R} =$

$\begin{bmatrix} -i & 1+i \\ 1-i & i \end{bmatrix}$. The frequency band under analysis was chosen from 1 Hz to 1.2 kHz, discretised by 1Hz, such that at least the first ten modes could be seen, and the excitation point was also at $x = L_1 = 0.35L$. For the plate strip, it was assumed thickness 0.01 m, width $L_y = 0.3$ m and length $L_x = 1$ m, with free-free boundary conditions, i.e. reflection matrices at left and right $\mathbf{\Gamma_L} = \mathbf{\Gamma_R} = \begin{bmatrix} -1 & 0 \\ 0 & -1 \end{bmatrix}$ and the excitation point at $x = L_{1x} = 0.65L$ and $y = L_{1y} = 0.375L_y$. The frequency band under analysis was chosen from 1 Hz to 1.5 kHz, discretised by 1Hz.

The PDF of the first, third, sixth and eighth natural frequencies for each one of the cases considered of random field variability are presented in Figure 5.3 to Figure 5.7 for the rod, Figure 5.8 to Figure 5.12 for the beam and, Figure 5.13 to Figure 5.17 for the plate strip, calculated using each of the presented approaches. All of the cases with big correlation length, i.e. $b = 2L$ and $b = 0.8L$, have shown a very good agreement for all of the approaches. For the cases with smaller correlation length, i.e. $b = 0.1L$ and $b = 0.05L$ it is possible to note that the wave solutions, i.e. the WKB and the piecewise constant, are in increased agreement with the FE and HFE for the higher natural frequencies, as expected from this kind of approximation. However, the closed form expression breaks down due to its first order approximation.

The mean value and the $\pm 3\sigma$ envelope of the phase change using a numerical evaluation as well as the first order approximation for the mean value and standard deviation are presented in Figure 5.18 to Figure 5.22, for the rod, and Figure 5.23 to Figure 5.27, for the beam. They are all normalized by the waveguide length L. In the plate strip case, the integral of one of the wavenumber solutions has a real and imaginary part i.e. $\theta_m = \varepsilon + i\delta$, due to the cut on wave modes. There is not only a phase change ε, but an amplitude change $e^{-\delta}$ where δ is known as the attenuation constant. The other wavenumber is always imaginary $\theta_{Nm} = i\delta$; these results are shown only in terms of attenuation constant δ. Results are shown from Figure 5.28 to Figure 5.37 normalized by L_x. For all of the cases, the approximations agree very well for the cases of higher correlation length, i.e. $b = 2L$ and $b = 0.8L$, as could be expected based on the results for the close form of the PDF of the natural frequency. The results show that the phase change variability increases not only for increasing σ, but also for increasing correlation length. This is also observed on the PDF of the natural frequency. The first order approximation of the phase change and attenuation

constant of the plate strip breaks down at frequencies close to the cut on frequency, as expected from Eq. (5.88) to (5.93) that tend to infinity at those frequencies. Only results for the phase and amplitude change from the left to the right boundary of the waveguide are shown, because the phase change from the left boundary to the excitation point and from the excitation point to the right boundary should give similar results.

The 95% percentile and mean value of the input mobility calculated using the presented approaches are shown in Figure 5.38 to Figure 5.42, for the rod, in Figure 5.43 to Figure 5.47, for the beam and Figure 5.48 to Figure 5.52 for the plate strip. For the plate strip case, the WKB cut on transition can be clearly seen, when compared with other methods, severely affecting the input mobility response, as expected. However, again, for all of the cases the agreement among the approaches is the same as seen in the PDF of the natural frequencies, i.e. very good agreement for the cases of larger correlation length. There is increasingly better agreement of the wave solutions, i.e. the WKB and the piecewise constant, with the FE and HFE the higher the frequency, for the cases of smaller correlation length. It is also observed that the variability increases not only for increasing σ, but also for increasing correlation length.

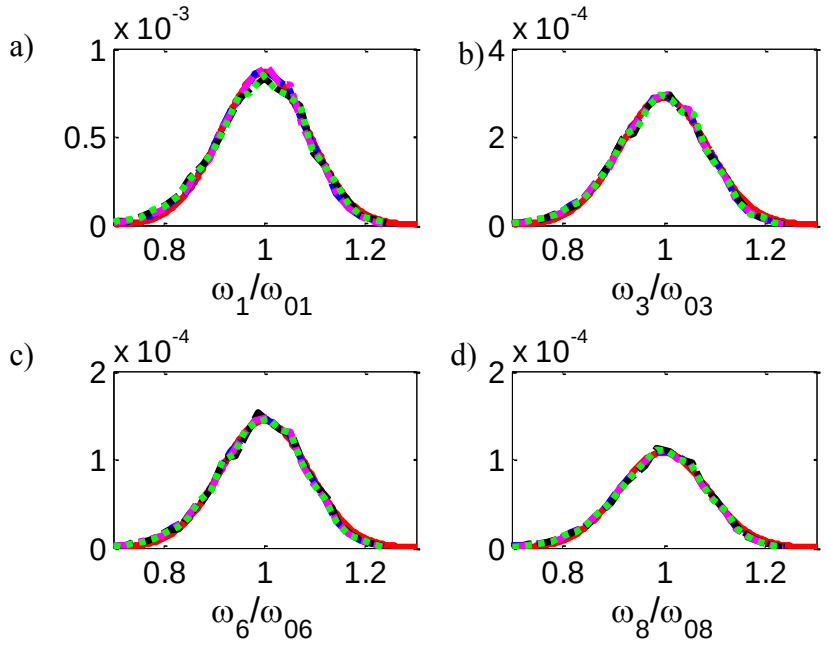

Figure 5.3. Normalized PDF of the rod (a) first, (b) third, (c) sixth and (d) eighth natural frequencies using the closed form expression (full red), the WKB (blue dashed), the piecewise constant (magenta dash-dot), the FE (black dashed) and the HFE (green dotted) for $\sigma = 0.1$, $b = 2L$.

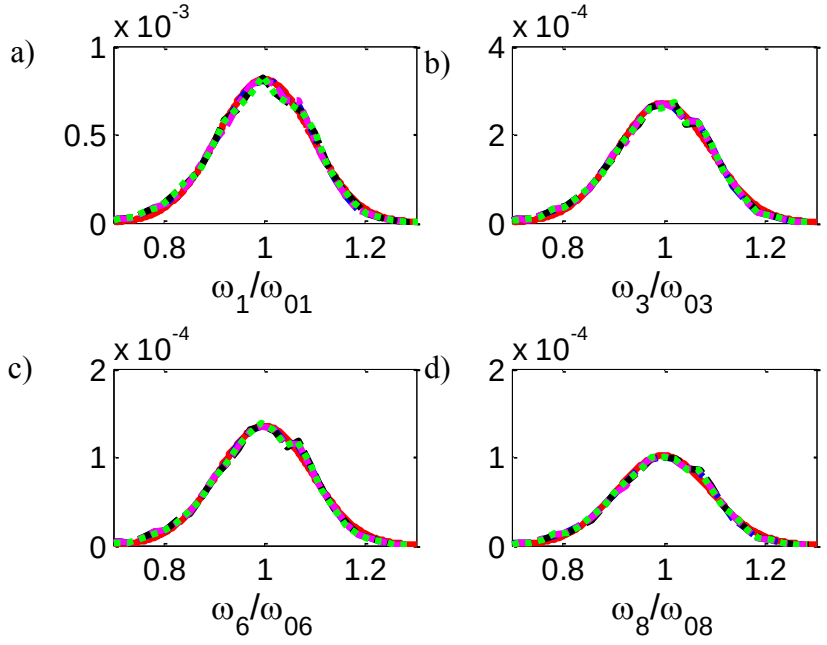

Figure 5.4. Normalized PDF of the rod (a) first, (b) third, (c) sixth and (d) eighth natural frequencies using the closed form expression (full red), the WKB (blue dashed), the piecewise constant (magenta dash-dot), the FE (black dashed) and the HFE (green dotted) for $\sigma = 0.2$, $b = 2L$.

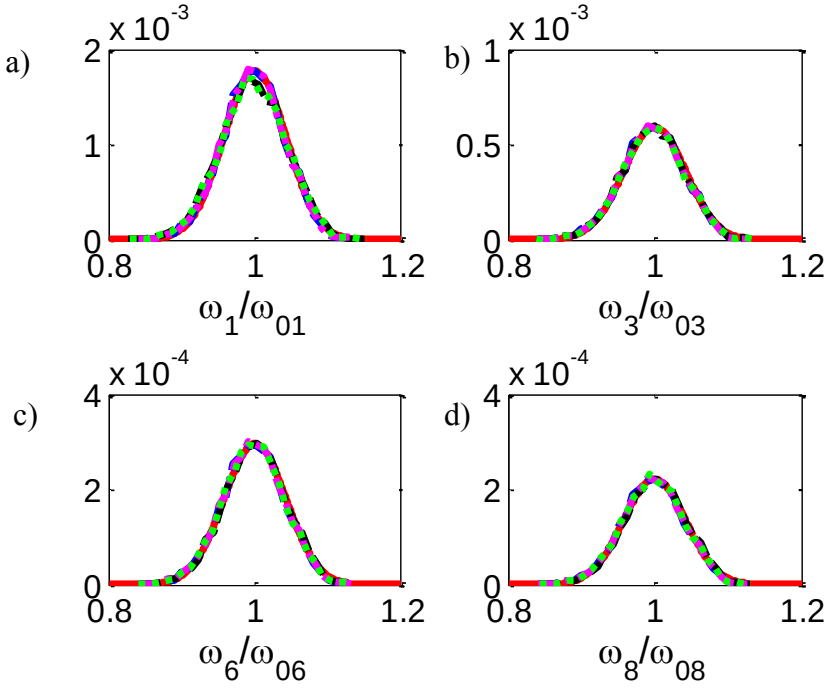

Figure 5.5. Normalized PDF of the rod (a) first, (b) third, (c) sixth and (d) eighth natural frequencies using the closed form expression (full red), the WKB (blue dashed), the piecewise constant (magenta dash-dot), the FE (black dashed) and the HFE (green dotted) for $\sigma = 0.1$, $b = 0.8L$.

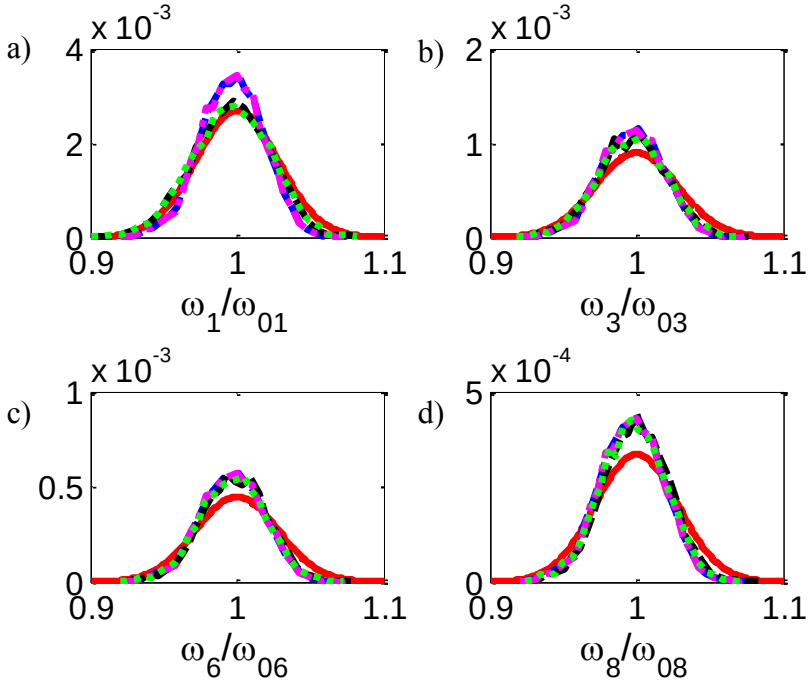

Figure 5.6. Normalized PDF of the rod (a) first, (b) third, (c) sixth and (d) eighth natural frequencies using the closed form expression (full red), the WKB (blue dashed), the piecewise constant (magenta dash-dot), the FE (black dashed) and the HFE (green dotted) for $\sigma = 0.1$, $b = 0.1L$.

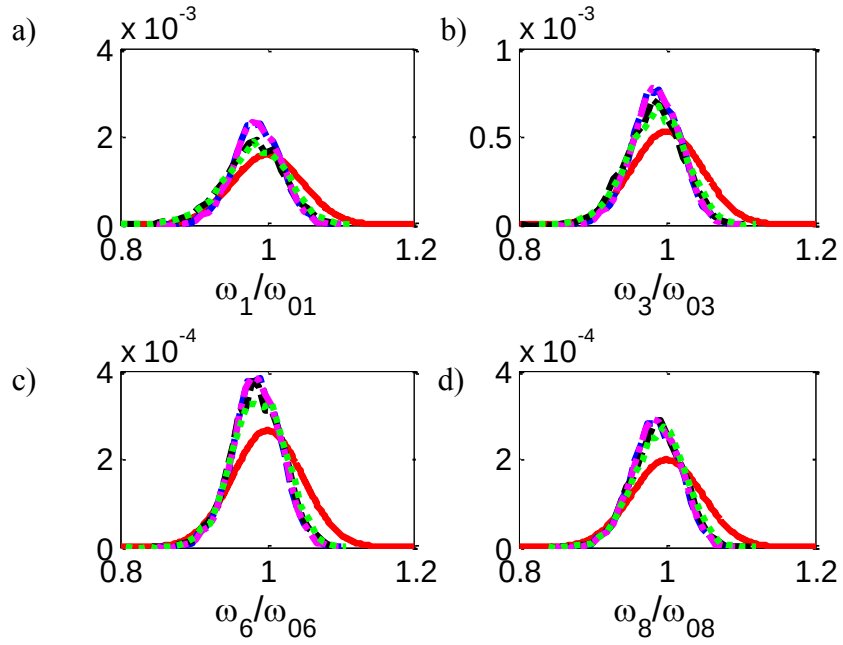

Figure 5.7. Normalized PDF of the rod (a) first, (b) third, (c) sixth and (d) eighth natural frequencies using the closed form expression (full red), the WKB (blue dashed), the piecewise constant (magenta dash-dot), the FE (black dashed) and the HFE (green dotted) for $\sigma = 0.2$, $b = 0.05L$.

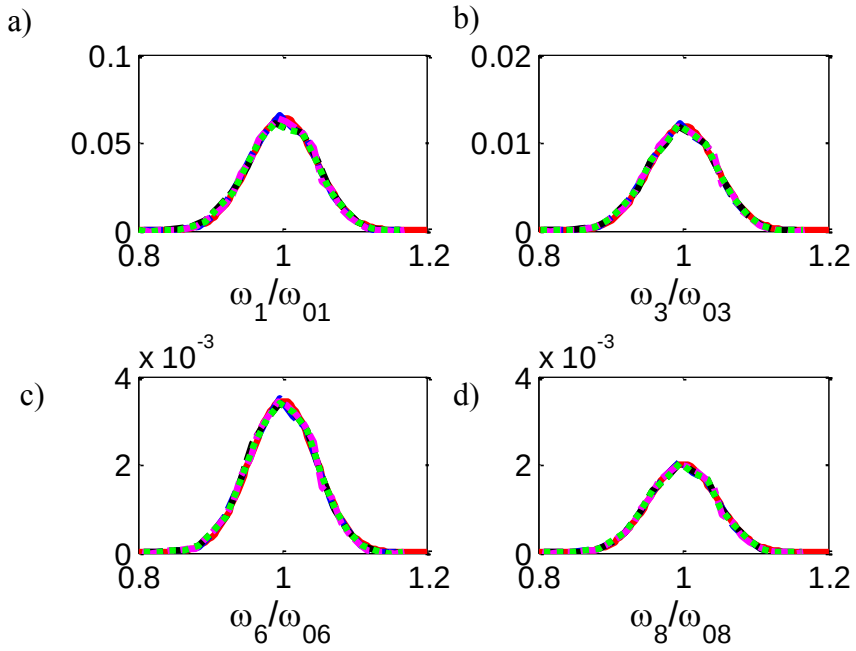

Figure 5.8. Normalized PDF of the beam (a) first, (b) third, (c) sixth and (d) eighth natural frequencies using the closed form expression (full red), the WKB (blue dashed), the piecewise constant (magenta dash-dot), the FE (black dashed) and the HFE (green dotted) for $\sigma = 0.1$, $b = 2L$.

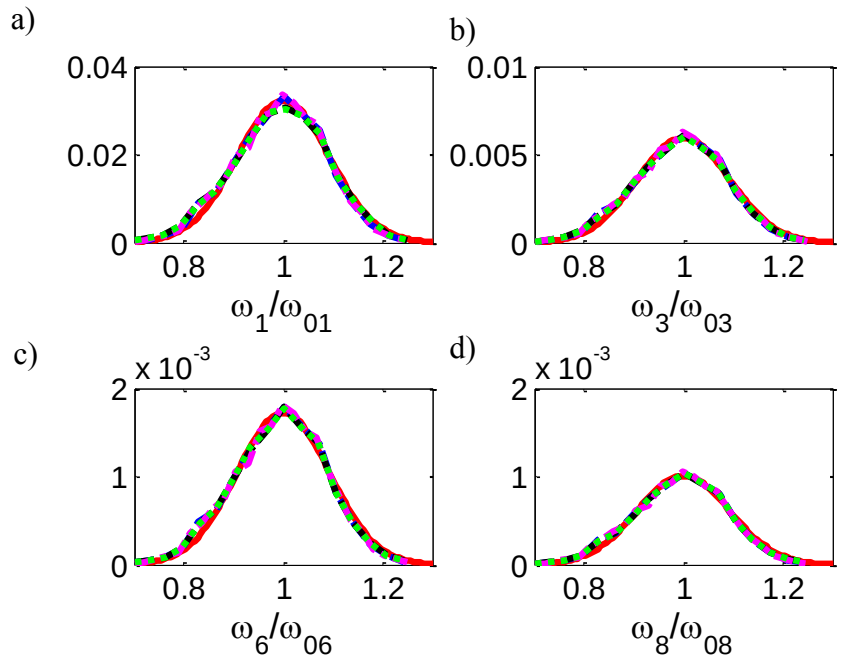

Figure 5.9. Normalized PDF of the beam (a) first, (b) third, (c) sixth and (d) eighth natural frequencies using the closed form expression (full red), the WKB (blue dashed), the piecewise constant (magenta dash-dot), the FE (black dashed) and the HFE (green dotted) for $\sigma = 0.2$, $b = 2L$.

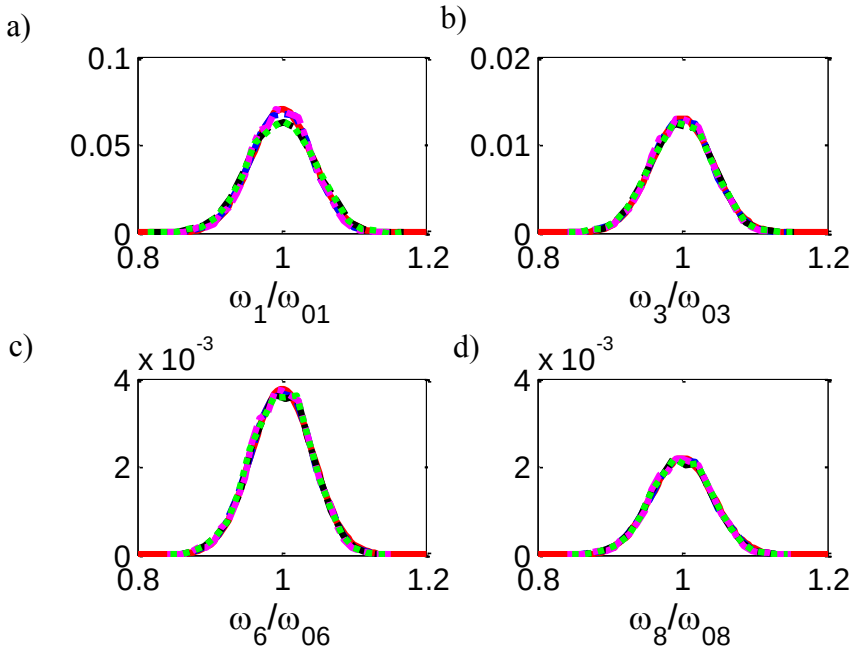

Figure 5.10. Normalized PDF of the beam (a) first, (b) third, (c) sixth and (d) eighth natural frequencies using the closed form expression (full red), the WKB (blue dashed), the piecewise constant (magenta dash-dot), the FE (black dashed) and the HFE (green dotted) for $\sigma = 0.1$, $b = 0.8L$.

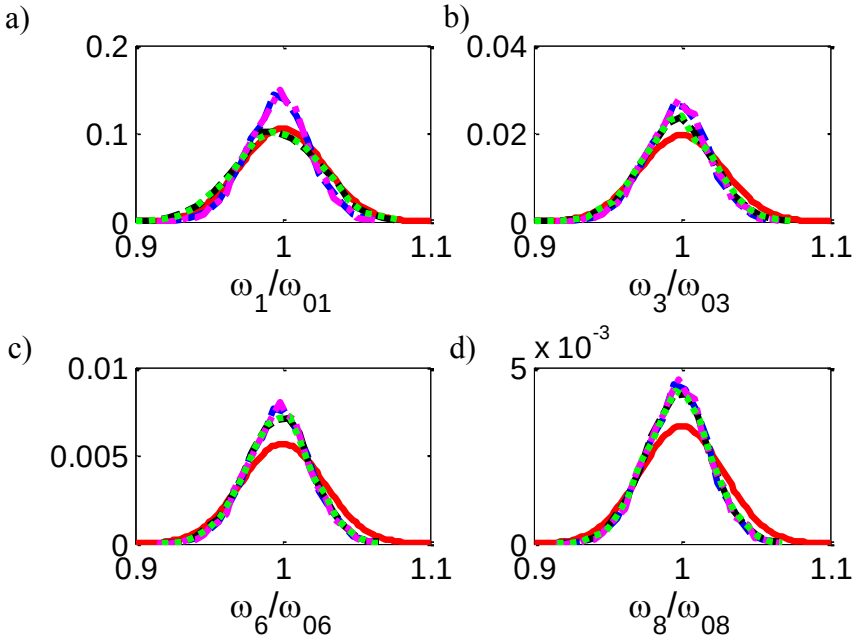

Figure 5.11. Normalized PDF of the beam (a) first, (b) third, (c) sixth and (d) eighth natural frequencies using the closed form expression (full red), the WKB (blue dashed), the piecewise constant (magenta dash-dot), the FE (black dashed) and the HFE (green dotted) for $\sigma = 0.1$, $b = 0.1L$.

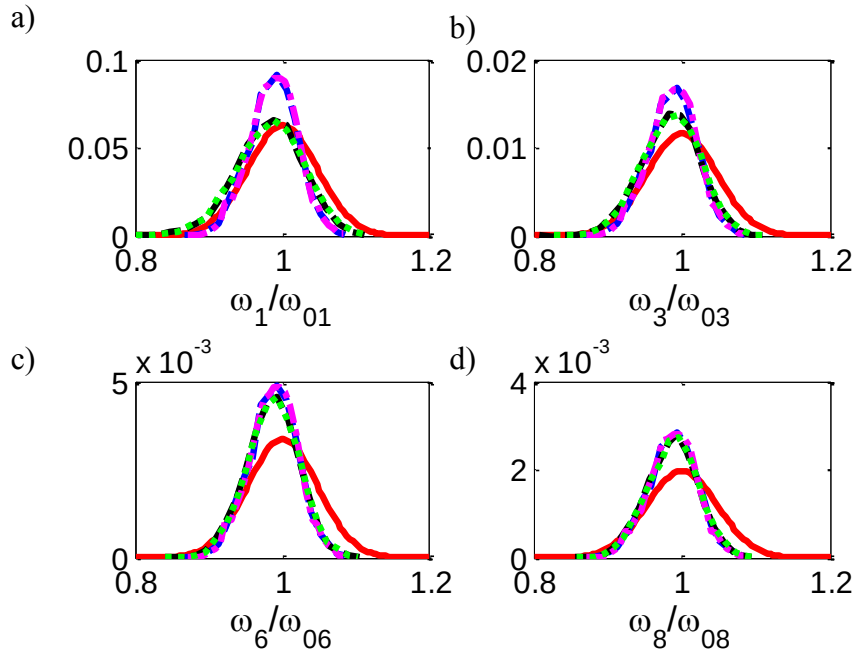

Figure 5.12. Normalized PDF of the beam (a) first, (b) third, (c) sixth and (d) eighth natural frequencies using the closed form expression (full red), the WKB (blue dashed), the piecewise constant (magenta dash-dot), the FE (black dashed) and the HFE (green dotted) for $\sigma = 0.2$, $b = 0.05L$.

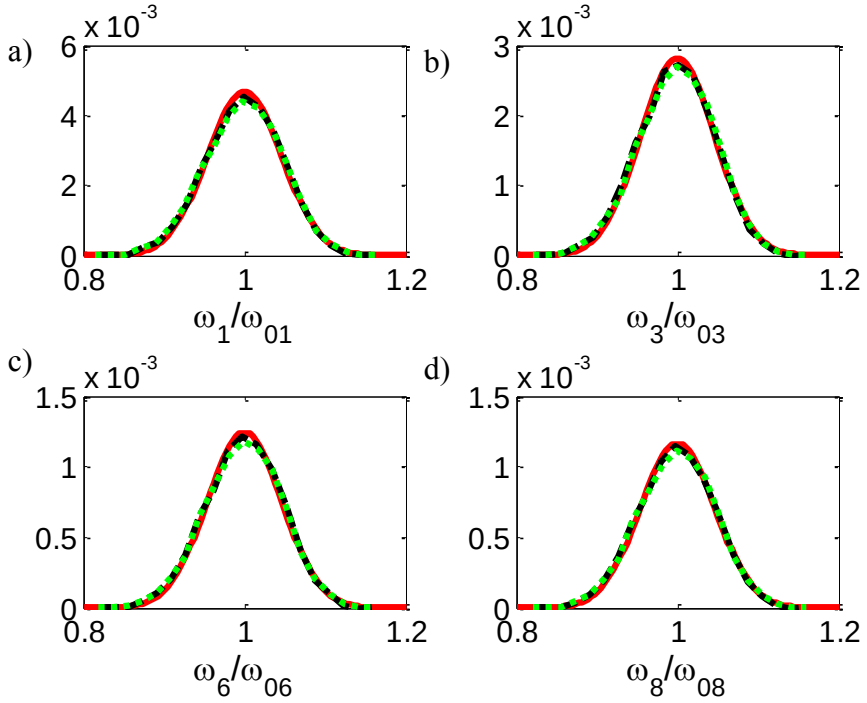

Figure 5.13. Normalized PDF of the plate strip (a) first, (b) third, (c) sixth and (d) eighth natural frequencies using the closed form expression (full red, the FE (black dashed) and the HFE (green dotted) for $\sigma = 0.1$, $b = 2L$.

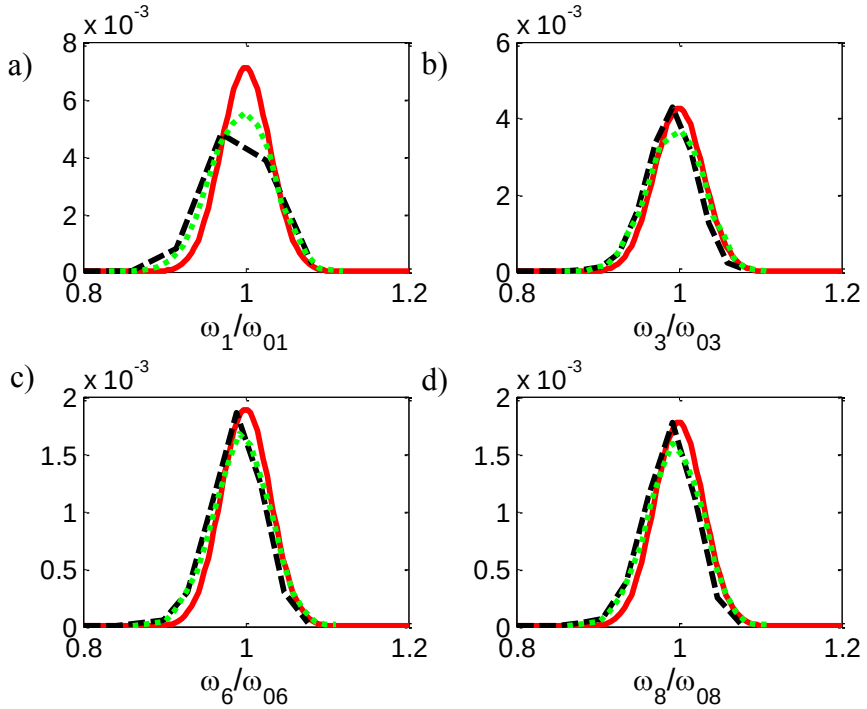

Figure 5.14. Normalized PDF of the plate strip (a) first, (b) third, (c) sixth and (d) eighth natural frequencies using the closed form expression (full red), the FE (black dashed) and the HFE (green dotted) for $\sigma = 0.2$, $b = 2L$.

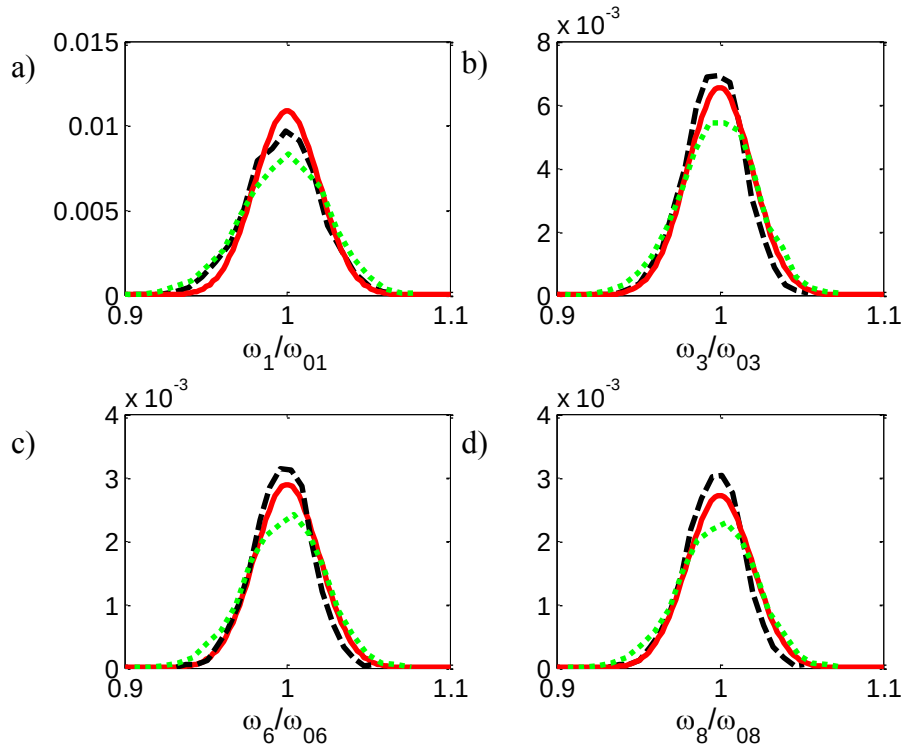

Figure 5.15. Normalized PDF of the plate strip (a) first, (b) third, (c) sixth and (d) eighth natural frequencies using the closed form expression (full red), the WKB (blue dashed), the FE (black dashed) and the HFE (green dotted) for $\sigma = 0.1$, $b = 0.8L$.

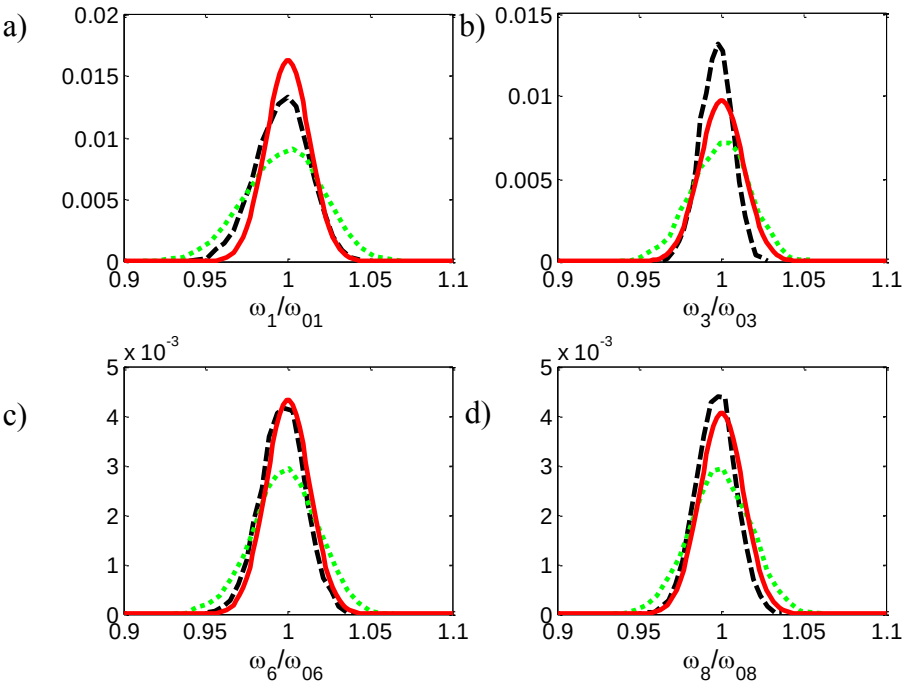

Figure 5.16. Normalized PDF of the plate strip (a) first, (b) third, (c) sixth and (d) eighth natural frequencies using the closed form expression (full red), the WKB (blue dashed), the FE (black dashed) and the HFE (green dotted) for $\sigma = 0.1$, $b = 0.1L$.

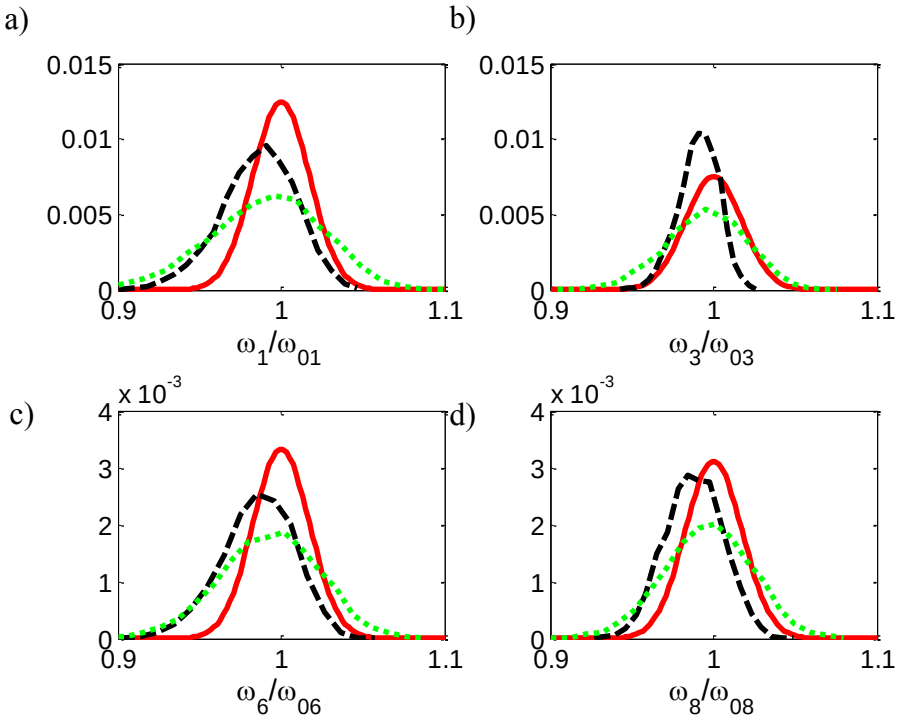

Figure 5.17. Normalized PDF of the plate strip (a) first, (b) third, (c) sixth and (d) eighth natural frequencies using the closed form expression (full red), the WKB (blue dashed), the FE (black dashed) and the HFE (green dotted) for $\sigma = 0.2$, $b = 0.05L$.

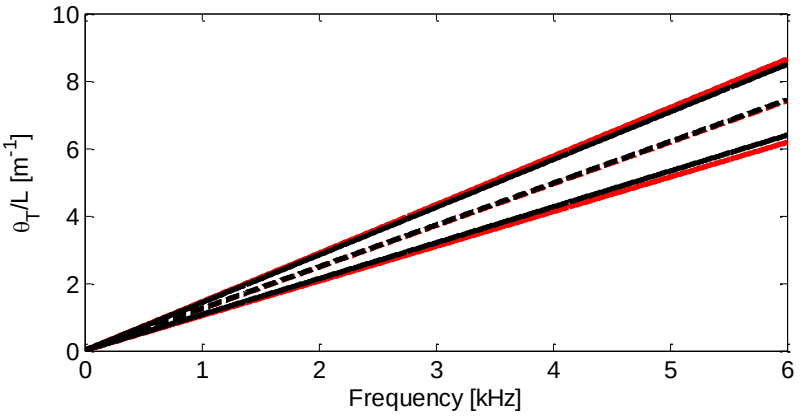

Figure 5.18. Mean value (dashed line) and mean value $\pm 3\sigma$ (full line) of the normalized phase change from the left to the right boundary, for the longitudinal waves and $\sigma = 0.1$, $b = 2L$, using numerical evaluation (black) and first order approximation (red).

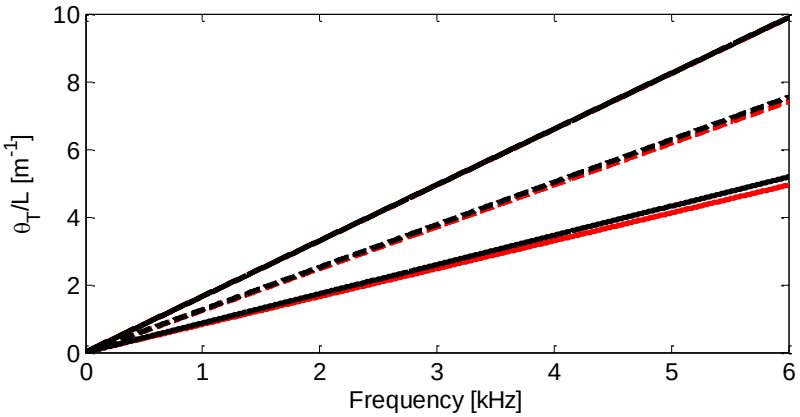

Figure 5.19. Mean value (dashed line) and mean value $\pm 3\sigma$ (full line) of the normalized phase change from the left to the right boundary, for the longitudinal waves and $\sigma = 0.2$, $b = 2L$, using numerical evaluation (black) and first order approximation (red).

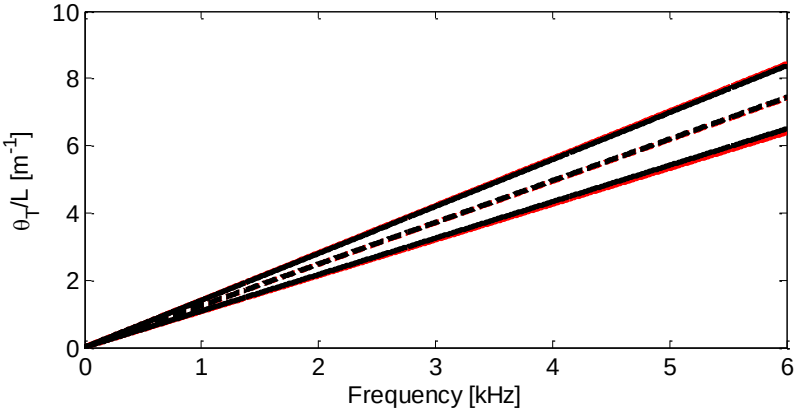

Figure 5.20. Mean value (dashed line) and mean value $\pm 3\sigma$ (full line) of the normalized phase change from the left to the right boundary, for the longitudinal waves and $\sigma = 0.1$, $b = 0.8L$, using numerical evaluation (black) and first order approximation (red).

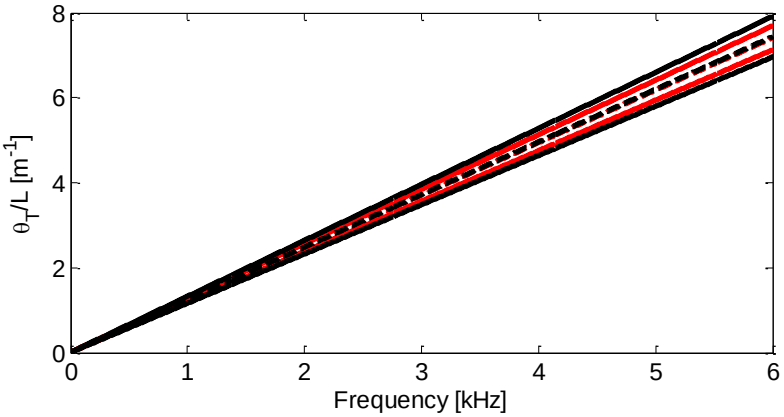

Figure 5.21. Mean value (dashed line) and mean value $\pm 3\sigma$ (full line) of the normalized phase change from the left to the right boundary, for the longitudinal waves and $\sigma = 0.1$, $b = 0.1L$, using numerical evaluation (black) and first order approximation (red).

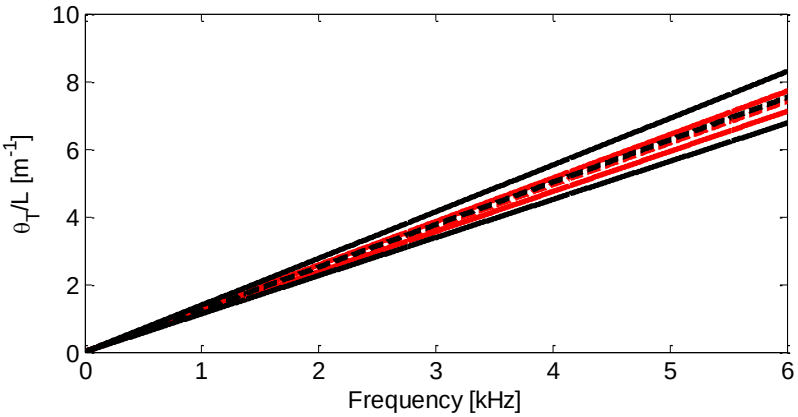

Figure 5.22. Mean value (dashed line) and mean value $\pm 3\sigma$ (full line) of the normalized phase change from the left to the right boundary, for the longitudinal waves and $\sigma = 0.2$, $b = 0.05L$, using numerical evaluation (black) and first order approximation (red).

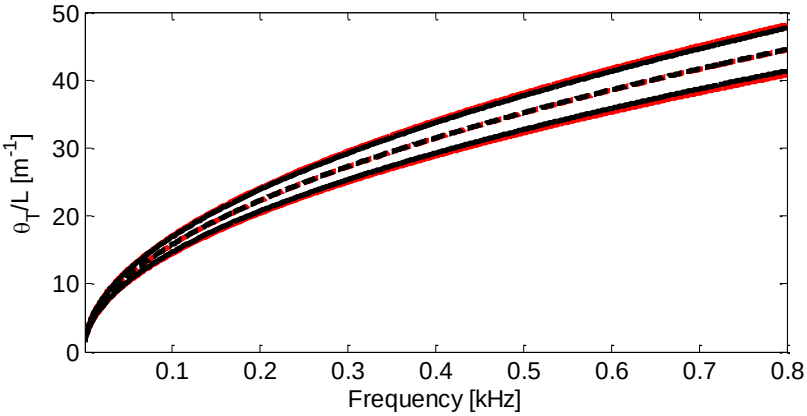

Figure 5.23. Mean value (dashed line) and mean value $\pm 3\sigma$ (full line) of the normalized phase change from the left to the right boundary, for the flexural waves and $\sigma = 0.1$, $b = 2L$, using numerical evaluation (black) and first order approximation (red)

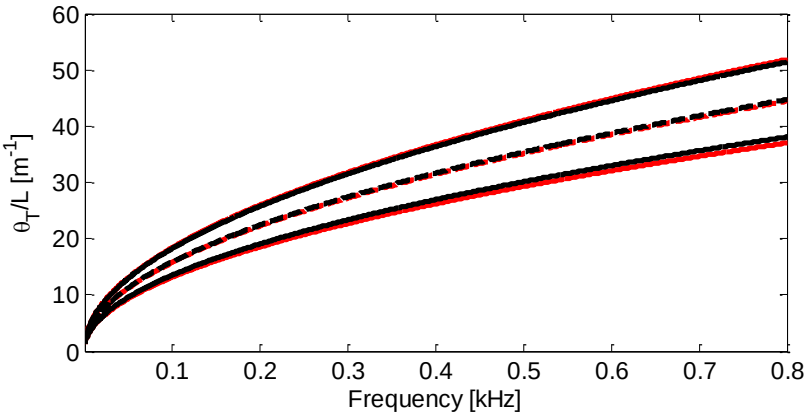

Figure 5.24. Mean value (dashed line) and mean value $\pm 3\sigma$ (full line) of the normalized phase change from the left to the right boundary, for the flexural waves and $\sigma = 0.2$, $b = 2L$, using numerical evaluation (black) and first order approximation (red).

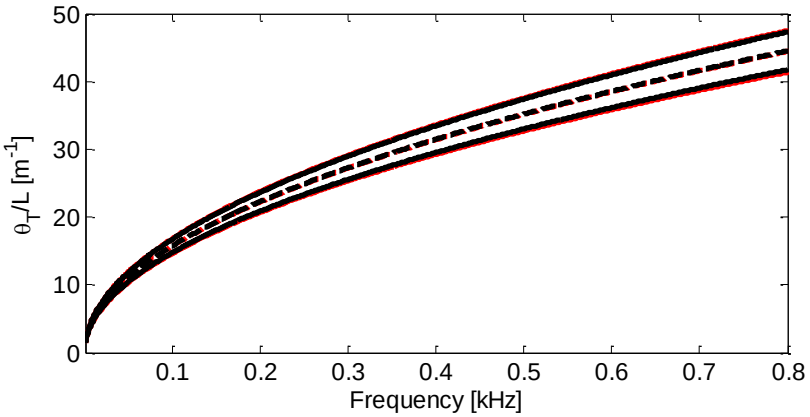

Figure 5.25. Mean value (dashed line) and mean value $\pm 3\sigma$ (full line) of the normalized phase change from the left to the right boundary, for the flexural waves and $\sigma = 0.1$, $b = 0.8L$, using numerical evaluation (black) and first order approximation (red).

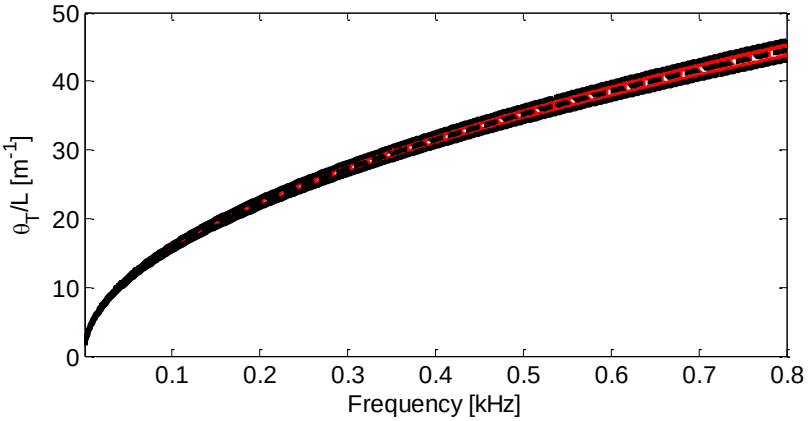

Figure 5.26. Mean value (dashed line) and mean value $\pm 3\sigma$ (full line) of the normalized phase change from the left to the right boundary, for the flexural waves and $\sigma = 0.1$, $b = 0.1L$, using numerical evaluation (black) and first order approximation (red).

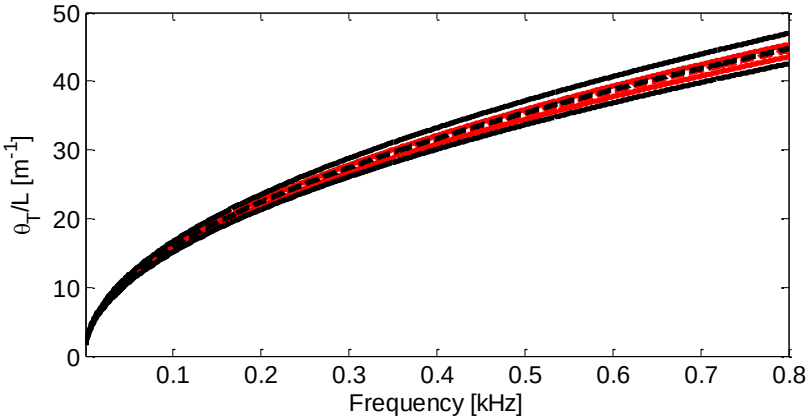

Figure 5.27. Mean value (dashed line) and mean value $\pm 3\sigma$ (full line) of the normalized phase change from the left to the right boundary, for the flexural waves and $\sigma = 0.2$, $b = 0.05L$,, using numerical evaluation (black) and first order approximation (red).

a)

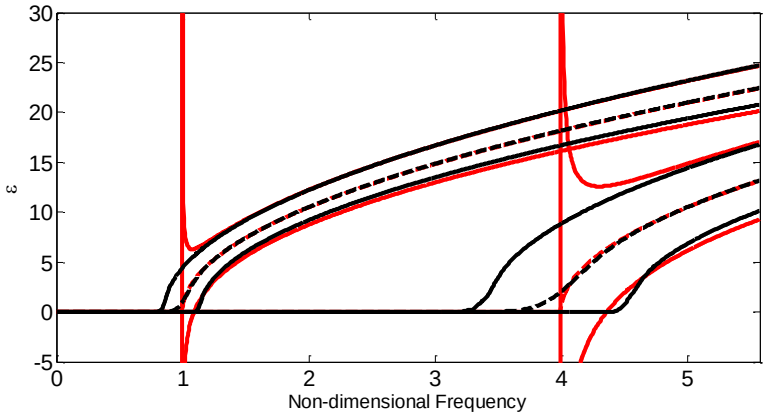

b)

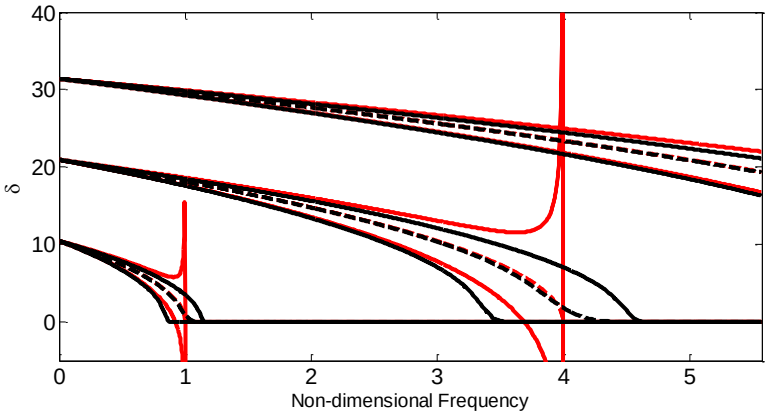

Figure 5.28. Mean value (dashed line) and 3σ envelope (full line) of a) the phase change ε and b) the attenuation constant δ for the 3 lowest propagating wave modes in the plate strip using and $\sigma = 0.1,\ b = 2L$, using numerical evaluation (black) and first order approximation (red). Frequency axis is normalized by the first cut-on frequency 269.3 Hz.

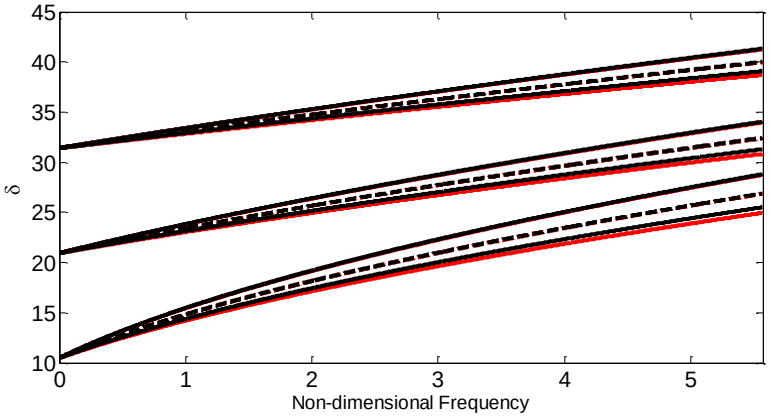

Figure 5.29. Mean value (dashed line) and 3σ envelope (full line) of the attenuation constant $\delta/\mathrm{L_x}$ for the 3 lowest evanescent wave modes in the plate strip using and $\sigma = 0.1,\ b = 2L$, using numerical evaluation (black) and first order approximation (red). Frequency axis is normalized by the first cut-on frequency 269.3 Hz.

a)

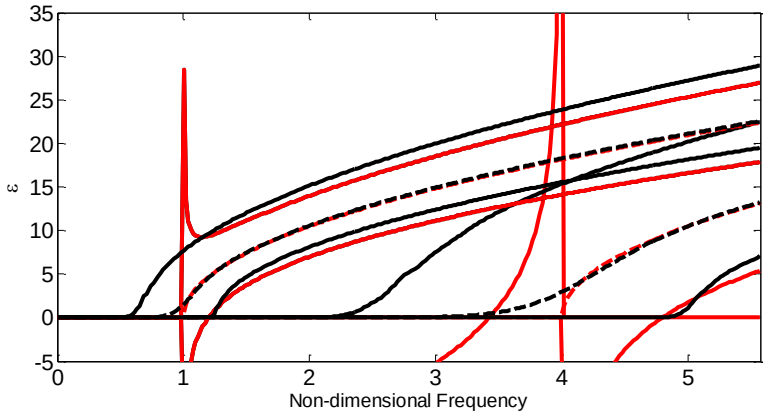

b)

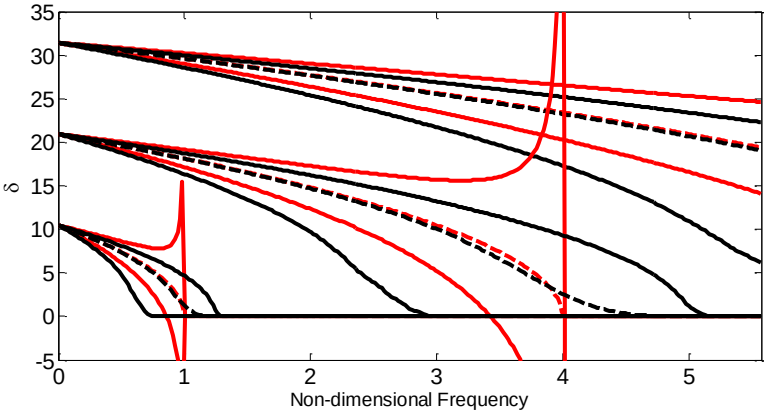

Figure 5.30. Mean value (dashed line) and 3σ envelope (full line) of a) the phase change ε and b) the attenuation constant δ for the 2 lowest propagating wave modes in the plate strip using and $\sigma = 0.2,\ b = 2L$, using numerical evaluation (black) and first order approximation (red). Frequency axis is normalized by the first cut-on frequency 269.3 Hz.

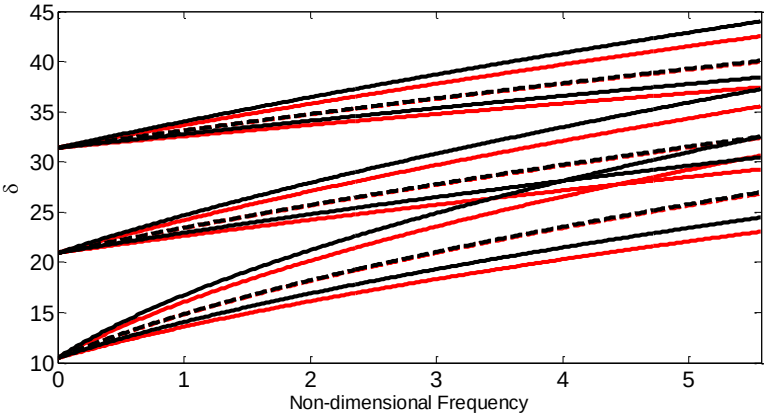

Figure 5.31. Mean value (dashed line) and 3σ envelope (full line) of the attenuation constant δ for the 3 lowest evanescent wave modes in the plate strip using and $\sigma = 0.2,\ b = 2L$, using numerical evaluation (black) and first order approximation (red). Frequency axis is normalized by the first cut-on frequency 269.3 Hz.

a)

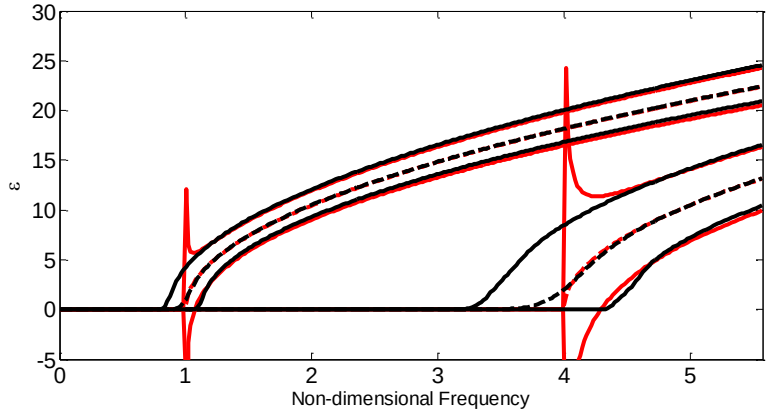

b)

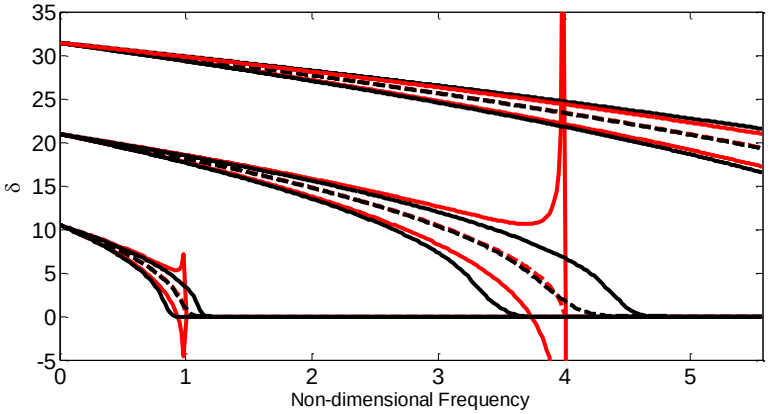

Figure 5.32. Mean value (dashed line) and 3σ envelope (full line) of a) the phase change ε and b) the attenuation constant δ for the 3 lowest propagating wave modes in the plate strip using and $\sigma = 0.1,\ b = 0.8L$, using numerical evaluation (black) and first order approximation (red). Frequency axis is normalized by the first cut-on frequency 269.3 Hz.

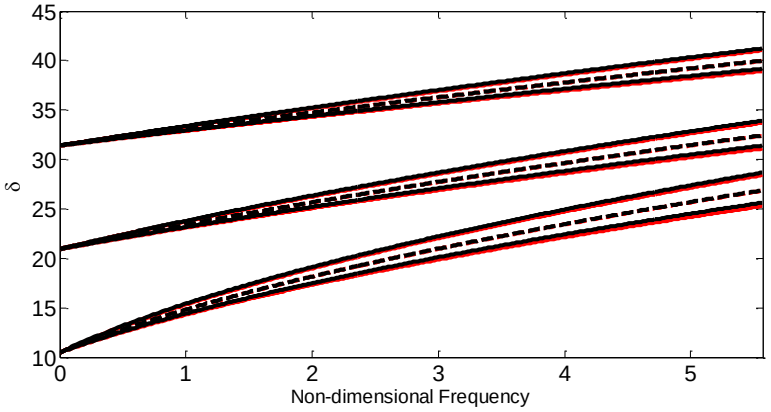

Figure 5.33. Mean value (dashed line) and 3σ envelope (full line) of the attenuation constant δ for the 3 lowest evanescent wave modes in the plate strip using and $\sigma = 0.1,\ b = 0.8L$, using numerical evaluation (black) and first order approximation (red). Frequency axis is normalized by the first cut-on frequency 269.3 Hz.

a)

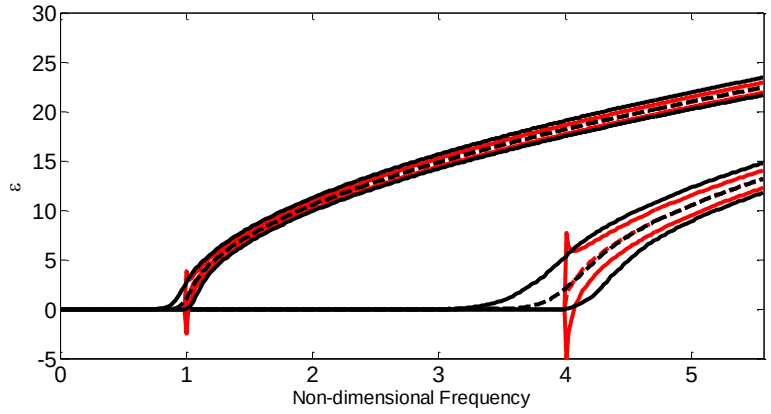

b)

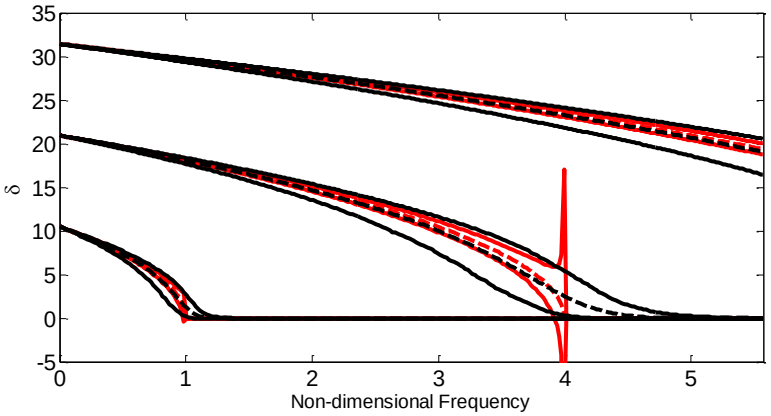

Figure 5.34. Mean value (dashed line) and 3σ envelope (full line) of a) the phase change ε and b) the attenuation constant δ for the 3 lowest propagating wave modes in the plate strip using and $\sigma = 0.1,\ b = 0.1L$, using numerical evaluation (black) and first order approximation (red). Frequency axis is normalized by the first cut-on frequency 269.3 Hz.

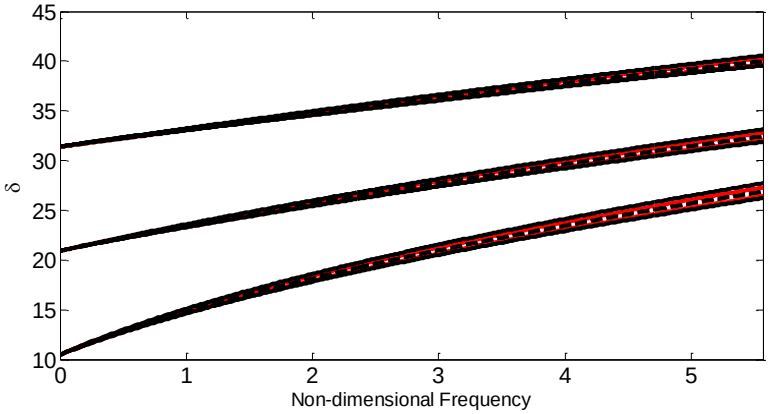

Figure 5.35. Mean value (dashed line) and 3σ envelope (full line) of the attenuation constant δ for the 3 lowest evanescent wave modes in the plate strip using and $\sigma = 0.1,\ b = 0.1L$, using numerical evaluation (black) and first order approximation (red). Frequency axis is normalized by the first cut-on frequency 269.3 Hz.

a)

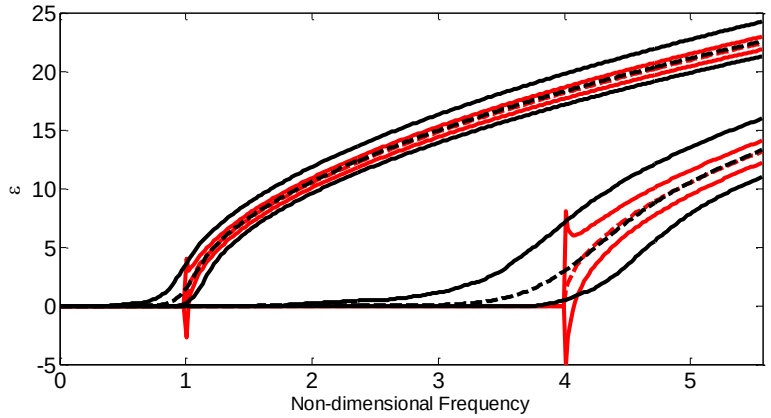

b)

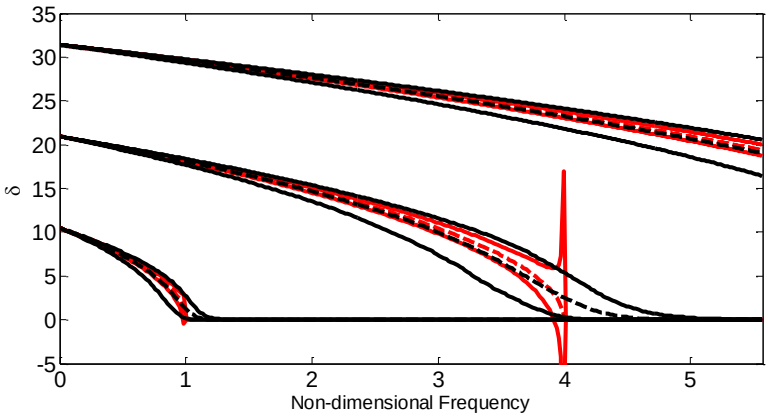

Figure 5.36. Mean value (dashed line) and 3σ envelope (full line) of a) the phase change ε and b) the attenuation constant δ for the 3 lowest propagating wave modes in the plate strip using and $\sigma = 0.2,\ b = 0.005L$, using numerical evaluation (black) and first order approximation (red). Frequency axis is normalized by the first cut-on frequency 269.3 Hz.

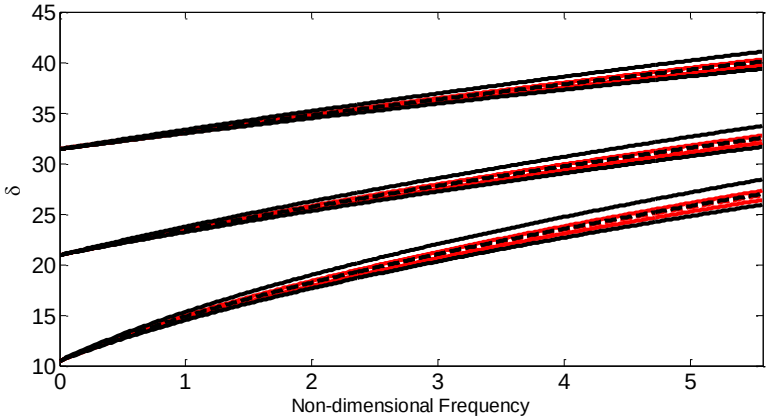

Figure 5.37. Mean value (dashed line) and 3σ envelope (full line) of the normalized attenuation constant δ for the 3 lowest evanescent wave modes in the plate strip using and $\sigma = 0.2,\ b = 0.05L$, using numerical evaluation (black) and first order approximation (red). Frequency axis is normalized by the first cut-on frequency 269.3 Hz.

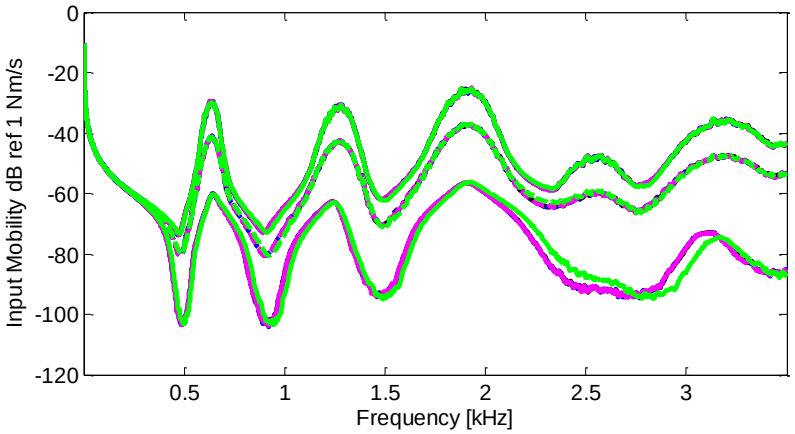

Figure 5.38. 95 % percentile and mean value of the input mobility of the rod using the WKB approach (blue dashed), the piecewise constant (magenta dash-dot), the FE (black dashed) and the HFE (green dotted) for $\sigma = 0.1$, $b = 2L$.

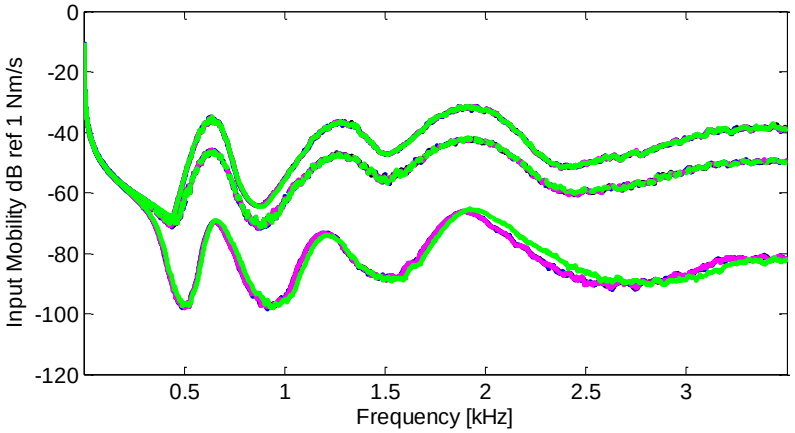

Figure 5.39. 95 % percentile and mean value of the input mobility of the rod using the WKB approach (blue dashed), the piecewise constant (magenta dash-dot), the FE (black dashed) and the HFE (green dotted) for $\sigma = 0.2$, $b = 2L$.

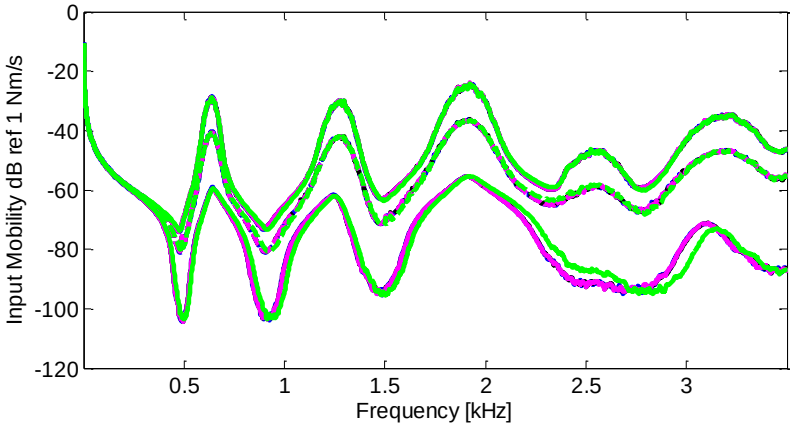

Figure 5.40. 95 % percentile and mean value of the input mobility of the rod using the WKB approach (blue dashed), the piecewise constant (magenta dash-dot), the FE (black dashed) and the HFE (green dotted) for $\sigma = 0.1$, $b = 0.8L$.

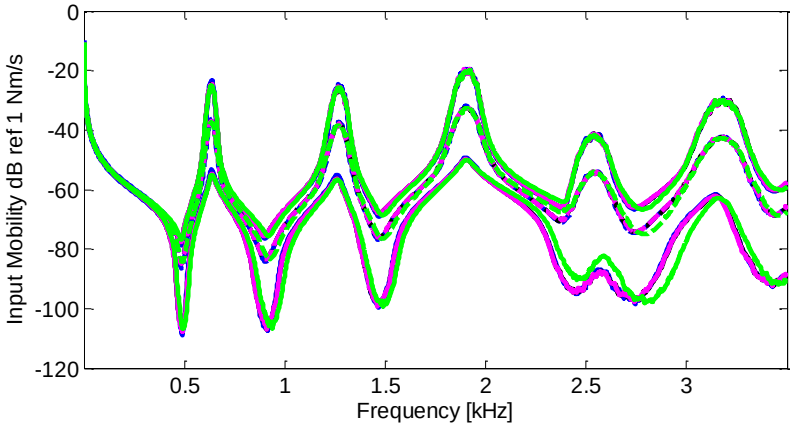

Figure 5.41. 95 % percentile and mean value of the input mobility of the rod using the WKB approach (blue dashed), the piecewise constant (magenta dash-dot), the FE (black dashed) and the HFE (green dotted) for $\sigma = 0.1$, $b = 0.1L$.

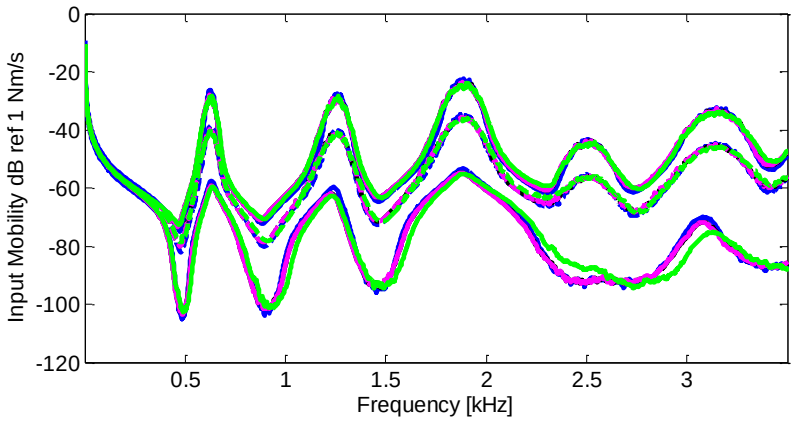

Figure 5.42. 95 % percentile and mean value of the input mobility of the rod using the WKB approach (blue dashed), the piecewise constant (magenta dash-dot), the FE (black dashed) and the HFE (green dotted) for $\sigma = 0.2$, $b = 0.05L$.

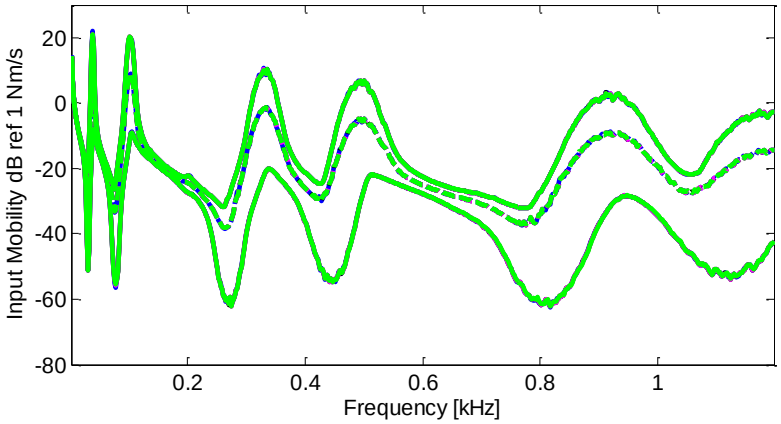

Figure 5.43. 95 % percentile and mean value of the input mobility of the beam using the WKB approach (blue dashed), the piecewise constant (magenta dash-dot), the FE (black dashed) and the HFE (green dotted) for $\sigma = 0.1$, $b = 2L$.

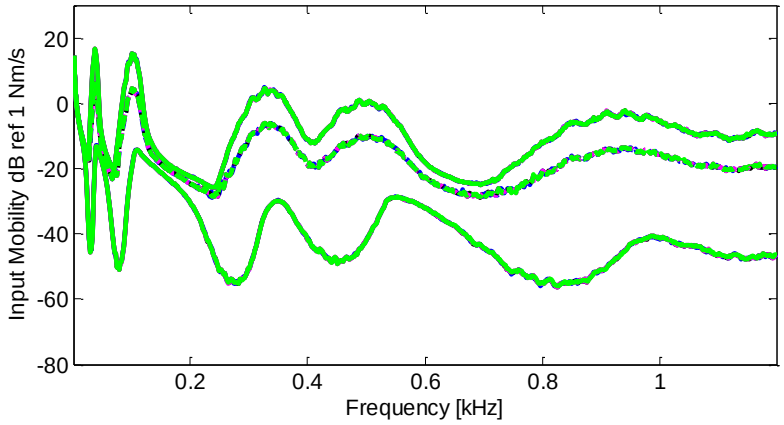

Figure 5.44. 95 % percentile and mean value of the input mobility of the beam using the WKB approach (blue dashed), the piecewise constant (magenta dash-dot), the FE (black dashed) and the HFE (green dotted) for $\sigma = 0.2$, $b = 2L$.

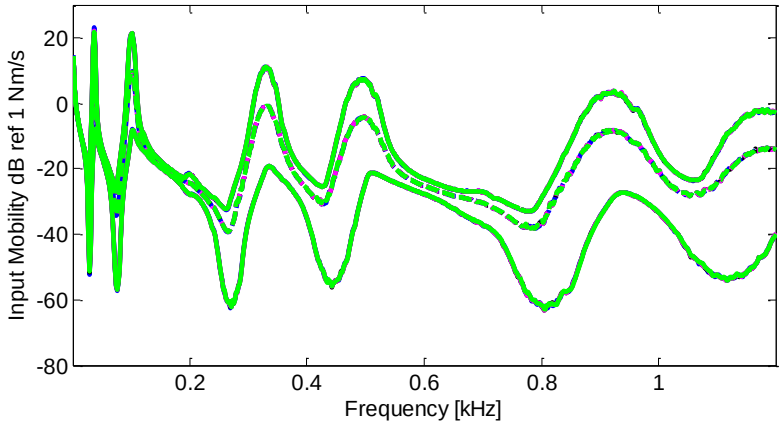

Figure 5.45. 95 % percentile and mean value of the input mobility of the beam using the WKB approach (blue dashed), the piecewise constant (magenta dash-dot), the FE (black dashed) and the HFE (green dotted) for $\sigma = 0.1$, $b = 0.8L$.

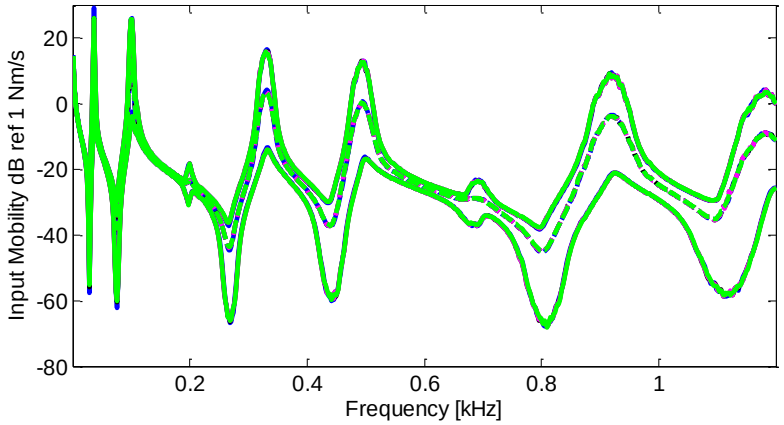

Figure 5.46. 95 % percentile and mean value of the input mobility of the beam using the WKB approach (blue dashed), the piecewise constant (magenta dash-dot), the FE (black dashed) and the HFE (green dotted) for $\sigma = 0.1$, $b = 0.1L$.

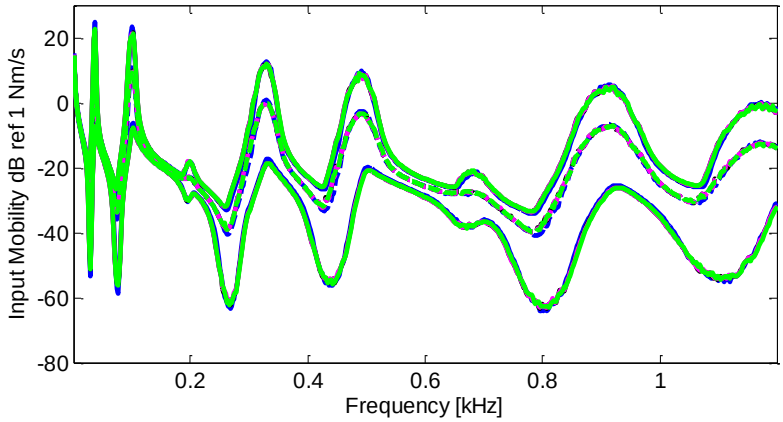

Figure 5.47. 95 % percentile and mean value of the input mobility of the beam using the WKB approach (blue dashed), the piecewise constant (magenta dash-dot), the FE (black dashed) and the HFE (green dotted) for $\sigma = 0.2$, $b = 0.05L$.

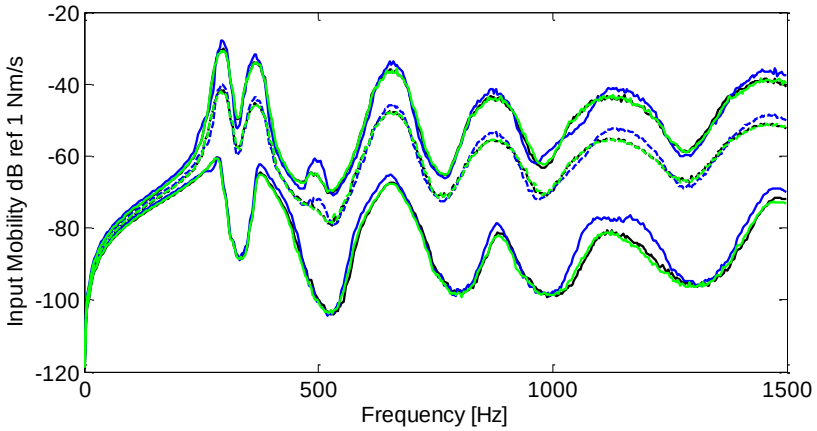

Figure 5.48. 95 % percentile and mean value of the input mobility of the plate strip using the WKB approach (blue dashed), the FE (black dashed) and the (green dotted) for $\sigma = 0.1$, $b = 2L$.

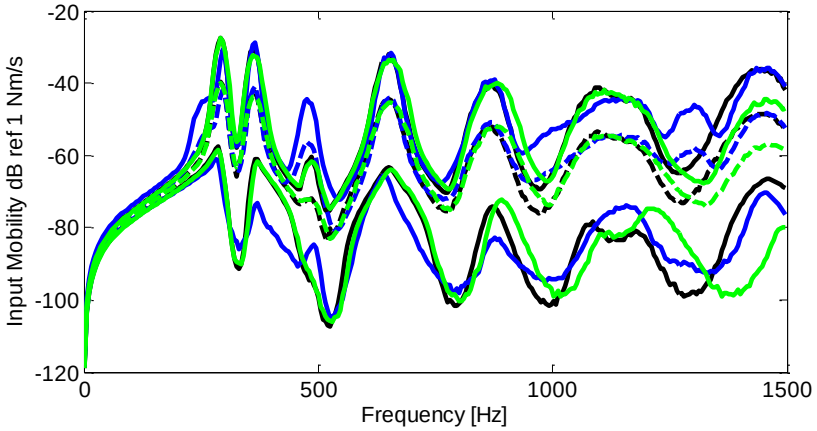

Figure 5.49. 95 % percentile and mean value of the input mobility of the plate strip using the WKB approach (blue dashed), the FE (black dashed) and the HFE(green dotted) for $\sigma = 0.2$, $b = 2L$.

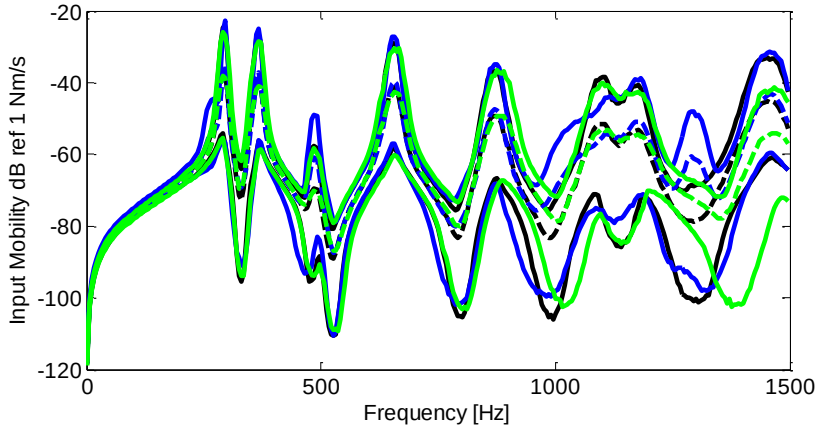

Figure 5.50. 95 % percentile and mean value of the input mobility of the plate strip using the WKB approach (blue dashed), the FE (black dashed) and the HFE (green dotted) for $\sigma = 0.1$, $b = 0.8L$.

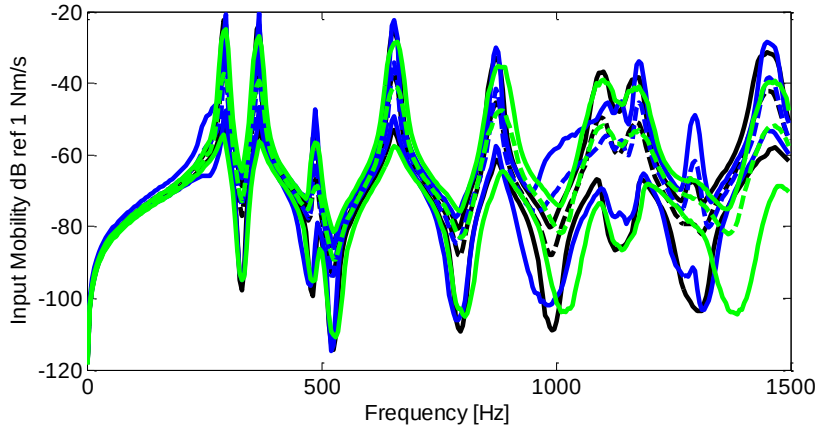

Figure 5.51. 95 % percentile and mean value of the input mobility of the plate strip using the WKB approach (blue dashed), the FE (black dashed) and the HFE (green dotted) for $\sigma = 0.1$, $b = 0.1L$.

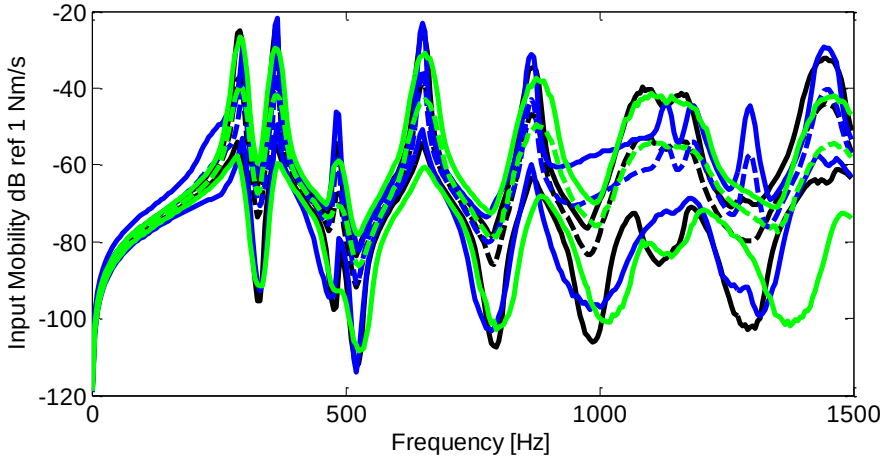

Figure 5.52. 95 % percentile and mean value of the input mobility of the plate strip using the WKB approach (blue dashed), the FE (black dashed) and the HFE(green dotted) for $\sigma = 0.2$, $b = 0.05L$.

5.7 Conclusions

In the this chapter, random variability was included in the framework of the proposed piecewise constant, WKB and HFE formulations for the longitudinal and flexural waves in rods and beams, and flexural waves in a plate strip with simply supported edges. Although the KL expansion was used as a series representation of the Gaussian and homogeneous random fields, the formulations presented are not restricted to this specific case, and can be extended to different to other types of spatially correlated randomness.

A first order approximation of the WKB solution for the natural frequencies was used to derive a closed form expression of the PDF, using an analytical expression for the KL expansion from a Gaussian random field with an exponentially decaying correlation function, and assuming small dispersion around the mean random field value. This approximation shows clearly that the statistics of the n^{th} natural frequency depends on the spatial variability, given by terms of the series expansion, and had a better agreement for the cases of larger correlation length. The same agreement was found for the first order approximation of the phase change, when compared with the numerical evaluation of the expressions given from the WKB formulation. This approximation broke down at frequencies close to the cut on frequencies at the plate strip waveguide, as would be expected from the WKB approximation.

The piecewise constant approach is also used to calculate the PDF for the rod and beam cases but neglecting the internal reflections, and the results are similar to the ones obtained with the WKB approach.

The input mobility envelopes were calculated using numerical integration of the phase changes and the agreement among the approaches is the same as seen in the PDF of the natural frequencies, i.e. very good agreement for the cases of larger correlation length, and increasingly better agreement the higher the frequency, for the cases with smaller correlation length. The WKB approximation benefited from its relatively low computational cost for speeding up the MC sampling.

The series representation of the random field was used in the HFE formulation to derive an element matrix for each term of the expansion. This procedure has to be done only once, and then the random coefficients of the expansion can be sampled in the MC framework to calculate the responses statistics. This avoids the element integration procedure that can be computationally costly and it is particularly efficient for highly

correlated random fields, because it needs fewer terms in the expansion. This procedure reduced considerably the computational cost of the MC sampling, when compared with the FE approach.The HFE results has shown overall a very good agreement with the FE approach for natural frequencies and input mobility, and it is not restricted to spatially slowly varying properties, and it can be extended to any FE element library.

In the next chapter, experimental results will be used to validate the approaches developed for calculating the response statistics, considering spatially correlated material variability.

6. Experimental validation

6.1 Introduction

Manufacturing processes often result in variability of properties compared to the nominal designed product. As the requirements for optimum design increase, it might be important to improve this prediction capability. It is usual that mechanical properties of composite structures are modelled by analytical models taking into account mean properties in the structure, although they can exhibit great spatial variability.

The characterisation of the spatial variability becomes even more relevant when dealing with fibre reinforced composite materials, for instance, for which different fibre arrangements can affect its mechanical properties [82]. Moreover, the use of a purely deterministic approach to model and, consequently, design structures using these materials can much limit its applicability and impose higher safety factors [83]. Even though the inclusion of spatial variability and uncertainties in mechanical models has received significant attention (e.g. [24, 28-30, 33, 79, 84]), it is very difficult to quantify the spatial variation of properties by procedures involving, for instance, manual measurement. A few experimental procedures for characterisation of the spatial variability in fibre reinforced composite materials have been recently proposed, based on the volume fraction or fibre distribution.

Baxter [85] presents a methodology for characterizing the randomness in a micromechanical model a moving-window technique using micrographs of fibre reinforced composites. Also, Gangadhar and Zehn [25] reviewed a some of methodologies to numerically simulate a number of different kind of microstructural patterns in composite materials and include it in the FE model. Guilleminot et al. [26, 86] proposed a theoretical framework and experimental identification based on a probabilistic model of the elasticity tensor random field and also and also on a probabilistic model based on of the volume fraction, using ultrasonic scanning measurements. They also investigate the effects of size of the Representative Volume Element [84] in the given statistical representation. Mehrez et al. [87, 88] present a technique of stochastic identification from limited experimental data, based on mobility frequency response functions in different parts of a number of cantilever beams of woven composite material. The technics accounts for both aleatory, i.e. the inherent uncertainty of the material proprieties from sample to sample, and epistemic

uncertainties, related to lack of sufficient experimental data, using a Hermite Polynomial Chaos[28] expansions of the random variables on the identified KL series.

In this chapter, validations are carried out using two different sets of experiments. In both cases, spatially correlated material properties are considered and the experimental results statistics are compared with the WKB approximation for flexural waves using a continuous random field as well as FE approximations.

In the first experiment, the natural frequencies of a cantilever beam with added masses along its length are measured. The added masses are generated according to a given correlation function for various correlation lengths, i.e. the properties of the random field are controlled *a priori*. The results will be used to investigate the effects of the correlation length on the subsequent natural frequency statistics. The experimental results will be compared with the WKB approximation for flexural waves using a continuous random field for the mass density, in order to approximate the mass distribution, and issues concerning this approximation will be discussed. In addition, results are considered for a simple added mass approximation using the assumed modes from a FE solution.

The second experiment consists of characterising the variability in the natural frequency and mobility in beams made of glass-fibre reinforced epoxy composite material. The chopped strand mat (CSM) is randomly distributed over the panel and the Young's modulus distribution is assumed to be isotropic. As opposed to the first experiment, the spatial distribution is not known *a priori* and a first measurement procedure is needed to identify it. This initial step is performed using light transmissibility measurements, from a digital image captured by DSLR camera, taken from a composite panel. An empirical relation from the pixel values to the fibre density along with a rule of mixture [89] can be used to find the spatial variation of the Young's modulus of elasticity. This information will be used to estimate, from a single sample, the mean value and the covariance function of the spatial distribution. Furthermore, by assuming that the random field has a Gaussian distribution then a Karhunen-Loeve (KL) expansion is used to represent it in terms of a reduced set of independent Gaussian random variables [28, 34]. The panel will then be cut into beams, from which mobility and measurements are possible, providing an ensemble of mobility and natural frequencies. Results will finally be compared with a FE and WKB approximations.

6.2 Natural frequency statistics of a beam with spatially correlated random masses

In this experiment, small masses were attached along of a uniform cantilever beam according to a certain spatial distribution, given by a covariance function and a number of different correlation lengths. The natural frequencies of the flexural modes of the cantilever beam with attached masses were measured and differences are identified on the statistics according to the correlation length of the random field. Some issues of representing a discrete implementation of a continuous random field are also discussed along with the results obtained in Chapter 3, using the WKB approximation for flexural waves, but using the spatially varying material density instead of the varying Young's modulus.

The measurements of the natural frequencies were performed at the Department of Mechanical Engineering of the University of Auckland, New Zealand, while the experimental design including the mass distribution was developed by the author of this thesis.

6.2.1 Random masses distribution

The attached masses are evenly distributed along the beam, i.e. their positions x_i always remain the same, as shown in Figure 6.1, but the values of each individual mass m_i vary according to a Gaussian random field $H(x)$ with exponentially decaying correlation function, i.e. $R(x_1, x_2) = \exp(-|x_1 - x_2|/b)$, where x_1 and x_2 are any two point within the beam.

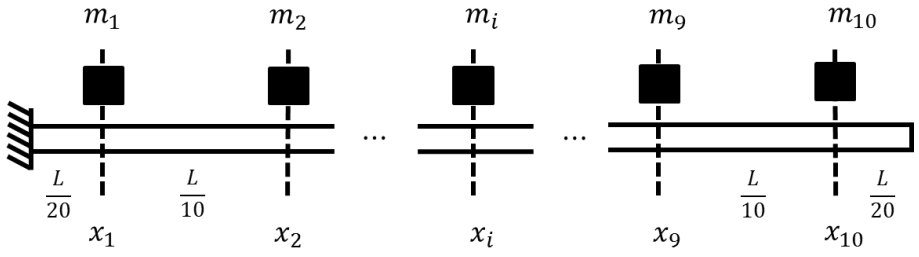

Figure 6.1. Evenly distributed masses along a cantilever beam, with values can varying from 0g to 12g added at each location.

The uniform beam is $L = 0.4$ m long with rectangular cross section, width $b = 39.85$ mm and thickness $h = 2$ mm. It has Young's modulus $E = 19094 \times 10^7$ Pa, estimated

using the uniform beam natural frequencies and a mass density $\rho = 7813.8\,\mathrm{kg/m^3}$ estimated by weighing a sample.

The masses are nuts and they are added at 10 different locations as multiples of 1 g or 2 g, such that the nominal or reference beam has 6 g added at each location, adding up 60 g total. Their values m_i are calculated by individual realisations of a zero-mean random field, with a given correlation length, at the point x_i, i.e. using the mid-point approach for the random field discretisation, and adding it to the baseline value 6g. This random field is generated using numerical a solution of the KL expansion, discretising the domain and solving an eigenproblem from the correlation matrix [28, 29]. The marginal distribution of this random field is given such that the values between -6g to 6g fall inside the 3σ region, i.e. they represent 99.73 % of the samples. Then they are rounded to the next integer, and any value sampled outside of this region is rounded to 6g or -6g accordingly. Figure 6.2 gives a normalized histogram obtained from this procedure.

Five different correlation lengths were used to generate the mass distributions: $b = 0$, meaning that the values generated for the masses are statistically independent or uncorrelated; $b = 0.10\,L$, it is equal the distance between two consecutive masses; $b = 0.25\,L$, two and a half times larger; $b = 0.60\,L$, it is six times larger; and $b = \infty$, meaning that the values for all of the masses are the same.

The mass distribution is expected to approximate a continuous mass density spatial distribution, for the flexural vibration of a straight beam, and also for a range of correlation lengths. This spatial distribution is represented in the form

$$\rho(x) = \rho_0 \left(1 + \eta_\rho + \sigma H(x)\right), \tag{6.1}$$

where η_ρ is an offset value added to the nominal density and σ is a dispersion parameter for the random field. The offset value $\eta_\rho = 0.2409$ is calculated using the reference beam, i.e. the nominal properties, having 6g at each location, and the dispersion parameter $\sigma = 0.0803$ is calculated based on the 3σ requirement.

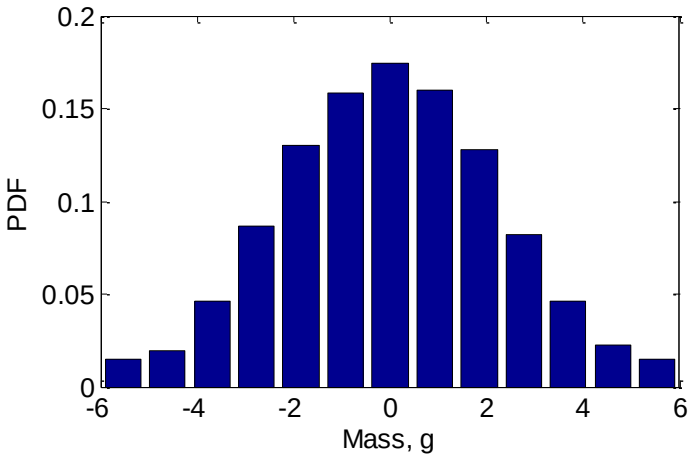

Figure 6.2. Marginal distribution of the values for the added masses m_i to the baseline value 6g.

The approximation from continuously varying to local values, or masses, is valid only up to a certain frequency limit. This can be found by considering that the distance between the masses l_m should not be greater than half wavelength, i.e. $l_m \leq \lambda/2$. For a bending wave, it follows that the upper frequency limit is

$$f_{max} \leq \frac{\pi}{2l_m^2}\sqrt{\frac{EI_{yy}}{(1+\eta_\rho)\rho_0 A}}. \tag{6.2}$$

For this case, one can find that $f_{max} \cong 1.5$ kHz, which is in excess of the modes considered.

6.2.2 Assumed modes with the lumped mass approximation model

A simple model for the lumped masses added into the FE model and solution, using Euler-Bernoulli beam elements [1], can provide an approximation for the natural frequencies that takes into account that the masses are not distributed over the beam but at discrete points. Assuming ϕ_j is the j^{th} mass normalized mode of the beam with homogenously added mass, i.e. for the nominal system $\phi_j \mathbf{M} \phi_j = 1$, then the modal stiffness are $k_j = \phi_j \mathbf{K} \phi_j$, and natural frequencies are given by $\omega_j^2 = k_j$.

The perturbation of the natural frequencies to changes in the added masses can be approximated by adding their kinetic energy contributions to each modal mass, using the mode shape of the homogeneous system, so

$$\delta_j = \sum_{i=1}^{N_m} \phi_{ij} m_i \phi_{ij} \tag{6.3}$$

where ϕ_{ij} is the j^{th} mode at the position of the i^{th} mass m_i. Then the updated natural frequency is estimated by

$$\widetilde{\omega}_j = \sqrt{\frac{k_j}{1+\delta_j}} \tag{6.4}$$

6.2.3 WKB approximation for flexural waves

So far, the results obtained from the WKB approximation considered the Young's modulus of elasticity as a random field. However, the same approach can be used in the case of varying mass density, of the form of Eq. (2.1). From chapter 3, the n^{th} natural frequency ω_n is given by

$$\omega_n = \frac{\theta_{Tn}^2}{\left(\int_0^L \sqrt[4]{\frac{\rho(x)A}{EI_{yy}}}\, dx \right)^2}, \tag{6.5}$$

where θ_{Tn} is the n^{th} root of a transcendental equation related to the cantilever boundary conditions [20]. The integral in the denominator can be calculated numerically, using a Gauss-Legendre scheme, and Monte Carlo sampling can be used to obtain its statistics.

6.2.4 Experimental results and discussion

The natural frequencies of the 2nd to the 7th mode of the cantilever beam with added masses were measured using 20 statistically independent samples for the mass configuration, for each correlation length except for the uniform sample corresponds to $b = \infty$. A slightly different procedure was used for the latter case. Because there are 13 possible integer values for the masses between -6g and 6g, the mean value and standard deviation of the latter case, $b = \infty$, was calculated by using the normalized discrete PDF, i.e.

$$\bar{\omega} = \sum_{i=1}^{13} \omega_i p_i, \tag{6.6}$$

$$\sigma_\omega = \sqrt{\sum_{i=1}^{13} (\omega_i - \bar{\omega})^2 p_i}, \tag{6.7}$$

where p_i is the normalized PDF for the discrete set of masses, as shown in Figure 6.2. Appendix 2 presents the values of the added masses used for each correlation length, as well as the natural frequencies, for each mode, for each individual sample.

Table 6.1 and Table 6.2 give the mean value and standard deviation of the measured natural frequencies for 2nd, 3rd and 4th modes and 5th , 6th and 7th modes, respectively, for each correlation length. Note that for all the correlation lengths, the natural frequencies mean values are practically the same for each individual mode. Moreover, the standard deviation values increase, the longer the correlation length for each individual mode. It also increases for the higher mode numbers.

Table 6.1. Mean value and standard deviation of the measured natural frequencies for the 2nd, 3rd and 4th modes for each correlation length.

	Mode 2		**Mode 3**		**Mode 4**	
Correlation Length b	$\bar{\omega}$	σ_ω	$\bar{\omega}$	σ_ω	$\bar{\omega}$	σ_ω
0	57.4	0.6292	159.6	2.1004	310.5	2.8271
0.10 L	57.5	0.8357	160.4	2.1806	310.5	4.2778
0.25 L	57.7	1.3004	160.1	3.1899	310.7	6.1999
0.60 L	57.9	1.5444	161.0	3.8930	311.1	7.3783
∞	57.6	1.5570	160.1	4.3048	309.9	8.0549

Table 6.2. Mean value and standard deviation of the measured natural frequencies for the 5th, 6th and 7th modes for each correlation length.

	Mode 5		**Mode 6**		**Mode 7**	
Correlation Length b	$\bar{\omega}$	σ_ω	$\bar{\omega}$	σ_ω	$\bar{\omega}$	σ_ω
0	506.7	4.2474	760.0	5.5633	1072.6	9.8085
0.10 L	506.3	5.3552	759.8	8.8770	1075.0	14.6893
0.25 L	508.4	9.0793	761.1	13.0576	1074.7	20.5209
0.60 L	509.3	11.8197	764.0	17.7766	1077.0	25.0999
∞	505.6	12.7224	757.9	18.6274	1069.1	27.3498

The sample mean $\bar{\omega}$ and standard deviation σ_ω for each mode and correlation length were used to calculate the Coefficient of Variation (COV) as

$$\text{COV} = \frac{\sigma_\omega}{\bar{\omega}}. \tag{6.8}$$

Figure 6.3 and Figure 6.4 show the COV values calculated for the 2nd, 3rd and 4th modes and 5th , 6th and 7th modes, respectively, for each correlation length. They also show the results using the simple added mass theory and the WKB approximation.

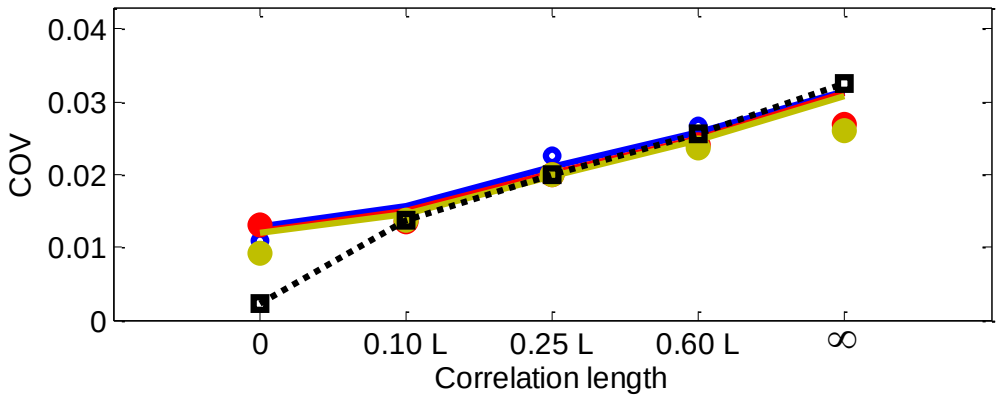

Figure 6.3. Coefficient of Variation for the 2nd (red), 3rd (blue) and 4th (yellow) mode for each correlation length from the measurements (circle), simple added mass theory (full line) and WKB (dotted black for all of the modes).

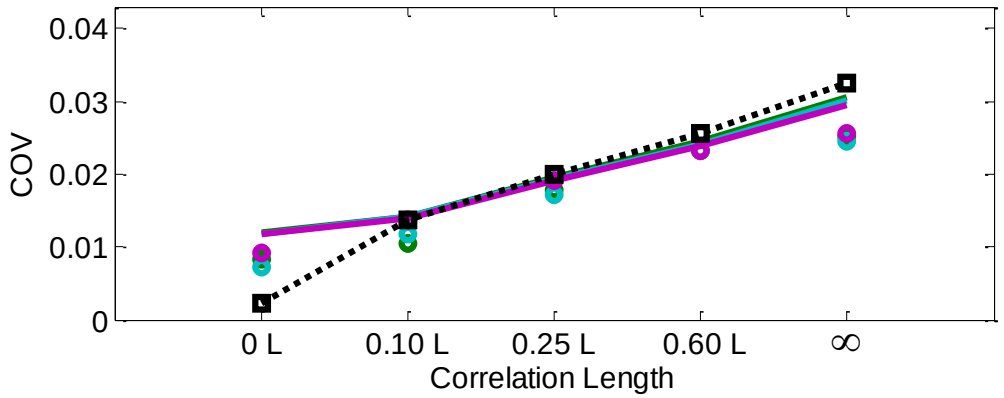

Figure 6.4. Coefficient of Variation for the 5th (green), 6th (cyan) and 7th (magenta) mode for each correlation length from the measurements (circle), simple added mass theory (full line) and WKB (dotted black for all of the modes).

Note that, in general, the results agree very well for all of the modes and correlation lengths except for the uncorrelated case, $b = 0$. In that specific case, not only is the approximation from the continuous case to the discrete one less accurate, because the correlation length is much smaller than the distance between the added masses, leading to spatial aliasing, but also the WKB approximation fails, due to the rapidly changing characteristic of the mass density.

It can be shown that representing a random field using the midpoint method along with a coarse mesh, i.e. the distance between two consecutive masses much bigger than the correlation length, may introduce higher variability into the stochastic response due to the associated aliasing effect [90]. This result agrees with the much higher COV found for the experimental and added mass theory prediction.

Similarly, this effect can also be seen during the element integration using the HFE approach, for beam elements, as shown in chapter 3, using the same mass density random field as for the WKB. Although it does not depend on any sort of mesh refinement, because of the white noise nature of the uncorrelated case, the number of points needed to numerically integrate the property along the beam starts to play a role. Figure 6.5 gives the typical COV value for a beam mode solved for various numbers of integration points for the HFE approach. Note that, the higher the number of points the closer to the WKB results. Although this case is not physically meaningful, one would expect the same issue when dealing with near zero correlation lengths, which is not whithin the scope of this work.

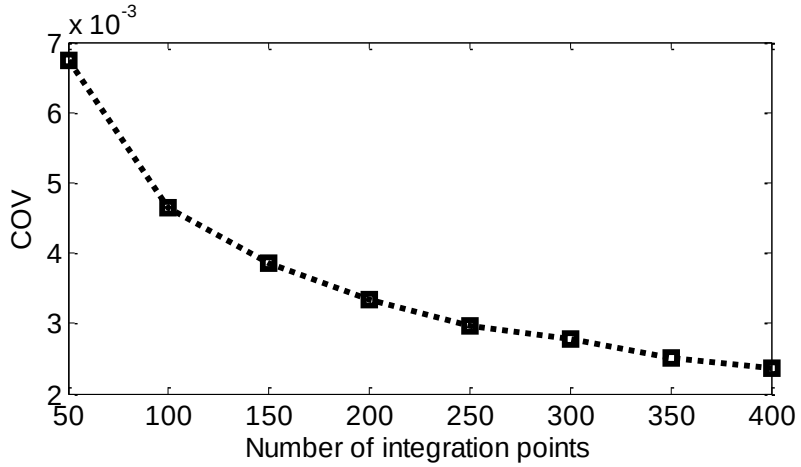

Figure 6.5. Typical coefficient of variation value for a beam mode varying the number of points used for the numerical integration using the HFE approach, for the case uncorrelated case.

For the case when $b = \infty$, the beam mass can be treated as a random variable, instead of a random field, i.e. Eq. (6.4) and Eq. (6.5) reduces, respectively, to

$$\widetilde{\omega}_j = \sqrt{\frac{k_j}{1 + m\sum_{i=1}^{N_m}\phi_{ij}^2}}, \tag{6.9}$$

$$\omega_n = \sqrt{\frac{EI_{yy}}{\rho A}}\frac{\theta_{Tn}^2}{L^2}. \tag{6.10}$$

where the random mass is given by $m = \sigma_m\xi_1$ and σ_m the standard deviation of the beam mass, and the mass density is a random variable given by $\rho = \rho_0(1 + \eta_\rho + \sigma\xi_2)$, from Eq. (2.1), being that ξ_1 and ξ_2 are Gaussian independent, zero-mean, unity standard deviation random variables. Using a first order approximation, it is possible to find analytically a COV value for the WKB approach,

$$\mathrm{COV} = \frac{\sigma}{2(1 + \eta_\rho)}, \tag{6.11}$$

and also for the added mass approximation,

$$\mathrm{COV} = \frac{\sigma_m}{2}\sum_{i=1}^{N_m}\phi_{ij}^2. \tag{6.12}$$

Results are shown in Table 6.3. Note that they have a good agreement with the results obtained from Monte Carlo sampling, Figure 6.3 and Figure 6.4, but they are different

from the experimental results. From the modal contribution in Eq. (6.12), it is possible to note that the positions of the masses along the beam affect the COV values differently for each mode. This bias due to the modal shape is also seen in the other correlation lengths as well as in the experimental results. However, it does happen when using the WKB approximation, as can be seen from Eq. (6.11) for $b = \infty$, because the mass is distributed over the beam. That is also the case for the other correlation lengths, as shown in Figure 6.3 and Figure 6.4.

Table 6.3. Coefficient of Variation for the 2nd, 3rd, 4th , 5th, 6th and 7th modes for the infinity correlation $b = \infty$, using the added mass and WKB approach from first order approximation on the natural frequencies.

	Mode 2	**Mode 3**	**Mode 4**	**Mode 5**	**Mode 6**	**Mode 7**	**WKB**
COV	0.0311	0.0308	0.0305	0.0303	0.300	0.0297	0.0324

6.2.5 Conclusions

In the proposed experiment, an approximation was made for the spatially varying mass density along the propagation axis of a cantilever beam by using a set of discrete distributed masses over its length. The values of the masses were generated using a random field with exponentially decaying correlation function using different correction lengths, rounded to integer values in grams with a clipped Gaussian distribution.

Natural frequencies were measured for five different correlation lengths; one where the masses are homogeneously distributed, i.e. all the masses along the beam with the same value, meaning an infinite correlation length; another such that they are uncorrelated, i.e. statistically independent from each other, meaning zero correlation length. These two are limiting cases, in the sense that they represent, respectively, the greater and smaller variability in the natural frequencies of the cantilever beam. Also, the natural frequencies were measured for other three correlation lengths, all equal or greater than the distance between two consecutive masses. It was shown that the larger the correlation length the higher the standard deviation of the natural frequencies.

The experimental results agreed with the proposed WKB approximation for flexural waves, considering the mass density as a continuous random field matching the mass distribution, except for the $b = 0$ uncorrelated case. This is because the number of masses used was not enough to represent a spatial distribution of zero or near-zero

correlation length random field. This caused a spatial aliasing increasing the variability of the natural frequencies. In this case, HFE and WKB results agreed but for an increased number of points in the numerical integration. Although the uncorrelated case is not physically meaningful, one would expect the same issue when dealing with near zero correlation lengths, which is not within the scope of this work, where gradually varying variability is of interest.

6.3 Vibration response statistics of a fibre reinforced composite panel

In this experiment, optical measurement, using light transmissibility over a short glass fibre reinforced epoxy panel, are used to estimate the spatially variable volume fraction over the panel [89]. This information, along with a simple rule of mixtures [91], is used to estimate the spatially varying Young's modulus of elasticity and mass density. It is assumed that the spatially correlated randomness is only due to the volume fraction [86]. The variability through the thickness is also neglected.

The panels were manufactured by the Centre of Advanced Composite Materials (CACM) at the University of Auckland, New Zealand, where also the light transmission images were taken using the setup described in the following section.

The images were subsequently used by the author to estimate the statistics of the area density spatial distribution, assuming a second order homogeneous random field representation. Therefore the estimation of mean value and correlation function is enough to give complete statistical description [27]. This information was used to reproduce numerically the random field, using a Karhunen-Loeve expansion.

A set of beams samples from the original panel was tested by the author and the flexural natural frequencies identified from mobility measurements, using a Laser Doppler Vibrometer (LDV). This procedure was performed within the Dynamics Group, ISVR, and produces an ensemble of natural frequencies whose statistics were estimated. The estimated random field, along with the given rule of mixtures, was used as an input for FE models, using beams and plate elements and also a HFE formulation for plate elements, including the spatial variability. The WKB approach for flexural waves, chapter 3, was also used to estimate numerically the flexural natural frequency statistics. This procedure was repeated for two different panels; one manufactured with a single layer of reinforcement and a second one with two layers of material.

6.3.1 Light transmission images from CSM

An apparatus, as proposed in [89], consisting of a light box and a digital SLR camera has been assembled to capture high resolution light transmission images of reinforcement layers, from which information is extracted. The light box is illuminated by three fluorescent tubes and uses a simple plastic diffuser screen to help disperse light evenly. A Canon EOS 400D digital SLR camera is mounted on an aluminium extrusion frame attached to the light box, ensuring minimum relative movement between the camera and the illuminating surface. Optimum camera settings such as aperture and exposure length varied between reinforcement types and were chosen to give the best lighting conditions.

Image distortion corrections are taken for two primary forms caused by the geometry of the lens, namely Barrel distortion and by uneven illumination. The former is taken into account by software correction and the latter by subtracting off an image of the background gradient such that the amount of light entering L_e is the amount of light blocked L_b plus the amount of light transmitted L_t [89]:

$$L_e = L_b + L_t. \tag{6.13}$$

Figure 6.6 shows the fibre reinforcement before the infusion process with the epoxy matrix for the single and double layer panels. An image of the light transmission for random chopped strand material (CSM) can be related to the area density, *AW*, in $\mathrm{g/m^2}$, through an empirically derived polynomial fitting [89]:

$$AW(L_b) = k_0 + k_1 L_b + k_2 L_b^2 + k_3 L_b^3 + k_4 L_b^4, \tag{6.14}$$

where L_b is the amount of light blocked, at pixel size, given in integer number from 0 - 255 (grey scale) and $k_0 = 2.62 \times 10^{-1}$ $\mathrm{g/m^2}$, $k_1 = 5.12 \times 10^{0}$ $\mathrm{g/m^2}$, $k_2 = -1.07 \times 10^{-3}$ $\mathrm{g/m^2}$ and $k_4 = 5.15 \times 10^{-6}$ $\mathrm{g/m^2}$. This approach neglects the fibre variability through the thickness.

a) b)

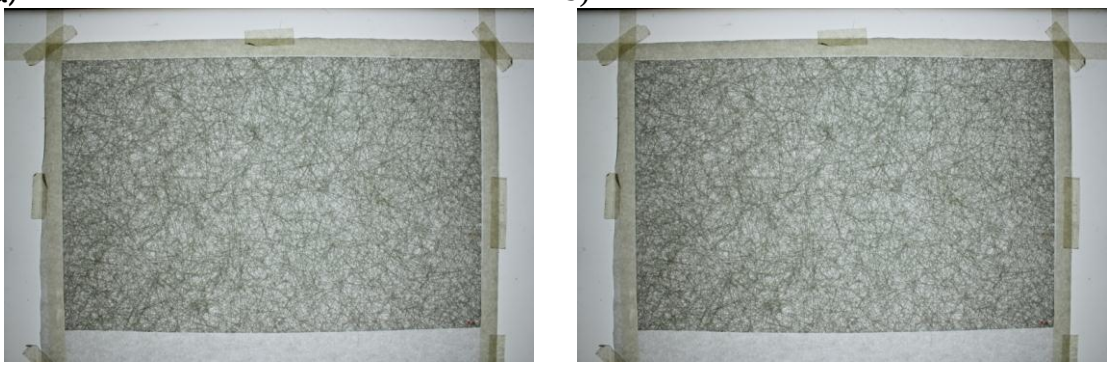

Figure 6.6. Fibre reinforcement detail before the infusion process with the epoxy matrix for the a) single layer panel and b) double layer panel.

The images were produced from pictures taken of two 450 mm $\times$ 290 mm panels, with single and double layer of the composite material. The images were downsized to 63×40 pixels resolution, such that each pixel corresponding approximately to an 7 mm $\times$ 7 mm area. Selection of this window size was based on a criterion for which the average pixelated area density had to match the macro-scale area density.

It is expected that the pixel resolution from the original image greatly affects the spatial variability of the area density. The pixel size averages the property within that area, applying a smoothing effect, i.e. the finer the pixel resolution, the bigger the variability the image is able to capture. Baxter and Graham [85] apply a moving window technique for characterizing the volume fraction of a fibre reinforced composite material and show the changes on the correlation structure and marginal PDF for different windows sizes. Stress calculations might require a much finer description to properly represent the material constitutive matrix [85].

Considering a constant thickness manufacturing process, the volume fraction V_f can be calculated as [89, 91]:

$$V_f(AW) = \frac{AW}{\rho_f t} \tag{6.15}$$

where ρ_f is the fibre density and t is the thickness. Assuming isotropy and multilayer laminates, it is possible to relate Eq. (6.13) to a local Young's modulus by a simple rule of mixture[91]:

$$E(E_L, E_T) = \frac{3}{8}E_L + \frac{5}{8}E_T \tag{6.16}$$

$$E_L(V_f) = E_f V_f + E_m(1 - V_f) \tag{6.17}$$

$$E_T(V_f) = \left(\frac{V_f}{E_f} + \frac{1 - V_f}{E_m}\right)^{-1} \tag{6.18}$$

where E_f and E_m are the isotropic stiffness of the E-glass and surrounding matrix, respectively, and E_L and E_T are the longitudinal and the transverse stiffness of the mixture, respectively. Also, the local density is given by

$$\rho(V_f) = \rho_f V_f + \rho_m(1 - V_f) \tag{6.19}$$

Table 6.4 summarizes the properties used for the rule given rule of mixture, based on the information provided by the manufactures of the fibre reinforcement and the epoxy resin. The thicknesses are different for each panel and are given by the mean value from measurements in specific points over the panels, as given in Table 6.5.

Figure 6.7 and Figure 6.8 shows spatial distribution of the area density in g/m^2, estimated from the optical measurements, the mass density in kg/m^3 and the Young's modulus in GPa, from the rule of mixtures, for the single and double layer, respectively, and Figure 6.9 to Figure 6.11 show their PDF normalized by the mean value μ and standard-deviation σ, for single and double layer.

Table 6.4. Material properties used in the rule of mixture for the Young's modulus and mass density of the chopped strand material (CSM).

E_M [GPa]	E_f [GPa]	ρ_f [kg/m^3]	ρ_f [kg/m^3]
3.2	72.3	2540	1150

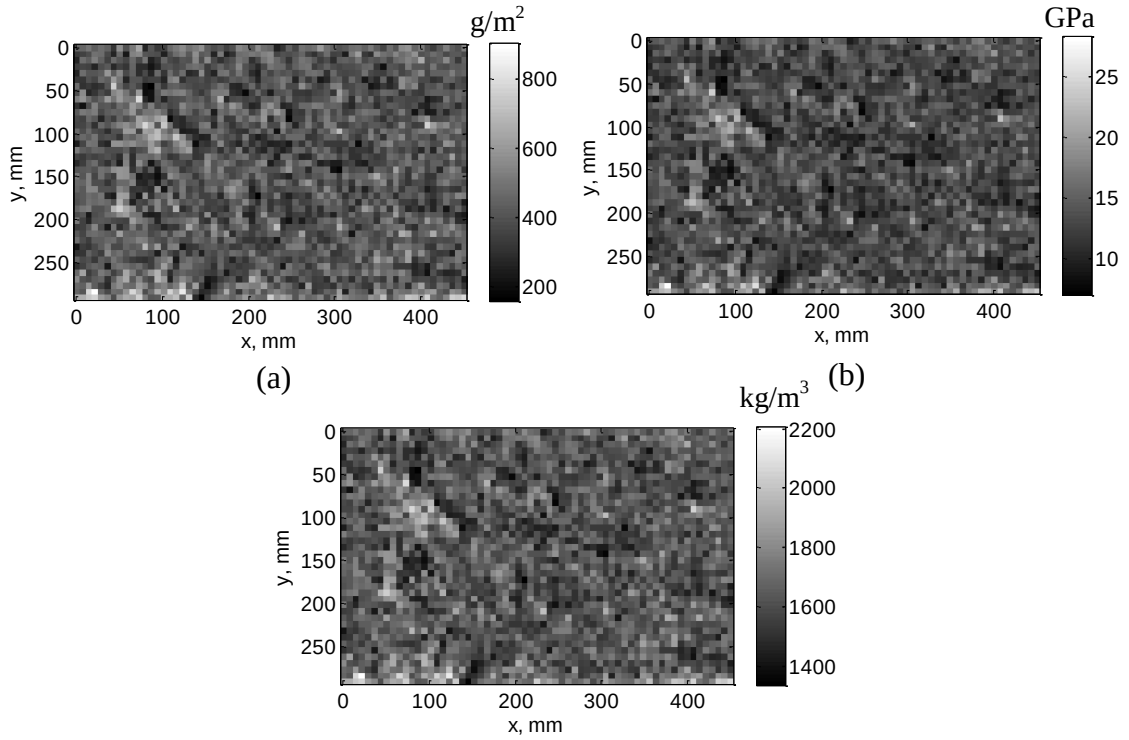

Figure 6.7. The a) area density in g/m^2 from the optical measurement, b) the Young's modulus in GPa and c) the mass density in kg/m^3 using a simple rule of mixture of the single layer panel.

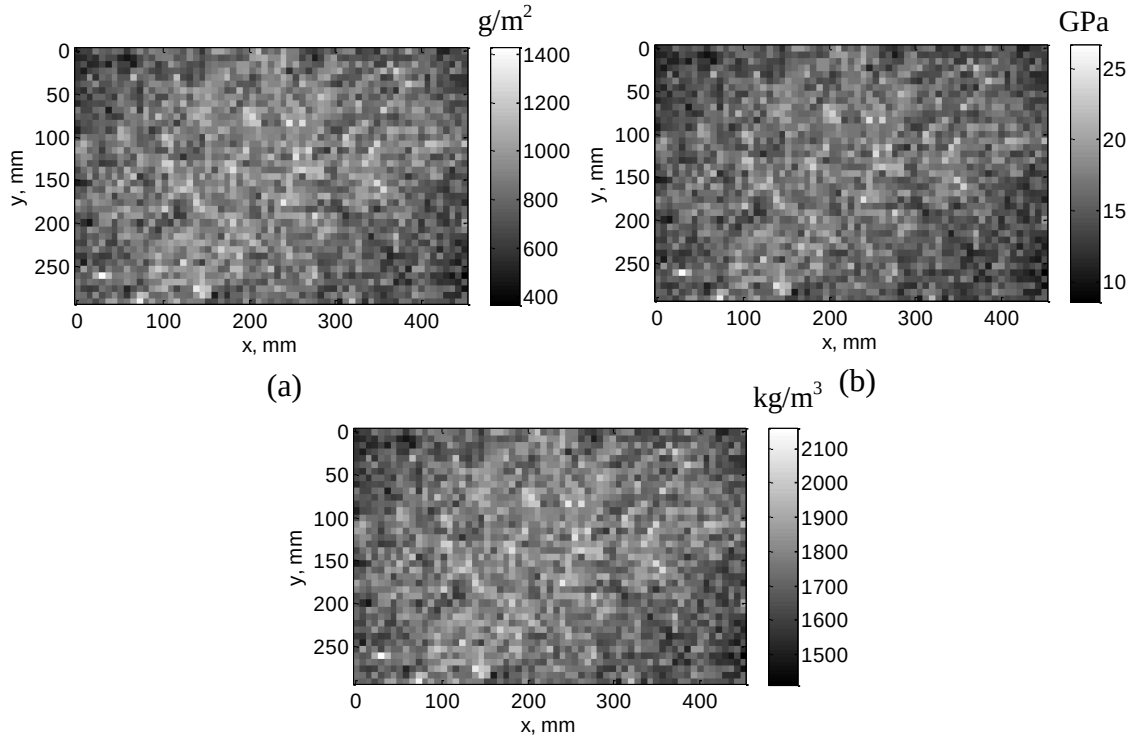

Figure 6.8. The a) area density in g/m^2 from the optical measurement, b) the Young's modulus in GPa and c) the mass density in kg/m^3 using a simple rule of mixture of the double layer panel.

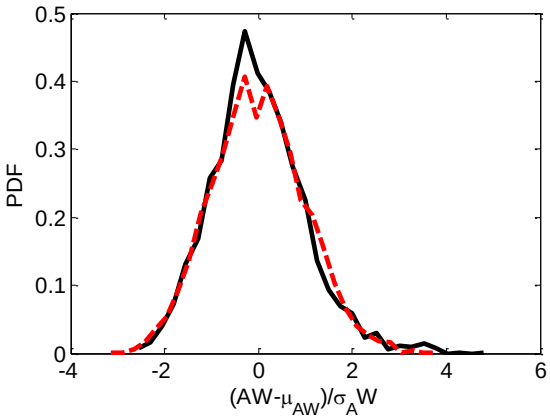

Figure 6.9. Marginal distribution from normalized the area density AW in g/m^2 from the optical measurements for the single layer (black full line) panel, with $\mu_{AW} = 421.4$ g/cm^2 and $\sigma_{AW} = 97.6$ g/cm^2, and the double layer (red dashed) panel , with $\mu_{AW} = 851.5$ g/cm^2 and $\sigma_{AW} = 148.5$ g/cm^2.

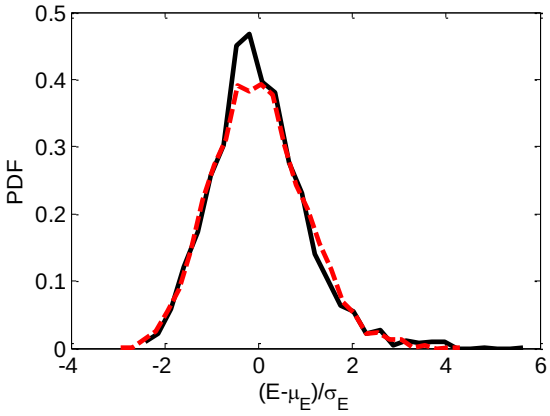

Figure 6.10. Marginal distribution from the Young's modulus in GPa from the optical measurements for the single layer (black full line) panel, with $\mu_E = 13.5$ GPa and $\sigma_E = 2.5$ GPa, and the double layer (red dashed) panel, with $\mu_E = 16.0$ GPa and $\sigma_E = 2.4$ GPa.

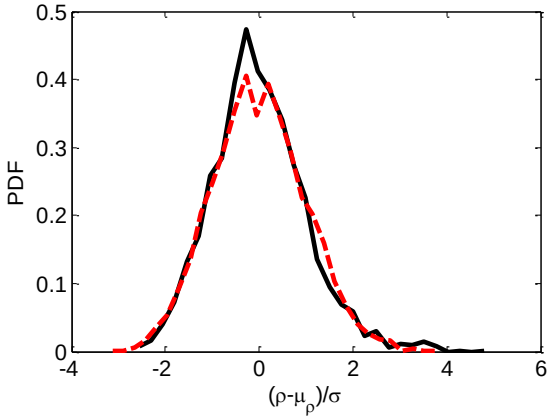

Figure 6.11. Marginal distribution from the mass density kg/m^3 from the optical measurements for the single layer (black full line) panel, with $\mu_\rho = 1150.0$ kg/m^3 and $\sigma_\rho = 114.1$ kg/m^3, and the double layer (red dashed) panel, with $\mu_\rho = 1752.8$ kg/m^3 and $\sigma_\rho = 105.1$ kg/m^3.

6.3.2 Thickness variability

The manufacturing process leads to variation of the panel thickness, as shown in Table 6.5, which gives some thicknesses measurements, in mm, at specific locations, see Figure 6.12, performed on both single and double layer panels, showing that the thickness is not constant over the panel, with significant variability.

The rule of mixture supposes constant thickness over the panel to calculate the volume fraction from the area density information, Eq. (6.15), obtained from the given images. This implies that the spatial variability of the thickness cannot be taken into account using this approximation. And thus, it is modelled as a single random variable. Because the panel was cut into beams in the fill direction, i.e. from positions 15 to 10 and 24 to 1, for instance, the overall variability is not a good indicator to model the variability of the thickness of the beams. The measurements suggest that the standard deviation of the beams thickness is smaller than that for the overall measurements.

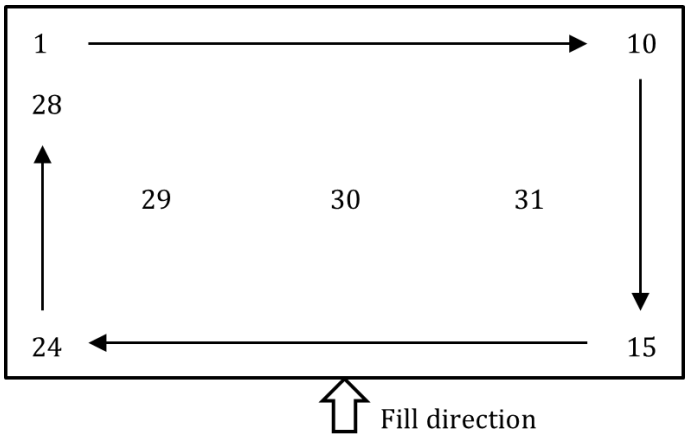

Figure 6.12. Position of thickness measurements over the single and double layer panels.

Table 6.5. Thickness measurements, in mm, on a number of positions over the single and double layer panel, and overall mean, standard deviation STD and Coefficient of Variation COV.

Position	Single Layer Thickness, mm	Double Layer Thickness, mm	Position	Single Layer Thickness, mm	Double Layer Thickness, mm
1	0.448	0.778	**18**	0.446	0.683
2	0.466	0.757	**19**	0.45	0.711
3	0.486	0.735	**20**	0.477	0.729
4	0.457	0.735	**21**	0.477	0.772
5	0.437	0.731	**22**	0.508	0.808
6	0.448	0.737	**23**	0.496	0.848
7	0.452	0.72	**24**	0.509	0.901
8	0.458	0.721	**25**	0.496	0.891
9	0.454	0.739	**26**	0.474	0.866
10	0.46	0.766	**27**	0.502	0.846
11	0.469	0.786	**28**	0.498	0.818
12	0.457	0.817	**29**	0.482	0.861
13	0.455	0.789	**30**	0.443	0.763
14	0.473	0.756	**31**	0.454	0.794
15	0.464	0.723	**Mean**	0.468	0.773
16	0.47	0.709	**STD**	0.021	0.059
17	0.442	0.681	**COV**	4.41%	7.69%

6.3.3 Random field model and simulation

The area density AW, is assumed to be a second order homogeneous random field with mean value AW_0 and autocorrelation function $\mathrm{R}(\tau_x, \tau_y)$, where τ_x and τ_y are the lag or delay in the *x* and *y* directions [92]. The mean value was estimated via sample mean over the image, and the autocorrelation function was estimated via the inverse Discrete Fourier Transform (DFT) of the two dimensional auto spectral density of the image, estimated via segment averaging approach, using a Hann window [93, 94].

Figure 6.13 shows the estimated normalised autocorrelation function for the single and double layer panel respectively. Figure 6.14 give the normalised autocorrelation function on the x-axis $\mathrm{R}(\tau_x, 0)/\mathrm{R}(0,0)$ and on the y-axis $\mathrm{R}(0, \tau_y)/\mathrm{R}(0,0)$ for the single and double layer panels respectively. Note that the correlation length of the single layer panel is roughly the same in all directions, i.e. it represents an isotropic correlation structure [92], which is expected since there might not be any preferential direction in

the fibre distribution. This is not so evident for the double layer panel, and it is possible to notice a small difference in the correlation depending on the direction.

a) b)

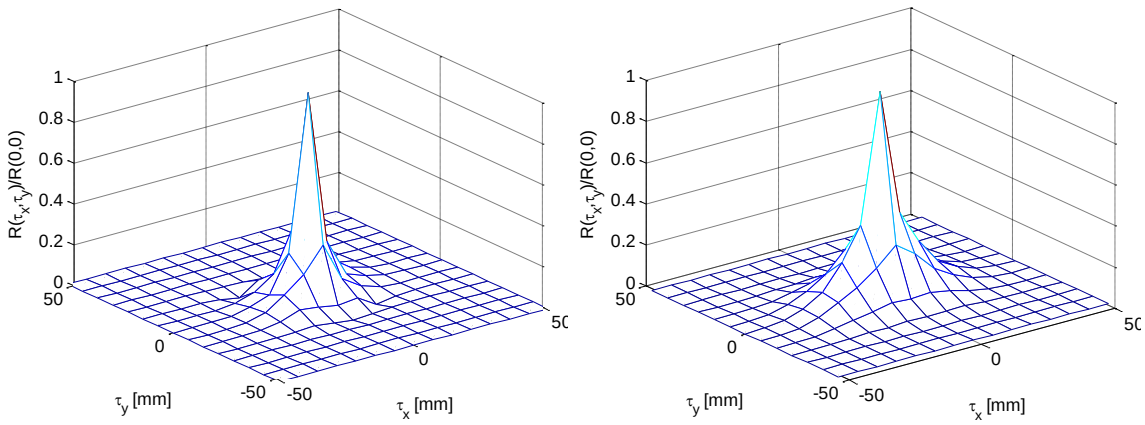

Figure 6.13. Normalized autocorrelation function $R(\tau_x, \tau_y)/R(0,0)$ from the area density *AW* spatial distribution of the a) single and b) double layer panel.

a) b)

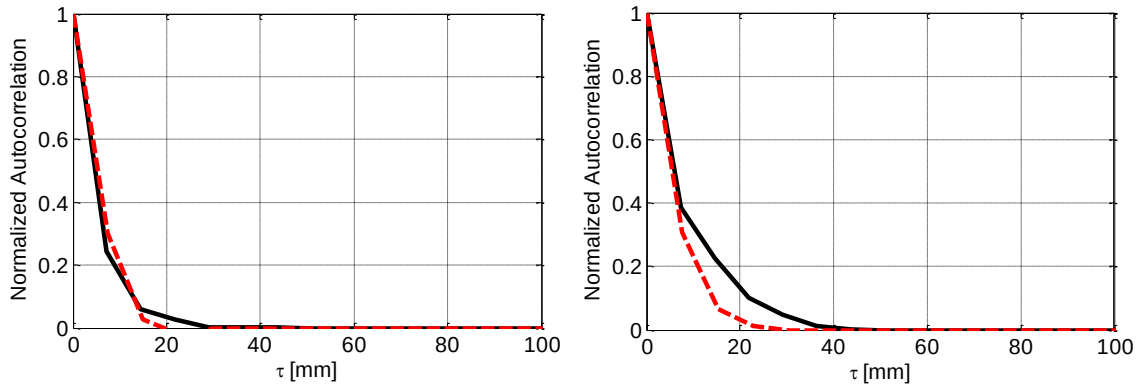

Figure 6.14. Normalised autocorrelation function in the x-axis $R(\tau_x, 0)/R(0,0)$ (red dashed line) and in the y-axis $R(0, \tau_y)/R(0,0)$ (black full line), for the a) single and b) double layer panel from the area density spatial distribution.

A collocation method was used for discretisation of the estimated two dimensional autocorrelation function $R(\tau_x, \tau_y)$ into a correlation matrix **R**. This matrix was used to solve the associate Karhunen-Loeve eigenproblem [28] into eigenvectors $\mathbf{f}_i$ and their respective eigenvalues λ_i, such that the zero mean random field is given by

$$\mathbf{H} = \sum_{i=1}^{N_{KL}} \xi_i \sqrt{\lambda_i}\, \mathbf{f}_i, \tag{6.20}$$

where ξ_i is a zero mean unity standard deviation Gaussian random variable and N_{KL} is the number of terms needed in the KL expansion for an appropriate representation of the random field [34]. The area density random field is then given by

$$\mathbf{AW} = \mathbf{AW_0} + \mathbf{H}, \tag{6.21}$$

where $\mathbf{AW_0}$ is its mean value. Figure 6.15 gives the normalised eigenvalues and Figure 6.16 the eigenvectors, from the single layer and double layer panel correlation matrix, respectively. It is possible to observe a difference in the spatial symmetry of the eigenfunctions from the single to the double layer due to the difference in the autocorrelation structure. The correlation function from the single layer panel has an isotropic structure, i.e. there is no preferential direction in the fibre arrangement. However, this is not so evident on the eigenvector obtained from the double layer panel. The series was truncated to N_{KL}, such that $\lambda_i/\lambda_1 > 0.05$, reducing the number of random variables needed to accurately represent the random field.

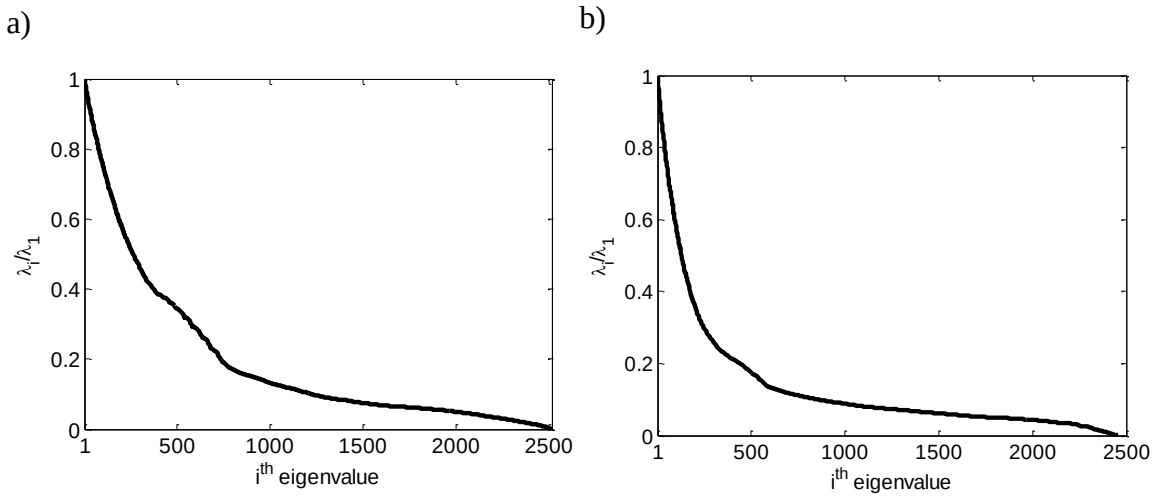

Figure 6.15. Normalized eigenvalues from the KL decomposition of the autocorrelation matrix from the a) single and b) double layer panel.

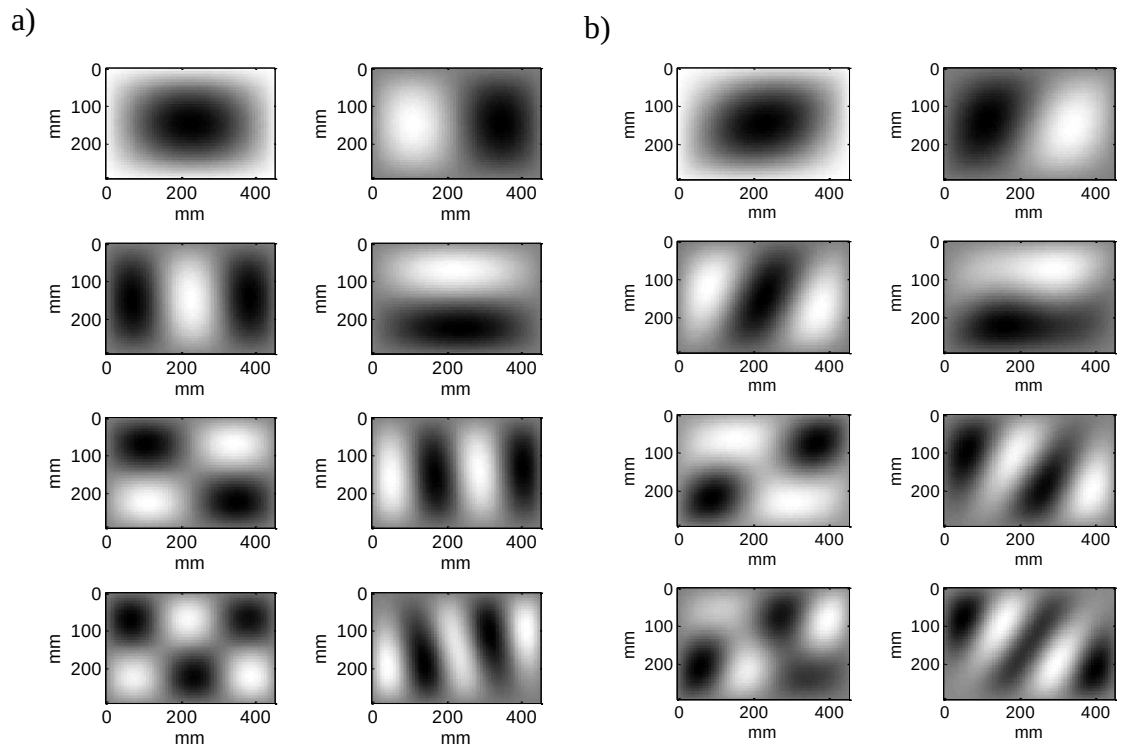

Figure 6.16. First eight eigenvectors from the KL decomposition of the autocorrelation matrix experimentally obtained from the a) single and b) layer panel.

Figure 6.17 compares the area density marginal PDF from the light transmissibility measurements to one generated numerically from the Gaussian model for the single and double layer panel respectively. Figure 6.18 and Figure 6.19 give the marginal PDF of the Young's modulus and mass density applying the rule of mixture on their respective experimental and numerical area density for the single and double layer panel. Figure 6.20 shows the numerical simulation of the Young's modulus using the Gaussian model for the single and double layer. This comparison shows qualitatively how the assumption of a Gaussian random field is accurate in representing the actual measurements. From visual inspection, it is possible to note that this assumption might not be as accurate for the single layer panel as it is for the double layer. There is a greater deviation from the Gaussian shape in the former case, while in the latter it is not so clear. However, it is possible to increase the accuracy of this model by updating the statistics of the random variables ξ_i based on the experimental data, and exploring the orthogonality of the eigenfunctions $\mathbf{f}_i$ [28]. In addition, these random variables can be represented in terms of Polynomial Chaos to include aleatory and epistemic uncertainties in the random field model [87, 95, 96] as well as non-Gaussian models [97-99]. The Gaussian random field assumption is used for sake of simplicity.

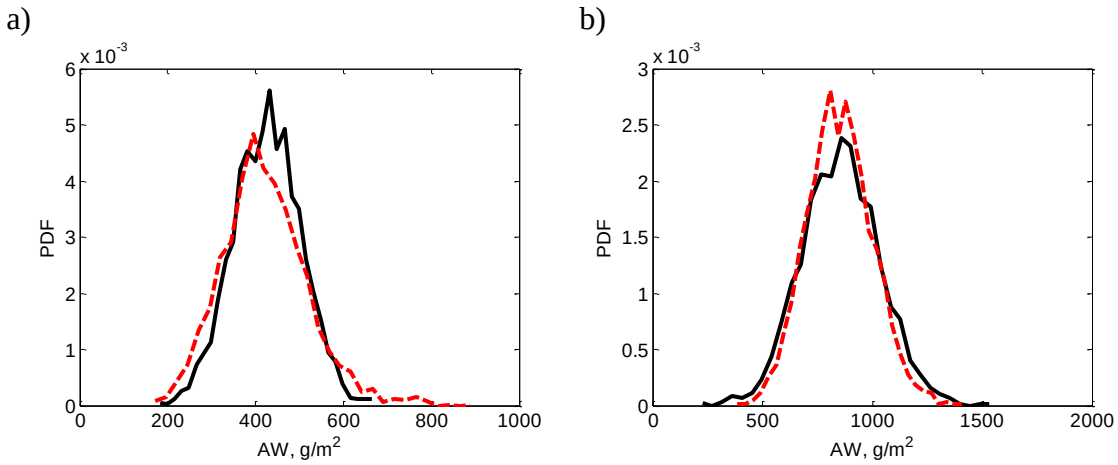

Figure 6.17. Marginal distribution from the area density g/m^2 estimated from the optical measurements for the a) single and b) double layer (red dashed line) and from the Gaussian model (black full line), generated from a single image.

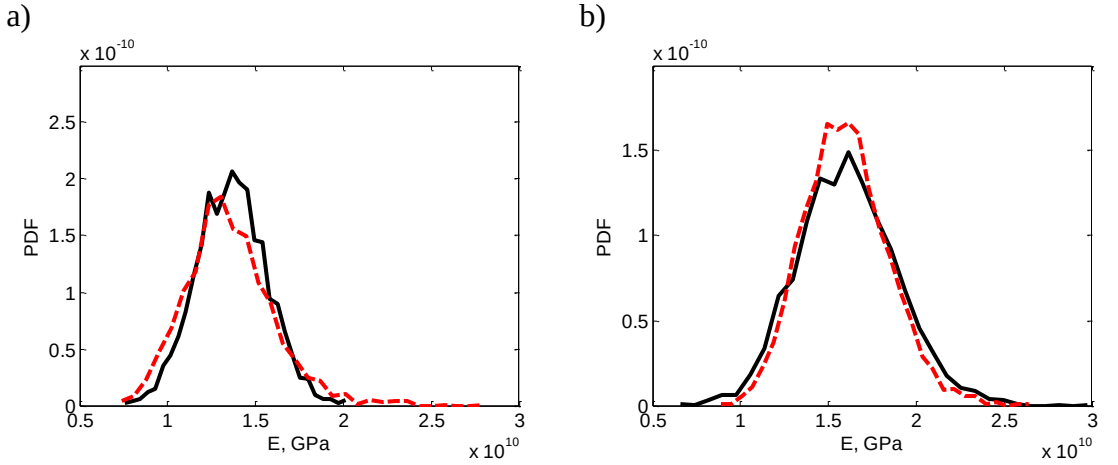

Figure 6.18. Marginal distribution from the Young's modulus in GPa estimated from the optical measurements for the a) single and b) double layer (red dashed line) and from the Gaussian model for the area density (black full line), generated from a single image.

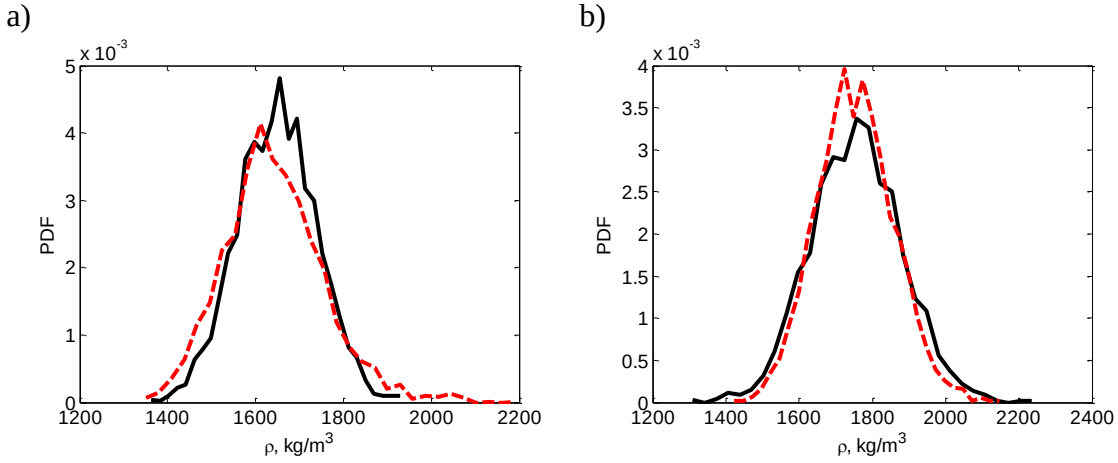

Figure 6.19. Marginal distribution from the mass density in kg/m^3 estimated from the optical measurements for the a) single and b) double layer (red dashed line) and from the Gaussian model for the area density (black full line), generated from a single image.

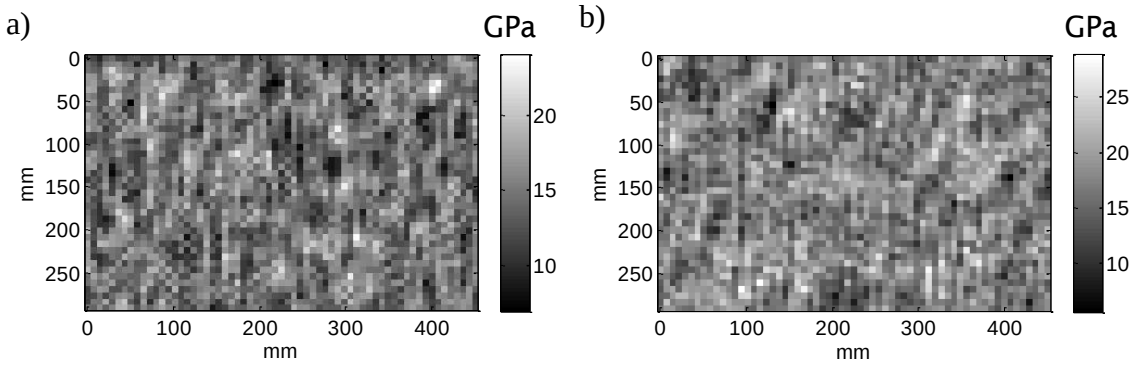

Figure 6.20. Numerically generated sample of Young's modulus of elasticity, in GPa, from the Karhunen-Loeve expansion and the estimated correlation function from the a) single and b) layer panel.

6.3.4 Random field discretisation in the FE models

Two FE models were used to represent the CSM beams, for both single layer and double layer cases: a two-dimensional model using thin, rectangular and isotropic plate elements and one-dimensional using Euler-Bernoulli beam bending elements [1]. The two-dimensional model used 117 elements, with 3 elements in the *x*-direction and 39 elements in the *y*-direction, as shown in Figure 6.21. The Young's modulus and mass density are constant inside each element and the random field mesh is the same than the FE mesh. Both models used free boundary conditions.

Each two-dimensional random field generated using the KL expansion, as described in the previous sections, is split into 21 samples and then used for the FE model. The one dimensional model used the same number of elements in the *y*-direction, also with constant value for the Young's modulus, calculated as the spatial average of the field in the *x*-direction.

The beams are 280 mm long and 21 mm wide with a rectangular cross section. The thickness was modelled as a Gaussian random variable, with mean values $t_0 = 0.47$ mm and standard deviation $\sigma_t = 0.0095$ mm for the single layer and $t_0 = 0.77$ mm and standard deviation $\sigma_t = 0.04$ mm for the double layer.

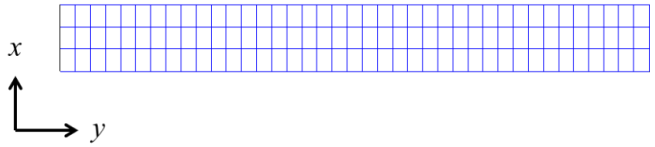

Figure 6.21. FE mesh of the CSM beam two dimensional model, for isotropic plate elements.

6.3.5 Two dimensional mode using the HFE approximation

The HFE approximation used the two-dimensional using thin, rectangular and isotropic plate element enriched with 10 hierarchical functions, as shown in Chapter 4. The integration was performed numerically using a Gauss –Legendre scheme with 39 points in the *x* direction and 3 points on the *y* direction.

6.3.6 WKB approximation for flexural waves

From chapter 3, the n^{th} natural frequency ω_n from a flexural wave model using the WKB approximation is given by

$$\omega_n = \frac{\theta_{Tn}^2}{\left(\int_0^L \sqrt[4]{\frac{\rho(x)A}{E(x)I_{yy}}}\, dx \right)^2}, \tag{6.22}$$

where $I_{yy} = wt^3/12$, w is cross section the width and t is the random thickness, θ_{Tn} are the roots of transcendental equation related to the free-free boundary conditions [20], $E(x)$ and $\rho(x)$ are the Young's modulus and mass density random fields, calculated in the same way as for the FE one dimensional bending elements, from the rule of mixture. The integration was performed numerically using a Gauss – Legendre scheme.

6.3.7 Experimental setup

An experiment was set up to provide a number of frequency response functions from point measurements on the set of CSM glass fibre beams, cut from both the single and double layers panels. This set of measurements provides an ensemble to be used to assess the material variability. The panels were manufactured using short chopped glass fibre reinforcement in a resin matrix and 21 samples (21×280 mm) were cut from

each panel. Each sample from the single layer was labelled from left to right as 1_A to 1_U. The specimen 1_C was damaged during the cutting and, therefore, discarded from the frequency response measurements. In the same manner, the 21 samples from the double layer panel were labelled from left to right as 2_A to 2_U.

The experiment consisted in measuring the point mobility with a Laser Doppler Vibrometer, LDV, on each beam for a hammer excitation, as shown in Figure 6.22. The vibrometer used was a Polytec PDV 100, with a sensitivity of 40mV/(mm/s), the miniature hammer, a PCB 086E80 with sensitivity 21.4 mV/N and a Dataphysics Quattro was used for the data acquisition. The beams were hung in a metallic frame using nylon string, in order to generate the free-free boundary condition and excited on the upper part with the micro hammer. A reflective tape was stuck to each beam at the position of the measurement. The measurements of the single layer beams were made from 0 to 250 Hz, with a frequency resolution of 0.3125 Hz; the double layer samples were measured from 0 to 800 Hz with a frequency resolution of 1 Hz.

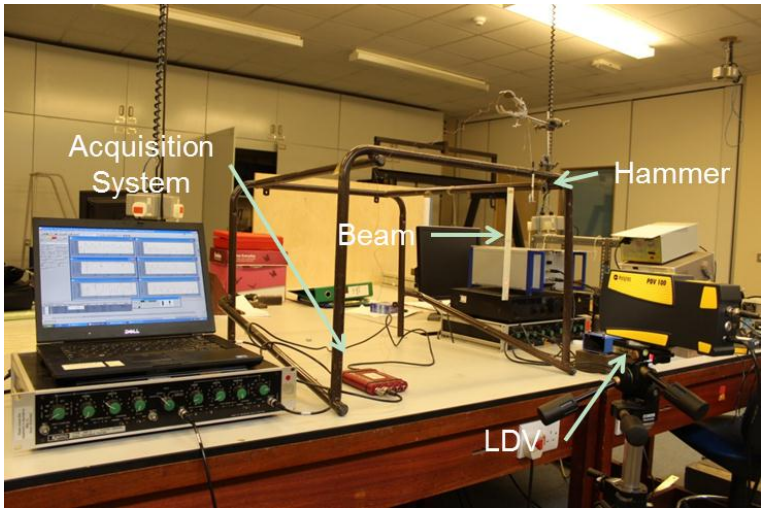

Figure 6.22. Experimental set up shown with the acquisition system, LDV, micro hammer and a beam sample.

6.3.8 Results and discussion

In this section, the natural frequencies of the flexural modes obtained from the mobility measurements in the CSM beams are compared with the ones obtained by using the numerical models and the identified random field.

The frequency response functions from the measurements in the free-free beams were calculated using the H1 estimator [94], with 5 measurements for averaging the spectral density functions.

Figure 6.23 gives the estimated mobility amplitude and phase of the 20 single layer CSM beams along with the upper and lower 95% percentile and mean value, and
Figure 6.24 shows a typical amplitude and coherence. Also, Figure 6.25 gives the estimated mobility amplitude and phase of the 21 double layers CSM beams along with 95% upper and lower percentile and mean value and Figure 6.26 shows a typical amplitude and coherence. One can observe that the coherence for the double layer beams is much better than for the single layer. This is not only because of the frequency resolution but also due to their extreme light weight of the single layer beams. From these two ensembles it is clear that the lowest order modes are not as sensitive to the material variability as the higher order modes.

The natural frequencies of the flexural modes, for each individual specimen, were identified from the mobility measurements from all of the CSM beams, using the circle-fit method [100]. These are shown in Table 2.9, the first three natural frequencies from all of the single layer beams, and in Table 6.7, the first five natural frequencies from the double layer beams measurements.

The random field models, for the single and double layer panels, are generated using the KL expansion, numerically solving the eigenproblem from the correlation matrix identified from the light transmissibility measurements. The given rule of mixture was then applied and the resulting Young's modulus and mass density used as input to the proposed FE one and two dimensional models, the HFE and also with the WKB approach for flexural waves.

Natural frequencies were calculated using the FE approach with beam and plate elements, the HFE with plate elements, and also the WKB solution for beams, as described in sections 6.3.4-6.3.6, respectively, using the identified random field and thickness variability. Response statistics were calculated using 5040 Monte Carlo samples and the Coefficient of Variation COV for both the single and double layers are shown in Figure 6.27 and Figure 6.28, respectively, along with the COV calculated from the experimental results.

It appears overall that the proposed models agree very well between themselves, and also with the experimental results. The WKB approach gives the same COV for all of the modes considered, as one could expect, from Eq. (6.22). Moreover, PDFs of the normalised natural frequencies are also compared with the histogram from the experimental results, for the single and double layers beams, Figure 6.29 and

Figure 6.30, respectively. The PDF for all of the approaches presented have good agreement, although there are not enough experimental samples to compare it to the histograms.

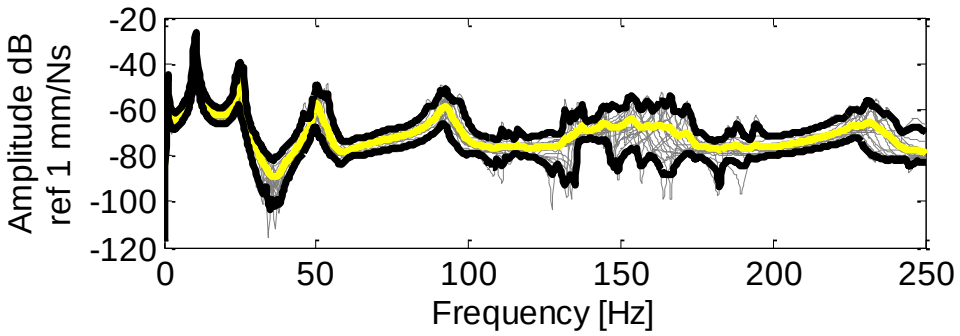

Figure 6.23. The point mobility measured on each of the 20 single layer CSM samples (grey) along with 95% upper and lower percentile (black) and mean value (yellow).

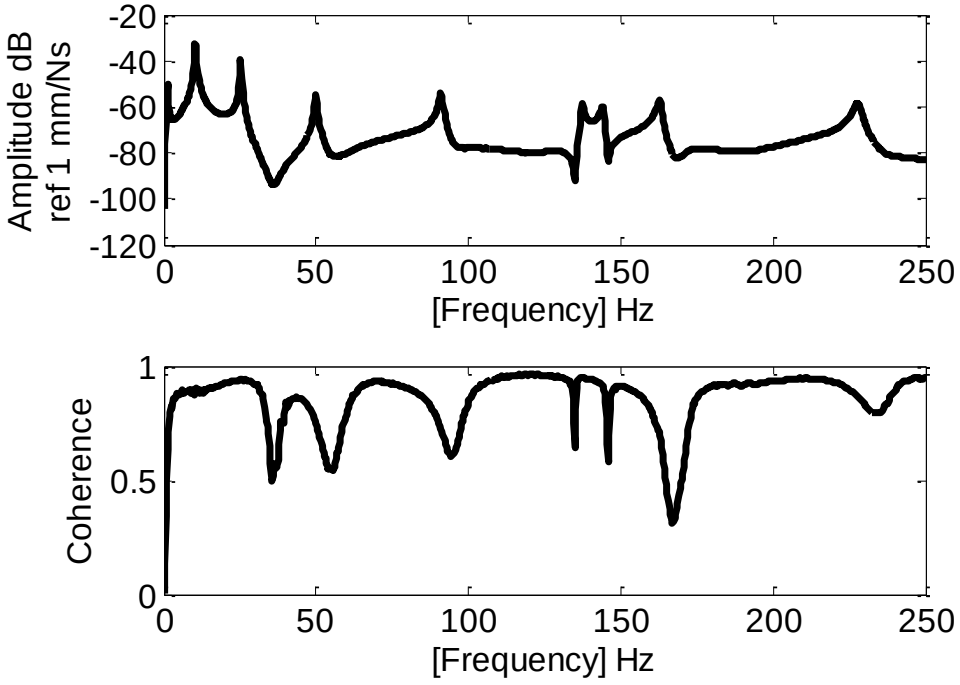

Figure 6.24. Typical amplitude of the mobility measurement along with the coherence for a single layer beam.

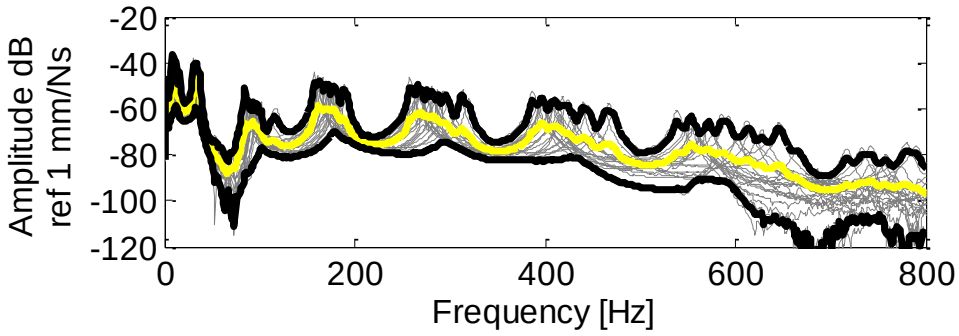

Figure 6.25. The point mobility measured on each of the 21 double layer CSM samples (grey) along with 95% percentile (black) and mean value (yellow).

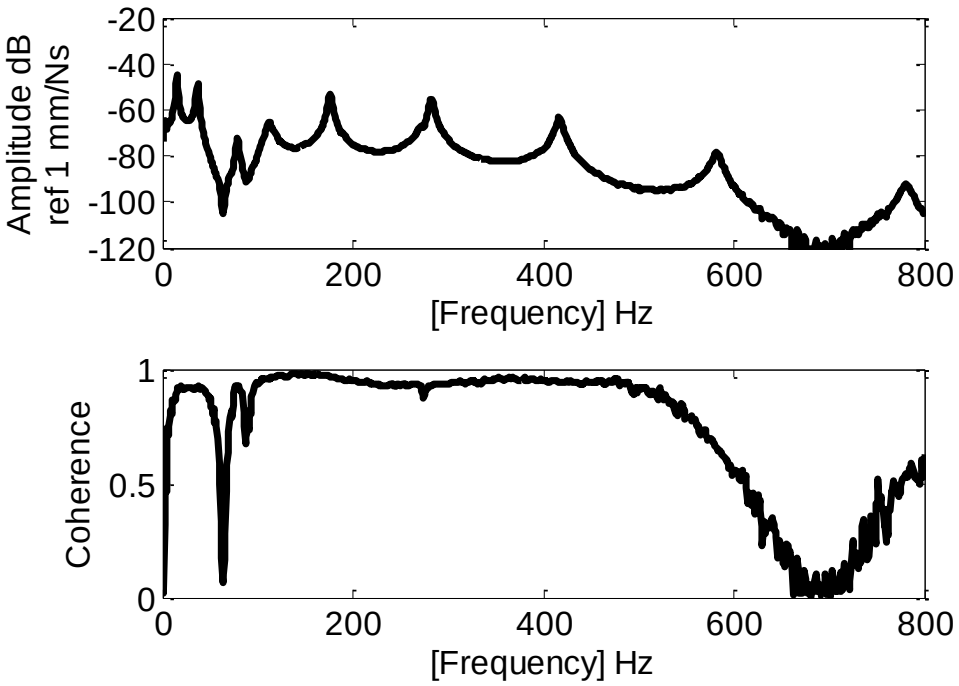

Figure 6.26. Typical amplitude of the mobility measurement along with the coherence for a double layer beam.

Table 6.6. Natural frequencies, in Hz, for the flexural modes of the single layer beams.

Specimen	Mode 1	Mode 2	Mode 3
1_A	24.4	50.0	91.6
1_B	24.4	50.6	93.1
1_D	24.7	53.8	97.2
1_E	24.4	52.5	91.6
1_F	25.0	50.9	95.6
1_G	24.7	50.3	93.4
1_H	25.3	50.9	93.8
1_I	25.0	49.7	92.5
1_J	23.4	46.3	86.9
1_K	24.1	49.4	92.2
1_L	25.9	50.0	91.3
1_M	26.3	50.6	92.5
1_N	25.6	51.9	93.1
1_O	25.0	48.8	89.4
1_P	25.3	50.0	90.9
1_Q	25.3	50.3	92.2
1_R	24.7	50.0	93.8
1_S	24.4	49.1	90.0
1_T	25.0	51.3	94.4
1_U	24.4	50.0	92.8

Table 6.7. Natural frequencies, in Hz, for the flexural modes of the double layer beams.

Specimen	Mode 1	Mode 2	Mode 3	Mode 4
2_A	36.4	102.7	190.5	319.5
2_B	34.5	96.9	188.5	313.5
2_C	35.6	97.5	187.4	311.6
2_D	35.4	98.9	182.5	299.1
2_E	33.5	91.9	178.5	293.5
2_F	33.5	92.8	179.5	296.1
2_G	33.4	92.6	177.6	288.1
2_H	32.6	89.5	173.5	287.1
2_I	33.5	94.6	172.5	281.5
2_J	31.5	87.5	165.6	268.1
2_K	30.5	83.5	161.5	270.1
2_L	32.4	87.8	169.5	275.4
2_M	33.5	94.4	169.5	276.5
2_N	29.5	83.9	157.5	256.9
2_O	31.5	87.5	161.6	266.5
2_P	32.5	91.9	163.4	266.5
2_Q	30.4	83.8	161.5	262.1
2_R	32.5	94.5	163.6	269.5
2_S	32.5	92.9	172.5	283.1
2_T	36.5	118.1*	177.6	281.6
2_U	36.5	111.5*	176.5	282.5

*Outliers replaced by the mean value, 91 Hz

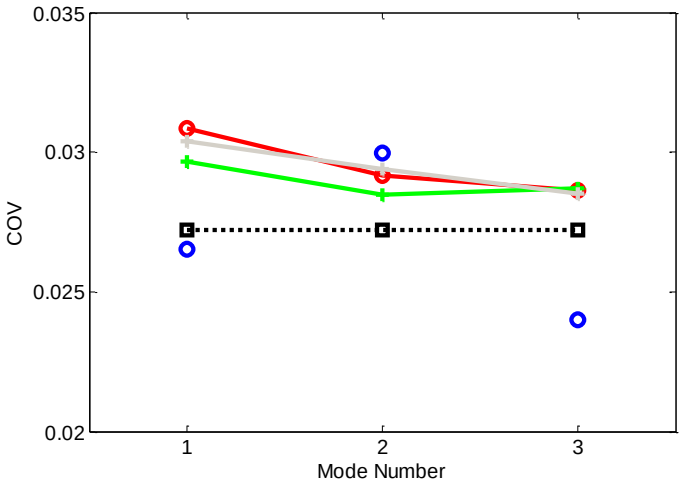

Figure 6.27. Coefficient of Variation COV for the first 3 flexural modes from the experimental results (blue circle), using the two dimensional thin isotropic plate FE elements (red circle), and HFE (grey +), the FE one dimensional EB beam flexural elements (green +) and WKB approximation for flexural waves (black square) on the CSM beams with single layer.

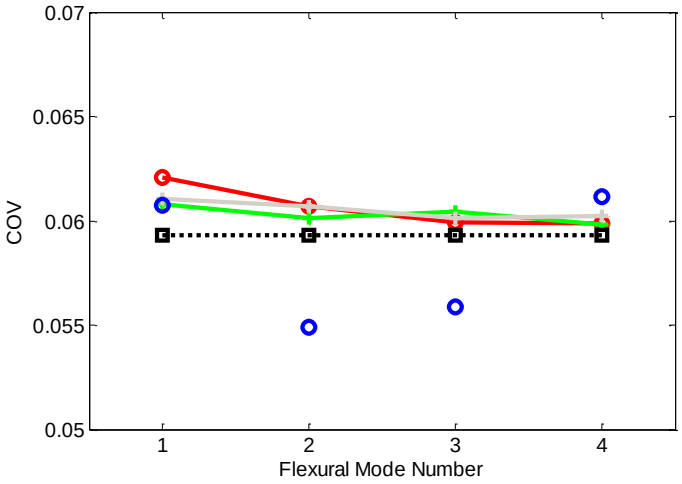

Figure 6.28. Coefficient of Variation COV for the first 4 flexural modes from the experimental results (blue circle), using the two dimensional thin isotropic plate FE elements (red circle), and HFE (grey +), the FE one dimensional EB beam flexural elements (green +) and WKB approximation for flexural waves (black square) on the CSM beams with two layers.

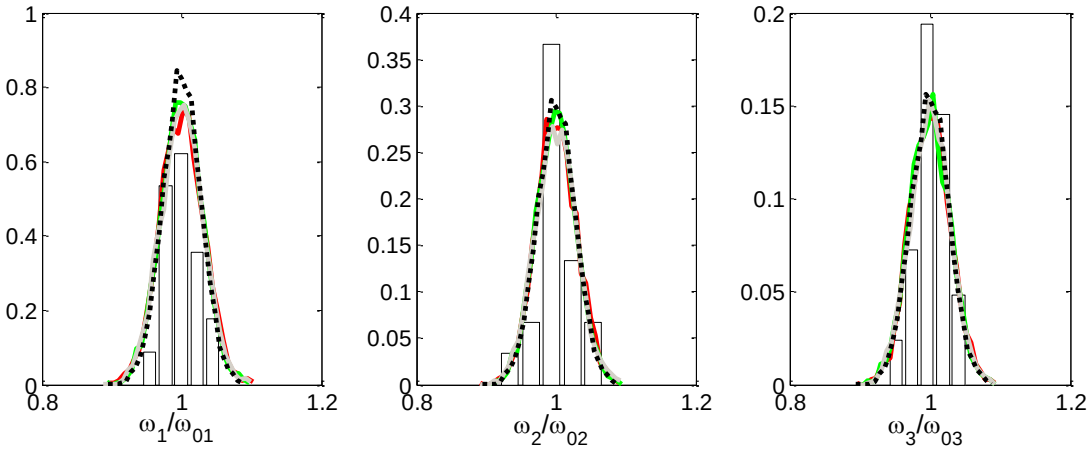

Figure 6.29. Normalized natural frequency PDFs for the first 3 flexural modes from the experimental results (bars) using the 2D thin isotropic plate FE (red full line) and HFE (grey), the FE one dimensional EB beam flexural elements (green dotted) and WKB approximation for flexural waves (black dashed) on the CSM beams with single layer.

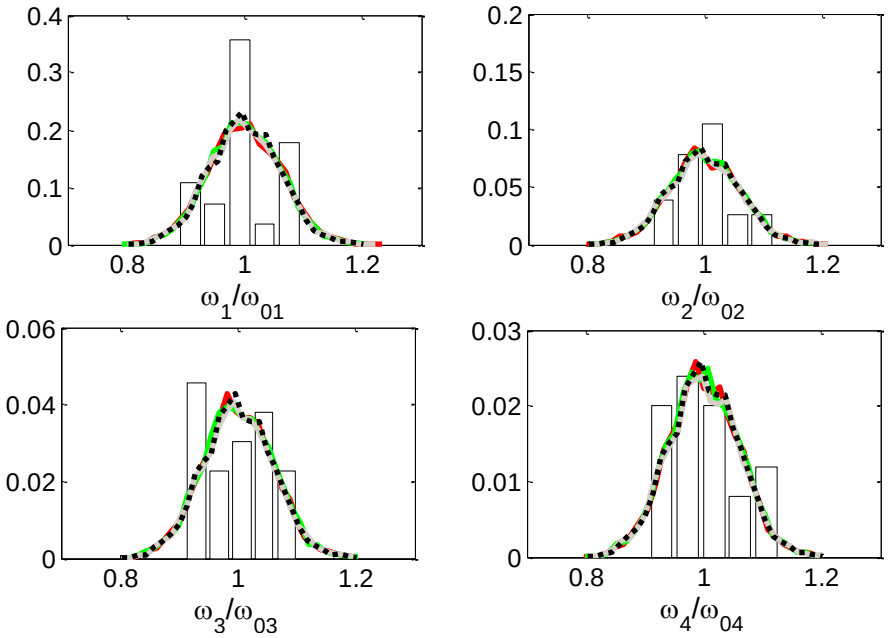

Figure 6.30. Normalized natural frequency PDFs for the first 4 flexural modes from the experimental results (bars) using the 2D thin isotropic plate FE (red full line) and HFE (grey), the FE one dimensional EB beam flexural elements (green dotted) and WKB approximation for flexural waves (blue dashed) on the CSM beams with double layer.

6.3.9 Conclusions

This section presented experimental validation of the proposed modelling approaches using an ensemble of free-free beams whose material variability is characterised by light transmissibility images, using a recently proposed technique examining a digital image with an empirical fitting to determine the variable volume fraction. Then a simple rule of mixture estimated the spatial variability of the nominally isotropic Young's modulus. Two panels were manufactured, one with a single layer of fibre reinforcement, and another with two layers. Based on the optical measurements, it was shown that the Gaussian assumption better represented the marginal distribution of the two layers panel than the single layer. This suggests that a different modelling procedure could be adopted to improve the random field model.

This data was used to calculate a spatial correlation function, assuming the area density as a Gaussian random field, and then to generate a KL expansion. This was applied to the proposed FE formulations – using thin, isotropic and rectangular plate elements, and a one dimensional Euler-Bernoulli beam element – and also the HFE and WKB approach for flexural waves.

The thickness variability also played an important role on the variability of the natural frequencies. Although some measurements were made along the panel, a more dense set of measurements would be needed to better characterise its spatial variability.

The panel was then cut into stripes and mobility measurements were made using a micro hammer excitation and LDV measurements. This procedure created an ensemble of natural frequencies and it was shown that its second order statistics, i.e. COV, agreed very well with the assumed Gaussian random field models. The WKB formulation was shown to agree very well with the other proposed FE models, using the numerically generated random field, but requiring just a fraction of the computational time. The natural frequencies' PDF for these models also have shown a very good agreement amongst themselves, as expected, but more experimental samples would be necessary to better estimate the natural frequency PDF.

6.4 Concluding remarks

In this chapter experimental validations were carried out using two different sets of experiments involving spatially correlated material variability. In both cases a WKB approximation for flexural waves was used, using the results from Chapter 3. In the first case, considering a spatially varying mass density and, in the second, considering varying Young's modulus. Both applications have shown very good agreement not only with the proposed FE models, but also with the experimental results.

In the first experiment, spatially varying material density is generated by adding masses along a cantilever beam, with values following a given random field. The natural frequencies were measured for different correlation lengths, and it is shown that the variability of the natural frequencies increases with larger correlation lengths. Issues concerning the approximation of a discrete set of masses to a continuous mass density distribution were also discussed. It was also shown, in general that a good agreement occurs between the experimental results with the predictions made by the numerical models, including the WKB approach.

The second experiment used a technique to measure the volume fraction spatial distribution along glass fibre reinforced panels, by using light transmission measurements. A simple model of the random field was proposed and its correlation function was estimated from a single panel measurement. This was used to predict the variability in the dynamic response of the beams made from the original panel. The

WKB approximation was shown to be accurate using this purely numerical derived random field, instead of the analytical solution of the KL expansion used so far.

The WKB approach for propagation in one dimension has shown to be as accurate as the FE models in predicting the statistics of the natural frequencies in more practical application, i.e. the modelling of a fibre reinforced composite material using random fields to include spatially correlated variability, and also, considering mass density spatial variability, in addition to the variable Young's modulus that has been considered in the previous chapters.

7. Concluding remarks

7.1 Summary of the present work

In this work, the propagation in one dimensional waveguides was modelled using the WKB approximation, an analytical formulation considering slowly varying properties, i.e. the change given by the random field is such that there is no backscattering from a propagating wave. It is assumed that when propagating over a finite distance, the total phase change of a wave is given by the integral of the spatially distributed wavenumber. This is used to find an analytical expression for the natural frequencies and input mobility of a finite length waveguides undergoing flexural and longitudinal waves.

In addition, a formulation, considering piecewise constant properties along the waveguide propagation axis, is presented together with expressions for natural frequencies and input mobility. This formulation, unlike the previous one, takes internal reflections into account, and is used to compare with the previous results.

A numerical approach based on a FE approximation using enriched hierarchical basis or HFE was presented, where the variability in the properties of the waveguide is included in the element formulation. The series representation of the random field was used in the HFE formulation to derive an element matrix for each term of the expansion. This procedure has to be done only once, and then the random coefficients of the expansion can be sampled in MC framework to calculate the responses statistics. This avoids the element integration procedure that can be computationally costly, for each MC sample of a h-version standard FE model, and it is particularly efficient for highly correlated random fields, because it needs fewer terms in the expansion. A FE model of the waveguide, with the element properties assumed piecewise constant, is assembled for comparison. A single sample of a random field is used to carry out the numerical analysis, being that all the formulations are purely deterministic, and can include both analytical and numerical descriptions of the variability.

The KL expansion, a series representation of random fields, is used to include spatially correlated material random variability in the proposed formulations. A closed form expression for the PDF of the natural frequencies is derived, using a first order approximation, and statistics of the phase change are also evaluated. It also allows an efficient calculation of the statistics of the input mobility to be performed.

In addition, experimental validations was carried out using two different sets of experiments. In both cases, spatially correlated material properties were considered and the statistics of the experimental results are compared with the WKB approximation for flexural waves using a continuous random field as well as the FE approximations. In one of the experiments, the spatial correlation is controlled a priori, and it was shown that the longer the correlation length the higher the standard deviation of the natural frequencies. The experimental results agreed with the proposed WKB approximation for flexural waves, considering the mass density as a continuous random field matching the mass distribution. The second experiment used a technique to measure the volume fraction spatial distribution in glass fibre reinforced panels, by using light transmission measurements. A simple model of the random field was proposed and its correlation function was estimated from a single panel measurement. This was used to predict the variability in the dynamic response of the beams made from the original panel. The WKB approximation was shown to be accurate using this purely numerical derived random field, instead of the analytical solution of the KL expansion used so far.

7.2 Conclusions

Overall, the WKB approximation has shown to be accurate, within its assumptions, i.e. considering slowly varying properties and away from cut on frequencies, using both numerical and analytical descriptions of the random field, with the KL expansion. Moreover, the HFE formulation has also shown to be very accurate when compared to the FE results not being restricted to spatially slowly varying properties and extended to any HFE element library. Moreover, the following general conclusions can be drawn from this study:

- Spatially correlated random variability in the material or geometrical properties plays a key role in the mid-frequency region. Changes not only in the dispersion term but also in the correlation length significantly affect the natural frequency statistics of the dynamic system.

- It has been shown that for a one-dimensional waveguide, the longer the correlation length of the random field representing the spatially correlated material or geometrical properties, the higher the variability in the natural

frequencies. Therefore random homogeneous properties along the waveguide introduce more variability than spatially correlated ones.

- A wave-based approach including variability on the direction in the travelling wave, for one-dimensional waveguides, was developed as a tool to bridge the mid-frequency gap. It reduces the computational time to a tenth when compared to the standard FE approach and provides a suitable framework to account for randomness, using random fields.

- The wave-based approach is restricted in that it considers one-dimensional waveguides with non-homogeneous properties in the direction of the travelling wave, and the WKB approximation is used as a tool to assemble propagation and reflection matrices. Once these matrices are available, the procedure to find forced and free vibration is the same as it have been used for homogeneous waveguides. The WKB approximation is accurate in the one-dimensional dispersive waves in the beam case when the correlation length if bigger than ten percent of the waveguide length.

- Random fields can be included in the WKB formulation both analytically or numerically and it is also extendable to other non-homogeneous random fields.

- The HFE approach can be used to two or three dimensional cases and using different element formulations including random variability and therefore benefits from the KL expansion formulation for speeding up the MC sampling. Moreover, it does not require any assumption on wave propagation, being also applicable to low frequencies, where the WKB method breaks down.

7.3 Suggestions for further research

Throughout this thesis, the WKB and HFE method have been used to model spatially correlated variability in waveguides and the KL expansion has been used as random field model. In this section suggestions for further research are proposed.

- The proposed methods have been used in simple structures, considering separately each wave type, and then a natural extension would be the application

of the proposed approaches to more complex structures and including different wave types and joints in order to evaluate its effects on wave mode conversion.

- Consider the effects of random variability in the joints and connections, along with the spatially correlated random variability.

- The WKB approach is an analytical tool and, as such, it can be very restrictive to be applied to waveguides with complex cross sections. But because it is a wave formulation, it could benefit from a numerical approach like the WFE to widen its applicability.

- In this study, the WKB method has only been applied to one dimensional waveguides, which allows for direct integration of the wavenumber equation. Further research would be required to employ the approach and develop it for two dimensional cases, using more general methods to solve the eikonal equation.

- The HFE could be extended to more complex structures by connecting it to standard FE elements. That would broaden the applicability of method.

- The typical application of the HFE is in the use of composite structures, with the formulation of elements with laminated or different fibres arrangements. This formulation could benefit from the inclusion of random variability in the formulation.

- Throughout the work, only a Gaussian homogenous random field were used to model the random spatial variability, although the formulation does not apply any restriction of this kind. The application of different random field models, using non-Gaussian distribution and different correlation structures could be investigated.

1. Appendix. Scattering and reflection matrices formulations at the piecewise constant waveguide approach

This sections explains the scattering matrix used in the piecewise constant waveguide approach, undergoing longitudinal and flexural vibration, used in Chapters 2 and 3. Assuming two waveguides connected by its degrees of freedom, Figure 1.1.

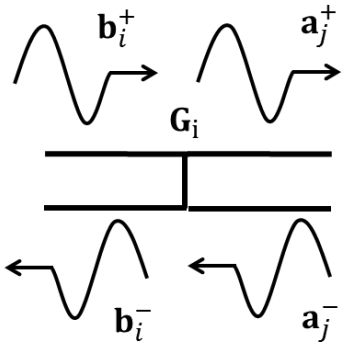

Figure 1.1. Waves at the waveguides junction.

It is convenient to group the displacements and internal forced into two vectors, for each waveguide, named *i* and *j* [22], as

$$\mathbf{W}_{aj} = \boldsymbol{\psi}_{aj}^{+}\mathbf{a}_j^{+} + \boldsymbol{\psi}_{aj}^{-}\mathbf{a}_j^{-}, \tag{1.1}$$

$$\mathbf{W}_{bi} = \boldsymbol{\psi}_{bi}^{+}\mathbf{b}_i^{+} + \boldsymbol{\psi}_{bi}^{-}\mathbf{b}_i^{-}, \tag{1.2}$$

where $\boldsymbol{\psi}_a^+$, $\boldsymbol{\psi}_a^-$, $\boldsymbol{\psi}_b^+$ and $\boldsymbol{\psi}_b^-$ are the displacement matrices for the positive and negative going waves at each respective waveguide, and

$$\mathbf{F}_{aj} = \boldsymbol{\phi}_{aj}^{+}\mathbf{a}_j^{+} + \boldsymbol{\phi}_{aj}^{-}\mathbf{a}_j^{-}, \tag{1.3}$$

$$\mathbf{F}_{bi} = \boldsymbol{\phi}_{bi}^{+}\mathbf{b}_i^{+} + \boldsymbol{\phi}_{bi}^{-}\mathbf{b}_i^{-}, \tag{1.4}$$

where $\boldsymbol{\phi}_{aj}^+$, $\boldsymbol{\phi}_{aj}^-$, $\boldsymbol{\phi}_{bi}^+$ and $\boldsymbol{\phi}_{bi}^-$ are the internal forces matrices for the positive and negative going waves at each respective waveguide. Equilibrium and continuity conditions, can be written as

$$\mathbf{C}_{aj}\mathbf{W}_{aj} = \mathbf{C}_{bi}\mathbf{W}_{bi}, \tag{1.5}$$

$$\mathbf{E}_{aj}\mathbf{F}_{aj} = \mathbf{E}_{bi}\mathbf{F}_{bi}, \tag{1.6}$$

where $\mathbf{C}_{aj}$ and $\mathbf{C}_{bi}$ are the continuity matrices and $\mathbf{E}_{aj}$ and $\mathbf{E}_{bi}$ are the equilibrium matrices. A scattering matrix $\mathbf{G_i}$, relating the waves from the left side of the junction to the waves at its right side, Figure 1.1, can be defined as

$$\begin{Bmatrix}\mathbf{a}_j^+\\ \mathbf{a}_j^-\end{Bmatrix} = \mathbf{G}_i \begin{Bmatrix}\mathbf{b}_i^+\\ \mathbf{b}_i^-\end{Bmatrix}. \tag{1.7}$$

Applying the equilibrium and continuity conditions, and assuming the matrix inversion exists, thus

$$\mathbf{G}_i = \begin{bmatrix}\mathbf{C}_{aj}\boldsymbol{\psi}_{aj}^+ & \mathbf{C}_{aj}\boldsymbol{\psi}_{aj}^-\\ \mathbf{E}_{aj}\boldsymbol{\phi}_{aj}^+ & \mathbf{E}_{aj}\boldsymbol{\phi}_{aj}^-\end{bmatrix}^{-1} \begin{bmatrix}\mathbf{C}_{bi}\boldsymbol{\psi}_{bi}^+ & \mathbf{C}_{bi}\boldsymbol{\psi}_{bi}^-\\ \mathbf{E}_{bi}\boldsymbol{\phi}_{bi}^+ & \mathbf{E}_{bi}\boldsymbol{\phi}_{bi}^-\end{bmatrix}. \tag{1.8}$$

Moreover, the block element $\mathbf{G}_{ij}$ can be given as

$$\begin{aligned}\mathbf{G}_{i11} = &-\mathbf{E}_{bi}\boldsymbol{\phi}_{bi}^+\left(\mathbf{C}_{aj}\boldsymbol{\psi}_{aj}^+\right)^{-1}\mathbf{C}_{aj}\boldsymbol{\psi}_{aj}^-\left(\mathbf{E}_{aj}\boldsymbol{\phi}_{aj}^-\right.\\ &\left.-\mathbf{E}_{aj}\boldsymbol{\phi}_{aj}^+\left(\mathbf{C}_{aj}\boldsymbol{\psi}_{aj}^+\right)^{-1}\mathbf{C}_{aj}\boldsymbol{\psi}_{aj}^-\right)^{-1}\\ &+\mathbf{C}_{bi}\boldsymbol{\psi}_{bi}^+\left(\mathbf{C}_{aj}\boldsymbol{\psi}_{aj}^+-\mathbf{C}_{aj}\boldsymbol{\psi}_{aj}^-\left(\mathbf{E}_{aj}\boldsymbol{\phi}_{aj}^-\right)^{-1}\mathbf{E}_{aj}\boldsymbol{\phi}_{aj}^+\right)^{-1},\end{aligned} \tag{1.9}$$

$$\begin{aligned}\mathbf{G}_{i12} = &-\mathbf{E}_{bi}\boldsymbol{\phi}_{bi}^-\left(\mathbf{C}_{aj}\boldsymbol{\psi}_{aj}^+\right)^{-1}\mathbf{C}_{aj}\boldsymbol{\psi}_{aj}^-\left(\mathbf{E}_{aj}\boldsymbol{\phi}_{aj}^-\right.\\ &\left.-\mathbf{E}_{aj}\boldsymbol{\phi}_{aj}^+\left(\mathbf{C}_{aj}\boldsymbol{\psi}_{aj}^+\right)^{-1}\mathbf{C}_{aj}\boldsymbol{\psi}_{aj}^-\right)^{-1}\\ &+\mathbf{C}_{bi}\boldsymbol{\psi}_{bi}^-\left(\mathbf{C}_{aj}\boldsymbol{\psi}_{aj}^+-\mathbf{C}_{aj}\boldsymbol{\psi}_{aj}^-\left(\mathbf{E}_{aj}\boldsymbol{\phi}_{aj}^-\right)^{-1}\mathbf{E}_{aj}\boldsymbol{\phi}_{aj}^+\right)^{-1},\end{aligned} \tag{1.10}$$

$$\begin{aligned}\mathbf{G}_{i21} = &-\mathbf{C}_{bi}\boldsymbol{\psi}_{bi}^+\left(\mathbf{E}_{aj}\boldsymbol{\phi}_{aj}^-\right)^{-1}\mathbf{E}_{aj}\boldsymbol{\phi}_{aj}^+\left(\mathbf{C}_{aj}\boldsymbol{\psi}_{aj}^+\right.\\ &\left.-\mathbf{C}_{aj}\boldsymbol{\psi}_{aj}^-\left(\mathbf{E}_{aj}\boldsymbol{\phi}_{aj}^-\right)^{-1}\mathbf{E}_{aj}\boldsymbol{\phi}_{aj}^+\right)^{-1}\\ &+\mathbf{E}_{bi}\boldsymbol{\phi}_{bi}^+\left(\mathbf{E}_{aj}\boldsymbol{\phi}_{aj}^--\mathbf{E}_{aj}\boldsymbol{\phi}_{aj}^+\left(\mathbf{C}_{aj}\boldsymbol{\psi}_{aj}^+\right)^{-1}\mathbf{C}_{aj}\boldsymbol{\psi}_{aj}^-\right)^{-1},\end{aligned} \tag{1.11}$$

$$\begin{aligned}\mathbf{G}_{i22} = &-\mathbf{C}_{bi}\boldsymbol{\psi}_{bi}^-\left(\mathbf{E}_{aj}\boldsymbol{\phi}_{aj}^-\right)^{-1}\mathbf{E}_{aj}\boldsymbol{\phi}_{aj}^+\left(\mathbf{C}_{aj}\boldsymbol{\psi}_{aj}^+\right.\\ &\left.-\mathbf{C}_{aj}\boldsymbol{\psi}_{aj}^-\left(\mathbf{E}_{aj}\boldsymbol{\phi}_{aj}^-\right)^{-1}\mathbf{E}_{aj}\boldsymbol{\phi}_{aj}^+\right)^{-1}\\ &+\mathbf{E}_{bi}\boldsymbol{\phi}_{bi}^-\left(\mathbf{E}_{aj}\boldsymbol{\phi}_{aj}^--\mathbf{E}_{aj}\boldsymbol{\phi}_{aj}^+\left(\mathbf{C}_{aj}\boldsymbol{\psi}_{aj}^+\right)^{-1}\mathbf{C}_{aj}\boldsymbol{\psi}_{aj}^-\right)^{-1},\end{aligned} \tag{1.12}$$

It is also possible to write the scattering matrix $\mathbf{T}_{\boldsymbol{i}}$, at the i^{th} junction relating the wave incoming to the junction to the waves going out of the junction

$$\begin{Bmatrix}\mathbf{a}^+\\ \mathbf{b}^-\end{Bmatrix} = \mathbf{T}_{\boldsymbol{i}} \begin{Bmatrix}\mathbf{a}^-\\ \mathbf{b}^+\end{Bmatrix}. \tag{1.13}$$

Also applying the equilibrium and continuity conditions, and assuming the matrix inversion exists, thus

$$\mathbf{T}_{\boldsymbol{i}} = \begin{bmatrix}\mathbf{C}_{ja}\boldsymbol{\psi}_{aj}^+ & -\mathbf{C}_{bi}\boldsymbol{\psi}_{bi}^-\\ \mathbf{E}_{aj}\boldsymbol{\phi}_{aj}^+ & -\mathbf{E}_{bi}\boldsymbol{\phi}_{bi}^-\end{bmatrix}^{-1} \begin{bmatrix}-\mathbf{C}_{aj}\boldsymbol{\psi}_{aj}^- & \mathbf{C}_{bi}\boldsymbol{\psi}_{bi}^+\\ -\mathbf{E}_{aj}\boldsymbol{\phi}_{aj}^+ & \mathbf{E}_{bi}\boldsymbol{\phi}_{bi}^+\end{bmatrix}. \tag{1.14}$$

Yet, this matrix can be partitioned in terms of reflection and transmission matrices

$$\mathbf{T}_i = \begin{bmatrix} \mathbf{r}_i^+ & \mathbf{t}_i^+ \\ \mathbf{t}_i^- & \mathbf{r}_i^- \end{bmatrix}, \tag{1.15}$$

where $\mathbf{t}_i^+$ and $\mathbf{r}_i^+$are the transmission and reflection matrices from the left to the right, and $\mathbf{t}_i^-$ and $\mathbf{r}_i^-$are the transmission and reflection matrices from the right to the left. They are related to $\mathbf{G}_i$ by

$$\mathbf{r}_i^+ = \mathbf{G}_{i12}\mathbf{G}_{i22}^{-1}, \tag{1.16}$$

$$\mathbf{t}_i^+ = \mathbf{G}_{i11} - \mathbf{G}_{i12}\mathbf{G}_{i22}^{-1}\mathbf{G}_{i21}, \tag{1.17}$$

$$\mathbf{t}_i^- = \mathbf{G}_{i22}^{-1} \tag{1.18}$$

$$\mathbf{r}_i^- = -\mathbf{G}_{i22}^{-1}\mathbf{G}_{i21}, \tag{1.19}$$

In the coupling between two waveguides undergoing longitudinal waves, *i* and *j*, with different properties, as used in Chapter 2, k_{Li} and k_{Lj} are their respective wavenumber, and EA_i and EA_j are the Young's modulus of elasticity times the area of the cross-section. The continuity and equilibrium matrices are $\mathbf{C_a} = \mathbf{C_b} = \mathbf{E_a} = \mathbf{E_b} = 1$, the displacement matrices are $\boldsymbol{\psi}_\mathbf{a}^+ = \boldsymbol{\psi}_\mathbf{a}^- = \boldsymbol{\psi}_\mathbf{b}^+ = \boldsymbol{\psi}_\mathbf{b}^- = 1$, and internal forces matrices are $\boldsymbol{\phi}_\mathbf{a}^+ = -iEA_jk_{Lj}$, $\boldsymbol{\phi}_\mathbf{a}^- = iEA_jk_{Lj}$, $\boldsymbol{\phi}_\mathbf{b}^+ = -iEA_ik_{Li}$, $\boldsymbol{\phi}_\mathbf{b}^- = iEA_ik_{Li}$. This leads to the scattering matrix

$$\mathbf{G} = \begin{pmatrix} \frac{1}{2} + \frac{EA_1k_1}{2EA_2k_2} & \frac{1}{2} - \frac{EA_1k_1}{2EA_2k_2} \\ \frac{1}{2} - \frac{EA_1k_1}{2EA_2k_2} & \frac{1}{2} + \frac{EA_1k_1}{2EA_2k_2} \end{pmatrix}. \tag{1.20}$$

Moreover, in the case of the coupling between two waveguides undergoing flexural waves, *i* and *j*, with different properties, as used in Chapter 3, k_{Bi} and k_{Bj} are their respective wavenumber, where EI_i and EI_j are the Young's modulus of elasticity times the moment of area. The continuity and equilibrium matrices are $\mathbf{C}_{aj} = \mathbf{C}_{bi} = \mathbf{E}_{aj} = \mathbf{E}_{bi} = \begin{pmatrix} 1 & 0 \\ 0 & 1 \end{pmatrix}$, the displacement matrices are $\boldsymbol{\psi}_{bi}^+ = \begin{pmatrix} 1 & 1 \\ -ik_{Bi} & -k_{Bi} \end{pmatrix}$, $\boldsymbol{\psi}_{bi}^- = \begin{pmatrix} 1 & 1 \\ ik_{Bi} & k_{BI} \end{pmatrix}$, $\boldsymbol{\psi}_{aj}^+ = \begin{pmatrix} 1 & 1 \\ -ik_{Bj} & -k_{Bj} \end{pmatrix}$, $\boldsymbol{\psi}_{aj}^- = \begin{pmatrix} 1 & 1 \\ ik_{Bj} & k_{Bj} \end{pmatrix}$, and internal forces matrices are $\boldsymbol{\phi}_{bi}^+ = EI_i \begin{pmatrix} -ik_{Bi}^3 & k_{BI}^3 \\ -k_{BI}^2 & k_{BI}^2 \end{pmatrix}$, $\boldsymbol{\phi}_{bi}^- = EI_i \begin{pmatrix} ik_{Bi}^3 & -k_{Bi}^3 \\ -k_{Bi}^2 & k_{Bi}^2 \end{pmatrix}$,

$\boldsymbol{\phi}_{aj}^{+} = EI_j \begin{pmatrix} -ik_{Bj}^3 & k_{Bj}^3 \\ -k_{Bj}^2 & k_{Bj}^2 \end{pmatrix}$, $\boldsymbol{\phi}_{aj}^{-} = EI_j \begin{pmatrix} ik_{Bj}^3 & -k_{Bj}^3 \\ -k_{Bj}^2 & k_{Bj}^2 \end{pmatrix}$. This leads to the scattering matrix

$$\mathbf{G}_{i11} = \frac{\mathbf{1}}{4Z_j k_{Bj}} \begin{pmatrix} (k_i + k_j)(Z_i + Z_j) & i(k_i + ik_j)(Z_i - Z_j) \\ -i(k_1 - ik_2)(Z_1 - Z_2) & (k_i + k_j)(Z_i + Z_j) \end{pmatrix}, \tag{1.21}$$

$$\mathbf{G}_{i12} = \frac{\mathbf{1}}{4Z_j k_{Bj}} \begin{pmatrix} -(k_i - k_j)(Z_i + Z_j) & -i(k_i - ik_j)(Z_i - Z_j) \\ i(k_1 + ik_2)(Z_1 - Z_2) & (k_i - k_j)(Z_i + Z_j) \end{pmatrix}, \tag{1.22}$$

$$\mathbf{G}_{i21} = \mathbf{G}_{i12}, \tag{1.23}$$

$$\mathbf{G}_{i22} = \mathbf{G}_{i11}, \tag{1.24}$$

where $Z_i = EI_i k_{Bi}^2$ and $Z_j = EI_j k_{Bj}^2$.

2. Appendix. Natural frequencies and added masses for each individual experimental case

In Chapter 6, the statistics of the experimentally obtained natural frequencies from a cantilever beam with attached equally spaced masses are shown. In this appendix, these results are presented for each specific case, as well as the values of the added masses for each one of the given correlation case.

Five different correlation lengths were used $b = 0$, or uncorrelated; $b = 0.10\,L$; $b = 0.25\,L$; $b = 0.60\,L$ and; $b = \infty$, i.e. fully correlated. For the former four cases, twenty samples of masses were generated for each one of the ten positions along the beam, from x_1 to x_{10}. Table 2.1 - Table 2.4 present the values of the masses, in grams, added to the bare uniform beam for each individual sample, and individual position, for the four former cases, respectively. Table 2.5 - Table 2.8 give their respective natural frequencies, in Hz, for the 2^{nd} to the 7^{th} flexural mode, obtained for each one of the individual samples.

For the former correlation length case, $b = \infty$, the values of the added masses were the same for each of the ten positions. Therefore, only thirteen different specimens were available in the set of integer numbers for masses between 0 g to 12 g. Table 2.9 presents the natural frequencies, in Hz, obtained from the measurements, for the 2^{nd} to 7^{th} mode, for each one of these individual values.

Table 2.1. The twenty specimens of added masses, in grams, to the cantilever beam in each one of the ten positions for the uncorrelated case.

Sample	x_1	x_2	x_3	x_4	x_5	x_6	x_7	x_8	x_9	x_{10}
1	4	7	4	8	6	7	4	8	5	6
2	5	7	10	8	6	5	6	4	6	8
3	6	8	5	7	7	3	5	8	4	6
4	4	4	4	8	6	7	5	6	8	3
5	4	8	9	4	7	4	7	6	4	7
6	9	6	4	4	4	7	7	4	8	4
7	9	2	5	8	6	6	5	10	5	7
8	8	5	9	7	3	5	6	7	7	7
9	3	3	9	8	7	9	10	4	6	7
10	6	6	6	8	1	6	5	5	6	7
11	5	6	3	4	5	6	4	4	7	6
12	9	7	4	2	6	6	7	8	6	6
13	5	8	6	5	5	10	7	7	7	7
14	7	6	9	6	4	5	8	8	8	6
15	6	2	8	6	6	8	5	7	5	5
16	7	6	3	5	12	7	6	5	2	6
17	0	4	3	6	8	7	5	3	5	4
18	7	5	9	6	3	6	7	5	7	7
19	7	5	6	6	6	3	6	4	6	4
20	9	8	5	10	8	8	2	3	5	5

Table 2.2. The twenty specimens of added masses, in grams, to the cantilever beam in each one of the ten positions for the correlation length $b = 0.10L$.

Sample	x_1	x_2	x_3	x_4	x_5	x_6	x_7	x_8	x_9	x_{10}
1	8	8	3	1	2	5	8	5	7	6
2	6	9	9	11	10	11	7	8	4	7
3	7	7	7	5	7	5	9	6	9	6
4	6	8	9	8	8	5	7	7	6	6
5	7	4	6	5	6	4	5	3	6	6
6	4	5	4	7	5	3	7	6	7	6
7	4	5	2	6	6	8	7	7	5	5
8	8	7	7	9	9	6	5	7	6	5
9	7	6	4	4	5	5	6	6	10	8
10	7	5	4	8	7	7	5	8	9	6
11	4	5	4	5	4	3	5	3	5	6
12	5	6	4	7	7	6	5	3	7	6
13	6	5	6	5	4	6	5	4	6	5
14	7	5	4	4	5	4	4	5	3	7
15	6	6	6	7	7	6	5	7	8	7
16	6	8	5	6	4	8	9	8	1	7
17	5	7	4	5	5	8	7	5	7	7
18	5	8	3	2	1	4	6	7	7	8
19	4	5	6	6	10	9	8	7	7	3
20	10	8	6	5	7	4	4	6	10	8

Table 2.3. The twenty specimens of added masses, in grams, to the cantilever beam in each one of the ten positions for the correlation length $b = 0.25L$.

Sample	x_1	x_2	x_3	x_4	x_5	x_6	x_7	x_8	x_9	x_{10}
1	7	4	5	6	5	7	5	4	4	3
2	5	5	6	6	8	8	8	8	6	7
3	8	8	8	8	9	8	9	7	8	8
4	8	7	7	7	7	7	6	6	6	8
5	7	6	5	5	2	3	6	9	9	9
6	5	3	4	3	3	3	3	5	7	9
7	4	3	4	6	7	4	5	6	7	9
8	4	4	4	5	7	6	7	6	5	4
9	6	6	5	1	0	1	2	2	2	3
10	11	11	12	11	8	7	6	7	5	6
11	6	4	5	4	4	6	8	7	5	5
12	7	8	5	2	3	4	7	5	4	4
13	9	11	9	7	9	6	6	4	3	5
14	9	7	7	4	7	5	4	6	5	6
15	5	5	8	8	10	9	9	9	8	7
16	4	4	3	3	4	2	5	6	7	6
17	9	11	10	7	7	6	6	9	12	10
18	4	5	4	4	3	4	5	8	10	9
19	8	9	10	7	3	2	2	4	4	8
20	6	6	8	8	7	8	7	4	2	4

Table 2.4. The twenty specimens of added masses, in grams, to the cantilever beam in each one of the ten positions for the correlation length $b = 0.60L$.

Sample	x_1	x_2	x_3	x_4	x_5	x_6	x_7	x_8	x_9	x_{10}
1	3	2	3	3	3	3	4	6	6	6
2	8	8	7	6	6	6	6	5	5	4
3	4	4	4	1	0	1	1	1	4	5
4	7	8	6	6	8	6	5	5	5	5
5	9	7	6	6	5	5	7	7	8	8
6	6	5	6	4	5	6	6	5	4	5
7	5	6	4	5	7	6	5	5	4	4
8	6	8	8	7	6	5	7	7	8	6
9	7	7	7	6	6	4	4	2	2	2
10	10	9	8	6	8	10	11	12	11	11
11	5	6	7	8	8	9	8	8	7	8
12	5	5	4	4	4	5	5	5	5	5
13	7	7	6	7	7	8	10	7	7	6
14	5	5	6	6	6	6	6	6	7	9
15	4	5	5	5	3	3	2	3	4	3
16	2	2	1	1	0	2	2	2	4	4
17	5	6	6	5	5	4	5	5	5	4
18	4	4	5	7	6	7	6	5	4	4
19	6	7	7	6	5	6	5	5	5	4
20	7	7	7	7	8	9	8	6	5	6

Table 2.5. Natural frequencies, in Hz, from the twenty specimens of added masses to the cantilever beam in each one of the ten positions for the uncorrelated case.

Sample	Mode 2	Mode 3	Mode 4	Mode 5	Mode 6	Mode 7
1	159.5	308.9	503.8	761.7	1072.9	57.4
2	156.6	307.6	502.6	751.7	1063.9	56.7
3	158.7	308.8	505.8	760.3	1078.4	57.7
4	160.9	313.0	510.3	759.0	1074.7	57.5
5	157.5	306.4	509.6	757.7	1074.3	57.3
6	162.5	314.0	507.6	759.9	1084.4	58.3
7	158.7	310.3	509.8	761.9	1068.0	57.2
8	157.3	309.5	505.1	754.8	1062.8	57.3
9	156.4	308.3	502.8	749.3	1058.0	55.7
10	159.1	313.8	506.3	765.9	1080.7	57.8
11	163.8	314.0	511.6	769.3	1088.4	58.2
12	161.6	309.4	508.7	760.3	1073.0	58.1
13	158.8	305.9	499.8	753.8	1063.2	56.8
14	157.3	308.5	502.4	753.7	1058.0	57.4
15	159.8	311.6	511.3	763.7	1062.3	57.4
16	161.1	310.0	509.8	764.7	1076.7	56.7
17	162.9	316.0	511.5	769.4	1089.6	57.5
18	158.2	311.0	507.0	757.3	1066.2	57.5
19	161.8	315.0	512.3	767.6	1088.3	58.4
20	160.2	308.8	496.4	757.8	1068.1	56.8

Table 2.6. Natural frequencies, in Hz, from the twenty specimens of added masses to the cantilever beam in each one of the ten positions for the correlation length $b = 0.10L$.

Sample	Mode 2	Mode 3	Mode 4	Mode 5	Mode 6	Mode 7
1	59.1	163.5	314.6	509.4	768.2	1089.9
2	55.4	154.7	299.8	494.0	745.0	1042.3
3	57.3	159.1	308.6	501.2	747.8	1063.0
4	56.9	156.9	305.5	500.9	749.0	1059.0
5	58.1	162.5	315.5	514.0	768.5	1086.5
6	58.0	161.0	314.7	507.9	763.5	1088.8
7	57.7	162.1	312.6	507.3	764.2	1082.4
8	56.8	158.3	306.0	502.4	750.0	1060.8
9	57.6	161.3	310.7	506.1	757.9	1076.5
10	56.9	159.7	308.4	501.9	752.8	1065.2
11	58.5	162.8	317.6	515.2	773.5	1103.2
12	57.3	161.7	313.0	507.2	761.8	1083.5
13	58.3	161.9	314.6	512.1	767.0	1082.3
14	58.2	162.7	314.6	516.3	774.6	1091.6
15	57.0	159.3	307.8	504.4	755.4	1065.2
16	57.3	158.1	308.9	505.2	764.0	1074.8
17	57.2	160.6	309.7	503.5	758.3	1073.7
18	58.8	162.3	313.2	510.6	771.0	1089.7
19	56.8	160.1	306.6	503.2	750.5	1056.2
20	57.3	160.4	307.1	503.4	752.5	1065.9

Table 2.7. Natural frequencies, in Hz, from the twenty specimens of added masses to the cantilever beam in each one of the ten positions for the correlation length $b = 0.25L$.

Sample	Mode 2	Mode 3	Mode 4	Mode 5	Mode 6	Mode 7
1	58.2	162.6	316.6	513.9	766.0	1084.2
2	56.5	158.2	307.1	504.2	751.2	1060.6
3	55.8	155.7	303.0	494.5	736.9	1049.5
4	56.7	158.3	307.6	503.4	751.3	1064.8
5	58.1	159.8	311.9	508.3	759.6	1077.9
6	58.6	164.1	318.0	521.1	775.4	1099.7
7	57.2	161.6	313.9	513.0	762.1	1087.5
8	57.8	162.0	314.2	511.9	760.8	1083.7
9	61.1	166.6	323.7	528.7	792.2	1121.8
10	56.2	154.1	301.0	493.9	739.4	1042.6
11	58.2	161.6	314.4	512.6	768.4	1077.9
12	59.3	162.7	314.3	513.2	770.7	1089.5
13	57.0	158.2	304.8	501.8	751.0	1066.3
14	57.9	161.5	308.7	511.6	762.7	1071.5
15	55.8	156.8	302.9	497.7	742.2	1045.3
16	59.1	164.1	317.6	518.1	776.1	1098.6
17	56.1	155.0	299.2	492.6	692.6*	1037.4
18	58.1	161.3	312.8	510.5	768.2	1082.8
19	58.2	158.9	311.4	510.0	769.5	1081.9
20	57.3	158.9	310.6	506.3	760.8	1070.2

*Outliner replaced by mean value, 761.

Table 2.8. Natural frequencies, in Hz, from the twenty specimens of added masses to the cantilever beam in each one of the ten positions for the correlation length $b = 0.60L$.

Sample	Mode 2	Mode 3	Mode 4	Mode 5	Mode 6	Mode 7
1	59.2	165.4	320.5	522.8	782.7	1103.6
2	57.8	160.3	309.0	505.4	756.7	1070.0
3	60.8	168.0	325.2	530.9	798.7	1127.3
4	57.2	160.0	307.5	503.5	756.1	1067.0
5	57.2	158.6	308.0	500.8	751.9	1062.4
6	58.1	161.6	312.5	512.7	768.2	1077.8
7	58.0	162.2	312.3	510.8	767.0	1082.8
8	57.1	157.1	306.2	499.1	747.4	1059.0
9	58.8	162.5	315.7	514.3	770.3	1091.8
10	54.9	153.1	295.9	483.6	727.0	1018.8
11	55.6	156.2	304.0	496.7	747.5	1047.9
12	58.4	162.6	315.3	512.1	771.8	1087.8
13	56.4	157.4	306.7	497.6	745.9	1057.4
14	56.8	159.0	310.0	504.4	759.8	1070.3
15	59.6	164.6	303.6	521.1	783.1	1098.8
16	61.2	170.0	328.6	534.4	803.6	1128.9
17	58.6	161.7	312.8	514.1	765.8	1082.0
18	57.8	161.5	313.3	512.9	763.8	1077.7
19	57.9	160.3	309.9	508.6	762.6	1071.6
20	56.2	157.9	305.1	499.7	750.5	1056.6

Table 2.9. Natural frequencies, in Hz from each sample of added masses, in grams, equally distributed to the cantilever beam in each one of the ten positions.

Added mass	Mode 2	Mode 3	Mode 4	Mode 5	Mode 6	Mode 7
0	63.0	174.9	337.6	546.3	820.7	1159.4
1	61.9	171.9	331.5	538.0	808.0	1142.5
2	60.9	169.2	326.7	531.8	796.7	1126.4
3	59.9	166.7	322.2	524.9	785.6	1111.6
4	59.1	164.3	318.1	519.1	776.2	1098.1
5	58.2	161.9	313.5	511.3	766.1	1079.9
6	57.5	159.8	309.6	504.9	757.8	1067.3
7	56.7	157.6	305.4	498.4	747.5	1053.8
8	56.2	156.1	302.4	493.6	740.1	1043.1
9	55.3	153.9	298.3	487.3	730.7	1030.5
10	54.6	152.2	295.0	481.8	722.3	1019.1
11	53.9	150.4	292.1	477.1	714.8	1009.0
12	53.3	149.1	289.3	472.2	707.4	999.5

List of References

[1] M. Petyt, Introduction to Finite Element Vibration Analysis, 2nd ed., Cambridge University Press, New York, USA, 2010.

[2] O.C. Zienkiewicz, K. Morgan, Finite Elements & Approximation, Dover Publications, 1983.

[3] A. Deraemaeker, I. Babuška, P. Bouillard, Dispersion and pollution of the FEM solution for the Helmholtz equation in one, two and three dimensions, International Journal for Numerical Methods in Engineering, 46 (1999) 471-499.

[4] R.Y. Rubinstein, D.P. Kroese, Simulation and the Monte Carlo Method, Second Edition ed., John Wiley & Sons, Inc., Hoboken, NJ, USA, 2007.

[5] R. Ohayon, C. Soize, Structural Acoustic and Vibration: Mechanical Models, Variational Formulations and Discretization, Academic Press, San Diego, CA, 1998.

[6] "MID-FREQUENCY" – CAE Methodologies for Mid-Frequency Analysis in Vibration and Acoustics, Katholieke Universiteit Leuven - Faculty of Engineering, Belgium, 2012.

[7] R.H. Lyon, R.G. Dejong, Theory and Application of Statistical Energy Analysis, Butterworth-Heinemann, Boston, 1995.

[8] B. Van Genechten, O. Atak, B. Bergen, E. Deckers, S. Jonckheere, J.S. Lee, A. Maressa, K. Vergote, B. Pluymers, D. Vandepitte, W. Desmet, An efficient Wave Based Method for solving Helmholtz problems in three-dimensional bounded domains, Engineering Analysis with Boundary Elements, 36 (2012) 63-75.

[9] O. Atak, B. Bergen, D. Huybrechs, B. Pluymers, W. Desmet, Coupling of Boundary Element and Wave Based Methods for the efficient solution of complex multiple scattering problems, Journal of Computational Physics, 258 (2014) 165-184.

[10] J.F. Doyle, Wave Propagation in Structures, Springer, New York, 1997.

[11] U. Lee, Spectral Element Method in Structural Dynamics, John Wiley & Sons, Singapore, 2009.

[12] L. Gavrić, Computation of propagative waves in free rail using a finite element technique, Journal of Sound and Vibration, 185 (1995) 531-543.

[13] B.R. Mace, D. Duhamel, M.J. Brennan, L. Hinke, Finite element prediction of wave motion in structural waveguides, The Journal of the Acoustical Society of America, 117 (2005) 2835-2843.

[14] B.R. Mace, E. Manconi, Modelling wave propagation in two-dimensional structures using finite element analysis, Journal of Sound and Vibration, 318 (2008) 884-902.

[15] M.N. Ichchou, J. Berthaut, M. Collet, Multi-mode wave propagation in ribbed plates: Part I, wavenumber-space characteristics, International Journal of Solids and Structures, 45 (2008) 1179-1195.

[16] M.N. Ichchou, F. Bouchoucha, M.A. Ben Souf, O. Dessombz, M. Haddar, Stochastic wave finite element for random periodic media through first-order perturbation, Computer Methods in Applied Mechanics and Engineering, 200 (2011) 2805-2813.

[17] M.A. Ben Souf, O. Bareille, M.N. Ichchou, F. Bouchoucha, M. Haddar, Waves and energy in random elastic guided media through the stochastic wave finite element method, Physics Letters A, 377 (2013) 2255-2264.

[18] F. Bouchoucha, M.N. Ichchou, M. Haddar, Guided wave propagation in uncertain elastic media, Ultrasonics, 53 (2013) 303-312.

[19] L. Cremer, M. Heckl, B.A.T. Petersson, Structure-Borne Sound: Structural Vibrations and Sound Radiation at Audio Frequencies Springer, 2010.

[20] K.F. Graff, Wave Motion in Elastic Solids, Dover, 1991.

[21] F. Fahy, P. Gardonio, Sound and Structural Vibration: Radiation, Transmission and Response, Academic Press, 2006.

[22] N.R. Harland, B.R. Mace, R.W. Jones, Wave Propagation, Reflection and Transmission in Tunable Fluid-Filled Beams, Journal of Sound and Vibration, 241 (2001) 735-754.

[23] L. Hinke, L. Pichler, H.J. Pradlwarter, B.R. Mace, T.P. Waters, Modelling of spatial variations in vibration analysis with application to an automotive windshield, Finite Elements in Analysis and Design, 47 (2011) 55-62.

[24] M.W. Zehn, A. Saitov, How can spatially distributed uncertainties be included in FEA and in parameter estimation for model updating?, Shock and Vibration, 10 (2003) 15-25.

[25] M. Gangadhar, M.W. Zehn, A methodology to model spatially distributed uncertainties in thin-walled structures, ZAMM - Journal of Applied Mathematics and Mechanics / Zeitschrift für Angewandte Mathematik und Mechanik, 87 (2007) 360-376.

[26] J. Guilleminot, C. Soize, D. Kondo, C. Binetruy, Theoretical framework and experimental procedure for modelling mesoscopic volume fraction stochastic fluctuations in fiber reinforced composites, International Journal of Solids and Structures, 45 (2008) 5567-5583.

[27] E. Vanmarcke, Random Field: Analysis and Synthesis, 2nd Revised and Expanded ed., Word Scientific, Cambridge, MA, 2010.

[28] R. Ghanem, P. Spanos, Stochastic Finite Elements: A Spectral Approach, Dover Publications, 1991.

[29] B. Sudret, A. Der Kiuereghian, Stochastic Finite Element Methods and Reliability: A State-of-Art Report, in, University of California, Berkeley, 2000.

[30] G. Stefanou, The stochastic finite element method: Past, present and future, Computer Methods in Applied Mechanics and Engineering, 198 (2009) 1031-1051.

[31] B. Sudret, A. Der Kiuereghian, Stochastic Finite Element Methods and Reliability: A State-of-Art Report, in, University of California, Berkeley, 2000.

[32] B.A. Zeldin, P.D. Spanos, On Random Field Discretization in Stochastic Finite Elements, Journal of Applied Mechanics, 65 (1998) 320-327.

[33] A. Der Kiureghian, J.-B. Ke, The stochastic finite element method in structural reliability, Probabilistic Engineering Mechanics, 3 (1988) 83-91.

[34] S.P. Huang, S.T. Quek, K.K. Phoon, Convergence study of the truncated Karhunen–Loeve expansion for simulation of stochastic processes, Int. J. Numer. Meth. Engng, 52 (2001) 1029–1043.

[35] Q.S. Li, Exact solutions for free longitudinal vibration of stepped non-uniform rods, Applied Acoustics, 60 (2000) 13-28.

[36] M. Eisenberger, Exact longitudinal vibration frequencies of a variable cross-section rod, Applied Acoustics, 34 (1991) 123-130.

[37] S. Guo, S. Yang, Wave motions in non-uniform one-dimensional waveguides, Journal of Vibration and Control, 18 (2012) 92-100.

[38] I. Elishakoff, S. Candan, Apparently first closed-form solution for vibrating: inhomogeneous beams, International Journal of Solids and Structures, 38 (2001) 3411-3441.

[39] B.N. Nagarkar, R.D. Finch, Sinusoidal Horns, The Journal of the Acoustical Society of America, 50 (1971) 23-31.

[40] R.S. Langley, Wave Evolution, Reflection, And Transmission Along Inhomogeneous Waveguides, Journal of Sound and Vibration, 227 (1999) 131-158.

[41] S.K. Lee, B.R. Mace, M.J. Brennan, Wave propagation, reflection and transmission in non-uniform one-dimensional waveguides, Journal of Sound and Vibration, 304 (2007) 31-49.

[42] J.F.M. Scott, The Statistics of Waves Propagating in a One-Dimensional Random Medium, Proceedings of the Royal Society of London. Series A, Mathematical and Physical Sciences, 398 (1985) 341-363.

[43] C.S. Manohar, A.J. Keane, Axial Vibrations of a Stochastic Rod, Journal of Sound and Vibration, 165 (1993) 341-359.

[44] A.J. Keane, C.S. Manohar, Energy Flow Variability In A Pair Of Coupled Stochastic Rods, Journal of Sound and Vibration, 168 (1993) 253-284.

[45] A.D. Pierce, Physical Interpretation of the WKB or Eikonal Approximation for Waves and Vibrations in Inhomogeneous Beams and Plates, The Journal of the Acoustical Society of America, 48 (1970) 275-284.

[46] R.D. Firouz-Abadi, H. Haddadpour, A.B. Novinzadeh, An asymptotic solution to transverse free vibrations of variable-section beams, Journal of Sound and Vibration, 304 (2007) 530-540.

[47] A.H. Nayfeh, Perturbation Methods, Wiley, New York, 1973.

[48] G.B. Whitham, Linear and Nonlinear Waves, John Wiley & Sons, 1974.

[49] F.B. Jensen, W.A. Kuperman, M.B. Porter, H. Schimidt, Computational Ocean Acoustics, Springer, New York, 2011.

[50] N.C. Ovenden, A uniformly valid multiple scales solution for cut-on cut-off transition of sound in flow ducts, Journal of Sound and Vibration, 286 (2005) 403-416.

[51] S.W. Rienstra, Sound propagation in slowly varying lined flow ducts of arbitrary cross-section, Journal of Fluid Mechanics, 495 (2003) 157-173.

[52] J.P. Arenas, M.J. Crocker, A note on a WKB application to a duct of varying cross-section, Applied Mathematics Letters, 14 (2001) 667-671.

[53] N.R.T. Biggs, Wave trapping in a two-dimensional sound-soft or sound-hard acoustic waveguide of slowly-varying width, Wave Motion, 49 (2012) 24-33.

[54] S.N. Gaulter, N.R.T. Biggs, Acoustic trapped modes in a three-dimensional waveguide of slowly varying cross section, Proceedings of the Royal Society A: Mathematical, Physical and Engineering Science, (2012).

[55] T. Saito, I. Oshida, The W.K.B. Method for the Differential Equations of the Fourth Order, Journal of the Physical Society of Japan, 14 (1959) 1816-1819.

[56] I.K. Chatjigeorgiou, Application of the WKB method to catenary-shaped slender structures, Mathematical and Computer Modelling, 48 (2008) 249-257.

[57] K.P. Burr, M.S. Triantafyllou, D.K.P. Yue, Asymptotic Analysis Of Wave Propagation Along Weakly Non-Uniform Repetitive Systems, Journal of Sound and Vibration, 229 (2000) 21-64.

[58] C.R. Steele, L.A. Taber, Comparison of WKB calculations and experimental results for three-dimensional cochlear models., J Acoust Soc Am. , 65 (1979) 1007-1018.

[59] S.J. Elliott, G. Ni, B.R. Mace, B. Lineton, A wave finite element analysis of the passive cochlea, The Journal of the Acoustical Society of America, 133 (2013) 1535-1545.

[60] B.R. Mace, Reciprocity, conservation of energy and some properties of reflection and transmission coefficients, Journal of Sound and Vibration, 155 (1992) 375-381.

[61] B.R. Mace, Wave reflection and transmission in beams, Journal of Sound and Vibration, 97 (1984) 237-246.

[62] F.P. Bretherton, Propagation in Slowly Varying Waveguides, Proceedings of the Royal Society of London. Series A. Mathematical and Physical Sciences, 302 (1968) 555-576.

[63] G. SN, N.R.T. Biggs, Acoustic trapped modes in a three-dimensional waveguide of slowly varying cross section, Proceedings of the Royal Society of London. Series A, Mathematical and Physical Sciences, 469 (2013).

[64] N.S. Bardell, The free vibration of skew plates using the hierarchical finite element method, Computers & Structures, 45 (1992) 841-874.

[65] N.S. Bardell, G.J. Gange, An efficient static analysis of sandwich beams, Composite Structures, 29 (1994) 107-117.

[66] A. Boukhalfa, A. Hadjoui, Free vibration analysis of an embarked rotating composite shaft using the hp-version of the FEM, Latin American Journal of Solids and Structures, 7 (2010) 105-141.

[67] N.S. Bardell, Free vibration analysis of a flat plate using the hierarchical finite element method, Journal of Sound and Vibration, 151 (1991) 263-289.

[68] W. Han, M. Petyt, Linear vibration analysis of laminated rectangular plates using the hierarchical finite element method—I. Free vibration analysis, Computers & Structures, 61 (1996) 705-712.

[69] A. Houmat, An Alternative Hierarchical Finite Element Formulation Applied To Plate Vibrations, Journal of Sound and Vibration, 206 (1997) 201-215.

[70] Y. Waki, B.R. Mace, M.J. Brennan, Numerical issues concerning the wave and finite element method for free and forced vibrations of waveguides, Journal of Sound and Vibration, 327 (2009) 92-108.

[71] J.M. Renno, B.R. Mace, On the forced response of waveguides using the wave and finite element method, Journal of Sound and Vibration, 329 (2010) 5474-5488.

[72] D. Dubin, Numerical and Analytical Methods for Scientists and Engineers, Using Mathematica, Wiley-Interscience, 2003.

[73] P. Filippi, D. Habault, J.P. Lefebvre, A. Bergassoli, Acoustics: Basic Physics, Theory and Methods, Academic Press, 1999.

[74] R.S. Langley, Wave Transmission Through One-Dimensional Near Periodic Structures: Optimum and Random Disorder, Journal of Sound and Vibration, 188 (1995) 717-743.

[75] Y.K. Lin, G.Q. Cai, Probabilistic Structural Dynamics: Advanced Theory and Applications, McGraw-Hill, 1995.

[76] W. Han, M. Petyt, Linear vibration analysis of laminated rectangular plates using the hierarchical finite element method—II. Forced vibration analysis, Computers & Structures, 61 (1996) 713-724.

[77] W. Han, M. Petyt, Geometrically nonlinear vibration analysis of thin, rectangular plates using the hierarchical finite element method—I: The fundamental mode of isotropic plates, Computers & Structures, 63 (1997) 295-308.

[78] A. Houmat, Nonlinear free vibration of a composite rectangular specially-orthotropic plate with variable fiber spacing, Composite Structures, 94 (2012) 3029-3036.

[79] G.I. Schueller, A state-of-the-art report on computational stochastic mechanics, Probabilistic Engineering Mechanics, 12 (1997) 197-321.

[80] H. Benaroya, S.M. Han, Probability Models in Engineering and Science, CRC Press, 2005

[81] P.S. Koutsourelakis, H.J. Pradlwarter, G.I. Schuëller, Reliability of structures in high dimensions, part I: algorithms and applications, Probabilistic Engineering Mechanics, 19 (2004) 409-417.

[82] H.F. Lei, Z.Q. Zhang, B. Liu, Effect of fiber arrangement on mechanical properties of short fiber reinforced composites, Composites Science and Technology, 72 (2012) 506-514.

[83] S. Sriramula, M.K. Chryssanthopoulos, Quantification of uncertainty modelling in stochastic analysis of FRP composites, Composites Part A: Applied Science and Manufacturing, 40 (2009) 1673-1684.

[84] M. Ostoja-Starzewski, Material spatial randomness: From statistical to representative volume element, Probabilistic Engineering Mechanics, 21 (2006) 112-132.

[85] S. Baxter, L. Graham, Characterization of Random Composites Using Moving-Window Technique, J. Eng. Mech., 126 (2000) 389-397.

[86] J. Guilleminot, C. Soize, D. Kondo, Mesoscale probabilistic models for the elasticity tensor of fiber reinforced composites: Experimental identification and numerical aspects, Mechanics of Materials, 41 (2009) 1309-1322.

[87] L. Mehrez, A. Doostan, D. Moens, D. Vandepitte, Stochastic identification of composite material properties from limited experimental databases, Part II: Uncertainty modelling, Mechanical Systems and Signal Processing, 27 (2012) 484-498.

[88] L. Mehrez, D. Moens, D. Vandepitte, Stochastic identification of composite material properties from limited experimental databases, part I: Experimental database construction, Mechanical Systems and Signal Processing, 27 (2012) 471-483.

[89] J.M. Gan, S. Bickerton, M. Battley, Automated Characterization of Variability in Glass Fibre Reinformcement Architecture, in: C. Binetruy, F. Boussu (Eds.) Proceeding of the 10th International Conference on Textile Composites - TEXCOMP10, Lille, France, 2010, pp. 148-156.

[90] B.A. Zeldin, P.D. Spanos, On Random Field Discretization in Stocastic Finite Elements, Transactions of ASME, 65 (1998) 320-327.

[91] B.P. Naughton, F. Panhuizen, A.C. Vermeulen, The Elastic Properties of Chopped Strand Mat and Woven Roving in G.R. Laminae, Journal of Reinforced Plastics and Composites, 4 (1985) 195-204.

[92] E. Vanmarcke, Random Field: Analysis and Synthesis, The MIT Press, Cambridge, MA, 1983.

[93] D.E. Newland, An introduction to random vibrations, spectral & wavelet analysis, Dover Publications, 2005.

[94] K. Shin, J.K. Hammond, Fundamentals of Signal Processing for Sound and Vibration Engineers, John Wiley & Sons Inc., 2008.

[95] R.G. Ghanem, A. Doostan, J. Red-Horse, A probabilistic construction of model validation, Computer Methods in Applied Mechanics and Engineering, 197 (2008) 2585-2595.

[96] R.G. Ghanem, A. Doostan, On the construction and analysis of stochastic models: Characterization and propagation of the errors associated with limited data, Journal of Computational Physics, 217 (2006) 63-81.

[97] C. Soize, Non-Gaussian positive-definite matrix-valued random fields for elliptic stochastic partial differential operators, Computer Methods in Applied Mechanics and Engineering, 195 (2006) 26-64.

[98] B. Puig, F. Poirion, C. Soize, Non-Gaussian simulation using Hermite polynomial expansion: convergences and algorithms, Probabilistic Engineering Mechanics, 17 (2002) 253-264.

[99] B. Puig, J.-L. Akian, Non-Gaussian simulation using Hermite polynomials expansion and maximum entropy principle, Probabilistic Engineering Mechanics, 19 (2004) 293-305.

[100] D.J. Ewins, Modal Testing: Theory, Practice and Application, John Wiley & Sons Ltd., 2000.